AN ABSTRACT OF THE DISSERTATION OF

Nitish Kumar for the degree of Doctor of Philosophy in Materials Science presented on September 15, 2016.

Title: Defect Mechanisms in Bismuth-based Perovskites.

Abstract approved:

_____

David P. Cann

The aim of this research is to develop a fundamental understanding of the dominant defect species and the relevant defect equilibrium conditions for bismuth-containing perovskites to help guide the development of these materials for emerging applications. This is of paramount importance for many demanding applications, because ultimately the defect equilibria have a profound influence on phenomena such as piezoelectric fatigue, reliability, and leakage current. At the same time, they can be used to tailor properties to make these materials better suited for specific applications. Perovskite materials with Bi^{3+} on the A-site have been the focus of great technical interest over the last decade. A number of compositions based on Bi-perovskites (*e.g.* $(Bi,Ba)(B^{2+},Ti)O_3$) are being studied for high energy density (or high temperature) capacitor applications. In addition, a number of Bi-based perovskite materials have shown great promise as a replacement for $Pb(Zr,Ti)O_3$ (PZT) for piezoelectric applications. Compounds such as $(Bi_{1/2}K_{1/2})TiO_3$ (BKT) and $(Bi_{1/2}Na_{1/2})TiO_3$ (BNT), and their solid solutions with $BaTiO_3$ and other tetragonal perovskites exhibit useful piezoelectric properties and are considered to be promising candidates to replace Pb-based materials if the underlying defect chemistry can be controlled. The technological impact of these materials is expected to grow because research in this area is being driven by increased environmental regulations and energy efficiency considerations. While much of the current research and progress on Bi-perovskites have been focused on primary materials properties like the

piezoelectric coefficient, relative permittivity, etc., there have been few studies on the underlying fundamental defect chemistry and they are not fully understood.

This research focuses mainly on two material systems to study their defect chemistry and transport properties. First is $Bi(Zn_{1/2}Ti_{1/2})O_3$–$BaTiO_3$, for high performance capacitor applications. Conventional approaches to this technical challenge include utilizing ferroelectric or antiferroelectric materials with permittivities in excess of 1000. However, these non-linear materials derive their high permittivity from domain contributions that saturate at relatively low fields ultimately resulting in limited energy densities. However, solid solutions based on $Bi\mathit{M}O_3$-$BaTiO_3$ that exhibit relaxor behavior can potentially demonstrate high energy densities. The second material system investigated was BNT-BKT- $Bi(Mg_{1/2}Ti_{1/2})O_3$. This material features a field-induced relaxor-to-ferroelectric transition that is accompanied by a large piezoelectric strain values.

The first part of the thesis focuses on polycrystalline $BaTiO_3$-$Bi(Zn_{1/2}Ti_{1/2})O_3$ (BT-BZT) ceramics, which have been shown to exhibit superior dielectric properties for high temperature and high energy density applications as compared to the existing materials. As miniaturization without compromising cost and performance is vital for several applications, chapter 9.1 shows the results on multilayer ceramic capacitors based on relaxor BT-BZT ceramics. In bulk ceramic embodiments, BT-BZT has been shown to exhibit relative permittivities greater than 1000, high resistivities ($\rho >$ 1 GΩ-cm at 300°C), and negligible saturation up to fields as high as 150 kV/cm. The multilayer capacitor embodiments exhibited similar dielectric and resistivity properties. The energy density for the multilayer ceramics reached values of ~2.8 J/cm^3 at room temperature at an applied electric field of ~330 kV/cm. This represents a significant improvement compared to commercially available multilayer capacitors. The dielectric properties were also found to be stable over a wide range of temperatures with a temperature coefficient of approximately -2000 ppm/K measured from 50 to 350 °C, an important criteria for high temperature applications. Finally,

the compatibility of inexpensive Ag-Pd electrodes with these ceramics was also demonstrated, which can have implications on minimizing the device cost.

Having demonstrated that BT-BZT exhibits promising properties, the primary focus of this thesis research is developing a fundamental understanding of the transport properties and defect chemistry. A significant improvement in insulation properties was measured with the addition of BZT to BT. Both low-field AC impedance and high field direct DC measurements indicated an increase in resistivity of at least 2 orders of magnitude at 400 °C with the addition of just 3% BZT (~10^7 Ω-cm) into the solid solution as compared to pure BT (~10^5 Ω-cm). This effect was also evident in dielectric loss data, which remained low at higher temperatures as the BZT content increased. In conjunction with band gap measurements, it was also concluded that the conduction mechanism transitioned from extrinsic for pure BT to intrinsic-like for 7.5% BZT suggesting a change in the fundamental defect equilibrium conditions. It was also shown that this improvement in insulation properties was not limited to BT-BZT, but could also be observed in $SrTiO_3$-BZT system.

While pure BT exhibits extrinsic p-type conduction, it is reported that BT-BZT ceramics exhibit intrinsic-like n-type conduction using atmosphere dependent conductivity measurements. Annealing studies and Seebeck measurements were performed and confirmed this result. For BT, resistivity values were higher for samples annealed in nitrogen as compared to oxygen, while the opposite responses were observed for BZT-containing solid solutions. This suggested a possibile unintentional donor doping upon addition of BZT to the solid solution, which may also be linked to the improvement in resistivity in BT-BZT ceramics as compared to pure BT.

Impedance spectroscopy in conjunction with small DC-bias provided further proof of the p-type to n-type transition and also demonstrated the field-stable properties of BT-BZT ceramics. For p-type $BaTiO_3$, the ceramics deviated from Ohm's law behavior at very low voltage levels along with a reversible drop in bulk

resistivity by several orders of magnitude starting at bias fields as low as 0.1 kV/cm (~8 V). In contrast, n-type BT-BZT ceramics exhibited a small (i.e. less than one order of magnitude) increase in resistivity on application of small field levels. These data indicate a hole-generation mechanism which becomes active at a low voltage threshold. The bulk capacitance values calculated using AC impedance spectroscopy, however, were relatively unaffected (<15% change) by this application of a DC bias (up to ~0.25 kV/cm). These findings provide further insights into the electric transport mechanisms in BT-based ceramics.

To investigate the possible presence of Bi^{5+} in BT-BZT ceramics, which was postulated to be one of the possible mechanisms for n-type behavior in BT-BZT ceramics, some BT-$BaBiO_3$ solid solutions were fabricated. The $BaBiO_3$ ceramics were sintered in oxygen to obtain a single phase with monoclinic *I*2/m symmetry as suggested by high-resolution x-ray diffraction. X-ray photoelectron spectroscopy confirmed the presence of bismuth in two valence states – 3+ and 5+. Optical spectroscopy showed presence of a direct band gap at ~2.2 eV and a possible indirect band gap at ~0.9 eV. This combined with determination of the activation energy for conduction of 0.25 eV, as obtained from *ac* impedance spectroscopy, suggested that a polaron-mediated conduction mechanism was prevalent in $BaBiO_3$. These $BaBiO_3$ ceramics were crushed, mixed with $BaTiO_3$, and sintered to obtain $BaTiO_3$-$BaBiO_3$ solid solutions. All the ceramics had tetragonal symmetry and exhibited a normal ferroelectric-like dielectric response. Using *ac* impedance and optical spectroscopy, it was shown that resistivity values of $BaTiO_3$-$BaBiO_3$ were orders of magnitude higher than $BaTiO_3$ or $BaBiO_3$ alone, indicating a change in the fundamental defect equilibrium conditions. A shift in the site occupancy of Bi to the A-site is proposed to be the mechanism for the increased electrical resistivity.

To investigate the effect of A-site nonstoichiometry in BT-Bi*M*O_3 ceramics, $BaTiO_3$-$BiScO_3$ (BT-BS) and $SrTiO_3$-$Bi(Zn_{1/2}Ti_{1/2})O_3$ (ST-BZT) were fabricated. The effect of nonstoichiometry on the dielectric and transport properties was studied using temperature- and oxygen partial pressure-dependent AC impedance spectroscopy. For

p-type BT-BS ceramics, the addition of excess Bi led to effective donor doping along with a significant improvement in insulation properties. A similar effect was observed on introducing Ba vacancies onto the A-sublattice. However, Bi deficiency had an opposite effect with effective acceptor doping and a deterioration in the bulk resistivity values. For n-type intrinsic ST-BZT ceramics, the addition of excess Sr onto the A-sublattice resulted in a decrease in resistivity values, as expected. Introduction of Sr vacancies or addition of excess Bi on A-site did not appear to affect the insulation properties in air. These results indicate that minor levels of non-stoichiometry can have an important impact on the material properties and furthermore it demonstrates the difficulties encountered in trying to establish a general model for the defect chemistry of Bi-containing perovskite systems.

Finally, the other prospective candidates for n-type behavior in BT-BZT were studied—loss of volatile cations, oxygen vacancies, bismuth present in multiple valence states and precipitation of secondary phases. Combined x-ray and neutron diffraction, prompt gamma neutron activation analysis and electron energy loss spectroscopy suggested much higher oxygen vacancy concentration in BT-BZT ceramics as compared to BT alone. X-ray photoelectron spectroscopy and x-ray absorption spectroscopy did not suggest presence of bismuth in multiple valence states. At the same time, using transmission electron microscopy, some secondary phases were observed, whose compositions were such that they could result in effective donor doping in BT-BZT ceramics. Using experimentally determined thermodynamic parameters for BT and slopes of conductivity-oxygen partial pressure curves, it has been suggested that an ionic compensation mechanism is prevalent in these ceramics instead of electronic compensation. However, these defects in BT-BZT ceramics have an effect of shifting the conductivity minimum in conductivity-oxygen partial pressure curves to higher oxygen partial pressure values, resulting in significantly higher resistivity values in air atmosphere. This provides an important tool to tailor transport properties and defects in BT-BiMO$_3$ ceramics, to make them better suited for dielectric applications.

The second Bi-based ceramic system which was looked at was lead-free $Bi(Mg_{1/2}Ti_{1/2})O_3$-$(Bi_{1/2}K_{1/2})TiO_3$-$(Bi_{1/2}Na_{1/2})TiO_3$ for sensors and actuator applications. There has been a huge drive to replace Pb from existing ceramics (*e.g.* lead zirconate titanate) due to health and environmental concerns. The dielectric spectra showed a T_{max} of more than 320 °C for all compositions and the transitions became increasingly diffuse as the $Bi(Mg_{1/2}Ti_{1/2})O_3$ content increased. A lower temperature transition, indicating a transformation from an ergodic to a non-ergodic relaxor state, was also seen for all compositions and this transition temperature decreased as the mole fraction of $Bi(Mg_{1/2}Ti_{1/2})O_3$ increased. The composition with 1% $Bi(Mg_{1/2}Ti_{1/2})O_3$ showed characteristic ferroelectric-like polarization and strain hysteresis. However, compositions with increased $Bi(Mg_{1/2}Ti_{1/2})O_3$ content became increasingly ergodic at room temperature with pinched polarization loops and no negative strain. Among these compositions, the magnitude of d_{33}* increased with $Bi(Mg_{1/2}Ti_{1/2})O_3$ content and the composition with 10% $Bi(Mg_{1/2}Ti_{1/2})O_3$ exhibited a d_{33}* of 422 pm/V . Fatigue measurements were conducted on all compositions and while the 1% $Bi(Mg_{1/2}Ti_{1/2})O_3$ composition exhibited a measurable, but small loss in maximum strain after a million cycles; all the other compositions from 2.5% to 10% $Bi(Mg_{1/2}Ti_{1/2})O_3$ were essentially fatigue-free. Lastly, optical and AC impedance measurements were employed to identify intrinsic conduction as the dominant conduction mechanism. These compositions were also highly insulating with high resistivities (~10^7 Ω-cm) at high temperatures (440 °C).

To investigate the role of point defects on the fatigue characteristics, the composition 5%BMT-40%BKT-55%BNT was doped to incorporate acceptor and donor defects on the A and B sites by adjusting the Bi/Na and Ti/Mg stoichiometries. All samples had pseudo-cubic symmetries based on x-ray diffraction, typical of relaxors. Dielectric measurements showed that the high and low temperature phase transitions were largely unaffected by doping. Acceptor doping resulted in the observation of a typical ferroelectric-like polarization with a remnant polarization and strain hysteresis loops with significant negative strain. Donor-doped compositions exhibited characteristics that were indicative of an ergodic relaxor phase. Fatigue

measurements were carried out on all of the compositions. While the A-site acceptor-doped composition showed a small degradation in maximum strain after 10^6 cycles, the other compositions were essentially fatigue free. Impedance measurements were used to identify the important conduction mechanisms in these compositions. As expected, the presence of defects did not strongly influence the fatigue behavior in donor-doped compositions owing to the nature of their reversible field-induced phase transformation. Even for the acceptor-doped compositions, which had stable domains in the absence of an electric field at room temperature, there was negligible degradation in the maximum strain due to fatigue. This suggests that either the defects introduced through stoichiometric variations do not play a prominent role in fatigue in these systems or it is compensated by factors like decrease in coercive field, an increase in ergodicity, symmetry change, or other factors.

The results obtained for these ceramic systems have provided significant insights in the defect chemistry and transport properties and are expected to help improve performance of these emerging materials for energy and MEMS technologies.

©Copyright by Nitish Kumar
September 15, 2016
All Rights Reserved

Defect Mechanisms in Bismuth-based Perovskites

by
Nitish Kumar

A DISSERTATION

submitted to

Oregon State University

in partial fulfillment of
the requirements for the
degree of

Doctor of Philosophy

Presented September 15, 2016
Commencement June 2017

Doctor of Philosophy dissertation of Nitish Kumar presented on September 15, 2016

APPROVED:

Major Professor, representing Materials Science

Director of the Materials Science Program

Dean of the Graduate School

I understand that my dissertation will become part of the permanent collection of Oregon State University libraries. My signature below authorizes release of my dissertation to any reader upon request.

Nitish Kumar, Author

ACKNOWLEDGEMENTS

First of all, I would like to thank my advisor Dr. David Cann for making my PhD journey memorable, I have thoroughly enjoyed it. Especially, I would like to thank him for constant support and freedom, which he has provided me for last five years. At the same time, I have learnt a lot from him—his friendliness and professionalism, student management skills, organization, time management and others. I am also grateful to him for the opportunities he provided me with for professional and personality development. Probably unprofessional on my part, but I always considered him as a friend and he was always there to help whenever required. I could not have asked for a better experience.

I could not have asked for a better research group as well. All the researchers who joined our group during my time here, were very helpful and supportive. They were always ready to sort out my troubles and answer my questions, no matter how stupid they sounded. I have benefitted from all the discussions with them and their help inside and outside of the laboratory. I would especially like to thank Sasiporn Prasertpalichat, Troy Ansell, Eric Patterson, Narit Traimnak, Natthaphon Raengthon, Whitney Schmidt and Alex Ionin—I don't think I can count how many times these guys have helped me out in situations of crisis.

I would like to thank my Committee members—Michelle Dolgos, Mas Subramanian, Greg Herman and Frank Tepley for their help, support and useful suggestions regarding my research, whenever required.

I had wonderful opportunities to do short internships at Technische Universität Darmstadt, Germany and Hewlett-Packard Company, Corvallis. I am grateful to Prof. Jürgen Rödel for providing me opportunity of internship at Darmstadt as it was useful in solving an important piece of my research puzzle. I would like to thank Eric Patterson and Till Frömling for their help with our experiments there. I would also like to convey my special thanks to Eric for being a good friend and all his help during my stay there, especially outside work. The internship at Hewlett-Packard Company was instrumental in teaching me about thin

films and their characterization, and I would like to thank Ken Vandehey for this nice opportunity. I would also like to thank Argonne National Laboratories, US Department of Energy and Oak Ridge National Laboratories for National School on Neutron and X-Ray Scattering, which was critical for my exposure to various scattering experiments, which turned out to be of great help during my research.

I have also made several awesome friends during my stay here at Oregon State University. It will take several pages to mention all of them, but at minimum I would like to mention Laura Oliveira, Ashley Mason, Trevor Howard, Connor McCue, Nopsiri Chaiyo, Divya Jain, Ankush Kothalkar, Rattiphorn Sumang and Mark Winseck. It's never easy to move halfway across the globe to start a new career, and I would like to thank the Indian Student Association—especially Saranam Rajesh, Kunal Kate and Atul Dhage for their help throughout my stay here and company for memorable cricket matches.

I would like to thank some people who have helped me with various experiments over the last five years—Austin Fox, Joel Walenza-Slabe, Brady Gibbons, Steve Golledge, Peter Escbach, Syed Khalid, Edward Gorzkowski, Goknur Tutuncu, Steve Reese, Ian Love and Michelle Dolgos and her group. I owe Brady Gibbons for many other things, including tolerating my personality at times!

Most importantly, I would like to thank my family—my mother, father and sister, who have supported me for everything over all these years. My demands from my parents were not always trivial and on most occasions we were not financially well off, but my parents did their best to make sure we didn't experience any inconvenience. Thank you for all your sacrifices! I am grateful to my sister as well for being lovingly annoying! No amounts of words are sufficient to express my gratitude and love to my family.

CONTRIBUTION OF AUTHORS

As my PhD advisor and principal investigator, Prof. David P. Cann has contributed to all the work shown in this thesis. Dr. Till Frömling and Dr. Eric Patterson helped me with impedance spectroscopy and other experiments during my internship at Technische Universität Darmstadt, Germany. Aleksey Ionin and Dr. Troy Ansell helped with characterization of multilayer ceramic capacitors. Seongtae Kwon and Wesley Hackenberger fabricated the multilayer ceramic capacitors and also characterized them. Dr. Stephen L. Golledge helped with the the x-ray photoelectron spectroscopy measurements. Dr. Edward Gorzkowski performed the thermogravimetric analysis with in-situ mass spectroscopy. Dr. Peter Eschbach helped with the transmission electron microscopy experiments. Ian Love and Dr. Steven R. Reese helped with prompt gamma neutron activation analysis. Dr. Syed Khalid helped with x-ray absorption experiments.

TABLE OF CONTENTS

Page

1 Introduction ..…… 1

2 Basic Terminologies ……..……...… 4

2.1 Dielectric Permittivity and Loss ……...……..….... 4

2.2 Polarization Mechanisms: Origins of dielectric constant.…….…….... 5

2.3 Piezoelectricity …….……..…… 7

2.4 Pyroelectricity ……..……..…… 9

2.5 Ferroelectricity …….…… 10

2.6 Antiferroelectricity ……...…… 14

2.7 Electrostriction …….…… 14

3 Crystal Structure in Piezoelectricity ……...…… 18

4 Perovskites ……....…….… 23

4.1 Tuning the properties of perovskites for practical applications ……... 26

5 Relaxor Ferroelectrics ….…… 30

5.1 Small-signal dielectric response …….. 31

5.2 Compositional disorder in relaxors …….……. 33

5.3 Temperature evolution of relaxors……..... 34

5.4 BaTiO3 (BT)-based relaxors ……..... 36

6 Review of Defect Chemistry of M_2O_3 ceramics …….…….. 41

7 Unique properties of $BaTiO_3$–$Bi(Zn_{1/2}Ti_{1/2}O)_3$ ceramics ……..… 54

8 Materials Synthesis and Characterization …….…… 62

9 The $BaTiO_3$–$Bi(Zn_{1/2}Ti_{1/2}O)_3$ (BT–BZT) ceramics ……...……..…….. 72

TABLE OF CONTENTS (Continued)

Page

9.1 Multilayer ceramic capacitors based on relaxor BT–BZT ceramics 73

9.2 Resistivity enhancement in BT–BZT and $SrTiO_3$–BZT ceramics …...… 86

9.3 Conductions mechanisms in BT–BZT ceramics ……..... 110

9.4 DC-bias dependent impedance spectroscopy of BT–BZT ceramics 140

9.5 Synthesis and electrical characterization of $BaBiO_3$ and BT–$BaBiO_3$ ceramics …….....…… 157

9.6 Nonstoichiometry in BT–$BiScO_3$ and $SrTiO_3$–BZT ceramics ……...… 183

9.7 Defect chemistry of BT–Bi$M$$O_3$ ceramics ……...…….. 208

10 The $Bi(Mg_{1/2}Ti_{1/2})O_3$–$(Bi_{1/2}K_{1/2})TiO_3$–$(Bi_{1/2}Na_{1/2})TiO_3$ (BMT–BKT–BNT) ceramics ……..……. 253

10.1 Electromechanical strain and bipolar fatigue in BMT–BKT–BNT ceramics ……...…… 253

10.2 Role of point defects in bipolar fatigue behavior of BMT–BKT–BNT relaxor ceramics ……..……. 271

11 Conclusions ……. 296

12 Future Work …… 303

LIST OF FIGURES

Figure Page

2.2.1 Various polarization mechanisms in common dielectric materials ……..... 6

2.2.2 Typical dielectric spectra of a solid showing both the real (a) and imaginary (b) components ……...….... 7

2.4.1 As $BaTiO_3$ cools down, it transforms from paraelectric cubic phase to ferroelectric tetragonal phase. The cubic phase has higher symmetry than tetragonal phase ……..... 11

2.4.2 Typical polarization and strain hysteresis loops in a ferroelectric material …….…… 13

4.1 Multifunctional perovskites, diagram taken from Bhalla *et al.* The acronym PZT stands for lead zirconate titanate, LCM for lanthanum cobaltates and manganates, GMR for giant magnetoresistance and YBCO for Yttrium Barium Copper Oxide …….…… 23

4.2 (a) A typical perovskite structure with A-cation at the cube corners (brown), B-cation at the center (purple) and the anions at face center (red), (b) An alternate presentation with A-cation at the center. The anion octahedra can be seen for both of them ……...… 24

5.1 Dielectric response of $BaTiO_3$-$Bi(Zn_{1/2}Ti_{1/2})O_3$, which exhibits a typical dielectric response of a relaxor ferroelectric material. Figure 5.1.1 can also be referred to for further details on relaxors ……..…… 30

5.1.1 Temperature evolution of dielectric properties for disordered perovskites. Four different possibilities have been shown: (a) Canonical relaxor, (b) ceramics with diffuse relaxor to ferroelectric transition, (c) ceramics with sharp relaxor to ferroelectric transition, and (d) ceramics with sharp relaxor to ferroelectric transition with T_c and T_m coinciding ……...……...…… 32

5.4.1 (a) Temperature evolution of dielectric constant for (1-x)BT-$La(Mg1/2Ti1/2)O_3$ ceramics, (b) Temperature evolution of inverse permittivity for the same compositions with Curie-Weiss fitting ……..…… 38

6.1 Typical defect diagram of acceptor-doped M_2O_3 adapted from Smyth et al. ….. 45

6.2 Typical defect diagram of donor-doped M_2O_3 …… 48

6.3 Electrical conductivity isotherms for BT adapted from Yoo *et al.* at various temperatures, which includes the data from several other authors as well …… 49

LIST OF FIGURES (Continued)

Figure Page

7.1 (a) Evolution of temperature-dependent relative permittivity with composition for (1-x)BT-xBZT ceramics, (b) relative permittivity versus temperature for 0.93BT-0.07BZT exhibiting moderate DPT behavior, (c) temperature-dependent relative permittivity for 0.89BT-0.11BZT exhibiting relaxor characteristics (from Triamnak et al.), and (d) evolution of dielectric behavior for BT-xBZT (x between 0.2 to 0.34) ceramic with increasing content adapted from Huang et al……..... 54

7.2 Figure showing temperature-dependent dielectric behavior of BT-BZT-ABO_3 ceramics and their potential to be tuned as per requirements ……...…. 55

7.3 Raman spectroscopy on BT-BZT adapted from Triamnak et al. …..…….…. 56

7.4 Figure showing polarization hysteresis loops for (1-x)BT-xBZT ceramics and their evolution with BZT content ……... 58

7.5 Plot comparing the field dependent permittivity of BT-BZT ceramics with other commercial ceramic capacitors …….……. 59

7.6 The lattice parameters obtained from PDFs are shown as red and black symbols. The blue lines indicate the tetragonal The lattice parameters obtained from the Rietveld refinements (blue lines for tetragonal and dashed pink for cubic space group) have also been shown for reference …….…….. 59

8.1 (a) X-ray diffraction patterns of calcined BT-20BZT ceramics at various temperatures. B = $BaCO_3$, T = TiO_2, * = perovskite phases, # = multiple phases, i = Bi_2O_3, z = ZnO …….……...…… 68

8.2 Densification (radial shrinkage) as a function of temperature for BT and BT-BZT ceramics, measured in-situ using a dilatometer and ex-situ by holding at a temperature for two hours, quenching it and measuring shrinkage ……... 69

9.1.1 Temperature dependence of relative permittivity and dielectric loss for (a) 80BT-20BZT and (b) 85BT-15BZT MLCCs from 250 Hz to 10 kHz …….…. 78

9.1.2 Nyquist plots for (a) 80BT-20BZT and (b) 85BT-15BZT MLCCs at 400 °C and (c) Arrhenius plots for AC and DC resistivity …….…….. 79

9.1.3 (a) Polarization as a function of electric field for 85BT-15BZT MLCCs and (b) the energy density of 85BT-15BZT as a function of electric field at various temperatures ……...… 80

LIST OF FIGURES (Continued)

Figure Page

9.1.4 (a) Polarization and (b) energy density as a function of electric field of 80BT-20BZT multi-layer capacitors with Ag-Pd electrodes ……... 81

9.1.5 SEM image of an internal cross-section of the MLCC with Ag-Pd internal electrodes ……..…. 82

9.2.1 X-ray diffraction patterns of as-sintered stoichiometric (1-x)BT-xBZT where x=0%, 3%, 5%, 7.5%,10% ……. 92

9.2.2 Temperature dependence of dielectric constant (solid lines) and dielectric loss (dashed lines) for (a) BT, (b) BT-3BZT, (c) BT-5BZT, (d) BT-7.5BZT, and (e) BT-10BZT samples …….. 94

9.2.3 The Z* complex plane plots for all the compositions have been shown. Contributions from both bulk and grain boundary could be observed. The Z'' and Z' represent the imaginary and real parts of complex impedance respectively ……. 95

9.2.4 The Arrhenius plots for all compositions are shown. The bulk and grain boundary (GB) components have been obtained from the Z* complex plane plots. The DC or the zero frequency (0Hz) component was obtained from Z* complex plane plots after extrapolating the AC impedance data on the low-frequency side. A clear increase in resistivity on adding BZT could be observed ……..…. 96

9.2.5. (a) The Arrhenius plots for all compositions obtained from direct DC measurements have been shown. The currents were swept on logarithmic scale and the voltages were measured to determine the resistivity from the slope of voltage-current plot. (b) The Arrhenius plots for AC (0 Hz) and direct DC measurements for BT and 10BZT ceramics have been shown for comparison …….. 97

9.2.6 Tauc plot, where F(R) is the ratio of effective absorption and scattering coefficients and hν is photon energy for various compositions ……..…. 100

9.2.7 X-ray diffraction patterns of as-sintered stoichiometric (1-x)ST-xBZT where x=0%, 5%, 10% ……...… 102

9.2.8 Temperature dependence of dielectric constant (solid lines) and dielectric loss (dashed lines) for (a) ST, (b) ST-5BZT and (c) ST-10BZT samples ……..…. 103

9.2.9 The Arrhenius plots for all compositions are shown. The bulk and grain boundary (GB) components have been obtained using the Z* complex plane plots. The DC or the zero frequency component was obtained from Z* complex plane plots after extrapolating the AC impedance data on the low-frequency side ……..……. 104

LIST OF FIGURES (Continued)

Figure Page

9.2.10 Thermally stimulated depolarization current (TSDC) plots for (a) ST and (b) ST-5BZT compositions with polarization fields varying from 1.25 kV/cm to 5 kV/cm ……... 104

9.3.1 The Arrhenius plots for the bulk resistivity of BT, 3BZT and 7.5BZT in air are shown. The resistivities were obtained from the Z* complex plane plots. The BZT containing ceramics had ~2 orders of magnitude higher resistivity as compared to the unmodified BT ……..…… 117

9.3.2 (a) Complex plane plots for BT in vacuum, air and oxygen at 400 °C. The Arrhenius plots for data taken in vacuum, air and oxygen are also shown for (b) bulk, (c) grain boundary and (d) DC resistivities. The arrows in Arrhenius plots indicate the direction of increasing pO_2 ……...…… 119

9.3.3 The idealized defect diagram for undoped or acceptor doped barium titanate adapted from Smyth *et al*. ……..... 124

9.3.4 (a) Complex plane plots for 3BZT ceramics in vacuum, air and oxygen at 400 °C. The Arrhenius plots in vacuum, air and oxygen have also been shown for (b) bulk, (c) grain boundary and (d) DC resistivities as a function of temperature. The arrows in Arrhenius plots indicate the direction of increasing pO_2 ……. 126

9.3.5 (a) Complex plane plots for 7.5BZT ceramics in vacuum, air and oxygen at 400 °C. The Arrhenius plots in vacuum, air and oxygen have also been shown for (b) bulk, (c) grain boundary and (d) DC resistivities. The arrows in Arrhenius plots indicate the direction of increasing pO_2 ……..……. 130

9.3.6 Variation of conductivity with oxygen partial pressure for the three compositions at 400 °C and 500 °C ……. 131

9.3.7 The Arrhenius plots for various compositions after annealing in oxygen or nitrogen at 1100 °C for 8 hours. Plots (a-c) show the bulk, grain boundary and DC resistivity for BT. Figures (d-f) and (g-i) show the same for 3BZT and 7.5BZT ceramics, respectively ……..…… 134

9.4.1 DC voltage-current characteristics of (a) BT, (b) BT-3BZT and (c) BT-7.5BZT ceramics at ~200 °C ……. 144

9.4.2 (a) Complex plane plots for BT with DC bias between 0-8 V at 300 °C, (b) Complex plane plots for 3BZT with DC bias between 0-20 V at 300 °C, (c) Complex plane plots for 7.5BZT with DC bias between 0-20 V at 300 °C. Variation in bulk, grain boundary and DC resistivities with DC bias for (d) BT, (e) 3BZT and (f) 7.5BZT ceramics. The DC resistivity reported here was obtained from Z* complex

Figure Page

plane plots by extrapolating the AC impedance data on the low-frequency side to the x-axis intercept ……..… 150

9.4.3 Imaginary modulus as a function of DC-bias (V) for (a) BT, (b) BT-3BZT and (c) BT-7.5BZT ceramics ……..……. 152

9.5.1 (a) X-ray diffraction pattern of $BaBiO_3$ sintered in air (bottom) and oxygen (top). The square boxes show the color of the pellets after being sintered in air and oxygen. (b) Rietveld refinement of a high-resolution XRD pattern of $BaBiO_3$ sintered in oxygen. The data presented with (+) symbol is the observed data and the black curves are calculated intensities. The bottom-most curve (blue) is the difference between observed and calculated intensities ……...……. 164

9.5.2 X-ray photoelectron spectroscopy on powdered $BaBiO_3$ ceramics. The data shown with "x" symbols are actual data obtained from the experiment. The background and fitted peaks have also been indicated. The low intensity fitted peaks (red) are from Bi^{5+}……..... 166

9.5.3 (a) Permittivity and dielectric loss as a function of temperature at 1 KHz, 10 KHz and 100 KHz for $BaBiO_3$ ceramics, and (b) Arrhenius plot of applied frequency and $1/T_m$, where T_m are the temperatures at dielectric tangent maximum ……... 168

9.5.4 Kubelka-Munk and Tauc plots for BB ceramics. The appropriate functions for direct and indirect band gaps were chosen for (a) and (b) respectively. Figures (a) and (b) also show representative fit lines used to estimate band gaps. Figure (c) shows Arrhenius plot with linear fit for bulk resistivity obtained from *ac* impedance spectroscopy ……..… 169

9.5.5 X-ray diffraction pattern of (1-x)BT-xBB ceramics, where x lies between 0.1 mol% and 2 mol%. The "*" indicates secondary phase, if present ……. 172

9.5.6 Permittivity and dielectric loss as a function of temperature at 1 KHz, 10 KHz and 100 KHz for (a) BT-0.1BB, (b) BT-0.3BB, (c) BT-0.5BB, (d) BT-1BB, and (e) BT-2BB ceramics ……. 173

9.5.7 (a) Arrhenius plots for bulk resistivity obtained from *ac* impedance spectroscopy for BT-BB ceramics. Plots for undoped BB and BT have been shown for reference. (b) Kubelka-Munk and Tauc plots for BT-BB ceramics. The appropriate function for indirect band gap was chosen. Representative fit lines have also been shown ……...… 174

LIST OF FIGURES (Continued)

Figure Page

9.5.8 Arrhenius plots for bulk resistivity obtained from *ac* impedance spectroscopy for Bi-doped BT ceramics. Data for BT-BB ceramics have been shown for reference ……..……. 176

9.6.1 X-ray diffraction patterns of as-sintered stoichiometric (S), barium deficient (Ba def), bismuth deficient (Bi def) and bismuth excess (Bi Xs) ceramics ……... 190

9.6.2 Temperature dependent dielectric constant (solid lines) and dielectric loss (dashed lines) for (a) S, (b) Ba def, (c) Bi def, and (d) Bi Xs ceramics ……..…. 192

9.6.3 The Arrhenius plots for bulk resistivity in air (pO_2 ~ 0.2 atm) for S, Ba def, Bi def and Bi Xs ceramics. The bulk resistivity values were extracted from AC impedance data. The top y-axis shows the corresponding temperatures in °C. The data for $BaTiO_3$ has also been shown for reference ……..…….. 193

9.6.4 The Z'' vs Z' Nyquist plots for S, Ba def, Bi def and Bi Xs ceramics for measurements performed in oxygen, air and nitrogen atmospheres. The measurements for Ba def and Bi Xs were performed at a higher temperature (~700 °C) for faster attainment of steady state. The frequencies decrease logarithmically on moving from left to right in these plots ……...…….. 196

9.6.5 X-ray diffraction patterns of as-sintered stoichiometric (S), strontium deficient (Sr def), strontium excess (Sr Xs) and bismuth excess (Bi Xs) ceramics …… 199

9.6.6 Temperature dependent dielectric constant (solid lines) and dielectric loss (dashed lines) for (a) S, (b) Sr def, (c) Sr Xs, and (d) Bi Xs ceramics …… 200

9.6.7 The Arrhenius plots for bulk resistivity in air (pO_2 ~ 0.2 atm) for S, Sr def, Sr Xs and Bi Xs ceramics. The bulk resistivity values were extracted from AC impedance data. The top y-axis shows the corresponding temperatures in °C. The data for $SrTiO_3$ has also been shown for reference ……. 201

9.6.8 The Z'' vs Z' Nyquist plots for S, Sr def, Sr Xs and Bi Xs ceramics for measurements performed in oxygen, air and nitrogen atmospheres. The frequencies decrease logarithmically on moving from left to right in these plots …….. 202

9.7.1. (a) Arrhenius plots of bulk resistivity showing orders of magnitude improvement in resistivity on adding Bi*Me*O_3 to BT, for BT-0.25BZT, BT-0.3BiScO3 and BT-0.2Bi($Ni_{1/2}Ti_{1/2}$)O_3. (b) Nyquist plots for BT in vacuum (pO2~10^{-5} atm), air and O2 demonstration p-type behavior. (c) Nyquist plots for 25BZT in N2, air and O2 demonstration n-type behavior …… 222

LIST OF FIGURES (Continued)

Figure Page

9.7.2. (a) Rietveld refinement of a neutron diffraction pattern for BT. Combined neutron (b) and X-ray diffraction (c) was performed on BT-25BZT ceramics. The data presented with (+) symbol is the observed data and the black curves are calculated intensities. The bottom-most curve (blue) is the difference between observed and calculated intensities …….. 226

9.7.3 Thermogravimetric analysis (TGA) with in-situ mass spectroscopy for BT-25BZT ceramics. The ion currents are shown for volatile Zn and Bi ……..…… 229

9.7.4 Prompt gamma neutron activation analysis for (a) BT and (b) BT-BZT, indicating lower oxygen content in 25BZT ceramics as compared to BT ……... 231

9.7.5 X-ray photoelectron spectroscopy on powdered BT-25BZT ceramics. The data shown with "x" symbols are actual data obtained from the experiment. The background and fitted peaks have also been indicated ……..... 232

9.7.6 X-ray absorption spectra focusing on XANES region for BT-25BZT sample. The data for Bi_2O_3 and $NaBiO_3$ have also been shown, which were used as a reference for 3+ and 5+ states ……..…… 234

9.7.7 Micrograph (Fig. a) EELS (Fig. b) and STEM EDS (Fig. c) and for BT-25BZT sample. It can be noted that relative amounts of cations were different in secondary phases (point B) as compared to bulk of 25BZT (point A) and that the secondary phases contain almost no Bi ……..…… 234

9.7.8. (a) A typical grain of BT-25BZT with a representative line across the grain along which EELS was performed. The average oxygen occupancy was found to be 95.98+/-1.90 for BT-25BZT from the EELS data (b). A red circle in Figure a shows another dark-colored secondary phase ……..…… 236

9.7.9 (a) A generic defect diagram of donor-doped BT, adapted from Smyth *et al.* (b) Various possible mechanisms for donor doping in BT-Bi*Me*O_3 leading to improvement in resistivity. The D_1 and D_2 (>D_1) are donor levels for Mechanism II. Plot of BT has also been included for reference ……..… 238

9.7.10 Arrhenius plot of resistivity for stoichiometric (S), 2% Ba deficient (Ba def) and 2% Bi deficient (Bi def) ceramics. The data for unmodified BT has also been shown ……...…… 246

10.1.1 XRD data for the indicated compositions where X-Y-Z corresponds to the BMT-BKT-BNT mole fractions, respectively …….. 258

LIST OF FIGURES (Continued)

Figure Page

10.1.2 Temperature dependence of dielectric constant (solid lines) and dielectric loss (dashed lines) for (a) 1-40-59, (b) 5-40-55 and (c) 10-40-50 compositions ……..... 259

10.1.3 (a) Polarization at 1 Hz and (b) electromechanical strain at 0.1 Hz for various compositions fatigued at 60 kV/cm and 10 Hz ……..... 260

10.1.4 Effect of fatigue on polarization (at 1 Hz) for (a) 1-40-59, (b) 2.5-40-57.5, (c) 5-40-55 and (d) 10-40-55 compositions tested at 50 kV/cm and 10 Hz up to a million cycles ……..... 262

10.1.5 Effect of fatigue on electromechanical strain (at 0.1 Hz) for (a) 1-40-59, (b) 2.5-40-57.5, (c) 5-40-55 and (d) 10-40-55 compositions tested at 50 kV/cm and 10 Hz up to a million cycles ……...…… 263

10.1.6 (a) Arrhenius plot, ln(resistivity) with inverse temperature and (b) Variation of resistivity with temperature ……..…… 264

10.1.7 Tauc plot, where F(R) is the ratio of effective absorption and scattering coefficients and hν is photon energy for various compositions ……... 265

10.2.1 Temperature dependence of dielectric constant (solid lines) and dielectric loss (dashed lines) for (a) A_A, (b) A_B, (c) D_A and (d) D_B compositions ……..… 277

10.2.2 The non-linear field dependent variation in dielectric response. The data for stoichiometric sample (S) has been included for reference ……. 279

10.2.3 Polarization and strain hysteresis loops for stoichiometric 5BMT-40BKT-55BNT measured at 1 Hz and 0.1 Hz respectively at room temperature ……..... 280

10.2.4 Effect of fatigue on polarization hysteresis (at 10 Hz) for (a) A_A, (b) A_B, (c) D_A and (d) D_B compositions tested at 50 kV/cm and 10 Hz up to a million cycles. The plots also show the P_{max} and P_r with number of cycles (top x-axis) …… 281

10.2.5 Effect of fatigue on electromechanical strain (at 0.1 Hz) for (a) A_A, (b) A_B, (c) D_A and (d) D_B compositions tested at 50 kV/cm and 10 Hz up to a million cycles 284

10.2.6 (a) XRD data for the indicated compositions, (b) Slow-scan {111} and {200} peaks for all compositions before (red solid lines) and after fatigue (black dashed lines) ……. 289

LIST OF TABLES

Table Page

1.1 Some important events in the field of piezoelectricity until 1980s ……..... 2

3.1 Crystallographic point groups classified with respect to polar axis and center of symmetry (COS). The green shades represent piezoelectric point groups and the orange ones represent point groups which are pyroelectric (and thus also piezoelectric) ……...……...……..……. 19

3.2 Table summarizing the fraction of single crystal polarization and distortion which can be realized in pseudocubic ceramics ……...……..... 20

4.1.1 Property differences between normal and relaxor ferroelectric materials ….. 27

6.1 Values of electron and hole mobilities as determined by Song *et al.* and others. 50

6.2 The values of K_i as reported by various authors ……..…… 51

6.3 The values of K_{red} as reported by various authors ……..….. 52

9.2.1: The activation energy for conduction and resistivity values for all compositions obtained from AC impedance measurements …… 97

9.5.1 Parameters for *I*2/m space group from the Rietveld refinement ……..… 165

9.7.1 Parameters for *P4mm* space group from the Rietveld refinement. Refinement was performed on neutron diffraction data for BT and combined x-ray and neutron data for BT-25BZT ……..…… 228

10.1.1 Table summarizing the bipolar fatigue results of bismuth-based compositions. The values represent the change in material properties due to fatigue with respect to their original values. '+' sign indicates increase and '–' sign a decrease in that property after fatigue. Data in asterisk (*) are approximate values extrapolated from plots wherever exact values were not available in the text …….. 266

10.2.1 The reversible and irreversible Rayleigh parameters and ratio of irreversible to reversible contributions to dielectric nonlinearity for all compositions at room temperature …….……. 280

10.2.2 Remnant and maximum polarizations, and coercive field before and after fatigue ……..… 283

10.2.3 The DC resistivity values calculated by extrapolating AC impedance data . 287

1. Introduction

Piezoelectric materials have the ability to develop a voltage difference across them on application of mechanical stress. It is commonly referred to as direct piezoelectric effect. The credit for discovery of direct piezoelectricity goes to Jacques and Pierre Curie. In 1880, they created charge in a quartz crystal on application of pressure. The opposite of above-mentioned effect is true as well i.e. it is possible to realize mechanical strain in these materials on application of voltage. This effect is commonly termed as converse piezoelectric effect. The discovery of ferroelectricity (discussed in section 2.5) in Rochelle salt in 1921 was a major breakthrough in field of piezoelectricity. [1] Subsequently, the discovery of ferroelectricity and superior dielectric and piezoelectric properties in barium titanate in 1940s and lead titanate-based ceramics in the 1950s led to their widespread use as capacitors, non-volatile memories, transducers, buzzers, switches and other applications. It is a well-established fact that all ferroelectric materials are piezoelectric as well.

The next giant step was probably the discovery of "poling" by Gray in 1945. [2] He discovered that polycrystalline ceramics, which until then were considered piezoelectrically inactive, could behave similar to single crystals on application of high enough temporary external electric field. This was a discovery of tremendous technological importance as polycrystalline ceramics are relatively easier to process and generally don't require any special set-up.

As Jaffe *et al.* mentioned in their book, there were three major steps in the discovery and understanding of piezoelectricity in ceramics. [3] The first was the discovery of high dielectric constant in barium titanate ($BaTiO_3$). The second was the

finding that the reason for the same was ferroelectricity, which led to development of a whole new class of ferroelectrics based on $BaTiO_3$. The third was the discovery of electrical poling process. Table 1.1 summarizes the important events until the 1980s in the history of piezoelectricity, the contents of which have been borrowed from a review paper by Haertling on ferroelectricity. [4]

Table 1.1: Some important events in the field of piezoelectricity until 1980s [4]

Year	Event
1824	Discovery of pyroelectricity in Rochelle salt
1880	Piezoelectricity discovered in quartz, Rochelle salt
1912	Concept of ferroelectricity introduced
1921	Ferroelectricity found in Rochelle salt
1941	$BaTiO_3$ was found to have a high dielectric constant (more than 1000)
1944	Ferroelctricity reported in $BaTiO_3$
1949	Phenomenological theory of $BaTiO_3$ introduced
1951	Concept of antiferroelectricity introduced
1952	Lead Zirconate Titanate (PZT) discovered as a new ferroelectric ceramic and its phase diagram reported
1955	Positive Temperature Coefficient (PTC) reported in $BaTiO_3$
1955	Alkali niobates reported as ferroelectric
1957	$BaTiO_3$ barrier layer capacitors developed
1961	Lattice dynamics theory for ferroelectric materials, soft modes introduced
1964	Ferroelectric semiconductor (PTC) devices developed
1969	Terms “ferroics” and “ferroelasticity” introduced
1969	Optical transparency reported in lead lanthanum zirconate titanate (PLZT) ceramics
1977	Ferroelectric thin films developed
1978	Ferroelectric composites developed
1980	Relaxor devices based on lead magnesium niobate (PMN) developed
1981	Sol-gel technique for making thin films developed

Recently, bismuth-containing ferroelectric materials have been widely researched. This work will focus on this class of ceramics and aims to develop a fundamental understanding of the dominant defect species and the relevant defect equilibrium conditions in them, which is of paramount importance if these materials have to be commercialized. These will be discussed extensively in later sections.

References

[1] Valasek J. Piezo-electric and allied phenomena in Rochelle salt. Physical review 1921;17:475.
[2] Gray RB. Transducer and method of making the same. US Patent 2,486,560; 1949.
[3] Jaffe B, Cook WR, Jaffe H. Piezoelectric ceramics: Academic Press London and New York; 1971.
[4] Haertling GH. Ferroelectric ceramics: history and technology. Journal of the American Ceramic Society 1999;82:797-818.

2. Basic Terminologies

2.1 Dielectric Permittivity and Loss

A dielectric or insulator is a material with high electrical resistivity in general. The basic function of a dielectric material is to increase stored electrical charge in a parallel plate capacitor for a given electrical field. The relative dielectric constant (K or ε_r) of a material is in practice given by the ratio of charge stored in a capacitor with the dielectric material filling the gaps between the plates to charge stored in the same capacitor with plates separated by vacuum under a constant electric field. Usually, ferroelectric materials have higher dielectric constants (>1000) as compared to less than 20 for most organic and inorganic materials.

The principle behind enhancement of charge storing capability of a capacitor on introduction of a dielectric is related to polarization (discussed in next section). The center of positive and negative charges in the unit cell get separated to create a dipole or the pre-existing randomly aligned dipoles get aligned in presence of external electric field giving rise to a net dipole moment. The polarization P_i introduced on application of electric field E_i is given by:

$$P_i = \chi_{ij} E_j \qquad \text{Eq. 2.1.1}$$

where, dielectric susceptibility (χ_{ij}, with units Fm^{-1}) of the material is a second-rank tensor. Also, the total surface charge density that is induced in the material is given by dielectric displacement vector (D_i with units Cm^{-2}):

$$D_i = \varepsilon_0 E_i + P_i \qquad \text{Eq. 2.1.2}$$

where, ε_0 is the dielectric permittivity of vacuum. From equations 2.1.1 and 2.1.2, it can be seen that,

$$D_i = \varepsilon_0 E_i + \chi_{ij} E_j = \varepsilon_0 \delta_{ij} E_j + \chi_{ij} E_j = \varepsilon_{ij} E_j \quad \text{Eq. 2.1.3}$$

where, $\varepsilon_{ij} = \varepsilon_0 \delta_{ij} + \chi_{ij}$ is the dielectric permittivity of the material and δ_{ij} is Kronecker's function whose value becomes 1 when $i = j$ and 0 otherwise. Relative dielectric constant (ε_r) is given by the ratio $\varepsilon_{ij}/\varepsilon_0$.

There is almost never an ideal dielectric material and to describe the deviation from ideality, it is usually expressed as a complex quantity. Under ac fields, the charge stored has both real and imaginary (due to resistive leakage or dielectric absorption) components.

$$\varepsilon^* = \varepsilon' - \iota\varepsilon'' \quad \text{Eq. 2.1.4}$$

The ratio $\varepsilon''/\varepsilon'$ is often referred to as dielectric loss in literature and is denoted by $\tan\delta$.

2.2 Polarization mechanisms: Origins of dielectric constant

Gases normally have dielectric constant close to 1. In contrast, insulators typically have much higher dielectric constant values. In general, dielectrics with higher covalent characteristics in their bonding have lower dielectric constant (silica glass~3.8). The dielectric constant increases with ionic character in the bonds (NaCl, Al_2O_3 ~ 6-10). Materials with very high dielectric constants (water ~ 80, BT ~ 1000), have other special polarization mechanisms like dipole rotation, phase transformation etc.

Figure 2.2.1 shows the primary polarization mechanisms.[1] The electronic polarization is a resonance phenomenon and arises due to distortion of electron cloud on application of external electric field. The ionic polarization arises from relative motion of anions and cations on applying electric field. It is normally independent of temperature except close to phase transition. The dipolar polarization comes from orientation of dipoles in external electric field. The space charge or interfacial polarization requires mobile charged defects and internal interface or barrier. Normally, conduction arises from acceleration of charge carriers into a steady state velocity and polarization arises from acceleration of charge carriers to a steady-state displacement. Space-charge polarization is boundary between these two. This can be caused by electrons, holes, vacancies, ions etc. in leaky dielectrics.

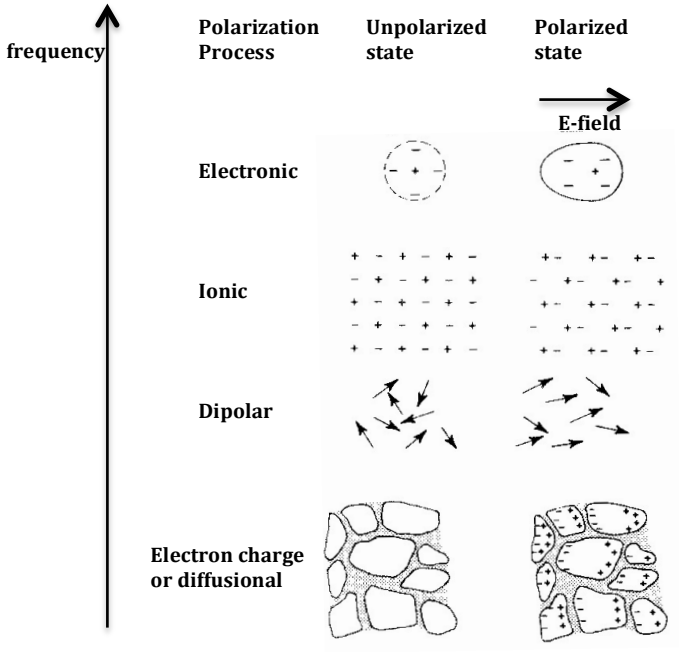

Fig. 2.2.1 Various polarization mechanisms in common dielectric materials [1]

Measuring dielectric constant at different frequencies helps to separate the various polarization components. Electronic polarization is dominant at higher frequencies due to small mass of electron. Ions are heavier, so they follow fields up to relatively lower frequencies. Rotation of dipole is even more sluggish and space charge effects can follow only up to kilohertz or so. Figure 2.2.2 shows a typical dielectric spectrum for various polarization mechanisms. Ferroelectric ceramics like PZT and BT have significant contributions from domain wall motion (extrinsic contribution) apart from intrinsic components (mostly ionic and electronic).

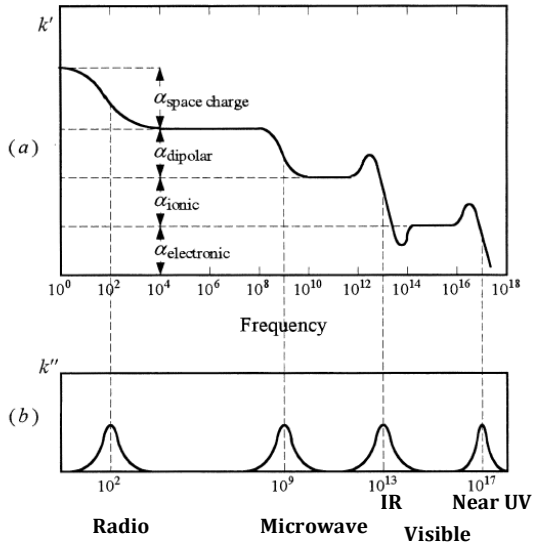

Fig. 2.2.2 Typical dielectric spectra of a solid showing both the real (a) and imaginary (b) components.[2]

2.3 Piezoelectricity

As mentioned earlier, piezoelectricity is the ability of certain materials to develop electric charge when stress is applied (direct effect). The charge is directly proportional to the force applied. For converse effect, the strain produced is directly proportional to

magnitude of applied electric field. The piezoelectric properties can be described in terms of parameters *D, E, x* and *X,* which stand for dielectric displacement, electric field, strain and stress respectively. The relationships are given by:

$D_i = d_{ijk}X_{jk}$ (direct effect) Eq. 2.2.1

$x_{ij} = d_{kij}E_k = d^t_{ijk}E_k$ (converse piezoelectric effect) Eq. 2.2.2

where, d_{ijk} (CN^{-1})is a third rank tensor of piezoelectric coefficients and the superscript *t* denotes the transposed matrix. The units of converse piezoelectric coefficient are (mV^{-1}). The piezoelectric coefficients *d* are thermodynamically identical for direct and converse effects. [3] In general, $d_{ijk} = d_{ikj}$ because of symmetry considerations. As a result the number of independent coefficients gets reduced to 18 from 27. They are further reduced by the symmetry of the material. It will be discussed later in detail in the section 3. The piezoelectric coefficient measured in the direction of applied electric field is normally referred to as longitudinal coefficient, while those measured in perpendicular direction are called transverse coefficients; the rest are called shear coefficients.

The symmetry of stress tensor also allows us to write the *d* coefficients as a second rank instead of a third rank tensor. In that case, d_{31} for example would relate the generation of polarization in the vertical direction and the stress applied in the lateral direction. The d_{33} would relate the polarization along the vertical direction when stress is applied in the same direction. The relationships then become:

$D_3 = d_{33}X_3$ (direct effect) Eq. 2.2.3

$x_3 = d_{33}E_3$ (converse effect) Eq. 2.2.4

High *d* coefficients are desirable for materials which are developed for motion or vibration, such as sonar or ultrasonic cleaner transducers.

Another coefficient frequently used in piezoelectrics is *g* (piezoelectric voltage coefficient), which is basically the ratio between field and stress and gives us field produced per unit stress applied. The *d* and *g* coefficients are related via permittivity.

$$d = gK\varepsilon_0 \qquad \text{Eq. 2.2.5}$$

where, K and ε_0 are relative dielectric constant and permittivity of free space respectively. High *g* coefficients are useful in materials for applications like phonograph pickup.

The electromechanical coupling factor *k* is widely used to report the strength of piezoelectric effect in a material. It tells the fraction of the input electrical/mechanical energy to mechanical/energy.[4]

$$k^2 = \frac{electrical/mechanical\ energy\ converted\ to\ mechanical/electrical\ energy}{input\ electrical/mechanical\ energy} \qquad \text{Eq. 2.2.6}$$

Since full conversion is not possible, *k* is always less than 1. The typical values of *k* are 0.4 for barium titanate ceramic, 0.5-0.7 for lead zirconate titanate ceramic and 0.9 for Rochelle salt. [4]

2.4 Pyroelectricity

Polarization can be induced in piezoelectric crystals on application of stress or electric field. In pyroelectric crystals, spontaneous polarization can be changed by changing temperature. Some pyroelectric materials have the property that the direction of spontaneous polarization can be changed by application of external electric field or stress.

When the change is mainly due to an electric field, the material is called ferroelectric and when it's due to a stress, the material is called ferroelastic. These additional features of pyroelectric materials have to be established experimentally and can't be predicted. [1] It's worth mentioning here that all the pyroelectric materials are piezoelectric, but the converse is not true. It will be elaborated further in a later section (section 3).

As discussed above, pyroelectric materials have spontaneous polarization (P_s) even in absence of electric field. However, it's usually masked by charges from surroundings and harder to observe. For experimental purposes, it is easier to measure the changes in P_s with temperature than P_s itself.

$$p_i = \frac{\partial}{\partial T}(P_{S,i}) \qquad \text{Eq. 2.3.1}$$

where, p_i ($Cm^{-2}K^{-1}$) is the vector of pyroelectric coefficients.

2.5 Ferroelectricity

This class of materials is polar and the spontaneous polarization can be switched between two or more equilibrium orientations by applying external electric field. Since ferroelectricity requires polarity in the crystal, all ferroelectric crystals are also pyroelectric. However, the reverse may not be true. A material can have spontaneous polarization, but it may not be reversible; the fields required may be greater than the breakdown field or the arrangement of atoms may be irreversible. Tourmaline and CdS (hexagonal) are pyroelectric but not ferroelectric.

Most ferroelectric materials are non-ferroelectric or paraelectric at high temperature. As temperature is decreased, they transition to low-symmetry ferroelectric

phases (figure 2.4.1). The temperature of transition is called Curie point. Above this temperature, the dielectric constant follows the Curie-Weiss law and decreases as temperature increases:

$$\varepsilon = \varepsilon_0 + C/(T-T_0) \qquad \text{Eq. 2.4.1}$$

where, T_0 is called Curie temperature and C is Curie constant. It should be noted that Curie point and Curie temperature are different quantities and generally do not coincide. In this case, there are multiple phase transitions like in the case of $BaTiO_3$, the highest transition temperature is the Curie point. The Curie point and T_0 are generally different for materials which exhibit first order phase transition, where properties like polarization, dielectric constant, and lattice parameters change discontinuously during transition. For second order phase transitions, where the properties change continuously, the Curie point and T_0 can be identical.

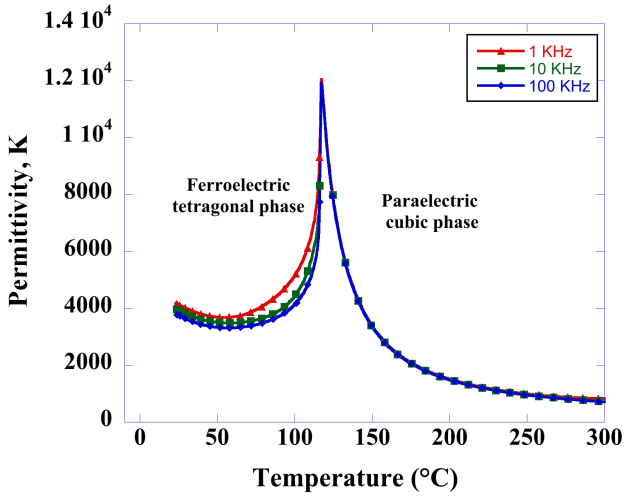

Fig. 2.4.1. As $BaTiO_3$ cools down, it transforms from paraelectric cubic phase to ferroelectric tetragonal phase. The cubic phase has higher symmetry than tetragonal phase.

Below the transition temperature, the ferroelectric unit cell has spontaneous polarization, but there is no fixed direction along which it will align. The paraelectric cubic phase has six equivalent directions along which spontaneous polarization can align below the transition temperature. However, there are regions in the crystal where there are uniformly oriented dipole moments. These regions are called domains. The regions between two domains are called domain walls. The walls which separate polarizations pointing in opposite direction are called 180° domain walls, otherwise they are called non-180° domain walls. The formation of domain walls can be attributed to depolarization fields and influence of mechanical stresses.[3] It is worth noting that both 90° (in tetragonal crystal) and 180° domain walls reduce the effects of depolarization fields, but only 90° walls reduce the elastic energy due to mechanical stresses.

Ferroelectric polarization hysteresis loop (Fig. 2.4.2) is considered to be one of the ways of confirming ferroelectricity in a material. It is basically polarization reversal on application of electric field and is caused by domain wall switching. However, the mechanism for polarization reversal is not fully understood. Growth of existing anti-parallel domains, domain wall motion, nucleation and growth of new antiparallel domains are some of several mechanisms proposed.[5-7] In ferroelectric materials, the strain-electric field loops also exhibit hysteresis. The shape of the hysteresis loops resembles the shape of a butterfly. Three effects are considered to contribute to this, converse piezoelectric effect of the lattice, switching and movement of the domain walls. [3]

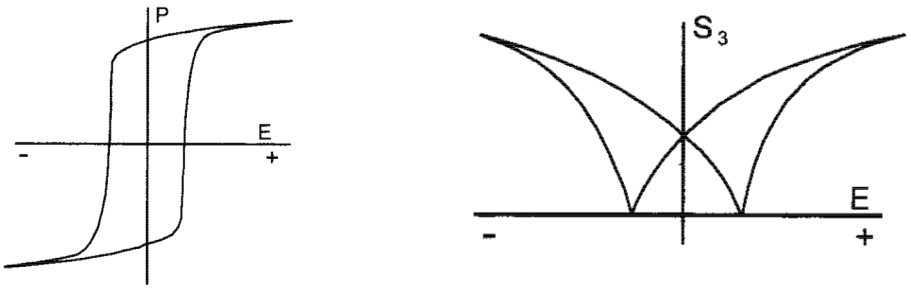

Fig. 2.4.2. Typical polarization and strain hysteresis loops in a ferroelectric material.[8]

Various models have tried to explain the observation of ferroelectricity in certain materials. One of the widely accepted ones is based on vibrational states of the crystal lattice. There can be two kinds of lattice vibrations, acoustic and optical. Roughly speaking, in acoustic mode all the ions move together and optical mode cations and anions move in opposite directions. Both the modes can occur as transverse or longitudinal waves. [1] A transition to ferroelectric phase is a limiting case of transverse optical mode. In this case, as the temperature decreases, force constant related to transverse optical mode decreases. The temperature at which the frequency reaches zero can be called the transition temperature to ferroelectric state. This vibration mode is also called a soft mode.

There is still no fixed criteria to predict whether a given material will be ferroelectric or not. Till date, establishment of ferroelectric nature of a material requires some basic experiments in a laboratory.

2.6 Antiferroelectricity

The concept was borrowed from anti-ferromagnetism. Kittel proposed that in anti-ferroelectric materials, the subcells are polar but the dipole moments of adjacent subcells point in opposite direction resulting in a net zero polarization. [9] Anti-ferroelectric materials generally exhibit high dielectric constant at Curie point. Jona *et al.* pointed out that at this peak the free energy of the antipolar crystal is comparable to a polar crystal. [10] The dielectric constant obeys Curie-Weiss law above this temperature. The unit cell for the antiferroelectric temperature range is in general a multiple of the unit cell above the Curie point.

The compensating antipolar arrangement need not exist in all the three directions. For example, in $PbZrO_3$ a net polarity exists in one of the crystallographic directions. [11]

The phases which are neither ferroelectric nor anti-ferroelectric, are generally termed as paraelectric.

2.7 Electrostriction

Electrostriction is present in all materials whether it be amorphous or crystalline, centrosymmetric or polar. If the strain produced is proportional to the square of the electric field, it's termed as electrostrictive effect. Clearly, the sign of deformation then would be independent of polarity of electric field. In ferroelectric materials, electrostriction is often noticeable above Curie point. When an electric field E_i is applied on a material, the electrostrictive strain x can be defined by:

$$x_{ij} = M_{ijkl}E_kE_l \qquad \text{Eq. 2.4.1}$$

where, M_{ijkl} are electrostrictive coefficients and form a fourth rank tensor. The equation can also be expressed in terms of induced polarization.

$$x_{ij} = Q_{ijkl}P_kP_l \qquad \text{Eq. 2.4.2}$$

Using equation 2.1.1, one can see that Q_{ijkl} and M_{ijkl} are related by the following relationship:

$$M_{ijkl} = \chi_{km}\chi_{ln}Q_{ijkl} \qquad \text{Eq. 2.4.3}$$

At high enough electric fields, polarization varies non-linearly with electric field. So both the equations 2.4.1 and 2.4.2 cannot be valid. It is commonly observed that equation 2.4.1 is valid only at weak fields while 2.4.2 is always valid for pure electrostrictive effect. [3]

As is nicely described by Damjanovic *et al.*, any material biased by a DC electric field will exhibit a piezoelectric effect under an AC electric field. [3] In other words, a material under constant DC field is always noncentrosymmetric. To see this mathematically let's apply DC+AC field simultaneously on a non-piezoelectric material. Equation 2.4.1 then becomes,

$$x = M(E_{DC} + E_{AC})^2 = M(E_{DC})^2 + 2ME_{DC}E_{AC} + (E_{AC})^2 \qquad \text{Eq. 2.4.4}$$

The term $(2ME_{DC})E_{AC}$ behaves like piezoelectric effect (linear with respect to electric field) and changes sign with direction of electric field. In most materials, the induced piezoelectric effect is generally very small, but can be large in relaxor-ferroelectrics (discussed in section 5) like $Pb(Mg_{1/3}Nb_{2/3})O_3$. [12]

Electrostriction can also be large in ferroelectric materials just above Curie temperature. Here, the electric field can cause a transition to unstable ferroelectric phase.

The actual mechanism for these large electrostrictive effects in not fully understood yet. However, there are some reports which relate it to coalescence of micropolar regions to macrodomains of the parent ferroelectric. [13, 14]

References

[1] Moulson AJ, Herbert JM. Electroceramics: materials, properties, applications: John Wiley & Sons; 2003.
[2] Newnham RE. Properties of Materials: Anisotropy, Symmetry, Structure: Anisotropy, Symmetry, Structure: Oxford University Press; 2004.
[3] Damjanovic D. Ferroelectric, dielectric and piezoelectric properties of ferroelectric thin films and ceramics. Reports on Progress in Physics 1998;61:1267.
[4] Jaffe B, Cook WR, Jaffe H. Piezoelectric ceramics: Academic Press London and New York; 1971.
[5] Fousek J, Janovec V. The Orientation of Domain Walls in Twinned Ferroelectric Crystals. Journal of Applied Physics 1969;40:135-42.
[6] Lines ME, Glass AM. Principles and applications of ferroelectrics and related materials: Oxford University Press; 1977.
[7] Shur VY. Fast polarization reversal process: evolution of ferroelectric domain structure in thin films. Ferroelectric Thin Films: Synthesis and Basic Properties 1996;10:153-92.
[8] Haertling GH. Ferroelectric ceramics: history and technology. Journal of the American Ceramic Society 1999;82:797-818.
[9] Kittel C. Theory of antiferroelectric crystals. Physical Review 1951;82:729.
[10] Jona F, Shirane G. Ferroelectrical Crystals. Macmillan, New York; 1962.
[11] Jona F, Shirane G, Mazzi F, Pepinsky R. X-Ray and Neutron Diffraction Study of Antiferroelectric Lead Zirconate, PbZr O 3. Physical Review 1957;105:849.
[12] Kuwata J, Uchino K, Nomura S. Electrostrictive coefficients of Pb (Mg1/3Nb2/3) O3 ceramics. Jpn J Appl Phys 1980;19:2099-103.
[13] Cross LE. Relaxor ferroelectrics. Ferroelectrics 1987;76:241-67.
[14] Harmer M, Smyth D. Nanostructure, Defect Chemistry and Properties of Relaxor Ferroelectrics. DTIC Document; 1992.

3. Crystal Symmetry in Piezoelectricity

Electric field and polarizations are directional (vectors), whereas stress and strain are tensors which in general don't have directional properties. Therefore, it is important to have polarity in the materials which exhibit piezoelectricity. This makes crystal chemistry an important part of piezoelectricity. Some materials can have polarity depending on their crystal symmetry while it's impossible for some materials to exhibit piezoelectricity.

Out of the 32 classical point groups, 21 lack a center of symmetry (non-centrosymmetric). Out of these 21 point groups, one cubic class 432 doesn't permit piezoelectricity, leaving 20 point groups which can exhibit piezoelectricity. Out of these 20, 10 have a unique polar axis even in the absence of external stress and can be considered as pyroelectric point groups; the other 10 are non-pyroelectric. Pyroelectric materials can be ferroelectric and can exhibit enhanced piezoelectricity owing to domain wall contributions. However, as mentioned in a previous section, the existence of a polar axis doesn't guarantee ferroelectricity. The polar axis needs to be reversible under external electric field. For example, hexagonal CdS and Tourmaline are pyroelectric but not ferroelectric. [1] Table 3.1 summarizes classifies the point groups with respect to polar axis and center of symmetry.[2]

Table 3.1. Crystallographic point groups classified with respect to polar axis and center of symmetry (COS). The green shades represent piezoelectric point groups and the orange ones represent point groups which are pyroelectric (and thus also piezoelectric). [2]

	COS	**Cubic**		**Hexagonal**		**Tetragonal**		**Trigonal**		**Ortho**	**Mono**	**Tri**
Non-Polar	$\bar{1}$	m3m	m3	6/mmm	6/m	4/mmm	4/m	$\bar{3}$m	$\bar{3}$	mmm	2/m	$\bar{1}$
	1	432	23	622	$\bar{6}$	422	$\bar{4}$	32		222		
		$\bar{4}$3m		$\bar{6}$m2		$\bar{4}$2m						
Polar				6mm	6	4mm	4	3m	3	mm2	2	1
											m	

Most of the piezoelectric materials used today in industry are ceramics, which are isotropic by nature. Even though the unit cells or crystals may be piezoelectric, the random orientation of various crystals cancels out the piezoelectric effect. However, they can be imparted polarity by application of strong electric field (poling) after which the polar axes of crystallites switch to a crystallographically allowed direction closer to that of electric field.

Even though poling helps with piezoelectricity, owing to the imperfection in alignment, the properties of ceramics are in general inferior to single crystals. Table 3.2 summarizes the fraction of single crystal polarization and strains which can be realized in pseudocubic ceramics (small distortions from cubic symmetry). [1, 3, 4] It can be noted that the fractions achievable are proportional to number of allowable polar directions.

Table 3.2. Table summarizing the fraction of single crystal polarization and distortion which can be realized in pseudocubic ceramics.[1, 3, 4]

Crystal symmetry and polar axis	Number of equivalent directions	Polarization fraction	Strain fraction
Tetragonal [001]	6	0.831	0.368
Orthorhombic [110]	12	0.912	Not calculated
Rhombohedral [111]	8	0.866	0.424

The point groups 4mm, 3m and mm2 are most common among ferroelectric materials. Symmetry of crystals has effects on piezoelectric matrices (mentioned in Section 2) as well.[5] Rewriting the equation 2.2.1,

$$D_i = d_{ijk}X_{jk} \qquad \text{Eq. 3.1}$$

where, X_{jk} is a 3x3 stress matrix with each element defined by F_j/A_k, where F_j is the force (N) directed along j-direction and A_k (m^2) is normal to the plane on which the force acts. The X_{11}, X_{22} and X_{33} are normal stresses ($j = k$) and when $j \neq k$, it's called shear stress. Now, in case of shear stresses, under the static equilibrium case, we also have $X_{jk} = X_{kj}$. This reduces the number of unique stresses from 9 to 6, three normal and three shear. So, a reduced notation can be used to express stresses, X_{11} can be denoted as just X_1, X_{22} as X_2, X_{33} as X_3, X_{23} as X_4, X_{13} as X_5 and X_{12} as X_6. The stress matrix can be written as a 6x1 matrix now. This allows us to reduce the d_{ijk} to just d_{ij}, where $i = 1$ to 3 and $j = 1$ to 6. The d-coefficients for $i = 1$ have been listed below:

$d_{11} = d_{111}$, $d_{12} = d_{122}$, $d_{13} = d_{133}$, $d_{14} = d_{123} + d_{132}$, $d_{15} = d_{113} + d_{131}$ and $d_{16} = d_{112} + d_{121}$

As a consequence, equation 2.2.1 can be re-written as,

$$\begin{pmatrix} D_1 \\ D_2 \\ D_3 \end{pmatrix} = \begin{pmatrix} d_{11} & d_{12} & d_{13} & d_{14} & d_{15} & d_{16} \\ d_{21} & d_{22} & d_{23} & d_{24} & d_{25} & d_{26} \\ d_{31} & d_{32} & d_{33} & d_{34} & d_{35} & d_{36} \end{pmatrix} \begin{pmatrix} X_1 \\ X_2 \\ X_3 \\ X_4 \\ X_5 \\ X_6 \end{pmatrix}$$

The values of *d*-coefficients depend on symmetry of crystal or ceramic. For example in centrosymmetric crystals, all $d_{ij} = 0$, and for triclinic point group 1, all of them are non-zero.

In case of piezoelectric ceramics, they are isotropic before poling. Polycrystalline ceramics with randomly oriented grains can be represented by Curie group ∞∞m. [6] But their isotropy is destroyed in the direction of poling and is maintained in directions perpendicular to it. Its symmetry can be represented as ∞m.[6] The *d*-coefficient matrix for the same has been shown below, assuming the polar axis to be along 3-direction.

$$\begin{pmatrix} 0 & 0 & 0 & 0 & d_{15} & 0 \\ 0 & 0 & 0 & d_{15} & 0 & 0 \\ d_{31} & d_{31} & d_{33} & 0 & 0 & 0 \end{pmatrix}$$

This is the matrix most commonly used in the field of ferroelectrics.

References

[1] Jaffe B, Cook WR, Jaffe H. Piezoelectric ceramics: Academic Press London and New York; 1971.
[2] Huang C-C. Structure and piezoelectric properties of lead-free bismuth-based perovskite solid solutions: ProQuest; 2008.
[3] Baerwald H. Thermodynamic theory of ferroelectric ceramics. Physical Review 1957;105:480.
[4] Rosenthal F. Bounds on the polarization and strain of tetragonal ferroelectric ceramics. Clevite Research Center, Cleveland; 1957.
[5] Cady WG. Piezoelectricity. An Introduction to the Theory and Applications of Electrochemical Phenomena in Crystals: McGraw-Hill; 1946.
[6] Newnham RE. Properties of Materials: Anisotropy, Symmetry, Structure: Anisotropy, Symmetry, Structure: Oxford University Press; 2004.

4. Perovskites

The perovskite structure is probably the most versatile structure known to date. Its beauty lies in the fact that it can accommodate almost every element in the periodic table and defects, giving a huge scope for structure and property engineering. It finds uses in a variety of applications like dielectric, conductors, superconductors and so forth. As Bhalla *et al.* point out, among thousands of ternary crystal structures, close to just a dozen accounts for all the useful ceramics.[1, 2] Among these, the spinel (A_2BX_4) and perovskite structure (ABX_3) are most common and the perovskite has a huge lead over spinel. It's not surprising that most piezoelectric ceramics have perovskite structure. Figure 4.1 summarizes the wide variety of applications possible using perovskites.

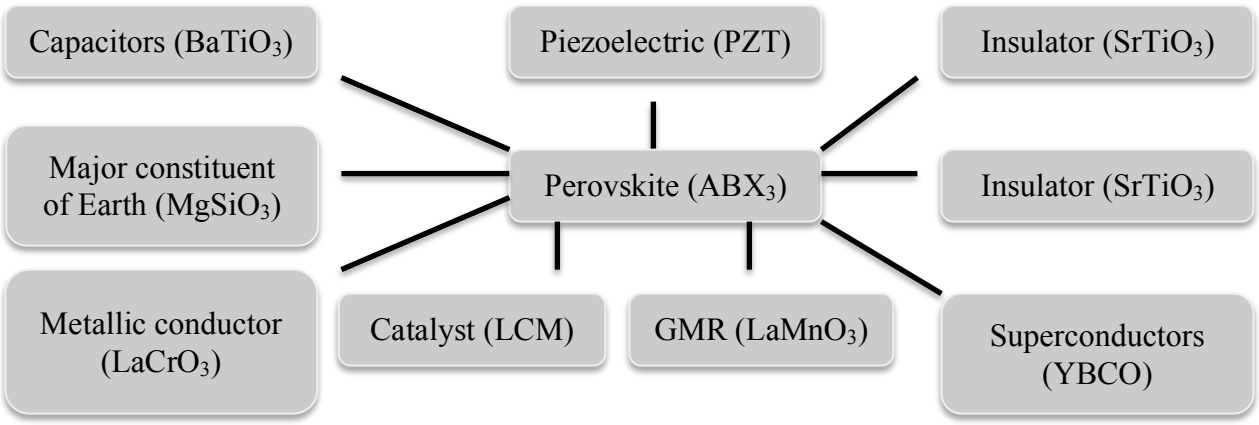

Fig. 4.1 Multifunctional perovskites, diagram taken from Bhalla *et al.* [1] The acronym PZT stands for lead zirconate titanate, LCM for lanthanum cobaltates and manganates, GMR for giant magnetoresistance and YBCO for Yttrium Barium Copper Oxide.

An ideal cubic perovskite has been shown in Fig. 4.2 (a) and (b). The figure on the left is a typical cubic perovskite with B cation at the center, A at the corners and anion at the face center. The structure can also be visualized as a network of corner-linked anion octahedrons, with A-cation going to the dodecahedral voids and B-cation at

the octahedral voids (fig. 4.2 (b)). In an ideal case (cubic perovskite), the cations would fit perfectly in the voids causing no distortions to the octahedra. However, if A-cation is smaller, the octahedra tend to bend inwards (octahedral tilting) to reduce the coordination of A-cation. This is accompanied by change in symmetry to rhombohedral/orthorhombic depending on tilting mechanism (in-phase/out of phase). When B-site cation is too small for the octahedra, one can get either tetragonal or hexagonal distortions. Hexagonal symmetry is usually non-ferroelectric.

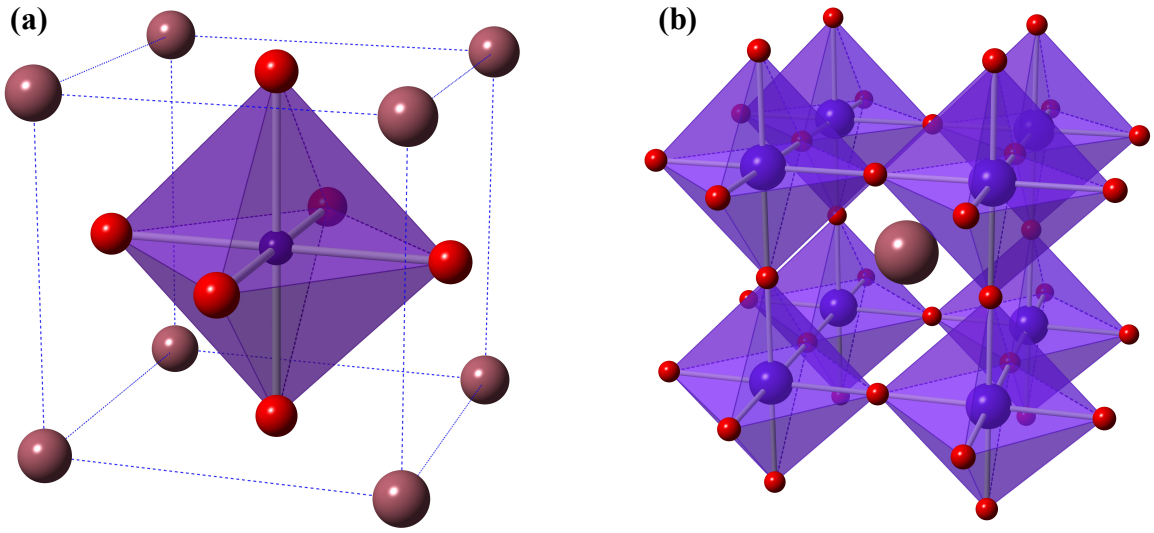

Fig 4.2. (a) A typical perovskite structure with A-cation at the cube corners (brown), B-cation at the center (purple) and the anions at face center (red), (b) An alternate presentation with A-cation at the center. The anion octahedra can be seen for both of them.

The concept of Goldschmidt tolerance factor (t) is often used to predict the structure of perovskites. For a perovskite ABX_3, it is defined as:

$$t = \frac{R_A + R_X}{\sqrt{2}(R_B + R_X)} \qquad \text{Eq. 4.1}$$

where, R_A, R_B *and* R_X are ionic radii of A-cation, B-cation and anion in appropriate coordination number. For ideal cubic perovskite, t=1 and there should not be any ferroelectric phase transitions on heating as cubic perovskites are usually formed after last ferroelectric phase transition. For t<1, A-cations are under-bonded i.e. the bond distance between A-cations and anion are too long. In this case octahedral tilting can be predicted to shorten the above mentioned bond length, leading to orthorhombic or rhombohedral distortions. It should be noted that perovskite structures are not stable for t<0.88 and ilmenite structures form. For t>1, B-cation should not be optimally coordinated and one should expect tetragonal or hexagonal distortions. A major drawback of this approach is that it assumes hard sphere model for ions and completely ionic bonding, which may not hold in practice. Nonetheless, the deviations are found to be minor in a lot of cases.

It's really hard to predict ferroelectricity based on tolerance factor or structure considerations. As Jaffe *et al.* point out, when t is between 0.95-1.0, one should expect cubic structure.[3] For lower t, structure should be distorted and non-ferroelectric, and higher t should be ferroelectric. One can agree with the argument that t>1 causes ferroelectricity as for these compounds there is no optimal coordination of B-cation and octahedral tilting, making it easier for it to move around and thus resulting in polar nature. (Cohen attributes ferroelectricity in $BaTiO_3$ and $PbTiO_3$ to hybridization between Ti-3d and O-2p states [4]) However, we know of examples where rhombohedral or orthorhombic structures are ferroelectric e.g. $BiFeO_3$ or $(Bi_{1/2}Na_{1/2})TiO_3$.

Normally ferroelectricity and octahedral tilt are considered incompatible. Among the perovskites which exhibit octahedral rotations, most of them are not polar. In their

work, Benedek *et al.* conclude from their first principle studies that for low enough tolerance factors octahedral rotation alone cannot suppress ferroelectricity. [5] They argued that cation displacements (A-site anti-polar displacements) that accompany the rotation play a pivotal role in suppressing ferroelectricity. They show that in absence of these A-site distortions, most perovskites would adopt *R3c* structure and would be polar. This points towards A-site driven ferroelectricity, contrary to the commonly held perception that ferroelectricity is controlled by B-cation.

The above paragraph mentioned about geometric ferroelectricity. However, it is not the only defining criteria for ferroelectricity. For example, $LaFeO_3$ has $t<1$ and is non-polar. However, when Bi^{3+} (which is almost of the same size as La^{3+}) replaces La^{3+} in the above compound to form $BiFeO_3$, it becomes polar with *R3c* symmetry. It points towards a critical role of having a cation with lone pair of electrons in the lattice. However, lone pair may not always guarantee ferroelectricity, for example in case of $BiScO_3$ or $BiGaO_3$. [6, 7] Apart from these, charge ordering can also lead to ferroelectricity. [8] Empirically it has also been seen that the d-orbitals also play a role; perovskites with empty d-orbital (d^0) are commonly seen to be ferroelectric like Ti^{4+} in $BaTiO_3$ or Nb^{5+} in $KNbO_3$.

4.1 Tuning the properties of perovskites for practical applications

Very often unsubstituted perovskites are not suitable for various applications. Therefore, A or B-site substitutions are very common. For example, a class of perovskites called relaxors are often suited for capacitor, actuators, transducer and other applications;

and morphotropic phase boundary (MPB) is often desired for piezoelectric applications. These have been described briefly here.

4.1.1 Relaxors

These substituted perovskites have very high dielectric permittivities. There is no long range ordering, ordered regions occur only at nanoscale levels. It's quite common to make solid solutions of a stable perovskites with unstable ones to destroy long range order and create relaxor nature. However it's not always the case. The following table compares the relaxor ferroelectrics with normal ferroelectrics (which have long range order).[1] It will be discussed in more details in section 5.

Table 4.1.1. Property differences between normal and relaxor ferroelectric materials. [1]

Property	Normal Ferroelectric	Relaxor Ferroelectric
Temperature dependence of permittivity	Sharp 1^{st} or 2^{nd} order transitions about curie point	Broad-diffuse phase transition
Frequency dependence of permittivity	Weak or no frequency dependence	Strong frequency dependence
Remnant Polarization	High remnant polarization	Low remnant polarization
Scattering of light	Strong anisotropy	Very weak anisotropy
Diffraction of x-rays	Peak splitting common	Often pseudo-cubic with no splitting

4.1.2 Morphotropic phase boundary (MPB)

The MPB is a border between two structures in a solid solution of multiple perovskites and marks an abrupt change in structure with variation in composition. At this point, phases on both the sides have almost equal Gibbs free energy. Dielectric constant, piezoelectric coefficients, pyroelectric behavior and others show a maxima at this composition. The PZT is the most widely studied and used MPB to date. The MPB

for this solid solution occurs at approximately 52:48 $PbZrO_3$:$PbTiO_3$ and marks a boundary between rhombohedral and tetragonal structures.

References

[1] Bhalla A, Guo R, Roy R. The perovskite structure–a review of its role in ceramic science and technology. Material Research Innovations 2000;4:3-26.
[2] Muller O, Roy R. The Major Ternary Structural Families, 1974. Springer-Verlag, New York.
[3] Jaffe B, Cook WR, Jaffe H. Piezoelectric ceramics: Academic Press London and New York; 1971.
[4] Cohen RE. Origin of ferroelectricity in perovskite oxides. Nature 1992;358:136-8.
[5] Benedek NA, Fennie CJ. Why are there so few perovskite ferroelectrics? The Journal of Physical Chemistry C 2013;117:13339-49.
[6] Belik AA, Iikubo S, Kodama K, Igawa N, Shamoto S-i, Maie M, et al. BiScO3: centrosymmetric BiMnO3-type oxide. Journal of the American Chemical Society 2006;128:706-7.
[7] Belik AA, Wuernisha T, Kamiyama T, Mori K, Maie M, Nagai T, et al. High-pressure synthesis, crystal structures, and properties of perovskite-like BiAlO3 and pyroxene-like BiGaO3. Chemistry of materials 2006;18:133-9.
[8] van den Brink J, Khomskii DI. Multiferroicity due to charge ordering. Journal of Physics: Condensed Matter 2008;20:434217.

5. Relaxor Ferroelectrics

Relaxor ferroelectrics or relaxors were discovered by Smolenskii *et al.* in 1954 and continue to attract interest among researchers around the world.[1, 2] They exhibit some interesting properties seen only in this class of compounds. As mentioned in section 4.1.1, they have broad maxima in temperature dependence of permittivity, unlike normal ferroelectrics; and the maximum permittivity is typically >1000. The feature which is often used to distinguish relaxors from normal ferroelectrics, is their frequency dependence of maximum permittivity. Usually, the temperature of maximum permittivity decreases as the frequency decreases (Fig 5.1).

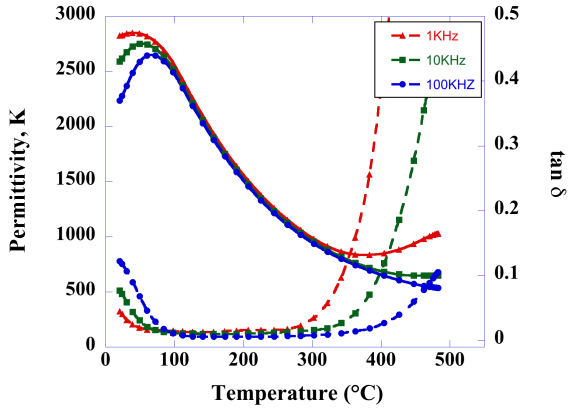

Fig 5.1 Dielectric response of $BaTiO_3$-$Bi(Zn_{1/2}Ti_{1/2})O_3$, which exhibits a typical dielectric response of a relaxor ferroelectric material. Figure 5.1.1 can also be referred to for further details on relaxors.

Typically, relaxors have multiple cations occupying a crystallographic site in the crystal. These cations can be either isovalent or non-isovalent. The temperature evolution of various phases in relaxors is quite different from normal ferroelectrics. Above the so-called Burns temperature (T_B), they exist as a non-polar paraelectric phase similar to normal ferroelectrics. Upon cooling below T_B, they transform into ergodic relaxor state, however the structure remains cubic on macroscopic scale like the paraelectric phase.

This T_B marks the beginning of nucleation of polar nano regions (PNRs) which consist of polar regions at nanometer scale. Even though most macroscopic properties don't change across T_B, properties like refractive index, specific heat and others get affected. From close to T_B down to a temperature called Freezing temperature (T_F), the PNRs remain mobile. However, close to T_F their mobility sharply decreases and the relaxors transform to a non-ergodic phase. The average symmetry of the crystal, however, still remains cubic on the macroscopic scale. One of the typical characteristics which can be used to distinguish ergodic from non-ergodic relaxors, is their response to external electric field. While on application of sufficient electric field, both ergodic and non-ergodic relaxors transform to a ferroelectric phase, only the ergodic relaxors come back to original relaxor state once the field is removed. The non-ergodic relaxors' transformation to ferroelectric state is generally irreversible. This induced ferroelectric state transforms to ergodic state on heating at a temperature called Curie temperature (T_C) which is typically close to T_F.

The following sections aim to look at relaxors more closely and are basically a summary of some excellent review articles on relaxor ferroelectrics.[3-5]

5.1 Small-signal dielectric response

The relaxors exhibit dielectric dispersion from the frequency of lattice vibrations to lowest measurable frequency (~0.01 mHz).[3] Since the field-induced polarization in relaxors has various components, so does the permittivity. A distribution of PNR sizes and random interactions between them give rise to a broad distribution of relaxation times and a peak in temperature dependence of permittivity.[5] In the temperature range of maximum permittivity, the total relative permittivity can be written as,

$$\varepsilon = 1 + \chi_e + \chi_{Ph} + \chi_R + \chi_U + \chi_{LF} \qquad \text{Eq. 5.1.1}$$

where, χ_e, χ_{Ph}, χ_R, χ_U and χ_{LF} are electronic, phonon, conventional relaxor (CR), universal relaxor (UR) and low-frequency contributions to susceptibilities. The electronic contribution is significant at all temperatures, but becomes small at lower frequencies. The phonon susceptibility is caused by displacements of cation and anion sublattices and contributes less than one percent to total low-frequency permittivity close to permittivity maximum. The χ_R and χ_U come from relaxation-type polarizations and are responsible for the typical peaks observed in temperature dependence of permittivity. The CR dispersion is observed towards the low-temperature slope of permittivity and is responsible for frequency dependence of maximum permittivity. The UR dispersion exists both below and above the temperature of maximum permittivity (Fig 5.1.1). The χ_{LF} combines all the other contributions not covered by other terms such as polarization of hopping charge carriers, Maxwell-Wagner polarization and others. Most of the dielectric measurements on relaxors are done in radio-audio frequency range. In this range χ_R is usually much larger than χ_U and almost exclusively contributes to the diffuse peak in the permittivity.

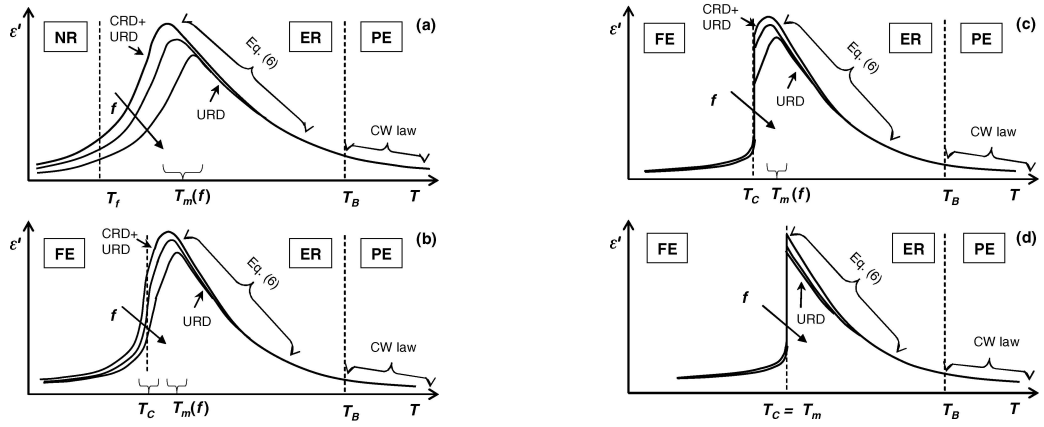

Fig 5.1.1 Temperature evolution of dielectric properties for disordered perovskites. Four different possibilities have been shown: (a) Canonical relaxor, (b) ceramics with diffuse relaxor to ferroelectric transition, (c) ceramics with sharp relaxor to ferroelectric

transition, and (d) ceramics with sharp relaxor to ferroelectric transition with T_c and T_m coinciding.[3]

5.2 Compositional disorder in relaxors

As mentioned above, a relaxor typically is a complex perovskite and has more than one kind of cations on at least one of the crystallographic sites in the crystal. This leads to compositional disorder and is essential for relaxor behavior. Ordering should be expected in these perovskites as an ordered state has lower electrostatic and elastic energies.[3] For example, in case of $A(B'_{1/2}B''_{1/2})O_3$, B′ or B″ should have their own sublattice within the structure in the ordered state. However, it should be noted that ordered structures can be made disordered if optimum thermal energies are provided. Thermal motion can also help with ordering, as at higher temperatures site exchange and diffusion of B′ or B″ is significantly faster. While some relaxors like $Pb(Sc_{1/2}Ta_{1/2})O_3$ (PST) and $Pb(In_{1/2}Nb_{1/2})O_3$ (PIN) can be ordered by annealing at appropriate temperatures, some others like $Pb(Mg_{1/3}Nb_{2/3})O_3$ (PMN) and $Pb(Fe_{1/2}Nb_{1/2})O_3$ (PFN) cannot be ordered by any heat treatment.

In $Pb(B'_{1/2}B''_{1/2})O_3$, the disordered $Pm\bar{3}m$ structure can theoretically be ordered to $Fm\bar{3}m$ structure (1:1 ordering). The ordering in case of $Pb(B'_{1/3}B''_{2/3})O_3$, however is not fully understood. The most cited models to explain relaxor behavior are “space charge” model and “random-site” model. The space charge model assumes 1:1 ordered nano-sized chemical nanoregions (CNRs) embedded in disordered surroundings.[3] In other words, alternating B′ and B″ ions will be present in CNRs similar to the case of $Pb(B'_{1/2}B''_{1/2})O_3$. One can note that, in this model CNRs will be non-stoichiometric and negatively charged. Consequently, the disordered matrix is also non-stoichiometric and

positively charged. However, Davies *et al.* were able to anneal some compositions and make samples consisting of only CNRs without the disordered regions.[6] This is inconsistent with space charge model. It was later found in case of PMN that the Mg/Nb ratio in CNRs was same as disordered matrix, which is again inconsistent with space-charge model.[7] The random-site model was proposed to explain this behavior. It was proposed that one of B-sublattice was exclusively occupied by B^{5+} cation and the other was occupied randomly by B^{5+} or B^{2+} preserving the local stoichiometry.[6]

It should be noted that relaxor behavior requires disordered state. If the crystal becomes ordered on annealing, it may cease to exhibit relaxor nature.

5.3 Temperature evolution of relaxors

The temperature evolution of relaxors was briefly discussed earlier, and terms such as freezing temperature, Burns temperature, polar nanoregions etc. were defined. In this section, some more details will be listed.

As it was mentioned earlier, the relaxors have cubic ($m\bar{3}m$) average symmetry. However, there can be deviations at local level. Due to the different sizes of the disordered cations and random fields, all ions should be displaced from their expected crystallographic sites. These displacements are not restricted to complex perovskites and have been found in perovskites like $PbZrO_3$ as well.[8] In the case of canonical relaxors like PMN, the average structure remains cubic even below T_B, the local structure, however, begins to change and we start observing PNRs, which are clusters with ferroelectric order in the ergodic state. At temperature below T_F, a non-ergodic state starts to appear in case of canonical relaxors. The average structure still remains cubic.

However, the average size of PNRs normally shows a steep rise close to T_F. As mentioned before, the macroscopic properties of non-ergodic relaxors become normal ferroelectric-like on applying sufficient electric field, but there remain differences at the microscopic level. Different from normal ferroelectrics, the local structure in poled non-ergodic relaxors still has inhomogeneity and fractions of cubic phase have been observed.[9] The T_F can be derived mathematically by fitting the frequency dependence of the dielectric maxima (T_m) to the Vogel-Fulcher law:

$$f = f_0 \exp\left(\frac{E_a}{k(T_m - T_F)}\right) \qquad \text{Eq. 5.3.1}$$

where E_a is activation energy, f_0 is attempt frequency and k is Boltzmann constant.[10]

Some relaxors, however, can spontaneously transform to ferroelectric state at T_C on cooling even in absence of an external field and for these relaxors non-ergodic phase doesn't exist. This normally happens in compositions which have less diffused peaks at transition. It is associated with a macroscopic symmetry change as well, as expected. The various scenarios have been shown in fig. 5.1.1.[3] It should be noted however, that the phase below T_C in case of these relaxors is not exactly normal ferroelectric, even though they may seem to have similar properties. The PNRs have been reported to exist in the low temperature ferroelectric phase, unlike normal ferroelectrics. [11] In some relaxor crystals which exhibit this phenomena like $Pb(Zn_{1/3}Nb_{2/3})O_3$ (PZN), it was reported that only the outer layer ("ferroelectric skin") undergoes transformation to a ferroelectric phase and the core remains as a non-ergodic relaxor which cubic symmetry.[12, 13] It should also be noted that sometimes the T_C and T_m can be really close to each other, as shown in fig. 5.1.1d (when CR dispersion is almost absent).

There is plenty of indirect experimental evidence available for the existence of PNRs in relaxors. In the absence of an electric field, the dipole moments of the PNRs are randomly oriented and the net polarization is zero. However, ΣP^2 is not zero, so the properties dependent on P^2 are affected by the presence of PNRs such as refractive index. The refractive index loses its linear temperature dependence as the temperature goes below T_B.[14] There is also evidence from elastic diffuse neutron and X-ray scattering for the PNRs.[15-18] These experiments can also tell about the size of the PNRs in the material. Transmission electron microscopy (TEM) has also been used to confirm the existence of PNRs.[19] There is sufficient scientific proof to confirm the existence of PNRs; however, the origin and mechanism of their formation is still not well understood.

5.4 $BaTiO_3$ (BT)-based relaxors

The BT-$BaSnO_3$ was the first BT-based solid solution reported to have relaxor characteristics.[1] The BT is a normal ferroelectric and follows Curie-Weiss Law (equation 2.4.1). Both isovalent and heterovalent substitutions can induce relaxor nature in the resulting solid solution. Heterovalent substitutions on A and/or B site can cause crossover to relaxor site; however, isovalent substitutions only on B-site show relaxor nature in general. The substitution type affects the degree of crossover from ferroelctric to relaxor state. For example, relatively low heterovalent substitutions on both A and B – sites can cause the relaxor state in the solid solution. For heterovalent substitution only on A-site, the crossover happens at moderate doping levels. For isovalent substitutions, the crossover is much more delayed (usually greater than 20%).[5]

The temperature evolution of dielectric permittivity with different substitution level is interesting. As mentioned earlier, pure BT is normal ferroelectric and has various transitions temperatures. In most cases, as the substitution levels increase, the transition temperature between different phases increase and come closer to each other. The Curie temperature comes down as well (figure 5.4.1). At certain higher substitution levels, the so-called "diffuse phase transition" (DPT) happens. This is the concentration level for which all transitions merge into one and the solid solution transforms from paraelectric to rhombohedral phase across this transition. The peaks are much broader and solid solution follows Curie-Weiss law at a temperature much higher than T_m like relaxors; however there is no frequency dependence yet. Santos *et al.* proposed an empirical relationship to describe the temperature dependence of dielectric permittivity close to T_m for compositions which exhibit DPT behavior.[20]

$$\varepsilon' = \frac{\varepsilon'_m}{1+\left(\frac{T-T_m}{\delta}\right)^{\gamma}} \qquad \text{Eq. 5.4.1}$$

where, ε'_m is dielectric maximum, T_m is temperature of dielectric maximum, δ is degree of diffuseness and γ gives information about character of phase transition. The value of γ close to 1 corresponds to normal ferroelectrics and 2 to DPT. At even higher substitution levels, in the relaxor state, Vogel-Fulcher law is followed (equation 5.3.1).

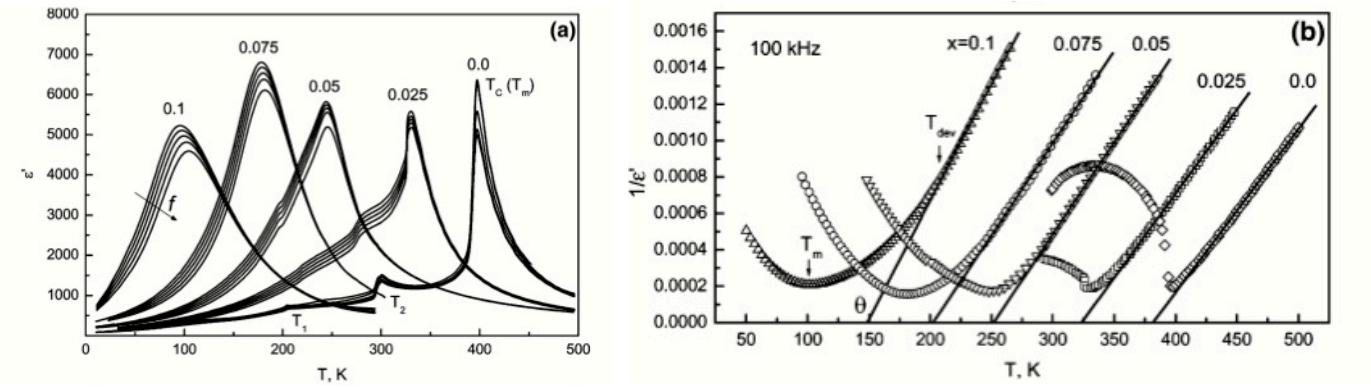

Fig. 5.4.1. (a) Temperature evolution of dielectric constant for (1-x)BT-La($Mg_{1/2}Ti_{1/2}$)O_3 ceramics, (b) Temperature evolution of inverse permittivity for the same compositions with Curie-Weiss fitting.[5, 21]

References

[1] Smolenskii G, Isupov V. * SEGNETOELEKTRICHESKIE SVOISTVA TVERDYKH RASTVOROV STANNATA BARIYA V TITANATE BARIYA. Zhurnal Tekhnicheskoi Fiziki 1954;24:1375-86.
[2] Smolenskii G, Isupov V, Agranovskaya A, Popov S. Ferroelectrics with diffuse phase transitions. Soviet Physics-Solid State 1961;2:2584-94.
[3] Bokov A, Ye Z-G. Recent progress in relaxor ferroelectrics with perovskite structure. Frontiers of Ferroelectricity: Springer; 2007. p. 31-52.
[4] Ravez J, Simon A. Some solid state chemistry aspects of lead-free relaxor ferroelectrics. Journal of Solid State Chemistry 2001;162:260-5.
[5] Shvartsman VV, Lupascu DC. Lead‐Free Relaxor Ferroelectrics. Journal of the American Ceramic Society 2012;95:1-26.
[6] Davies P, Akbas M. Chemical order in PMN-related relaxors: structure, stability, modification, and impact on properties. Journal of Physics and Chemistry of Solids 2000;61:159-66.
[7] Jin H, Zhu J, Miao S, Zhang X, Cheng Z. Ordered domains and polar clusters in lead magnesium niobate Pb (Mg1/3Nb2/3) O3. Journal of Applied Physics 2001;89:5048-52.
[8] Colla E, Koroleva EY, Okuneva N, Vakhrushev S. Long-time relaxation of the dielectric response in lead magnoniobate. Physical review letters 1995;74:1681.
[9] Vakhrushev S, Kiat J-M, Dkhil B. X-ray study of the kinetics of field induced transition from the glass-like to the ferroelectric phase in lead magnoniobate. Solid state communications 1997;103:477-82.
[10] Viehland D, Jang S, Cross LE, Wuttig M. Freezing of the polarization fluctuations in lead magnesium niobate relaxors. Journal of Applied Physics 1990;68:2916-21.
[11] Jiang F, Kojima S. Relaxation mode in 0. 6 5 P b (M g 1/3 Nb 2/3) O 3-0.35 PbTiO 3 relaxor single crystals studied by micro-Brillouin scattering. Physical Review B 2000;62:8572.
[12] Xu G, Zhong Z, Bing Y, Ye Z-G, Stock C, Shirane G. Ground state of the relaxor ferroelectric P b (Z n 1/3 Nb 2/3) O 3. Physical Review B 2003;67:104102.
[13] Xu G, Zhong Z, Bing Y, Ye Z-G, Stock C, Shirane G. Anomalous phase in the relaxor ferroelectric Pb (Zn 1⁄3 Nb 2⁄3) O 3. Physical Review B 2004;70:064107.
[14] Burns G, Dacol F. Glassy polarization behavior in ferroelectric compounds Pb (Mg13Nb23) O3 and Pb (Zn13Nb23) O3. Solid state communications 1983;48:853-6.
[15] Hirota K, Ye Z-G, Wakimoto S, Gehring P, Shirane G. Neutron diffuse scattering from polar nanoregions in the relaxor Pb (Mg 1/3 Nb 2/3) O 3. Physical Review B 2002;65:104105.
[16] Naberezhnov A, Vakhrushev S, Dorner B, Strauch D, Moudden H. Inelastic neutron scattering study of the relaxor ferroelectric PbMg1/3Nb2/3O3 at high temperatures. The European Physical Journal B-Condensed Matter and Complex Systems 1999;11:13-20.
[17] Vakhrushev S, Kvyatkovsky B, Naberezhnov A, Okuneva N, Toperverg B. Glassy phenomena in disordered perovskite-like crystals. Ferroelectrics 1989;90:173-6.
[18] Vakhrushev S, Nabereznov A, Sinha S, Feng Y, Egami T. Synchrotron X-ray scattering study of lead magnoniobate relaxor ferroelectric crystals. Journal of Physics and Chemistry of Solids 1996;57:1517-23.

[19] Yoshida M, Mori S, Yamamoto N, Uesu Y, Kiat J. TEM observation of polar domains in relaxor ferroelectric Pb (Mg1/3Nb2/3) O3. Ferroelectrics 1998;217:327-33.
[20] Santos I, Eiras J. Phenomenological description of the diffuse phase transition in ferroelectrics. Journal of Physics: Condensed Matter 2001;13:11733.
[21] Salak A, Seabra M, Ferreira V. Evolution from Ferroelectric to Relaxor Behavior in the (1− x) BaTiO3− x La (Mg1/2Ti1/2) O3 System. Ferroelectrics 2005;318:185-92.

Chapter 6: Review of Defect Chemistry of M_2O_3 ceramics

Most ceramics prepared via solid-state route have aliovalent impurities present which can exceed the concentration of intrinsic defects. At the same time, doping is often intentionally done in most ceramics to achieve desired properties to suit application-specific requirements. For this reason, for M_2O_3 ceramics studied here, it will be assumed that impurity defects are always present, whether in small or large quantities. Whether the impurities or intrinsic defects dominate transport properties, depends on specific circumstances, as will be seen later. It should be noted that these defects affect the defect chemistry only when they are capable of affecting the charge neutrality i.e. they need to be aliovalent.

Larger dopant concentrations can change the enthalpies of defect formation. For this section, all the solid solutions will be assumed to be dilute so as to neglect such effects. It will be assumed that the dopant concentration is "frozen-in" *i.e.* it will be assumed that impurities are almost always incorporated during processing (from precursors, solid state reaction and others), and then concentrations are fixed and don't change with temperature (at relatively low temperatures) or activity or non-metal. Therefore, the impurity content may affect the concentration of ionic and electronic defects, however, the other way round may not be possible.

For the M_2O_3 ceramics under discussion here, let's divide the discussion into two categories- acceptor doped M_2O_3 and donor doped M_2O_3. Let's start by looking at the case of acceptor doped M_2O_3.

Acceptor-doped M_2O_3

Often, undoped M_2O_3 have low valence impurities present in them acting as acceptors. Therefore, the defect chemistry of undoped and acceptor-doped M_2O_3 are expected to look similar—the only difference being the amount of acceptor concentration. We make three assumptions for the sake of simplicity:

(1) Schottky defects are dominant type of ionic intrinsic disorder present

(2) Addition of impurities don't change the thermodynamic parameters

The equilibrium reactions along with their mass action expressions can be given as the following.

Schottky Reaction:

$$nil \leftrightarrow 2V_M''' + 3V_O^{\cdot\cdot} \qquad \text{Eq. 6.1}$$
$$K_s = [V_M'''][V_O^{\cdot\cdot}]^3$$

Intrinsic electronic disorder:

$$nil \leftrightarrow e' + h^{\cdot} \qquad \text{Eq. 6.2}$$
$$K_i = np$$

Oxidation Reaction:

$$V_O^{\cdot\cdot} + \tfrac{1}{2}O_2 \leftrightarrow O_O^X + 2h^{\cdot} \qquad \text{Eq. 6.3}$$
$$K_{ox} = p^2 * pO_2^{-1/2}/[V_O^{\cdot\cdot}]$$

Reduction Reaction:

$$O_O^X \leftrightarrow V_O^{\cdot\cdot} + 2e' + \tfrac{1}{2}O_2 \qquad \text{Eq. 6.4}$$
$$K_{red} = [V_O^{\cdot\cdot}]n^2 pO_2^{1/2}$$

where, V_M''', $V_O^{\cdot\cdot}$, K_s, K_i, e', $h^{\cdot}$, n, p, K_{ox}, K_{red}, and pO_2 are metal vacancy, oxygen vacancy, rate constant for Schottky reaction, rate constant for intrinsic electronic disorder, electron, hole, electron concentration, hole concentration, rate constant for oxidation reaction, rate constant for reduction reaction and oxygen partial pressure respectively.

Ignoring the interstitials, which are often not preferred energetically, the acceptor defects can be compensated either by oxygen vacancies or holes, as given by following reactions.

$$2AO \overset{M_2O_3}{\longleftrightarrow} 2A_M' + 2O_O + V_O^{\cdot\cdot} \qquad \text{Eq. 6.5}$$

$$2AO + 1/2O_2 \overset{M_2O_3}{\longleftrightarrow} 2A_M' + 3O_O + 2h^{\cdot} \qquad \text{Eq. 6.6}$$

The A_M' is the acceptor impurity in an M_2O_3 lattice. The equation 6.5 shows the case of a stoichiometric solid solution and ionic compensation. Equation 6.6 represents the case of electronic compensation and the product is nonstoichiometric, since there is an extra oxygen present. The charge neutrality equation can be given as:

$$n + [A_M'] + 3[V_M'''] = p + 2[V_O^{\cdot\cdot}] \qquad \text{Eq. 6.7}$$

A typical defect diagram looks like as shown in Figure 6.1. The defect diagram can be divided into four regions, depending upon dominant defect species and compensation mechanism, as has been discussed below.

Region I: Very high pO_2: Nonstoichiometric region

In this region, the cation vacancies will be the dominant defect species such that $[V_M'''] \gg [A_M']$. In such a case, the acceptor impurities will be insignificant and following relationship will hold:

$$p \approx 3[V_M'''] \qquad \text{Eq. 6.8}$$

Region II: Impurity controlled region, acceptor compensation

It is expected to occur at lower pO_2 values than Region I. In this case, $[V_M'''] \ll [A_M']$, and the following condition of charge neutrality holds:

$$p \approx [A_M'] \quad \text{Eq. 6.9}$$

Using equations 6.1-6.7, one can note that:

$$[V_M'''] \approx K_s^{1/2} K_{ox}^{3/2} pO_2^{3/4} / p^3 \quad \text{Eq. 6.10}$$

$$[V_O^{\cdot\cdot}]\, K_{ox} \approx p^2 * pO_2^{-1/2} / K_{ox} \quad \text{Eq. 6.11}$$

Region III: Impurity controlled region, acceptor compensation

This is expected to occur at even lower pO_2 values, and the concentration of oxygen vacancies is constrained to be fixes as there is no negatively charged defect species to change their concentration with it

$$[A_M'] \approx 2[V_O^{\cdot\cdot}] \quad \text{Eq. 6.12}$$

Again, it can be readily seen using above equations that,

$$n \approx K_{red}^{-1/2} (2/[A_M'])^{1/2}\, pO_2^{-1/4} \quad \text{Eq. 6.13}$$

$$p \approx K_{ox}^{1/2}\, ([A_M']/2)^{1/2}\, pO_2^{+1/4} \quad \text{Eq. 6.14}$$

From equation 7.1, it can be seen that, if $[V_O^{\cdot\cdot}]$ is held constant, then $[V_M''']$ should be constant as well.

Region IV: Very low pO2: Nonstoichiometric region

$$n \approx 2[V_O^{\cdot\cdot}] \quad \text{Eq. 6.15}$$

All the defect concentrations can be derived using the same approach as above. Using the knowledge developed so far, a defect diagram can be created, assuming that the defect concentrations should be continuous across all the four regions.

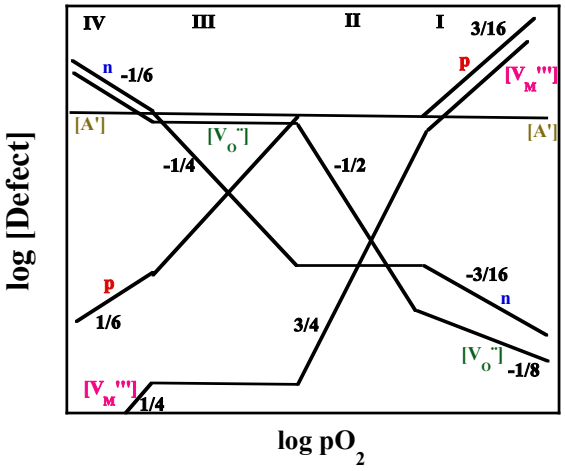

Fig. 6.1 Typical defect diagram of acceptor-doped M_2O_3 adapted from Smyth et al.[1]

Donor-doped M_2O_3

Figure 6.2 shows a typical defect diagram of M_2O_3 doped with higher DO_2. Equations 6.1-6.4 developed for acceptor doped M_2O_3 should be valid here as well. Following similar approach, the donor defect incorporation reactions can be given as:

$$3DO_2 \xrightarrow{2M_2O_3} 3D_M^{\bullet} + 6O_O + V_M''' \qquad \text{Eq. 6.16}$$

$$2DO_2 \xrightarrow{M_2O_3} 2D_M^{\bullet} + 3O_O + 2e' + 1/2O_2 \qquad \text{Eq. 6.17}$$

The equations 6.16 and 6.17 show the ionic and electronic compensations respectively. The charge neutrality equation can be given as:

$$n + 3[V_M'''] = p + 2[V_O^{\cdot\cdot}] + [D_M^{\bullet}] \qquad \text{Eq. 6.18}$$

Similar to Figure 6.1, the defect diagram of donor doped M_2O_3 can be divided into four regions, depending upon dominant defect species and compensation mechanism, as has been discussed below.

Region I and IV

The extrinsic donor impurities are expected to alter defect chemistry only at intermediate oxygen partial pressures. As was the case for Fig. 6.1, at extremely low pO_2 and extremely high pO_2, the intrinsic defects dominate and therefore the defect diagram should remain largely unaffected in these regions. Therefore, equations 6.8 and 6.15 hold true for donor-doped M_2O_3 as well.

Region II.

The case where ionic compensation may be the dominant mechanism, the following relationship may hold for cation donors,

$$[D^{\bullet}] = 2[V_M''] \qquad \text{Eq. 6.19}$$

Therefore, $[V_M'']$ will be fixed by donor level and be independent of pO_2. The $[V_O^{\cdot\cdot}]$ should also be then independent of pO_2, as enthalpy of intrinsic Schottky disorder (*e.g.* equation 6.1) should be a constant at a given temperature. Similar to equations 6.13 and 6.14, one can see that

$$(n,p) \propto \text{constant} * pO_2^{\pm 1/4} \qquad \text{Eq. 6.20}$$

Therefore, the log-plot between conductivity and pO_2 should have a slope of ±1/4. It can also be noted that the point of intrinsic conduction minimum occurs within the region of dominant ionic compensation for both acceptor and donor-doped BT (Figure 6.1, 6.2 and ref[1, 2]).

Region III

When conduction is controlled by concentration of high valence cation impurities and electronic compensation is dominant, the following relationship should hold:

$$[D^{\bullet}] \approx n \qquad \text{Eq. 6.21}$$

In this case, one can note that conductivity should be independent of pO_2,

$$\sigma \propto n \propto \text{constant} * pO_2^{\,0} \qquad \text{Eq. 6.22}$$

If this mechanism is dominant, the conductivity can also be expected to independent of temperature, if the temperature dependence of mobilities are ignored.[3] Using equations 6.1-6.4, one can also note that

$$[V_O^{\cdot\cdot}]n^2 = pO_2^{\,-1/2} K_{red} \qquad \text{Eq. 6.23}$$

$$[V_M''] = K_s^{\,1/2} K_{red}^{\,-3/2} n^6 pO_2^{\,3/4} \qquad \text{Eq. 6.24}$$

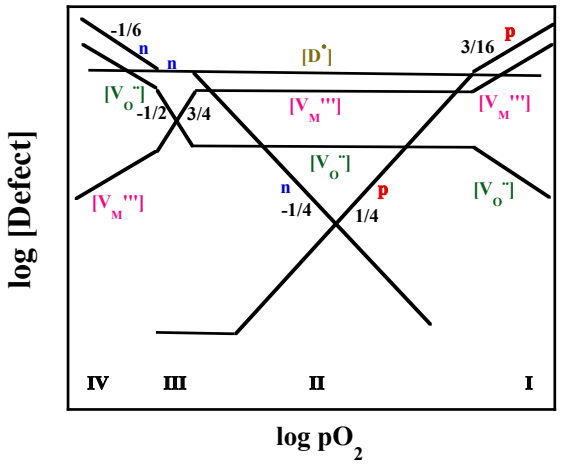

Fig. 6.2 Typical defect diagram of donor-doped M_2O_3

The $BaTiO_3$ ceramics (doped and undoped) are one of the most widely studied ceramics in terms of defect chemistry. Several authors have reported extensive measurements including pO_2- and temperature-dependent conductivity measurements to extract defect-chemical parameters. Some of them have been summarized here. Figure 6.3 shows electrical conductivity isotherms reported by various authors for BT. One can note that all these reports predict BT to be p-type conducting in air (pO_2~0.2 atm).

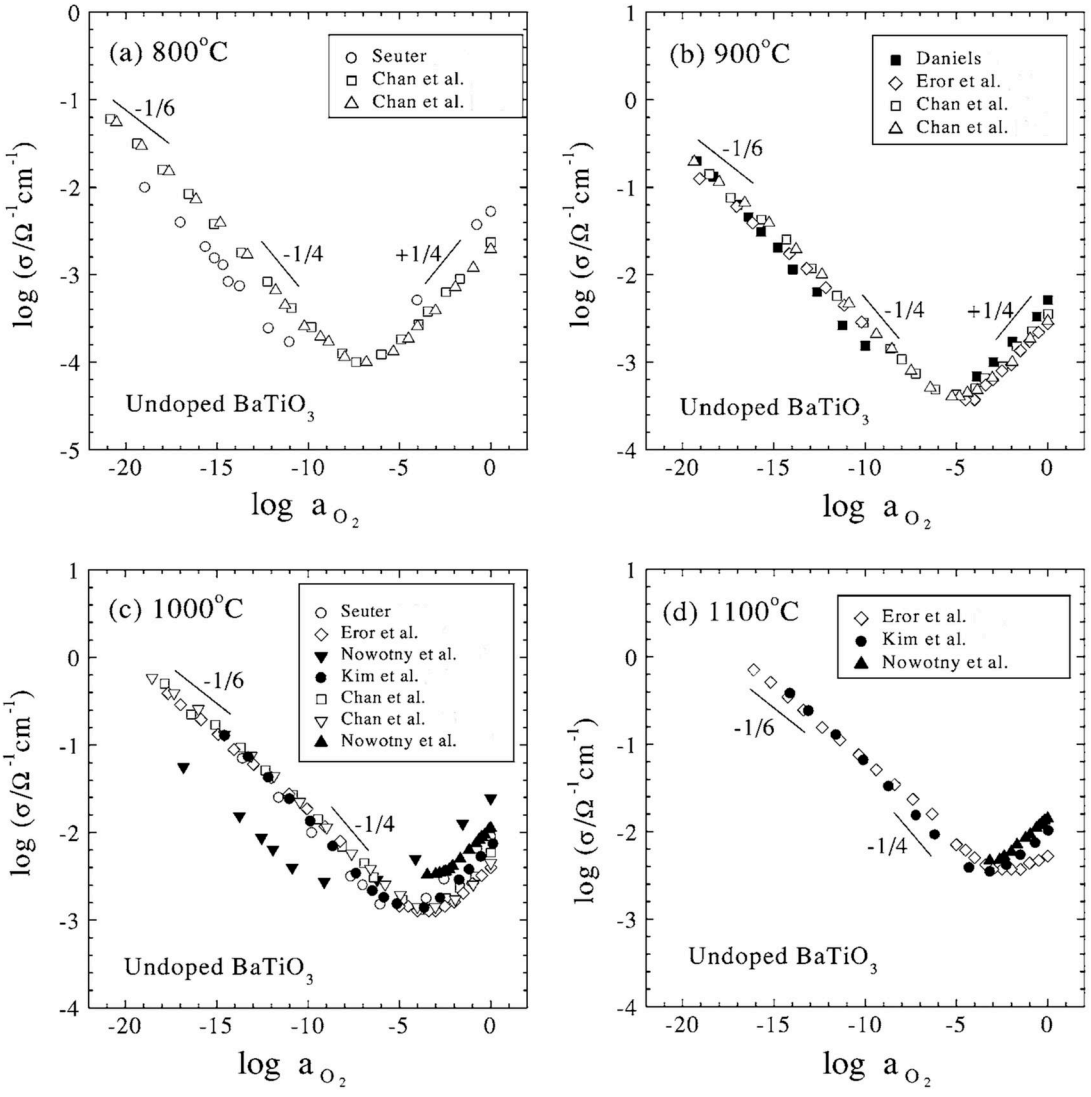

Fig. 6.3 Electrical conductivity isotherms for BT adapted from Yoo *et al*.[4] at various temperatures, which includes the data from several other authors as well.[5-12]

The data shown in Figure 6.3 is for undoped (or slightly acceptor doped) BT. It can be noted that, close to conductivity minima, the sloped are ±1/4, indicating a regime of ionic compensation. At low pO_2, it changes to -1/6, indicating that the compensation mechanism changes to the following, as was seen for doped M_2O_3 system above.

$$n \approx 2[V_O^{\cdot\cdot}] \qquad \text{Eq. 6.25}$$

Using the equations above, it can be shown that the electronic conductivity at the conductivity minima (where, $\sigma_n = \sigma_p$) in the isotherms above, can be given by:

$$\sigma_{el,m} = 2e\sqrt{K_i}\sqrt{\mu_n \mu_p} \quad \text{Eq. 6.26}$$

where, μ_n and μ_p are electron and hole mobility values respectively . Ihrig et al.[13] reported the value of μ_n to vary as per following equation:

$$\mu_n = 8080T^{-3/2}e^{-0.021eV/kT}\ cm^2/V.s \quad \text{Eq. 6.27}$$

Hole mobility was assumed to be half of electron mobility at all temperatures. Song *et. al*. reported the mobility values, as has been shown in Table 7.1.[14]

Table 6.1. Values of electron and hole mobilities as determined by Song *et al.* and others[14]

Temperature (°C)	**Electron Mobility (cm^2/V.s)**	**Hole Mobility (cm^2/V.s)**
900	0.121±0.025	0.065±0.013
1000	0.151±0.036	0.099±0.024
1100	0.110±0.031	0.080±0.023

The reported values of K_i have been summarized in Table 6.2. The reported values of ΔH_i are very close to the band gap values of BT.

Table 6.2 The values of K_i as reported by various authors.

K_i [cm^{-6}]	**Measurement**	**Reference**
$1.06 \times 10^{45} \exp(\frac{-3.15\ eV}{kT})$	Conductivity, chemical diffusivity	[14]
$6.80 \times 10^{44} \exp(\frac{-2.90\ eV}{kT})$	Conductivity, thermoelectric power	[12]
$3.96 \times 10^{46} \exp(\frac{-3.15\ eV}{kT})$	Conductivity, thermoelectric power	[11]
$8.55 \times 10^{44} \exp(\frac{-2.91\ eV}{kT})$	Conductivity, thermoelectric power	[15]

Apart from direct band gap (E_g^0) measurements using techniques like optical spectroscopy, the values of conductivity at the minima can be used to calculate band gap for BT, after correcting for small ionic contribution. Also, the enthalpy values for oxidation and reduction are related to band gap as per following relationship for BT:

$$\Delta H_{red} + \Delta H_{ox} = 2E_g^0 \qquad \text{Eq. 6.28}$$

The reported values of ΔH_{red} have been summarized in Table 6.3.

Table 6.3 The values of K_{red} as reported by various authors.

K_{red} [cm^{-9}]	**Measurement**	**Reference**
$7.09 \times 10^{70} \exp(\frac{-5.89\ eV}{kT})$	Conductivity	[16]
$1.30 \times 10^{72} \exp(\frac{-5.70\ eV}{kT})$	Conductivity	[11]
$2.56 \times 10^{71} \exp(\frac{-6.10\ eV}{kT})$	Conductivity	[7]
$1.06 \times 10^{71} \exp(\frac{-5.69\ eV}{kT})$	Conductivity	[15]
$9.43 \times 10^{72} \exp(\frac{-5.99\ eV}{kT})$	Nonstoichiometry	[17]
$3.06 \times 10^{77} \exp(\frac{-7.30\ eV}{kT})$	Conductivity, chemical diffusivity	[4]

The enthalpy values for oxidation (ΔH_{ox}) are typically much smaller (~0.9 eV) as compared to ΔH_{red}, and indicates the relative ease of oxidation when there are extrinsic oxygen vacancies present.[1]

References

[1] Smyth DM. The defect chemistry of metal oxides. The Defect Chemistry of Metal Oxides, by DM Smyth, pp 304 Foreword by DM Smyth Oxford University Press, Jun 2000 ISBN-10: 0195110145 ISBN-13: 9780195110142 2000;1.
[2] Smyth DM. The defect chemistry of donor-doped BaTiO3: a rebuttal. Journal of electroceramics 2002;9:179-86.
[3] Chan HM, HARMER MR, SMYTH DM. Compensating Defects in Highly Donor‐Doped BaTiO3. Journal of the American Ceramic Society 1986;69:507-10.
[4] Yoo H-I, Song C-R, Lee D-K. BaTiO3− δ: defect structure, electrical conductivity, chemical diffusivity, thermoelectric power, and oxygen nonstoichiometry. Journal of electroceramics 2002;8:5-36.
[5] Chan NH, Sharma R, Smyth DM. Nonstoichiometry in undoped BaTiO3. Journal of the American Ceramic Society 1981;64:556-62.
[6] Chan NH, Smyth D. Defect chemistry of BaTiO3. Journal of The Electrochemical Society 1976;123:1584-5.
[7] Daniels J, Härdtl K. Electrical conductivity at high temperatures of donor-doped barium titanate ceramics. Philips Res Rep 1976;31:489-504.
[8] Eror N, Smyth D. Nonstoichiometric disorder in single-crystalline BaTiO 3 at elevated temperatures. Journal of Solid State Chemistry 1978;24:235-44.
[9] Nowotny J, Rekas M. Electrical properties and defect structure of barium metatitanate within the p-type regime. Journal of the European Ceramic Society 1989;5:173-82.
[10] Nowotny J, Rekas M. Defect structure, electrical properties and transport in barium titanate. III. Electrical conductivity, thermopower and transport in single crystalline BaTiO 3. Ceramics international 1994;20:225-35.
[11] Seuter AMJH. Defect chemistry and electrical transport properties of barium titanate: Philips Research Laboratories; 1974.
[12] Song C-R, Yoo H-I, Kim J-Y. Mn-doped BaTiO3: electrical transport properties in equilibrium state. Journal of Electroceramics 1997;1:27-39.
[13] Ihrig H. On the polaron nature of the charge transport in BaTiO3. Journal of Physics C: Solid State Physics 1976;9:3469.
[14] Song C-R, Yoo H-I. Chemical diffusivity of BaTiO 3− δ: Defect chemical analysis. Physical Review B 2000;61:3975.
[15] Nowotny J, Rekas M. Defect structure, electrical properties and transport in barium titanate. VI. General defect model. Ceramics international 1994;20:257-63.
[16] CHAN NH, Sharma R, Smyth DM. Nonstoichiometry in Acceptor‐Doped BaTiO3. Journal of the American Ceramic Society 1982;65:167-70.
[17] Hagemann HJ, Hennings D. Reversible Weight Change of Acceptor‐Doped BaTiO3. Journal of the American Ceramic Society 1981;64:590-4.

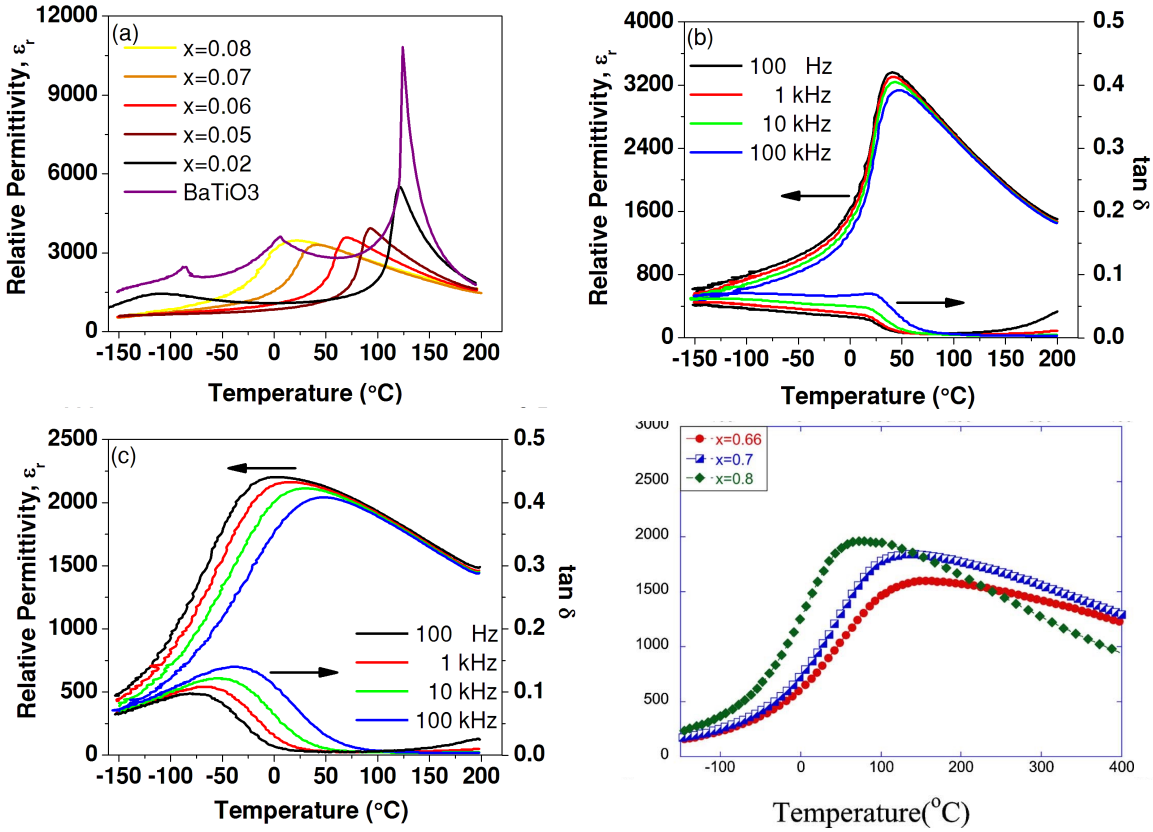

Figure 7.1. (a) Evolution of temperature-dependent relative permittivity with composition for (1-x)BT-xBZT ceramics, (b) relative permittivity versus temperature for 0.93BT-0.07BZT exhibiting moderate DPT behavior, (c) temperature-dependent relative permittivity for 0.89BT-0.11BZT exhibiting relaxor characteristics (from Triamnak et al.[1]), and (d) evolution of dielectric behavior for BT-xBZT (x between 0.2 to 0.34) ceramic with increasing content adapted from Huang et al.[2]

The Bi-perovskites gained attention owing to their similar electronic structure as Pb, and their relative friendliness to environment and health. Owing to these reasons, there were many reports of solid solutions between $PbTiO_3$ and $BiMO_3$ (where, $M = Sc^{3+}$, Ti^{4+}, Zn^{2+}, Nb^{5+} and others).[3, 4] This work is mainly focused on BT-BZT ceramics and Fig. 7.1 shows their temperature dependent dielectric evolution. For pure BT, one can notice the characteristic peaks indicating phase transitions at -90 °C, 0 °C and 130 °C.

However, with addition of just 5% BZT, the peaks at or below 0 °C vanish and is replaced by one broad peak. As the amount of BZT increases further, the degree of diffuseness increases before reaching solubility limit ~34 mol% BZT, as reported by Huang et al.[2] The dielectric losses also improved on adding BZT to BT. They were higher than 5% for BT at a temperature of ~350 °C, however for BT-10%BZT they remained below 5% even at 500 °C.[5] The temperature-stability of permittivity is an important parameter for emerging high temperature applications. In Fig. 8.1, it was shown that this stability can be improved on adding BZT to BT, and in Fig. 8.2 it has been shown that it can be further tuned by adding third end members to BT-BZT like $BiInO_3$ and $BiScO_3$.[6] Especially, the composition 50BT-25BZT-25BS had its dielectric permittivity almost unaffected from 100 °C to 500 °C.

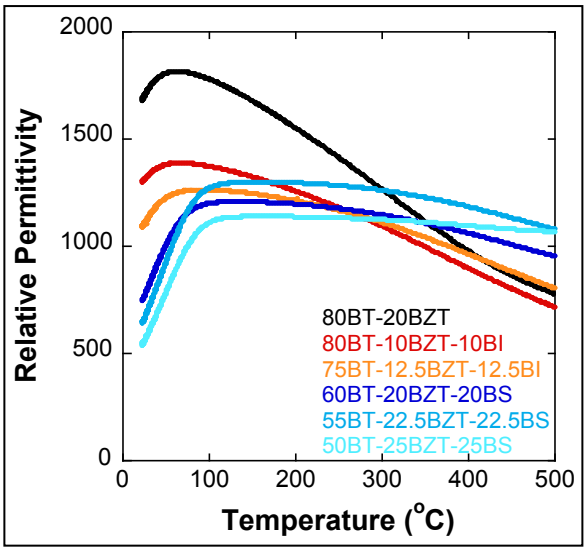

Fig. 7.2. Figure showing temperature-dependent dielectric behavior of BT-BZT-ABO_3 ceramics and their potential to be tuned as per requirements.[6]

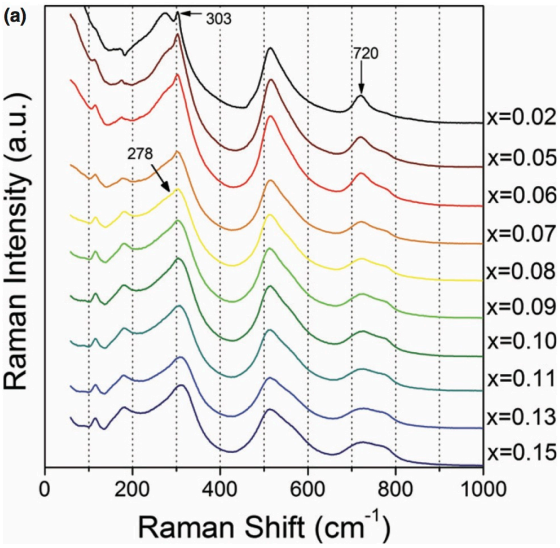

Fig. 7.3. Raman spectroscopy on BT-BZT adapted from Triamnak et al.[1]

Figure 7.3 shows the room temperature Raman spectra of BT-BZT ceramics for various BZT content. It can be seen that for higher BZT content, the peaks are broader as compared to sharp peaks (at 303 and 720 cm^{-1}) characteristic of a normal ferroelectric for lower BZT ceramics. The transition occurs ~8 mol% BZT composition, where a shoulder started to develop on low wavenumber side of 303 cm^{-1} peak at ~278 cm^{-1}. A broad peak ~770 cm-1 is characteristic of a disordered system[7] and was apparent for ceramics with higher BZT content. The results are consistent with low-field dielectric and high-filed P-E measurements.

Typically, ferroelectric perovskites exhibit high relative permittivity values (>1000), and since the mechanisms controlling the permittivity and macroscopic polarization are related, typically these also exhibit high values of macroscopic polarization on application of an external electric field. Some relaxor materials can exhibit an electric field-induced phase transition to a ferroelectric state on the

application of an electric field, which results in increased polarization and strain values.[8] The ergodic relaxors (especially those with T_f below room temperature) are of particular interest, as they can exhibit a reversible phase change with electric field and negligible remanent polarization. At moderate fields, an approximately linear dielectric response is observed for these relaxors, where the polarization, *P*, can be given by, $P = \varepsilon_0 \chi_1 E$, where, ε_0 is the permittivity of free space and χ_1 is the linear susceptibility of the material. This is technologically important for high energy-density applications, since the energy density per unit volume ($U_{vol} = \int E \, \mathrm{d}P$), which can be calculated by the area enclosed by the *P*-*E* loop (decreasing field) and the polarization axis, is enhanced versus a hysteretic normal ferroelectric because of the tiny remanence associated with relaxors. The evolution of P-E hysteresis loops for BT-BZT with compositions has been shown in Figure 7.4. It can be noted that the hysteretic behavior of the loops almost vanish after a BZT content of 8 mol%.

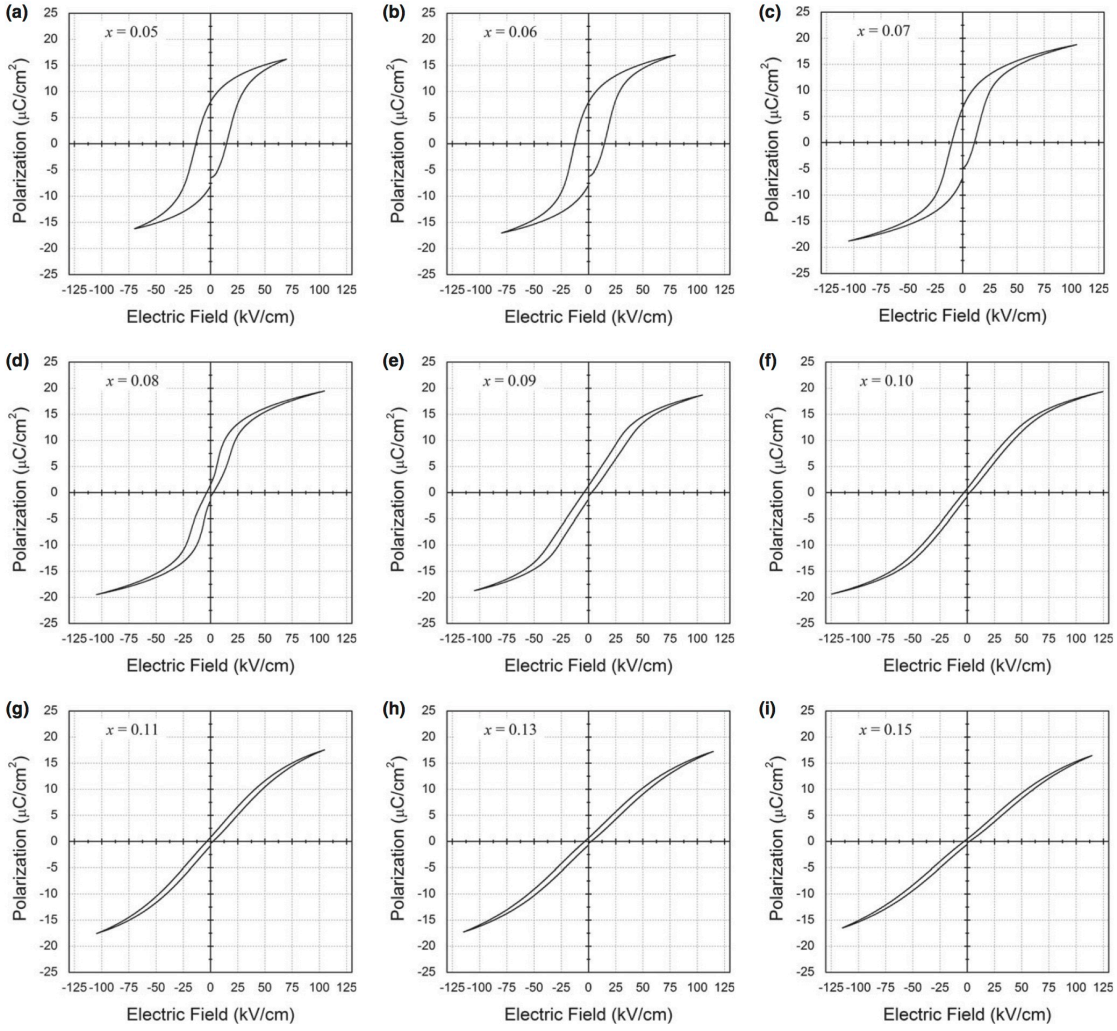

Fig 7.4 Figure showing polarization hysteresis loops for (1-x)BT-xBZT ceramics and their evolution with BZT content.[1]

Figure 8.5 shows the electric-field dependent permittivity of BT-BZT ceramics as compared to other commercial ceramics capacitors and it can be noticed that the BT-BZT ceramics have better electric-field stability of permittivity as compared to various others shown in the figure.

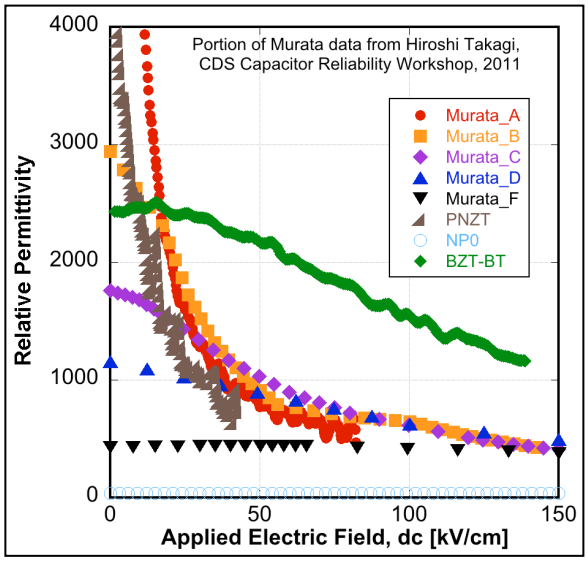

Fig. 7.5 Plot comparing the field dependent permittivity of BT-BZT ceramics with other commercial ceramic capacitors.

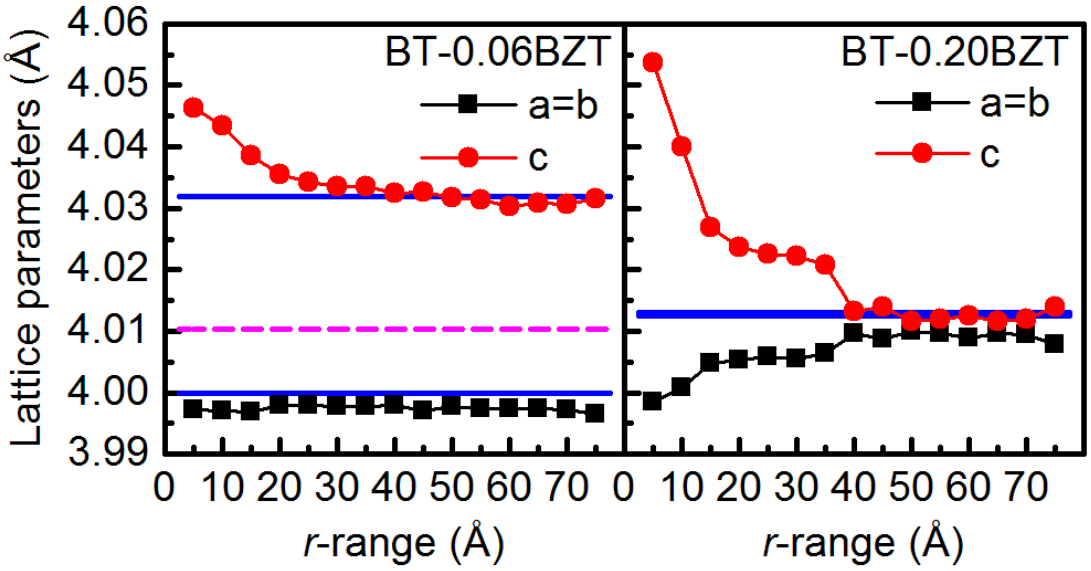

Fig. 7.6 The lattice parameters obtained from PDFs are shown as red and black symbols. The blue lines indicate the tetragonal The lattice parameters obtained from the Rietveld refinements (blue lines for tetragonal and dashed pink for cubic space group) have also been shown for reference.[9]

Tedi-Marie *et al.* performed PDF measurements on BT-BZT ceramics to investigate the relationship between short-range and long-range structures.[9] The results

showed that local distortions are present in PNRs, however, over large length scales, they average out leading to a pseudo-cubic structure. The PDFs of 94BT-6BZT and 80BT-20BZT were analyzed using a small-box model using PDFgui program, using a P4*mm* space group.[10] The results demonstrating a length-scale dependent structure have been shown in Figure 8.6. For 20BZT ceramics, the local tetragonal distortion (c/a ration) was ~ 1.01375 and it reduced to ~1 at approximately a length scale value of 40 Å.

References

[1] Triamnak N, Yimnirun R, Pokorny J, Cann DP. Relaxor Characteristics of the Phase Transformation in (1− x) BaTiO3–xBi (Zn1/2Ti1/2) O3 Perovskite Ceramics. J Am Ceram Soc 2013;96:3176-82.
[2] Huang C-C, Cann DP. Phase transitions and dielectric properties in Bi(Zn{sub 1/2}Ti{sub 1/2})O{sub 3}-BaTiO{sub 3} perovskite solid solutions. Journal of Applied Physics 2008:Medium: X; Size: page(s) 024117-.4.
[3] Eitel RE, Randall CA, Shrout TR, Rehrig PW, Hackenberger W, Park S-E. New high temperature morphotropic phase boundary piezoelectrics based on Bi (Me) O3–PbTiO3 ceramics. Japanese Journal of Applied Physics 2001;40:5999.
[4] Suchomel MR, Davies PK. Enhanced tetragonality in (x) PbTiO3-(1-x) Bi (Zn1/2Ti1/2) O3 and related solid solution systems. Applied Physics Letters 2005;86:2905.
[5] Bhalla A, Guo R, Roy R. The perovskite structure–a review of its role in ceramic science and technology. Material Research Innovations 2000;4:3-26.
[6] Raengthon N, Sebastian T, Cumming D, Reaney IM, Cann DP. BaTiO3–Bi (Zn1/2Ti1/2) O3‐BiScO3 Ceramics for High‐Temperature Capacitor Applications. Journal of the American Ceramic Society 2012;95:3554-61.
[7] Zheng H, de Györgyfalva GC, Quimby R, Bagshaw H, Ubic R, Reaney I, et al. Raman spectroscopy of B-site order–disorder in CaTiO 3-based microwave ceramics. Journal of the European Ceramic Society 2003;23:2653-9.
[8] Jo W, Dittmer R, Acosta M, Zang J, Groh C, Sapper E, et al. Giant electric-field-induced strains in lead-free ceramics for actuator applications–status and perspective. Journal of electroceramics 2012;29:71-93.
[9] Beuerlein MA, Kumar N, Usher T-M, Brown-Shaklee HJ, Raengthon N, Reaney IM, et al. Current Understanding of Structure–Processing–Property Relationships inBaTiO3–Bi(M)O3 Dielectrics. Journal of the American Ceramics Society 2016.
[10] Farrow CL, Juhas P, Liu JW, Bryndin D, Bozin ES, Bloch J, et al. PDFfit2 and PDFgui: computer programs for studying nanostructure in crystals. Journal of Physics-Condensed Matter 2007;19:335219.

8. Materials Synthesis and Characterization

Experimental details for Chapter 9

Ceramic powders of the composition (1-x)$BaTiO_3$-x$Bi(Zn_{1/2}Ti_{1/2})O_3$, (1-x)$SrTiO_3$-x$Bi(Zn_{1/2}Ti_{1/2})O_3$, (1-x)$BaTiO_3$-x$BiScO_3$ and (1-x)$BaTiO_3$-x$BaBiO_3$ have been prepared using conventional solid state methods. The detailed synthesis conditions, including temperatures, milling conditions, binders used and others, have been mentioned in the subchapters 9.1-9.5. Most of the ceramics were sintered in air, except $BaBiO_3$, which was sintered in oxygen.

X-ray diffraction (XRD) measurements have been performed on all of the samples (crushed ceramics) to check phase purity, determine crystal structure and determine site occupancies. Laboratory XRD instrument (Bruker AXS D8 Discover, Madison, WI, USA) was predominantly used to check phase purity and verify crystal structures. High-resolution synchrotron powder diffraction data were collected on $BaBiO_3$ and some BT-BZT ceramics powders using beamline 11-BM at the Advanced Photon Source (APS), Argonne National Laboratory. An appropriate amount of the sample was loaded into a Kapton tube, sealed and mounted on the base provided by the 11-BM beamline of the APS. The diffraction experiments were carried out at room temperature using monochromatic synchrotron radiation of wavelength 0.413639 Å and a step size of 0.001°. The crystal structure was refined using the Rietveld refinement program GSAS-II.[1] The Chebyschev profile was used to fit the background. Parameters refined included peak-shape parameters, scale, lattice

parameters, atomic positions, isotropic displacement parameters, thermal occupancies and others.

Time of flight (TOF) powder neutron diffraction data were also collected on the POWGEN instrument at the Spallation Neutron Source (SNS) in the Oak Ridge National Lab (ORNL) for BT and BT-25BZT powders obtained by crushing sintered pellets. A vanadium container was filled with appropriate amount of powder and sent via the mail-in service to the SNS. Data were collected to cover a d-spacing range of 0.3−3.0 Å.

Prior to any electrical measurements, the ceramics were polished to sub-millimeter thicknesses. Silver electrodes were applied on both sides of the pellets and then fired at 700°C for 30 min. For measurements sensitive to oxygen partial pressure, Pt electrodes were used. They were in general fired at 700°C for 30 min. For some samples, sputtered Pt was also used, and has been mentioned later whenever relevant. For most dielectric and impedance measurements, the pellets were placed in a high temperature measurement cell (NorECs AS ProbostatTM, Oslo, Norway) or low temperature furnace (Delta Design 9023, California, USA). Temperature dependent dielectric properties were measured using an LCR meter (Agilent 4284A, Santa Clara, CA, USA). An impedance analyzer (Solartron SI1260A equipped with Solartron 1296A dielectric interface, Farnborough, UK) was used to measure the impedance in the frequency range 0.1 Hz to 1 MHz. The SMaRT impedance measurement software program was used to collect the data. Some of the impedance spectroscopy was performed using a home-built high-temperature sample holder and an impedance analyzer (Novocontrol Technologies,

Montabaur, Germany) at Technische Universität Darmstadt, Germany. The WinDETA software was used to collect data in that case. Some impedance measurements were performed on sintered ceramics, where conduction was monitored as a function of oxygen partial pressure or applied DC-bias. For each data point, in order to establish close to steady-state values, the change in resistivity was monitored by conducting consecutive impedance measurements until no further noticeable change could be observed.

The optical measurements were carried out on the sintered pellets over the wavelength range of 200-1100 nm at room temperature using an Ocean Optics HR4000 UV-Vis Spectrometer (Ocean Optics, Dunedin, FL) with a balanced deuterium/tungsten halogen source.

For performing thermally stimulated depolarization current (TSDC) measurements, polarized samples were heated at a rate of 2 K/min and depolarization currents were detected with a Keithley 6517B electrometer. No bias fields were applied during measurements. Sputtered Pt electrodes were used for the same.

Seebeck measurements were performed on selected samples using the Probostat set-up and a Keithley 6517A Electrometer, using fired Pt electrodes. For this measurement, bar samples with lengths of ~23 mm and cross-section of 4x4 mm^2 were used. They were cut to suitable size from a larger disc sample, prepared via conventional

solid-state route. The temperature difference across the sample was measured using two different thermocouples.

The temperature dependent high-field DC-resistivity measurements (25 °C – 500 °C) were performed on some samples at electric field levels up to ~1.5 kV/cm using a high voltage source (Keithley 237 High Voltage Source Measure Unit, USA) and the probostat mentioned above. For each measurement, the currents were applied and increased logarithmically and the corresponding voltages were measured.

X-ray Photoelectron Spectroscopy (XPS) spectra were acquired on a ThermoScientific ESCALAB 250 spectrometer located at the Center for Advanced Materials Characterization in Oregon (CAMCOR). Photoemission was stimulated by a beam of monochromatized Al Kα x-rays with a nominal spot size at the sample surface of 500μm. A low energy electron source was used for charge neutralization. The spectra were acquired at a pass energy of 20 eV (high resolution spectra) or 150 eV (survey spectra). Data analysis, including peak fitting, was performed with Avantage software, provided by the manufacturer.

High-resolution transmission electron microscopy (TEM), Energy-dispersive X-ray spectroscopy (EDS) and Electron Energy Loss spectroscopy (EELS) were used to investigate microstructural and microchemical features. The TEM samples were prepared using low-energy Focussed-ion beam (FIB), at cryogenic temperatures to minimize any structural damage and oxygen rearrangement due to local heating at Center for Advanced Materials Characterization in Oregon (CAMCOR). The measurements were also performed at cryogenic temperatures using FEI TITAN TEM operated at 200 kV, at

Oregon State University. The spectra were recorded at an approximate collection angle of 7.7 mrad and convergence angle of 9.8 mrad. Gatan DigitalMicrograph and TIA software were used for image processing and acquirirng EDS and EELS spectra. The EELS spectra were taken from thin (<100 nm) regions of the sample to avoid plural scattering contribution. For background removal, a power law function was used. A constant signal integration window was used for all the spectra, which also covered near-edge fine structures. The quantification was performed through the following equation:

$$\frac{N_A}{N_B} = \frac{\sigma_B(\beta, \Delta)}{\sigma_A(\beta, \Delta)} \times \frac{I_A(\beta, \Delta)}{I_B(\beta, \Delta)}$$

where, N is relative number of atoms, I is integrated intensity, σ is partial cross-section for a given collection angle (β) and a given integration window (Δ). The theoretical cross section were not expected to be reliable for some atoms *e.g.* Ba $M_{4,5}$ edge, and there a *k*-factor approach was used for quantification, which basically provides quantification relative to a known standard.[2]

Extended X-ray absorption fine structure (EXAFS) was measured for L3 edges of bismuth in transmission and florescence modes, at Stanford Synchrotron Radiation Lightsource. The data was processed using Athena software.[3]

The TGA was performed on calcined powders at United States Naval Research Laboratory using a Netzsch STA 449 F1 Jupiter TGA and Coupling TA-QMS 403C

Aëolos mass spectrometer (Netzsch Instruments North America, LLC, Burlington, MA, USA).

Prompt gamma neutron activation analysis (PGNAA) was performed on BT and BT-BZT samples at Oregon State University (OSU) TRIGA reactor.

Multilayer ceramic capacitors (MLCCs) were fabricated for some compositions. The calcined ceramic powders were mixed with various organic binders and solvents and cast to thin tapes for multilayer fabrication. Uniformly mixed slurry was passed through a doctor blade on a steel belt and was dried as the belt traveled through a heated cabinet. The internal electrode of multilayer capacitor was screen printed on ceramic tapes. Lamination of the printed stack of 30 active layers was conducted under hydraulic pressure at 21 MPa at 65 °C. A laminated stack was cut into individual multilayer capacitors. Cut multilayer capacitors went through a binder removal process that involves slowly heating to 550 °C. After burnout the capacitors were sintered at 1200 °C for 1 h in a tube furnace with flowing oxygen and then hot isostatically pressed (HIP'ed) at 1100 °C and 5000 psi for 3hrs. The HIP is effective in removing residual pores or defects after sintering. Capacitors were then tumbled to expose internal electrode for 30 min and then silver terminal electrode was applied and fired at 590 °C using tunnel kiln. For these MLCCs, the ceramic-electrode interface was exposed to a focused ion beam (FIB) and imaged using an SEM (Quanta 3D Dual Beam SEM/FIB, FEI, Hillsboro, OR, USA).

While preparing a ceramic of new composition, the general approach was to first get an optimum calcination temperature, and then take the calcined powders and sinter them at several temperatures, to get optimum phase purity and densification. Typical examples have been shown in Figures 8.1 and 8.2. Figure 8.1 shows phase evolution with temperature. Figure 8.2 shows temperature evolution of density using ex-situ technique and a dilatometer.[4]

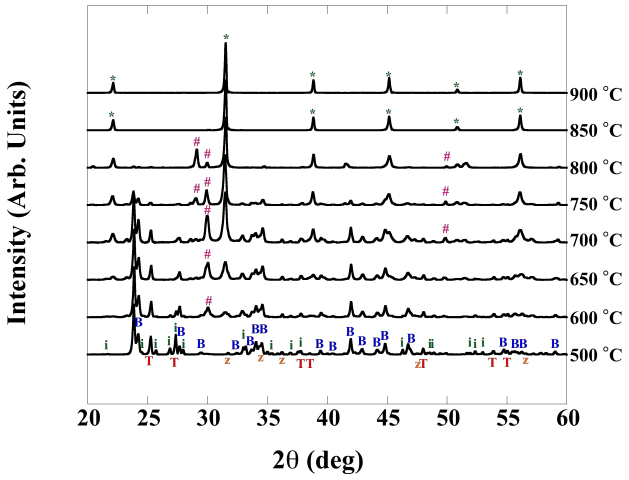

Fig. 8.1 (a) X-ray diffraction patterns of calcined BT-20BZT ceramics at various temperatures. B = $BaCO_3$, T = TiO_2, * = perovskite phases, # = multiple phases, i = Bi_2O_3, z = ZnO.

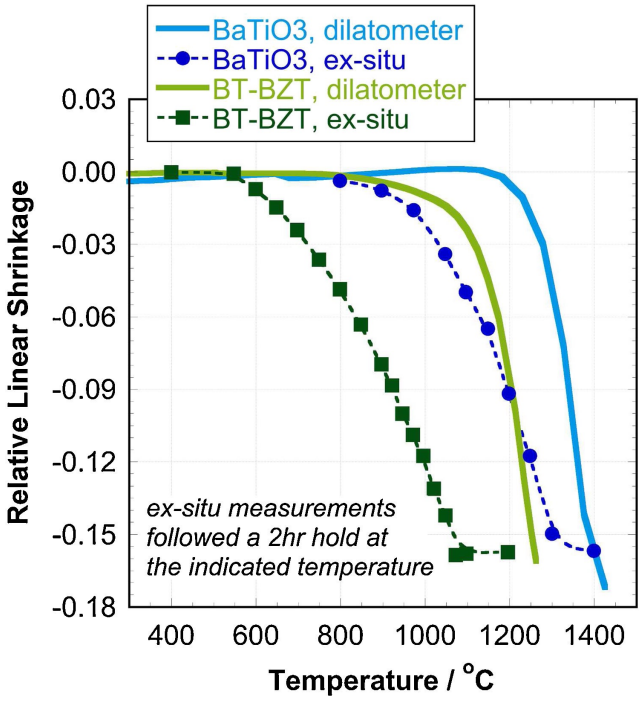

Fig. 8.2 Densification (radial shrinkage) as a function of temperature for BT and BT-BZT ceramics, measured in-situ using a dilatometer and ex-situ by holding at a temperature for two hours, quenching it and measuring shrinkage.[4]

Experimental details for Chapter 10

Ceramics of the composition $xBi(Mg_{1/2}Ti_{1/2})O_3$-0.4BKT-(0.6-x)BNT were prepared via conventional solid state processing. The precursor powders used were Bi_2O_3 (>99.9%), $MgCO_3$ (>99%), TiO_2 (>99.9%), K_2CO_3(>99%) and Na_2CO_3(>99.5%). The precise synthesis conditions have been mentioned in Chapters 10.1 and 10.2.

X-ray diffraction (Bruker AXS D8 Discover, Madison, WI, USA) was used for phase and crystal structure determination. Prior to any electrical measurements, silver electrodes were applied on both sides of the pellets and then fired at 700°C for 30 min. The pellets were placed in a high temperature measurement cell (NorECs AS

ProbostatTM, Oslo, Norway) and temperature dependent dielectric properties were measured using an LCR meter (Agilent 4284A, Santa Clara, CA, USA). An impedance analyzer (Solartron SI1260A equipped with Solartron 1296A dielectric interface, Farnborough, UK) was used to measure the impedance in the frequency range 0.1 Hz to 1 MHz. The SMaRT impedance measurement software program was used to collect the data. Polarization hysteresis was measured at room temperature and 1 Hz (using Radiant Technologies RT66A, Albuquerque, New Mexico). Strain measurements were conducted at 0.1 Hz in conjunction with a interferometric sensor (MTI Instruments 2100 Fotonic Sensor, Albany, New York). Fatigue tests were conducted on unpoled samples by applying a bipolar triangular waveform at 10 Hz with a peak field of 50 kV/cm. The optical measurements were carried out on the sintered pellets over the wavelength range of 200-1100 nm at room temperature using an Ocean Optics HR4000 UV-Vis Spectrometer (Ocean Optics, Dunedin, FL) with a balanced deuterium/tungsten halogen source.

Further details on synthesis and characterization will be provided in later sections whenever required.

References

[1] Toby BH, Von Dreele RB. GSAS-II: the genesis of a modern open-source all purpose crystallography software package. Journal of Applied Crystallography 2013;46:544-9.
[2] Hofer F. EELS quantification of M edges by using oxidic standards. Ultramicroscopy 1987;21:63-8.
[3] Ravel B, Newville M. ATHENA, ARTEMIS, HEPHAESTUS: data analysis for X-ray absorption spectroscopy using IFEFFIT. Journal of synchrotron radiation 2005;12:537-41.
[4] TRIAMNAK N, BRENNECKA GL, BROWN-SHAKLEE HJ, RODRIGUEZ MA, CANN DP. Phase formation of BaTiO 3–Bi (Zn 1/2 Ti 1/2) O 3 perovskite ceramics. Journal of the Ceramic Society of Japan 2014;122:260-6.

Chapter 9. The $BaTiO_3$–$Bi(Zn_{1/2}Ti_{1/2}O)_3$ (BT–BZT) ceramics

As mentioned in abstract and introduction sections, this research is focused on studying defect structure and transport properties in Bi-based perovskites, which can be potentially used for high temperature, high energy density capacitors, piezoelectric actuators and others. For the sake of convenience, the results have been divided into two chapters. Chapter 9 discusses the defect and transport properties of $BaTiO_3$-$Bi(Zn_{1/2}Ti_{1/2})O_3$ (BT-BZT) ceramics. Chapter 10 studies the $Bi(Mg_{1/2}Ti_{1/2})O_3$-$(Bi_{1/2}K_{1/2})TiO_3$-$(Bi_{1/2}Na_{1/2})TiO_3$ relaxor ceramics.

Sub-chapter 9.1 demonstrates the compatibility of BT-BZT ceramics in the Multilayer Ceramic Capacitor (MLCC) configuration. Sub-chapter 9.2 demonstrates the improved insulation properties in BT-BZT ceramics on adding BZT to the solid solution. Sub-chapter 9.3 and 9.4 show the p-type to n-type transition of adding BZT to BT using various experiments and discuss the possible defect mechanisms. One of the potential mechanisms for resistivity enhancement and change in majority charge carrier, as was discussed in sub-chapter 9.3 and 9.4, has been investigated in sub-chapter 9.5. Sub-chapter 9.6 demonstrates the versatility of the concepts developed in previous chapters and shows that the phenomenon of resistivity enhancement and change in type of majority charge carriers can be seen in other ceramic systems as well. Sub-chapter 9.7 knits all the knowledge from previous papers together, and with the help of some extensive experiments, proposes the underlying defect chemistry of BT-BiMO$_3$ ceramics.

Chapter 10 focuses on developing a Pb-free alternative for PZT for the actuator applications (Sub-chapter 10.1) and then discusses the role of point defects (sub-chapter 10.2) in an attempt to explore their defect chemistry.

9.1 Multilayer ceramic capacitors based on relaxor $BaTiO_3$-$Bi(Zn_{1/2}Ti_{1/2})O_3$ for temperature stable and high energy density capacitor applications

Nitish Kumar,[1] Aleksey Ionin,[1] Troy Ansell,[1] Seongtae Kwon,[2] Wesley Hackenberger,[2] and David Cann[1]

[1]Materials Science, School of Mechanical, Industrial, and Manufacturing Engineering, Oregon State University, Corvallis, Oregon 97331, USA

[2]TRS Technologies, State College, PA, 16801, USA

Published in

Applied Physics Letters

Vol.106, 252901 (2015)

Abstract

The need for miniaturization without compromising cost and performance continues to drive research in capacitor devices. In this report, multilayer ceramic capacitors based on relaxor $BaTiO_3$-$Bi(Zn_{1/2}Ti_{1/2})O_3$ (BT-BZT) were fabricated and characterized. In bulk ceramic embodiments, BT-BZT has been shown to exhibit relative permittivities greater than 1000, high resistivities (ρ > 1 GΩ-cm at 300°C), and negligible saturation up to fields as high as 150 kV/cm. Multilayer capacitor embodiments were fabricated and found to exhibit similar dielectric and resistivity properties. The energy density for the multilayer ceramics reached values of ~2.8 J/cm^3 at room temperature at an applied electric field of ~330 kV/cm. This represents a significant improvement compared to commercially available multilayer capacitors. The dielectric properties were also found to be stable over a wide range of temperatures with a temperature coefficient of approximately -2000 ppm/K measured from 50 to 350 °C, an important criteria for high temperature applications. Finally, the compatibility of inexpensive Ag-Pd electrodes with these ceramics was also demonstrated, which can have implications on minimizing the device cost.

Main Text

Current state-of-the-art capacitors require a relatively large fraction of the volume of the electronic components in power electronics systems. Multilayer ceramic capacitors (MLCCs) are an effective means for improving the volumetric efficiency of

the capacitive components. With dielectric layers with small thicknesses together with their parallel arrangement, higher capacitance levels and higher levels of energy density (J/cm^3) can be achieved along with miniaturization of the electronic circuitry. However, the manufacturing of high quality MLCCs is challenging and often faces problems such as inter-diffusion or chemical reaction between the metal electrode and ceramic, oxidation of electrodes during the co-firing step, residual stresses, and the need to add significant levels of dopants to lower the sintering temperature during co-firing which may affect the properties adversely.[1-7] The growing need for further miniaturization, higher volumetric efficiency, lower cost, and the need to resolve the issues associated with the current manufacturing technology motivate the current research activities in the field of MLCCs.

Ceramic capacitors have the potential to achieve the requirements for high temperature power conversion and energy storage systems. Traditionally, MLCCs based on chemically inhomogeneous and doped $BaTiO_3$ (X7R specification, Electronic Industries Association standards) are used to attain temperature-stable dielectric properties.[6, 8-11] However, there is a constant effort to explore materials with better properties, especially at higher temperatures and specifically designed for use at high fields (E >100 kV/cm). Recently, MLCCs based on relaxor perovskites have shown great promise with improved properties compared to traditional X7R capacitors.[12-16] Previous research has shown that relaxor dielectrics based on compositions in the $BaTiO_3$-$Bi(Zn_{1/2}Ti_{1/2})O_3$ (BT-BZT) system have unique properties including a high dielectric constant (>1000) which remains stable up to high temperatures (T>300°C) and

that persists to high electric fields (E>100 kV/cm).[17, 18] They also maintain a high insulation resistance even at high temperatures which enables these materials to withstand large electric fields without breaking down. In addition, they exhibit negligible hysteresis due to the relaxor mechanism in compositions with greater than 8 mol% BZT. This results in MLCC devices with low dielectric loss and the potential for high energy densities.

In this study, high energy density multilayer ceramic capacitors based on the (1-x)BT-xBZT system (where x=15%, 20%) were fabricated. The MLCCs were fabricated with two internal electrode systems, an Ag-Pd alloy and a Pt-Au-Pd alloy. The MLCC devices were characterized and the properties were compared to the bulk ceramic material.

Ceramic powders of the composition (1-x)$BaTiO_3$-x$Bi(Zn_{1/2}Ti_{1/2})O_3$ (x=15%, 20%) have been prepared using conventional solid state methods following the methods described in reference.[19] The calcined ceramic powders were mixed with various organic binders and solvents and cast to thin tapes for multilayer fabrication. Uniformly mixed slurry was passed through a doctor blade on a steel belt and was dried as the belt traveled through a heated cabinet. The internal electrode of multilayer capacitor was screen printed on ceramic tapes. Lamination of the printed stack of 30 active layers was conducted under hydraulic pressure at 21 MPa at 65 °C. A laminated stack was cut into individual multilayer capacitors. Cut multilayer capacitors went through a binder removal process that involves slowly heating to 550 °C. After burnout the capacitors

were sintered at 1200 °C for 1 h in a tube furnace with flowing oxygen and then hot isostatically pressed (HIP'ed) at 1100 °C and 5000 psi for 3hrs. The HIP is effective in removing residual pores or defects after sintering. Capacitors were then tumbled to expose internal electrode for 30 min and then silver terminal electrode was applied and fired at 590 °C using tunnel kiln. The dielectric properties of the MLCCs were measured using a high temperature measurement cell (NorECs AS ProbostatTM, Oslo, Norway) and an LCR meter (Agilent 4284A, Santa Clara, CA, USA). The MLCCs had a parallel arrangement of layers of capacitor, which was taken into account while calculating permittivity from MLCC capacitance. The energy density can be estimated from polarization-electric field curves by calculating the area enclosed by the curve and polarization axis. An impedance analyzer (Solartron SI1260A) equipped with a dielectric interface (Solartron 1296A, Farnborough, UK) was used over the frequency range 1 Hz to 1 MHz, in conjunction with SMaRT impedance measurement software program to collect the data. Polarization hysteresis measurements were performed at room temperature and 1 Hz using Radiant Technologies RT66A, Albuquerque, NM. The ceramic-electrode interface was exposed with a focused ion beam (FIB) and imaged using an SEM (Quanta 3D Dual Beam SEM/FIB, FEI, Hillsboro, OR, USA).

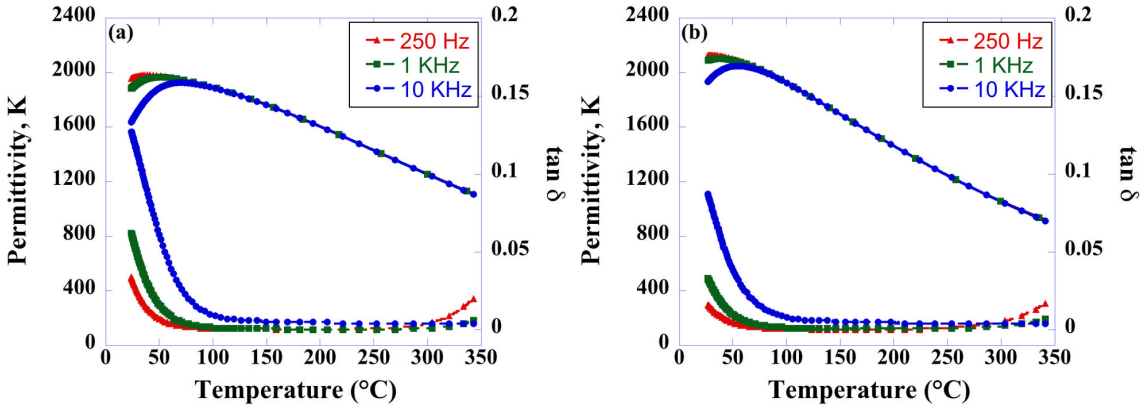

FIG. 9.1.1. Temperature dependence of relative permittivity and dielectric loss for (a) 80BT-20BZT and (b) 85BT-15BZT MLCCs from 250 Hz to 10 kHz.

Figure 9.1.1 (a) and (b) show the dielectric properties as a function of temperature for MLCC devices of the compositions 80BT-20BZT and 85BT-15BZT with Pt-Pd-Au electrodes. These results closely match the dielectric behavior of bulk ceramics in terms of temperature stability and dielectric loss values.[17, 18] The room temperature dielectric constant for the MLCCs were found to be comparable (<10% different) to their bulk ceramic counterparts. Some of the disparity in the dielectric constant values can be attributed to uncertainties associated with the calculation of the layer thickness and internal electrode area. The close correspondence between the MLCC and ceramic properties is significant because the dielectric properties of MLCC devices are often inferior due to electrode interactions, low porosity, and other factors.

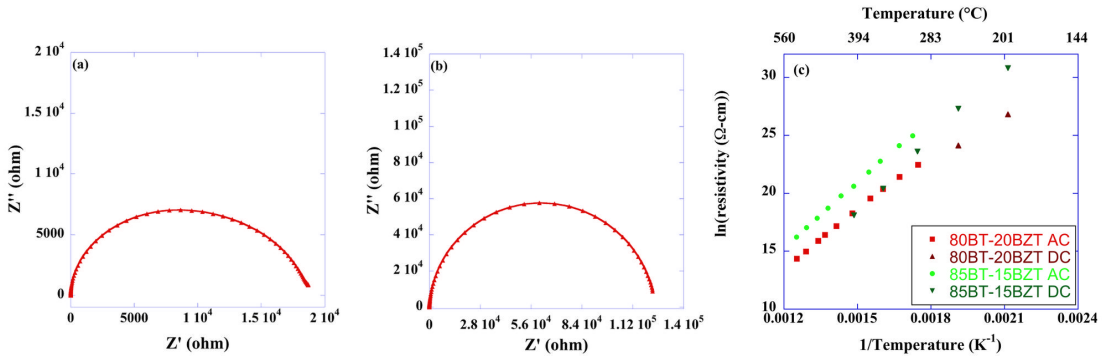

FIG. 9.1.2. Nyquist plots for (a) 80BT-20BZT and (b) 85BT-15BZT MLCCs at 400 °C and (c) Arrhenius plots for AC and DC resistivity.

Low-field AC impedance measurements were performed on MLCCs of both compositions and Pt-Pd-Au internal electrodes and the data is shown in Figure 9.1.2. From the Nyquist plots, it appears that the 15BZT composition exhibited some degree of electrical heterogeneity with an apparent low frequency shoulder, while the 20BZT composition appeared more electrically homogeneous. The activation energies derived from the Arrhenius plots were approximately 1.6 eV which is close to half of the optical band gap which suggests intrinsic conduction as the dominant mechanism.[20] These data indicate that the transport behavior in the MLCC devices was similar to that obtained in the bulk ceramics. This implies that no significant defects were introduced during the multilayer fabrication process. [20, 21] Figure 9.1.2c shows the Arrhenius plots from the data obtained from high-field DC measurements superposed onto the Arrhenius data obtained from low-field AC measurements. While the AC and DC behavior were quite similar for 20BZT composition, the resistivity calculated for the 15BZT composition was one order of magnitude lower for high-field DC measurement as compared to the low-field AC measurement. The measurement of high resistivity values at high temperatures

(~10^{10} Ω-cm at 300 °C) indicates that these devices can withstand high E-fields which can extend the operational temperature range of these MLCCs.

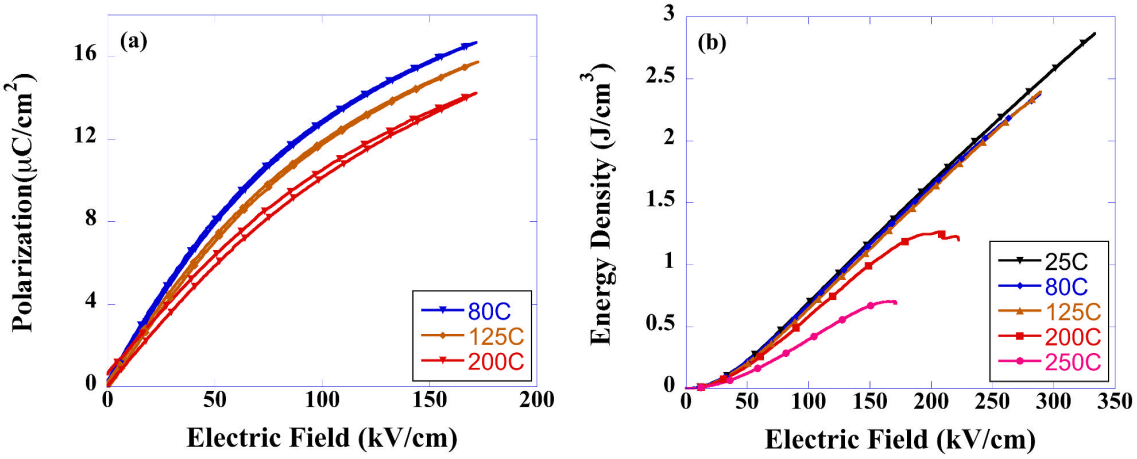

FIG. 9.1.3. (a) Polarization as a function of electric field for 85BT-15BZT MLCCs and (b) the energy density of 85BT-15BZT as a function of electric field at various temperatures.

Figure 9.1.3a displays an example of a polarization data for a 15BZT MLCC with Pt-Pd-Au internal electrodes at various temperatures. The overall polarization decreased slightly as the temperature increased, however there was minimal hysteresis up to 200 °C. The minimal hysteresis is important in order to maximize the energy storage capability of these devices. The low hysteresis is also indicative of low dielectric losses up to higher temperatures. Figure 9.1.3b shows the energy densities obtained at different temperatures. At room temperature, the energy density for the MLCC with thirty ~29 μm dielectric layers was calculated to be at least ~2.8 J/cm^3 at a field of ~330 kV/cm. This represents a significant improvement compared to several commercial X7R capacitors. [14, 22, 23] For example, an X7R capacitor with precious metal electrodes had energy density values of ~1.5 J/cm^3 at room temperature and electric field levels of ~350

kV/cm.[14] The energy density curves also appeared relatively insensitive to temperature. This can be attributed to the high insulation resistances in these compositions even at high temperatures, as shown in Figure 9.1.2.

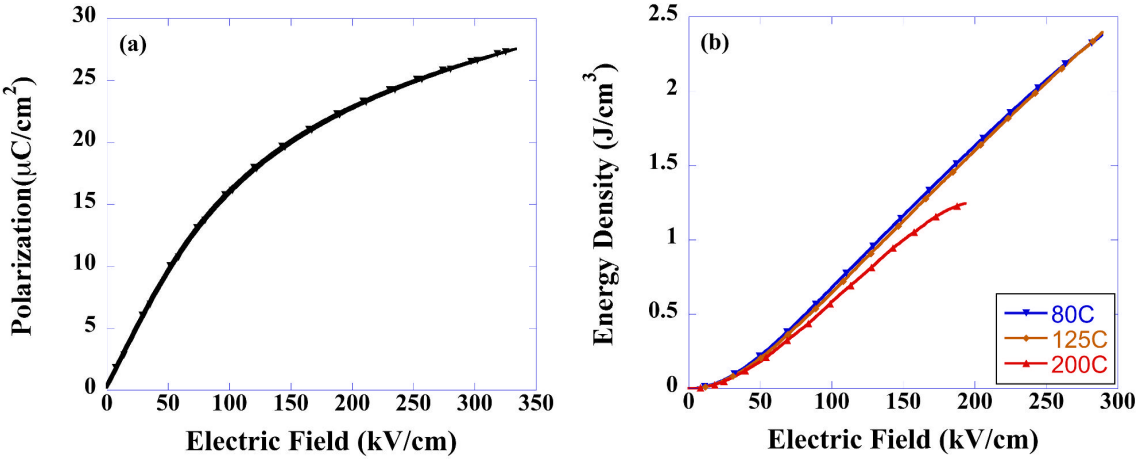

FIG. 9.1.4. (a) Polarization and (b) energy density as a function of electric field of 80BT-20BZT multi-layer capacitors with Ag-Pd electrodes.

The results shown in Fig 9.1.1-9.1.3 were obtained for MLCCs fabricated with Pt-Au-Pd internal electrodes. The Pt-alloys have natural advantages over other internal electrode systems because of their low reactivity with dielectric layers and higher melting temperatures, which can support higher co-firing temperatures. However, these advantages are accompanied with a higher cost for fabricating the MLCC devices. Research over the past two decades has explored the viability of inexpensive Ni internal electrodes. However, because of the thermochemistry of Ni/NiO this requires the MLCCs to be co-fired in reducing atmospheres which are incompatible with the stability of Bi/Bi_2O_3 in the BZT-BT as well as the formation of oxygen vacancy-related defects.[24-27] Internal electrodes based on Ag-Pd alloys require lower co-firing temperatures which may not be suitable for MLCC compositions without the addition of low-melting additives that may degrade the electrical properties. There are also issues

associated with Pd due to chemical reactions with Bi and also its characteristic volume expansion.[2, 28] Nevertheless, Figure 9.1.4 shows the polarization and energy density behavior for the 20BZT composition with Ag-Pd internal electrodes. The results indicate that the properties of MLCCs were largely unaffected by the change in electrodes and energy densities greater than 2 J/cm^3 could be obtained similar to MLCCs with Pt-Pd-Au internal electrodes. The polarization data show no hysteresis and the energy densities were high and essentially insensitive to temperature. While more detailed reliability tests are needed to assess the long term stability of the Ag-Pd-alloy electrodes, these results show great potential for cost reduction.

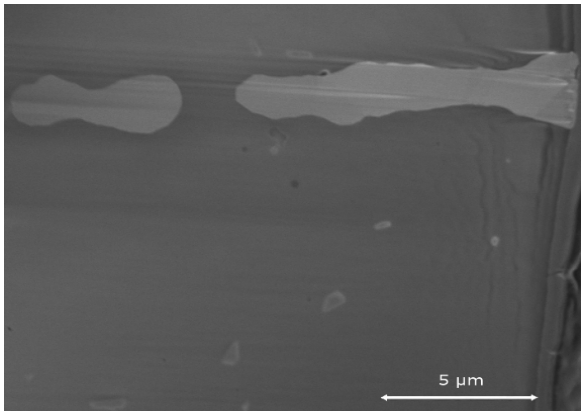

FIG. 9.1.5. SEM image of an internal cross-section of the MLCC with Ag-Pd internal electrodes.

Figure 9.1.5 shows an SEM cross-section of an MLCC with no evidence of electrode interactions at the electrode-ceramic interface and no delamination. This demonstrates that MLCCs based on BT-BZT can be fabricated into dense embodiments without the need for sintering fluxes or other additives.

In summary, multilayer capacitors based on (1-x)BT-xBZT, had high capacitance values greater than 1 μF at room temperature and a temperature stable capacitance up to 350 °C. Energy density values greater than ~2.0 J/cm^3 were obtained at room temperature. The compatibility of Ag-Pd electrodes with BZT-BT-based MLCCs was also demonstrated, which is critical in reducing the cost. The electrical properties of the MLCC devices closely matched the properties of bulk ceramics which is indicative of the high quality of the MLCC devices.

Acknowledgements:

TRS and OSU appreciate DOE's support on this research through contract DE-SC0010109. The authors would like to thank Dr. Peter Eschbach and Teresa Sawyer of the OSU Microscopy Lab for their help with the SEM-FIB.

References

[1] Morita K, Mizuno Y, Kishi H. Reliability design of Multilayer Ceramic Capacitor against thinning of dielectric layers. Applications of Ferroelectrics, 2007 ISAF 2007 Sixteenth IEEE International Symposium on: IEEE; 2007. p. 549-52.
[2] Pepin JG. High fire multilayer ceramic capacitor electrode technology. Electronic Components and Technology Conference, 1991 Proceedings, 41st: IEEE; 1991. p. 328-34.
[3] Lee WH, Su CY. Characterization of silver interdiffusion into (Zn, Mg) TiO3+ x: Bi: Sb multilayer ceramic capacitor. Journal of the American Ceramic Society 2007;90:2454-60.
[4] Niimi H, Mihara K, Sakabe Y, Kuwabara M. Preparation of multilayer semiconducting BaTiO3 ceramics co-fired with Ni inner electrodes. Japanese Journal of Applied Physics 2007;46:6715.
[5] Kishi H, Mizuno Y, Chazono H. Base-metal electrode-multilayer ceramic capacitors: past, present and future perspectives. Japanese journal of applied physics 2003;42:1.
[6] Park D-H, Jung Y-G, Paik U. Evaluation of residual stress in BaTiO3-based Ni-MLCCs with X7R characteristics. Journal of Materials Science: Materials in Electronics 2004;15:253-9.
[7] Shin Y-I, Kang K-M, Jung Y-G, Yeo J-G, Lee S-G, Paik U. Internal stresses in BaTiO< sub> 3</sub>/Ni MLCCs. Journal of the European Ceramic Society 2003;23:1427-34.
[8] Yang G, Yue Z, Zhao J, Wen H, Wang X, Li L. Dielectric behaviour of BaTiO3-based ceramic multilayer capacitors under high dc bias field. Journal of Physics D: Applied Physics 2006;39:3702.
[9] Tsurumi T, Adachi H, Kakemoto H, Wada S, Mizuno Y, Chazono H, et al. Dielectric properties of BaTiO3-based ceramics under high electric field. Japanese journal of applied physics 2002;41:6929.
[10] Hennings D, Rosenstein G. Temperature‐Stable Dielectrics Based on Chemically Inhomogeneous BaTiO3. Journal of the American Ceramic Society 1984;67:249-54.
[11] Lee HW, Chu MS, Lu HY. Crystal Symmetry of BaTiO3 Grains in X7R Multilayer Ceramic Capacitors. Journal of the American Ceramic Society 2011;94:1289-96.
[12] Yamashita Y, Kanai H, Furukawa O, Hasegawa K, Mukaeda S, Handa K. Relaxor dielectric materials for multilayer ceramic capacitor in high-temperature applications. Japanese journal of applied physics 1995;34:5364.
[13] Randall CA, Ogihara H, Kim J-R, Yang G-Y, Stringer CS, Trolier-McKinstry S, et al. High temperature and high energy density dielectric materials. Pulsed Power Conference, 2009 PPC'09 IEEE: IEEE; 2009. p. 346-51.
[14] Ogihara H, Randall CA, Trolier‐McKinstry S. High‐Energy Density Capacitors Utilizing 0.7 BaTiO3‐0.3 BiScO3 Ceramics. Journal of the American Ceramic Society 2009;92:1719-24.
[15] Choi DH, Baker A, Lanagan M, Trolier‐McKinstry S, Randall C. Structural and Dielectric Properties in (1− x) BaTiO3–xBi (Mg1/2Ti1/2) O3 Ceramics (0.1≤ x≤ 0.5) and Potential for High‐Voltage Multilayer Capacitors. Journal of the American Ceramic Society 2013;96:2197-202.

[16] Raengthon N, Sebastian T, Cumming D, Reaney IM, Cann DP. BaTiO3‐Bi (Zn1/2Ti1/2) O3‐BiScO3 Ceramics for High‐Temperature Capacitor Applications. Journal of the American Ceramic Society 2012;95:3554-61.
[17] Raengthon N, Cann DP. Dielectric Relaxation in BaTiO3–Bi (Zn1/2Ti1/2) O3 Ceramics. journal of the American Ceramic Society 2012;95:1604-12.
[18] Triamnak N, Yimnirun R, Pokorny J, Cann DP. Relaxor Characteristics of the Phase Transformation in (1− x) BaTiO3–xBi (Zn1/2Ti1/2) O3 Perovskite Ceramics. Journal of the American Ceramic Society 2013;96:3176-82.
[19] Triamnak N, Brennecka GL, Brown-Shaklee HJ, Rodriguez MA, Cann DP. Phase formation of BaTiO 3–Bi (Zn 1/2 Ti 1/2) O 3 perovskite ceramics. Journal of the Ceramic Society of Japan 2014;122:260-6.
[20] Raengthon N, DeRose VJ, Brennecka GL, Cann DP. Defect mechanisms in high resistivity BaTiO3–Bi (Zn1/2Ti1/2) O3 ceramics. Applied Physics Letters 2012;101:112904.
[21] Triamnak N. Relaxor characteristic and phase evolution of complex perovskite barium titanate bismuth zinc titanate ceramics. 2013.
[22] Love GR. Energy storage in ceramic dielectrics. Journal of the American Ceramic Society 1990;73:323-8.
[23] AVX AKgc. AVX Advanced Ceramic Capacitorsfor Power Supply, High Voltage and Tip and Ring Applications.
[24] Yang G, Dickey E, Randall C, Randall M, Mann L. Modulated and ordered defect structures in electrically degraded Ni–BaTiO3 multilayer ceramic capacitors. Journal of applied physics 2003;94:5990-6.
[25] Yang G, Dickey E, Randall C, Barber D, Pinceloup P, Henderson M, et al. Oxygen nonstoichiometry and dielectric evolution of BaTiO3. Part I—improvement of insulation resistance with reoxidation. Journal of applied physics 2004;96:7492-9.
[26] Yang G, Lian G, Dickey E, Randall C, Barber D, Pinceloup P, et al. Oxygen nonstoichiometry and dielectric evolution of BaTiO3. Part II—insulation resistance degradation under applied dc bias. Journal of applied physics 2004;96:7500-8.
[27] Yang G, Lee S, Liu Z, Anthony C, Dickey E, Liu Z, et al. Effect of local oxygen activity on Ni–BaTiO< sub> 3</sub> interfacial reactions. Acta materialia 2006;54:3513-23.
[28] Wang SF, Huebner W. Interaction of Silver/Palladium Electrodes with Lead‐and Bismuth‐Based Electroceramics. Journal of the American Ceramic Society 1993;76:474-80.

9.2 **Resistivity enhancement and transport mechanisms in $BaTiO_3$-$Bi(Zn_{1/2}Ti_{1/2})O_3$ and $SrTiO_3$-$Bi(Zn_{1/2}Ti_{1/2})O_3$ ceramics**

Nitish Kumar and David P. Cann

Materials Science, School of Mechanical, Industrial, and Manufacturing Engineering,

Oregon State University, Corvallis, Oregon 97331, USA

Published in

Journal of the American Ceramics Society

Vol. 98, 2548 (2015)

Abstract

Ceramics of composition (1-x)$BaTiO_3$-x$Bi(Zn_{1/2}Ti_{1/2})O_3$ (BT-BZT) were prepared by solid state synthesis; they have been shown to exhibit excellent properties suited for high temperature dielectric applications. The x-ray diffraction data showed a single-phase perovskite structure for all the compositions prepared ($x \leq 10\%$ BZT). The compositions with less than 7.5% BZT exhibited tetragonal symmetry at room temperature and pseudo-cubic symmetry above it. A significant improvement in insulation properties was measured with the addition of BZT. Both low-field AC impedance and high field direct DC measurements indicated an increase in resistivity of at least 2 orders of magnitude at 400 °C with the addition of just 3% BZT (~10^7 Ω-cm) into the solid solution as compared to pure BT (~10^5 Ω-cm). This effect was also evident in dielectric loss data, which remained low at higher temperatures as the BZT content increased. In conjunction with band gap measurements, it was also concluded that the conduction mechanism transitioned from extrinsic for pure BT to intrinsic for 7.5% BZT suggesting a change in the fundamental defect equilibrium conditions. It was also shown that this improvement in insulation properties was not limited to BT-BZT, but could also be observed in $SrTiO_3$-BZT system.

Introduction

Numerous modifications have been made to $BaTiO_3$ (BT) since its discovery with an aim to minimize the temperature dependence of its dielectric properties and to make it more suitable for high temperature, high energy density applications.[1-5] Efforts have been made to engineer stable dielectric properties over a wider temperature range through

modification of the phase transition to mitigate its characteristic sharp phase transition at the Curie point (T_c).[4, 6] Amongst these approaches, the Bi-containing end member perovskites have attracted special attention in recent years.[7-9] The similar electronic structure of Bi and Pb and the solid solution of Bi-based perovskites with Pb-based systems were the main motivation behind the widespread investigation of these perovskites. [10, 11] Solid solutions of BT with unstable Bi-perovskites have been shown to introduce relaxor behavior in them.[8, 9] Previous research has established the potential of Bi-based perovskites for high temperature and other applications.[12-19] This article is based on one of these solid solutions developed by Cann *et. al*. with $Bi(Zn_{1/2}Ti_{1/2})O_3$ (BZT) as one of the end members in the solid solution.[9, 13, 17, 20] It has been shown that BT-BZT solid solutions have properties suited for high energy density and high temperature linear dielectrics. Above ~9% BZT content, they exhibit relaxor characteristics with slim polarization hysteresis loops even at substantially high fields and maintain their high dielectric constant (>1000) up to high temperatures.[21-24]

It has been suspected that the high resistivities of these solid solutions play an important role in the properties exhibited by these compositions. However, it was noticed that these compositions became fairly conducting at close to 300 °C. It was also reported that intentionally introduced Ba-deficiencies improved the resistivities and dielectric properties dramatically and the effect was more pronounced at higher temperatures.[25] It underscored the importance of defect equilibrium on important material properties like resistivity. Later, Raengthon *et al.*, with the help of impedance spectroscopy and electron paramagnetic resonance (EPR), ascribed this to barium vacancy-oxygen vacancy pairs,

which could act as electron traps.[26] Intentionally introduced Ba-vacancies increased the amount of these traps and affected the electronic structure as was seen from the EPR signal and optical absorption spectra.

This study is focused on the change in dielectric and insulation behavior of BT-BZT solid solution with BZT content. It will be shown that this solid solution normally has resistivities which are appreciably higher than BT alone. Small concentrations of BZT were adequate to improve the resistivity values and activation energy for conduction; this effect is likely related to defect chemistry as well. Impedance spectroscopy will be used to gain greater insight into this.

The authors could not find a systematic study in literature stressing on the above mentioned effect apart from a few scattered reports. Ogihara *et al.* reported that 0.7BT-0.3$BiScO_3$ had resistivity value of ~10^{12} Ω.cm at 250 °C.[16] This is typically 3-4 orders of magnitude higher than the resistivity value of BT at this temperature, indicating that $BiScO_3$ may have similar effect as BZT in this study. Chen *et al.* reported that BZT improved the resistivity values of $PbTiO_3$-BZT solid solution.[27] They attributed this to d^0 electronic structure of PT-BZT. However, their conclusion was based on dielectric loss data and no direct resistivity measurements were performed. It was reported that solid solution of novel perovskites $Ba(Li_{1/4}Nb_{3/4})O_3$ (BLN) and $Ba(Cu_{1/3}Nb_{2/3})O_3$ (BCN) had two orders of magnitude higher resistivity than BCN alone.[28] However, it might be just because pure BLN has much higher resistivity than pure BCN, as was reported in the same paper.

To establish that this phenomenon of increase in resistivity on adding BZT to the solid solution was not limited to BT-based systems only, some $SrTiO_3$-BZT (ST-BZT) compositions were characterized as well. The ST-based compositions were not expected to have complex domain structure at room temperature and above and thus could also help determine if domains had a role to play in the occurrence of this phenomenon.[29]

Experimental Procedure

The samples were prepared using conventional solid-state method. High purity powders of $BaTiO_3$, $SrTiO_3$ (>99%), $BaCO_3$ (>99.8%), $SrCO_3$ (>99.9%), Bi_2O_3 (>99.9%), TiO_2 (>99.9%), and ZnO (>99.9%) were mixed in appropriate amounts to prepare stoichiometric compositions based on $(1-x)BaTiO_3$-$xBi(Zn_{1/2}Ti_{1/2})O_3$ (BT-BZT) ($0\%\leq x\leq 10\%$) and $(1-x)SrTiO_3$-$xBi(Zn_{1/2}Ti_{1/2})O_3$ (ST-BZT) ($0\%\leq x\leq 10\%$). It should be noted that compositions which contained no BZT, were prepared from pure $BaTiO_3$ and $SrTiO_3$ powders from Sakai Chemical Industry and Alfa Aesar respectively and required no calcination. For the rest of the compositions, the mixed powders were ground using a vibratory mill for 6 hours and then dried overnight in an oven (~80 °C). The BT-BZT and ST-BZT powders were calcined in alumina crucibles at 950 °C-1000 °C for 4 hours and 1000 °C for 6 hours respectively, and then milled with ~3 wt% Rhoplex binder and dried again. Green pellets in the shape of thin discs were made by cold-pressing uniaxially at a pressure of ~200 MPa and then sintered on a bed of calcined powder in a closed alumina crucible at 1250 °C-1350 °C for 4 hours (for BT-BZT) and 1200 °C-1400 °C for 4 hours (for ST-BZT). All the sintered pellets were polished to around 0.9 mm thickness. X-ray diffraction (XRD) (Bruker AXS D8 Discover, Madison, WI, USA) was performed on

ground pellets for phase and crystal structure determination. Prior to any electrical measurements, silver electrodes were applied on both sides of the pellets and then fired at 700°C for 30 min. The pellets were placed in a high temperature measurement cell (NorECs AS ProbostatTM, Oslo, Norway) or low temperature furnace (Delta Design 9023, California, USA) and temperature dependent dielectric properties were measured using an LCR meter (Agilent 4284A, Santa Clara, CA, USA). An impedance analyzer (Solartron SI1260A equipped with Solartron 1296A dielectric interface, Farnborough, UK) was used to measure the impedance in the frequency range 1 Hz to 1 MHz. The SMaRT impedance measurement software program was used to collect the data. The optical measurements were carried out on the sintered pellets over the wavelength range of 200-1100 nm at room temperature using an Ocean Optics HR4000 UV-Vis Spectrometer (Ocean Optics, Dunedin, FL) with a balanced deuterium/tungsten halogen source. For performing thermally stimulated depolarization current (TSDC) measurements, polarized samples were heated at a rate of 2 K/min and depolarization currents were detected with a Keithley 6517B electrometer. No bias fields were applied during measurements. Sputtered Pt electrodes were used for the same.

Results and Discussions

Part I: BT-BZT

The XRD data for solid solutions of BT-BZT system are shown in Fig. 9.2.1. All compositions exhibited a single perovskite phase within the resolution of the laboratory XRD instrument. While compositions with less than 7.5 mol% BZT exhibited tetragonal symmetry at room temperature, beyond this composition the perovskite phase

transitioned to pseudo-cubic symmetry. These findings are also consistent with the results reported by Triamnak *et al*. [30] The specimens were sintered to high densities with a measured radial shrinkage after sintering being more than 14% as compared to green pellets. These shrinkage values are close to maximum sintered densities possible in these compositions via solid-state processing route.[31]

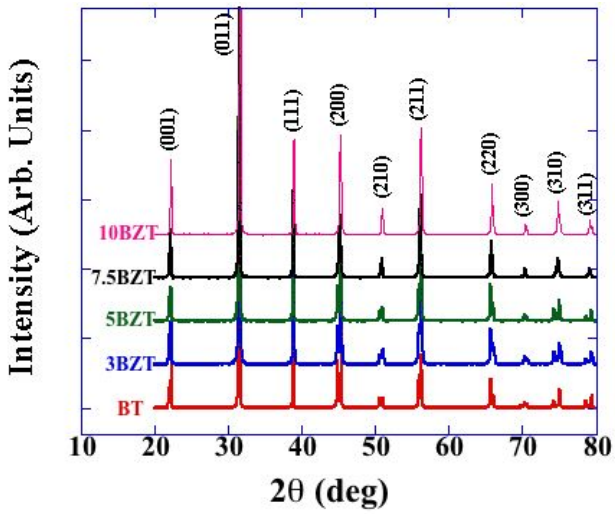

Fig. 9.2.1. X-ray diffraction patterns of as-sintered stoichiometric (1-x)BT-xBZT where x=0%, 3%, 5%, 7.5%,10%.

The dielectric properties for various compositions of BT-BZT have been shown in Fig. 9.2.2. The compositions up to x=5% BZT exhibited a typical ferroelectric transition and the transitions became increasingly diffuse as the BZT mole fraction in the solid solution increased. It should be noted that the dielectric loss decreased and remained low up to higher temperatures with the addition of BZT to BT, which is an indication of improved insulation properties. The composition with 7.5% BZT appeared to have a core-shell-like structure as suggested from observation of two peaks in the dielectric

behavior. With the addition of 10% BZT the dielectric maximum did not exhibit any features that are characteristic of a normal ferroelectric phase transition. Instead, typical relaxor-like behavior, likely linked to disorder introduced with the addition of $Bi(Zn_{1/2}Ti_{1/2})O_3$, was observed with a broad dielectric maximum and an increase in the peak temperature with increased frequency.[5, 9] Also, the peak permittivity decreased with frequency and losses were lower at higher frequencies at higher temperatures. In general, relaxors exhibit a significant frequency dependence of the permittivity as well as the absence of both a spontaneous polarization and a structural macroscopic symmetry.[32-36] The relaxor behavior has been attributed to the presence of polar nanoregions (PNRs) in mixed perovskites such as the BZT-BT material.[32-36] Chemical substitution introduces dipolar entities in these perovskites which are barred from having any well-defined dipole moments at high temperatures due to thermal fluctuations. On cooling however, PNRs are formed which grow as the temperature decreases. At the same time, the fluctuations in these PNRs slow down, leading to a relaxor state with random orientation of polar domains. The interactions between the PNRs grow stronger as the temperature decreases.[34, 35] The PNRs have a statistical distribution in their size and dipolar strength, which along with the randomness of their interactions yields a broad distribution of relaxation times giving rise to broad peak of dielectric permittivity and as well as the observed frequency dependence.[36]

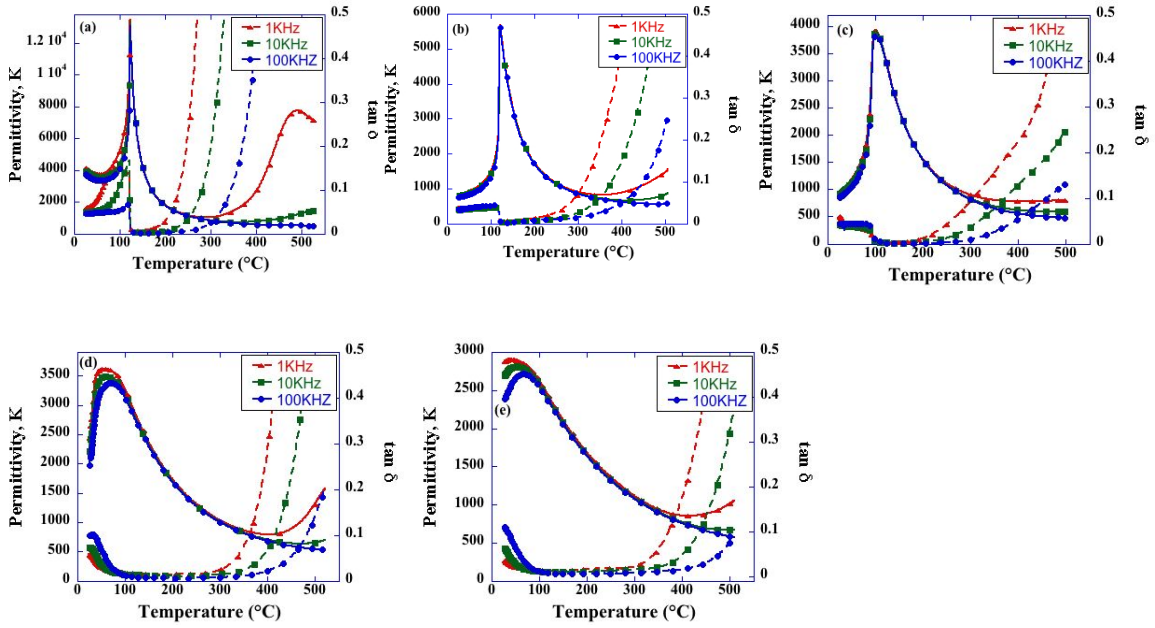

Fig. 9.2.2. Temperature dependence of dielectric constant (solid lines) and dielectric loss (dashed lines) for (a) BT, (b) BT-3BZT, (c) BT-5BZT, (d) BT-7.5BZT, and (e) BT-10BZT samples.

In order to study the transport properties of these compositions, AC impedance measurements were carried out. The Z* complex plane plots for all the compositions at ~400 °C are shown in Fig. 9.2.3. The existence of at least two semi-circles could be seen in all the compositions; while they were distinct for pure BT, they were superimposed on each other for the BZT-BT compositions. This indicates an electrical inhomogeneity tied to the presence of both bulk and grain boundary contributions to conduction. For these plots, the frequency of measurement decreases from left to right. Most often, a semicircle due to the bulk *RC* network occurs at higher frequencies (left) and the semicircle due to the grain boundary is seen at comparatively lower frequencies. The contribution from space charge or electrode effects is observed at even lower frequencies.[37] It could be seen that the bulk resistivities (related to the diameter of higher frequency semicircle),

were higher or comparable to the grain boundary resistivity values for all compositions. It could also be noted that the points where the extrapolation of the plots intersected the x-axis on the low frequency side, had much higher values for BT-BZT compositions as compared to pure BT. This indicated that the addition of BZT resulted in a significant increase in low field DC-resistance values for these compositions. The resistivity values are listed in Table 9.2.1 and indicate a two order of magnitude increase in resistivity with the addition of just 3% BZT to the solid solution at ~400 °C.

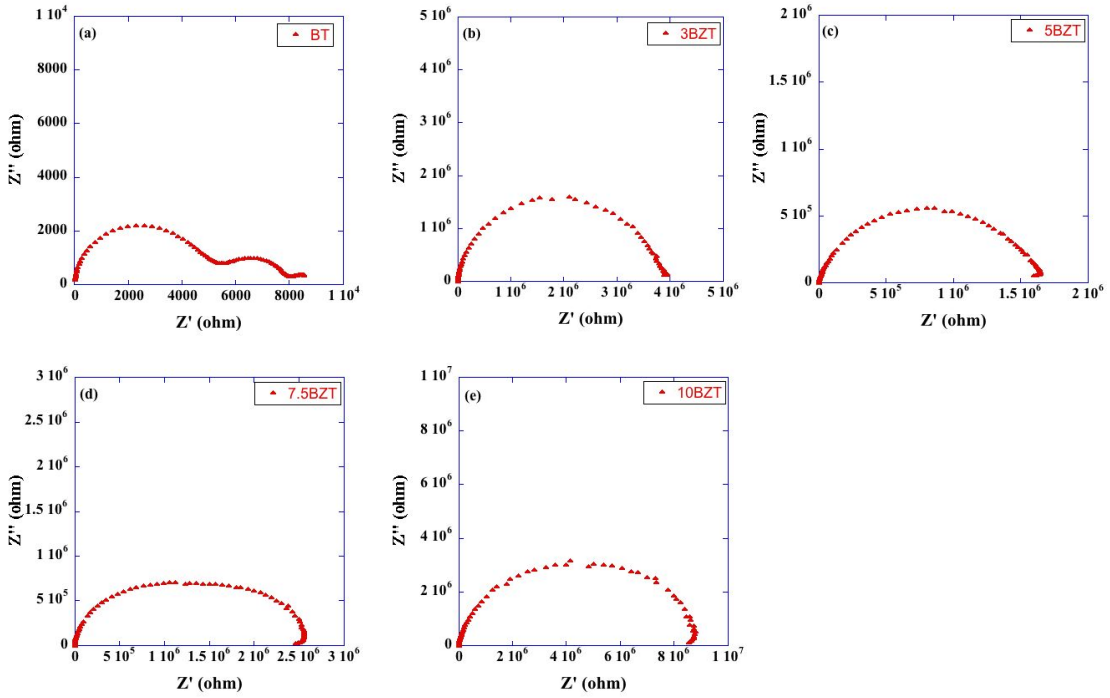

Fig. 9.2.3. The Z* complex plane plots for all the compositions have been shown. Contributions from both bulk and grain boundary could be observed. The Z′′ and Z′ represent the imaginary and real parts of complex impedance respectively.

The activation energies for conduction were obtained from Arrhenius fits over the temperature range of 275 °C to 525 °C. The plots are shown in Fig. 9.2.4 for bulk resistivity, grain boundary resistivity, and the resistivity extrapolated from zero frequency which includes both bulk and grain boundary components. The zero frequency

extrapolations are indicative of low field DC resistances, as mentioned in previously. All of the plots exhibited approximately linear behavior over this temperature range. It could be seen that the slopes of the plots for the bulk and zero frequency components, which are indicative of activation energy for conduction, increased as the BZT content in the solid solution increased. The values for activation energies have been listed in Table 9.2.1.

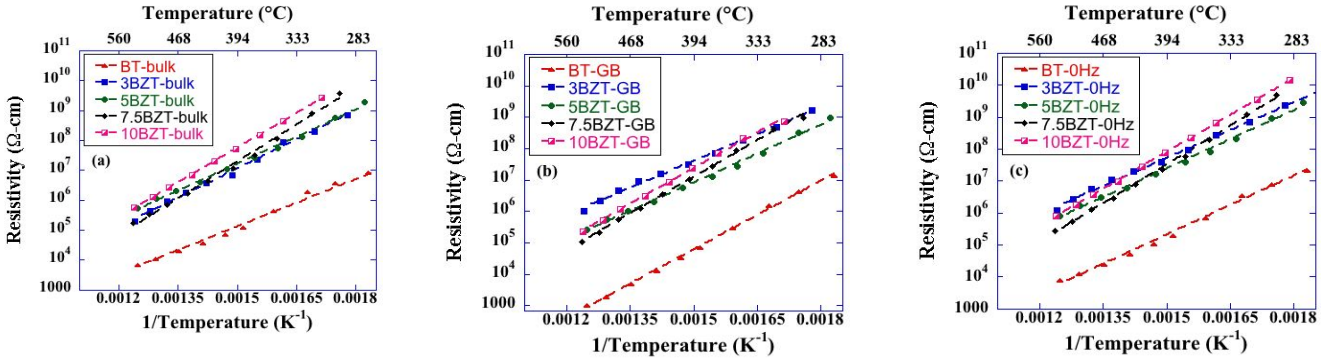

Fig. 9.2.4. The Arrhenius plots for all compositions are shown. The bulk and grain boundary (GB) components have been obtained from the Z* complex plane plots. The DC or the zero frequency (0Hz) component was obtained from Z* complex plane plots after extrapolating the AC impedance data on the low-frequency side. A clear increase in resistivity on adding BZT could be observed.

Table 9.2.1: The activation energy for conduction and resistivity values for all compositions obtained from AC impedance measurements.

Composition	Bulk Activation Energy (eV)	GB Activation Energy (eV)	DC (0 Hz) Activation Energy (eV)	DC (0 Hz) resistivity at 400 °C (Ω-cm)
BT	1.03	1.44	1.21	1.3×10^5
3BZT	1.28	1.13	1.16	3.8×10^7
5BZT	1.20	1.21	1.20	1.7×10^7
7.5BZT	1.63	1.54	1.62	2.2×10^7
10BZT	1.53	1.51	1.53	7.5×10^7

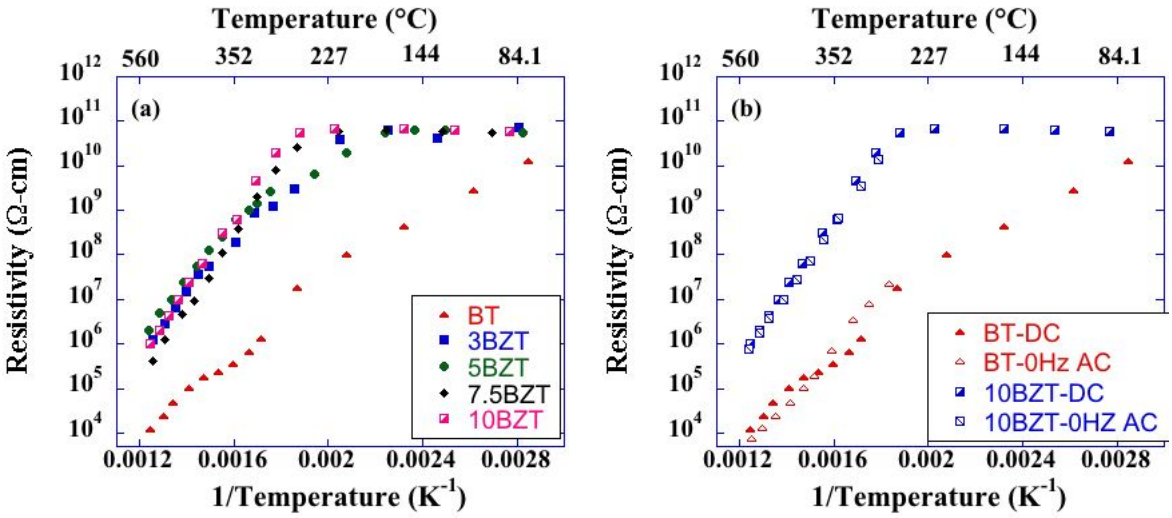

Fig. 9.2.5. (a) The Arrhenius plots for all compositions obtained from direct DC measurements have been shown. The currents were swept on logarithmic scale and the voltages were measured to determine the resistivity from the slope of voltage-current plot. (b) The Arrhenius plots for AC (0 Hz) and direct DC measurements for BT and 10BZT ceramics have been shown for comparison.

As mentioned earlier, Fig. 9.2.4(c) and Table 9.2.1 present DC data extrapolated from AC impedance measurements. On most occasions AC measurements are

advantageous because they provide additional information beyond what DC measurements provide. Typically, DC measurements employ higher electric field levels and are sometimes complicated by artifacts coming from interfacial polarization, etc. However, AC-extrapolations can become erroneous for highly insulating samples like BT-BZT due to instrumentation artifacts and contributions from sample fixturing. Therefore, direct DC measurements were performed on all BT-BZT samples at electric field levels up to ~1.5 kV/cm depending upon temperature and the results are shown in the Arrhenius plot in Fig. 9.2.5. At each temperature, the currents were swept over a logarithmic scale and the voltages were measured to determine the resistivity assuming Ohmic behavior. The resistivity data for pure BT showed signs of non-linearity with respect to temperature (Fig. 9.2.5(a)), which is commonly seen in reports in the literature. [38-41] The data for BT-BZT solid solutions were linear at higher temperatures and the resistivity appeared to saturate at lower temperatures. Again, this behavior has been reported earlier in the literature in BT-BZT-based compositions.[25] The activation energies were calculated over the same temperature range as AC impedance data, so as to have a direct comparison. The activation energy for pure BT was found to be ~0.8 eV as compared to ~1 eV calculated from AC impedance data. The resistivity value at 400 °C was found to be 1.8E5 Ω-cm which was quite consistent with the value obtained from AC data of 1.3E5 Ω-cm. For the 3BZT sample, the resistivity at 400 °C was calculated to be 5.7E7 Ω-cm, again it was of the same order of magnitude as the values calculated from AC data. Thus, the direct DC measurements also showed that addition of minor amounts of BZT improved the resistivity by ~2 orders of magnitude. For 7.5BZT composition, the activation energy for conduction was ~1.6 eV and resistivity was ~3E7 Ω-cm at 400 °C,

again consistent with AC measurements and indicating that intrinsic conduction was dominant in this composition. In summary, the data from high-field direct DC measurements closely correspond to the low-field AC impedance measurements. Figure 9.2.5(b) displays AC and DC data for BT and 10BZT ceramics for direct comparison. It may be worth noting here that, as mentioned earlier, current-voltage plots were used to determine DC resistivity at each temperature by estimating their slopes. The current-voltage (I-V) characteristics of the BZT-containing compositions were linear and closely followed Ohm's law behavior within the range of applied voltages (up to ~1.5 kV/cm). However, for BT linear I-V behavior was only observed for lower voltages and current values. At 200 °C for example, the curves for BT started to deviate from Ohm's law behavior and resistivity values appeared to drop on applying fields at as low as 0.08 kV/cm. For the plots in Fig. 9.2.5, only the linear portions were used to calculate resistivity values.

Diffuse reflectance measurements were carried out following the method of related work using Kubelka-Munk and Tauc equations as shown in Fig. 9.2.6.[42-44] The optical band gap energies derived from the absorption threshold energies are useful in considering the relevant conduction mechanisms in these systems. The optical band gaps (E_g), extracted from extrapolation of linear portion of the plots, were estimated to be in the range of 3.02 eV to 3.08 eV for these compositions, which is in good agreement with previous reports. [26, 40, 45]

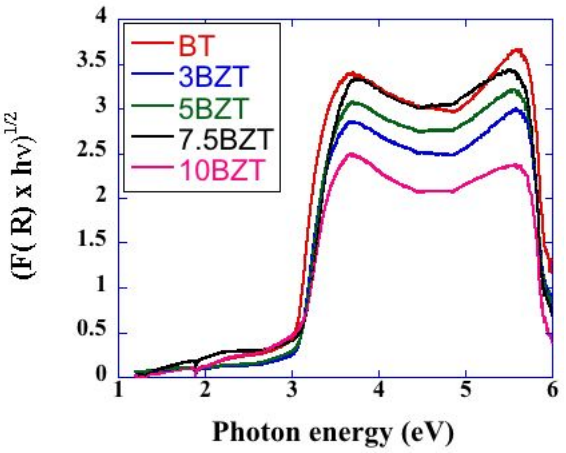

Fig. 9.2.6 Tauc plot, where F(R) is the ratio of effective absorption and scattering coefficients and hν is photon energy for various compositions.

Impedance data and optical measurements can provide important insights into the transport mechanisms in these compositions. For pure BT, the activation energy for conduction was found to be ~1 eV for the bulk component. In general, activation energies close to 1 eV in titanate perovskites are often associated with oxygen vacancies.[4, 46] However, low transference number values for pure and mildly doped BT indicate that the conduction in pure BT is predominantly electronic and not ionic.[37] Now, as can be observed from Table 9.2.1, the activation energies for bulk and DC conduction increase to values close to $0.5E_g$ as the BZT mole fraction increased to 7.5% in the solid solution. High activation energies for conduction coupled with high resistivity values (two orders of magnitude higher than BT) for the 7.5% and 10% compositions indicate that intrinsic conduction was the dominant mechanism in these compositions rather than conduction dominated by extrinsic defects.[40] These results showed a significant improvement in insulation properties with addition of BZT, and can have important implications for engineering properties in titanate perovskites in general. The improvement in insulation properties with the addition of BZT may be due to the suppression of other conduction mechanisms due to formation of defect traps or defect clusters among other possibilities.

A series of BZT-BT specimens were annealed in air at temperatures of 1000 °C and 1100 °C for 7 days. The objective was to ascertain whether or not the observed change in resistivity was due to some metastable microstructure or defect concentration or whether it was a stable equilibrium-based state. Impedance measurements on the annealed specimens were nearly identical to the original as-sintered specimens. This suggests the electrical properties of the BZT-BT specimens does not originate from a metastable state but is stable.

Part II: ST-BZT

Following same approach as with BT-BZT, a range of compositions were prepared in the $SrTiO_3$-BZT system to investigate the change in resistivity. In contrast to the ferroelectric BT, ST is a cubic paraelectric at room temperature (Fig. 9.2.7). The XRD data for the (1-x)ST-xBZT (where x=0%, 5% and 10%) compositions are shown in Fig. 9.2.7. The structure of the ST-BZT solid solutions remained cubic throughout the range of compositions examined in this study. At higher BZT mole fractions, second phases could be observed in the XRD data. The lattice parameters calculated from Cohen's method were found to be 3.9084, 3.9128 and 3.9161 A° for compositions with 0%, 5% and 10% BZT, respectively.[47] No distortions or asymmetries were observed in the {200} peaks of all compositions unlike the pseudo-cubic compositions of BT-BZT, which suggests that these compositions are paraelectric at room temperature.

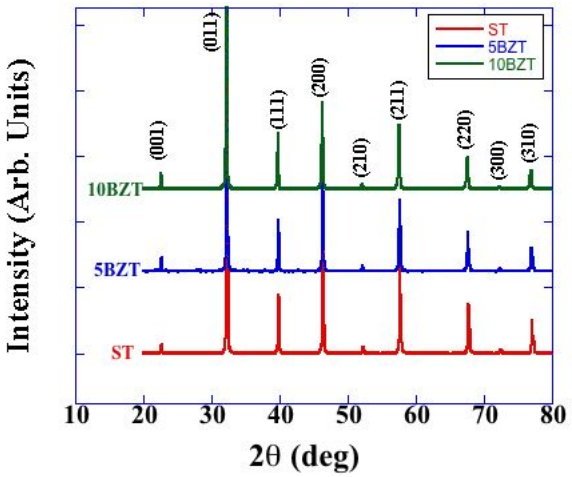

Fig. 9.2.7. X-ray diffraction patterns of as-sintered stoichiometric (1-x)ST-xBZT where x=0%, 5%, 10%.

The dielectric response of these compositions has been shown in Fig. 9.2.8 in the temperature range of -150 °C to 550 °C. Consistent with the XRD data, no peaks associated with structural phase transition were observed in the dielectric data above room temperature. Interestingly, the room temperature dielectric constant increased from ~300 for pure ST to ~600 for the ST-10BZT composition. The temperature of the dielectric maxima also appears to shift to higher temperatures with the addition of BZT. While there was no peak over the temperature range of measurement for ST, the emergence of a dielectric maximum was observed for ST-5BZT at ~-150 °C and a clear dielectric maxima could be resolved for ST-10BZT ceramics. A minor frequency dependence in the dielectric maxima could also be seen for BZT-containing ceramics. In addition, similar to the BT-BZT compositions the dielectric loss decreased at higher temperatures with the addition of BZT to ST, which is indicative of better insulation properties.

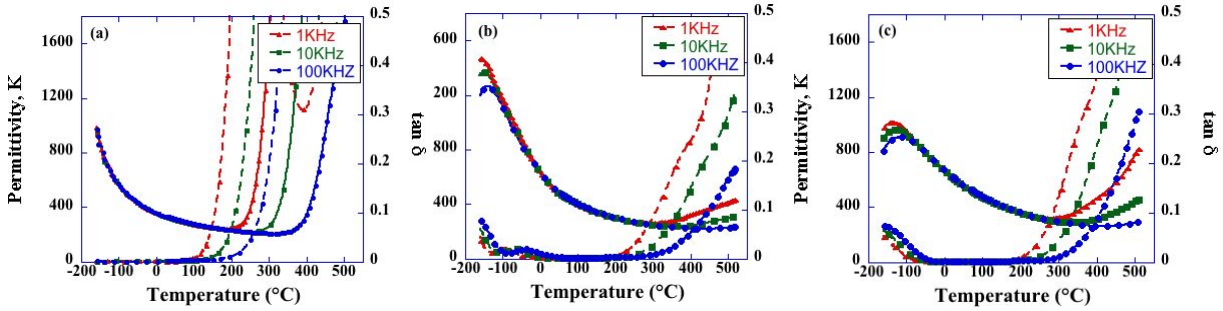

Fig. 9.2.8 Temperature dependence of dielectric constant (solid lines) and dielectric loss (dashed lines) for (a) ST, (b) ST-5BZT and (c) ST-10BZT samples.

Similar to BT-BZT samples, AC impedance measurements were performed on ST-BZT samples as well. The Arrhenius plots obtained from AC impedance measurements have been shown in Fig. 9.2.9. It showed similar trends as the BT-BZT samples. The bulk component of the resistivity increased by approximately two orders of magnitude on addition of BZT. The activation energy for conduction also increased from ~0.9 eV for pure ST to ~1.5 eV for 5% BZT and 10% BZT compositions. Hence, it was shown that improvements in insulation properties on adding BZT was not limited to BT-based systems. Additionally it was established that domain structure played little role in this phenomenon, as ST-BZT solid solution is not expected to have domains at or above room temperature and still exhibited improvement in insulation properties with the addition of BZT.

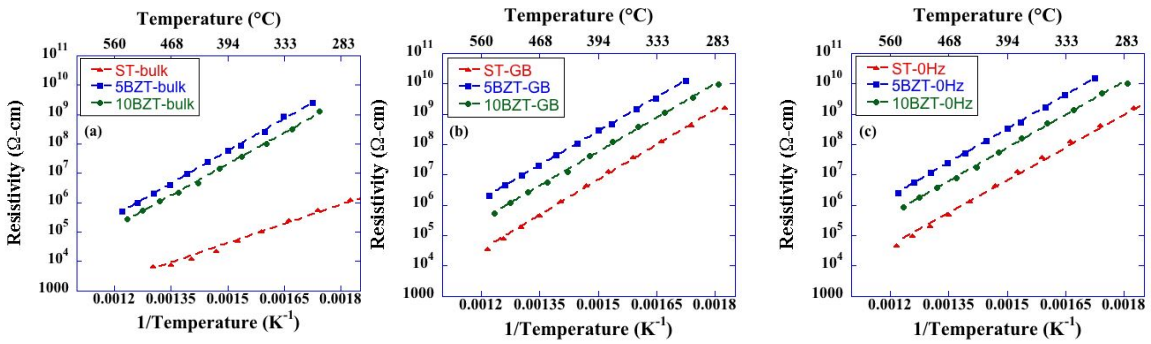

Fig. 9.2.9 The Arrhenius plots for all compositions are shown. The bulk and grain boundary (GB) components have been obtained using the Z* complex plane plots. The DC or the zero frequency component was obtained from Z* complex plane plots after extrapolating the AC impedance data on the low-frequency side.

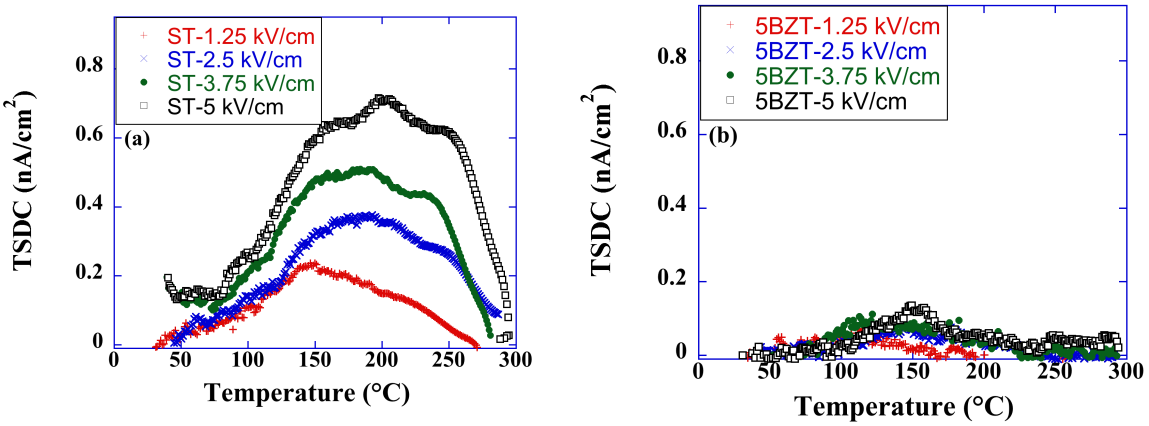

Fig. 9.2.10. Thermally stimulated depolarization current (TSDC) plots for (a) ST and (b) ST-5BZT compositions with polarization fields varying from 1.25 kV/cm to 5 kV/cm.

It has been shown recently that TSDC can yield important insight into the degradation mechanisms in ferroelectric ceramics.[48, 49] In their work, Liu *et al.* suggested that oxygen vacancies can strongly influence resistance degradation and other failure mechanisms and also TSDC can be a powerful tool to glean information about oxygen vacancy concentrations, along with dipoles, trap charges and other defects.[48, 49] In TSDC measurements on 1% Fe-doped ST, the peak at approximately 150 °C has

been attributed to oxygen vacancies that are relaxed inside each grain and the peak at approximately 250 °C is linked to oxygen vacancies that relax across the grain boundary. Figure 9.2.10 shows the thermally stimulated depolarization current (TSDC) data for ST and ST-5BZT samples. The samples were polarized at electric fields between 1.25 kV/cm and 5 kV/cm for 20 minutes at a temperature of 190 °C and then rapidly cooled while maintaining the field. The samples were then heated at a rate of 2 °C/min and the depolarization currents were recorded as shown. As shown in Fig. 9.2.10, the TSDC data for pure ST largely reproduces the literature results, however the addition of BZT had a significant impact on reducing the TSDC current. This suggests a change in defect mechanisms in ST-BZT which might have implications on the degradation behavior.

Conclusions

With the help of dielectric measurements, AC-impedance measurements and DC measurements, it was demonstrated that there was a significant increase in resistivity with the addition BZT to BT and ST. The resistivity increased from ~10^5 Ω-cm for pure BT to ~10^7 Ω-cm for a solid solution containing only 3% BZT at 400 °C. The activation energy for conduction also increased gradually from ~1 eV for pure BT to ~1.5 eV (equivalent to ~$0.5E_g$) for the 7.5% BZT composition, signifying a change in conduction mechanism from one dominated by impurities or defects to an intrinsic mechanism. The effect persisted even after annealing for BT-BZT compositions. A similar improvement in insulation resistance was also demonstrated for ST-BZT system. This presents an

important result as the increased resistivity can enable these materials to be used for demanding applications where high temperatures or high electric fields are needed.

Acknowledgements

This material is based upon work supported by the National Science Foundation under Grant No. DMR-1308032. The authors would also like to thank Prof. Dr. Jürgen Rödel, Deborah Schneider and Deutsche Forschungsgemeinschaft (DFG) through SFB595 for their help with TSDC measurements.

References

[1] Campbell C, Van Wyk J, Holm MK, Prinsloo J, Schoeman J. Relaxation effects in high-voltage barium titanate nonlinear ceramic disk capacitors. Components, Hybrids, and Manufacturing Technology, IEEE Transactions on 1993;16:418-23.
[2] MacChesney J, Gallagher P, DiMarcello F. Stabilized barium titanate ceramics for capacitor dielectrics. Journal of the American Ceramic Society 1963;46:197-202.
[3] McAneney J, Sinnamon L, Bowman R, Gregg J. Temperature and frequency characteristics of the interfacial capacitance in thin-film barium–strontium–titanate capacitors. Journal of applied physics 2003;94:4566-70.
[4] Morrison FD, Sinclair DC, West AR. Electrical and structural characteristics of lanthanum-doped barium titanate ceramics. Journal of applied physics 1999;86:6355-66.
[5] Moulson AJ, Herbert JM. Electroceramics: materials, properties, applications: John Wiley & Sons; 2003.
[6] Xiaoyong W, Yujun F, Xi Y. Dielectric relaxation behavior in barium stannate titanate ferroelectric ceramics with diffused phase transition. Applied physics letters 2003;83:2031-3.
[7] Alberta EF, Bhalla AS, Takenaka T. Large hydrostatic piezoelectric constant and temperature dependence of the piezoelectric properties of Bi (NiTi) 1/2O3: PbTiO3 ceramics. Ferroelectrics Letters Section 1999;25:45-52.
[8] Okuda T, Yamada M, Takenaka T. Piezoelectric Properties of Solid-Solution (Bii-a.(PbBa)¡ c)(Ni (ia.)/2Ti (i+ a;)/2) 03 Ceramics. Jpn J Appi Phys Vol 1994;33:5356-60.
[9] Raengthon N, Cann DP. High temperature electronic properties of BaTiO3–Bi (Zn1/2Ti1/2) O3–BiInO3 for capacitor applications. journal of Electroceramics 2012;28:165-71.
[10] Choi SM, Stringer CJ, Shrout TR, Randall CA. Structure and property investigation of a Bi-based perovskite solid solution:(1-x) Bi (Ni 1/2 Ti 1/2) O 3–xPbTiO 3. Journal of applied physics 2005;98:034108--4.
[11] Smolenskii G, Isupov V, Agranovskaya A, Popov S. Ferroelectrics with diffuse phase transitions. Soviet Physics-Solid State 1961;2:2584-94.
[12] Dittmer R, Jo W, Damjanovic D, Rödel J. Lead-free high-temperature dielectrics with wide operational range. Journal of Applied Physics 2011;109:034107.
[13] Huang C-C, Cann DP, Tan X, Vittayakorn N. Phase transitions and ferroelectric properties in BiScO 3-Bi (Zn 1/2 Ti 1/2) O 3-BaTiO 3 solid solutions. Journal of Applied Physics 2007;102:044103--5.
[14] Kwon D-K, Lee MH. Temperature-stable high-energy-density capacitors using complex perovskite thin films. Ultrasonics, Ferroelectrics and Frequency Control, IEEE Transactions on 2012;59:1894-9.
[15] Liu Y, Norén L, Studer AJ, Withers RL, Guo Y, Li Y, et al. Response of intergrown microstructure to an electric field and its consequences in the lead-free piezoelectric bismuth sodium titanate. Journal of Solid State Chemistry 2012;187:309-15.
[16] Ogihara H, Randall CA, Trolier‐McKinstry S. High‐Energy Density Capacitors Utilizing 0.7 BaTiO3‐0.3 BiScO3 Ceramics. Journal of the American Ceramic Society 2009;92:1719-24.

[17] Raengthon N, Cann DP. High-K (Ba 0.8 Bi 0.2)(Zn 0.1 Ti 0.9) O 3 ceramics for high-temperature capacitor applications. Ultrasonics, Ferroelectrics and Frequency Control, IEEE Transactions on 2011;58:1954-8.
[18] Yuan Y, Zhao C, Zhou X, Tang B, Zhang S. High-temperature stable dielectrics in Mn-modified (1-x) Bi0. 5Na0. 5TiO3-xCaTiO3 ceramics. Journal of electroceramics 2010;25:212-7.
[19] Fujii I, Nakashima K, Kumada N, Wada S. Structural, dielectric, and piezoelectric properties of BaTiO3-Bi (Ni1/2Ti1/2) O3 ceramics. Journal of the Ceramic Society of Japan 2012;120:30-4.
[20] Huang C-C. Structure and piezoelectric properties of lead-free bismuth-based perovskite solid solutions: ProQuest; 2008.
[21] Belik AA, Iikubo S, Kodama K, Igawa N, Shamoto S-i, Maie M, et al. BiScO3: centrosymmetric BiMnO3-type oxide. Journal of the American Chemical Society 2006;128:706-7.
[22] Benedek NA, Fennie CJ. Why are there so few perovskite ferroelectrics? The Journal of Physical Chemistry C 2013;117:13339-49.
[23] Vakhrushev S, Nabereznov A, Sinha S, Feng Y, Egami T. Synchrotron X-ray scattering study of lead magnoniobate relaxor ferroelectric crystals. Journal of Physics and Chemistry of Solids 1996;57:1517-23.
[24] Yoshida M, Mori S, Yamamoto N, Uesu Y, Kiat J. TEM observation of polar domains in relaxor ferroelectric Pb (Mg1/3Nb2/3) O3. Ferroelectrics 1998;217:327-33.
[25] Raengthon N, Sebastian T, Cumming D, Reaney IM, Cann DP. BaTiO3‐Bi (Zn1/2Ti1/2) O3‐BiScO3 Ceramics for High‐Temperature Capacitor Applications. Journal of the American Ceramic Society 2012;95:3554-61.
[26] Raengthon N, DeRose VJ, Brennecka GL, Cann DP. Defect mechanisms in high resistivity BaTiO3–Bi (Zn1/2Ti1/2) O3 ceramics. Applied Physics Letters 2012;101:112904.
[27] Chen J, Sun X, Deng J, Zu Y, Liu Y, Li J, et al. Structure and lattice dynamics in PbTiO 3–Bi (Zn 1/2 Ti 1/2) O 3 solid solutions. Journal of Applied Physics 2009;105:044105--5.
[28] Priya S, Ando A, Sakabe Y. Nonlead perovskite materials: Ba (Li1/4Nb3/4) O3 and Ba (Cu1/3Nb2/3) O3. Journal of applied physics 2003;94:1171-7.
[29] Pandey R, Pillutla RK, Shankar U, Singh AK. Absence of tetragonal distortion in (1− x) SrTiO3-xBi (Zn1/2Ti1/2) O3 solid solution. Journal of Applied Physics 2013;113:184109.
[30] Triamnak N, Yimnirun R, Pokorny J, Cann DP. Relaxor Characteristics of the Phase Transformation in (1− x) BaTiO3–xBi (Zn1/2Ti1/2) O3 Perovskite Ceramics. Journal of the American Ceramic Society 2013;96:3176-82.
[31] TRIAMNAK N, BRENNECKA GL, BROWN-SHAKLEE HJ, RODRIGUEZ MA, CANN DP. Phase formation of BaTiO 3–Bi (Zn 1/2 Ti 1/2) O 3 perovskite ceramics. Journal of the Ceramic Society of Japan 2014;122:260-6.
[32] Cross LE. Relaxor ferroelectrics. Ferroelectrics 1987;76:241-67.
[33] Dittmer R, Anton EM, Jo W, Simons H, Daniels JE, Hoffman M, et al. A High‐Temperature‐Capacitor Dielectric Based on K0. 5Na0. 5NbO3‐Modified Bi1/2Na1/2TiO3‐Bi1/2K1/2TiO3. Journal of the American Ceramic Society 2012;95:3519-24.

[34] Kleemann W. The relaxor enigma—charge disorder and random fields in ferroelectrics. Frontiers of Ferroelectricity: Springer; 2007. p. 129-36.
[35] Samara GA. The relaxational properties of compositionally disordered ABO3 perovskites. Journal of Physics: Condensed Matter 2003;15:R367.
[36] Shvartsman VV, Lupascu DC. Lead‐Free Relaxor Ferroelectrics. Journal of the American Ceramic Society 2012;95:1-26.
[37] Yoon SH, Randall CA, Hur KH. Effect of Acceptor (Mg) Concentration on the Resistance Degradation Behavior in Acceptor (Mg)‐Doped BaTiO3 Bulk Ceramics: I. Impedance Analysis. Journal of the American Ceramic Society 2009;92:1758-65.
[38] Takeda T, Watanabe A. Electron Spin Resonances in Reduced BaTiO3. Journal of the Physical Society of Japan 1966;21:267-74.
[39] Tennery VJ, Cook RL. Investigation of Rare‐Earth Doped Barium Titanate. Journal of the American Ceramic Society 1961;44:187-93.
[40] Hirose N, West AR. Impedance spectroscopy of undoped BaTiO3 ceramics. Journal of the American Ceramic Society 1996;79:1633-41.
[41] Schulze W, Cross L, Buessem W. Degradation of BaTiO3 ceramic under high AC electric field. Journal of the American Ceramic Society 1980;63:83-7.
[42] Klaas J, Schulz-Ekloff G, Jaeger NI. UV-visible diffuse reflectance spectroscopy of zeolite-hosted mononuclear titanium oxide species. The Journal of Physical Chemistry B 1997;101:1305-11.
[43] Tauc J, Grigorovici R, Vancu A. Optical properties and electronic structure of amorphous germanium. physica status solidi (b) 1966;15:627-37.
[44] Umebayashi T, Yamaki T, Itoh H, Asai K. Band gap narrowing of titanium dioxide by sulfur doping. Applied Physics Letters 2002;81:454-6.
[45] Lee S, Levi RD, Qu W, Lee SC, Randall CA. Band-gap nonlinearity in perovskite structured solid solutions. Journal of Applied Physics 2010;107:023523.
[46] CHAN NH, Sharma R, Smyth DM. Nonstoichiometry in Acceptor‐Doped BaTiO3. Journal of the American Ceramic Society 1982;65:167-70.
[47] Cullity BD. Elements of X-ray Diffraction. American Journal of Physics 1957;25:394-5.
[48] Liu W, Randall CA. Thermally Stimulated Relaxation in Fe‐Doped SrTiO3 Systems: I. Single Crystals. Journal of the American Ceramic Society 2008;91:3245-50.
[49] Liu W, Randall CA. Thermally Stimulated Relaxation in Fe‐Doped SrTiO3 Systems: II. Degradation of SrTiO3 Dielectrics. Journal of the American Ceramic Society 2008;91:3251-7.

9.3 Conduction mechanisms in $BaTiO_3$-$Bi(Zn_{1/2}Ti_{1/2})O_3$ ceramics

Nitish Kumar[1], Eric A. Patterson[2], Till Frömling[2] and David P. Cann[1]

[1]Materials Science, School of Mechanical, Industrial, and Manufacturing Engineering, Oregon State University, Corvallis, Oregon, USA

[2]Institute of Materials Science, Technische Universität Darmstadt, Darmstadt, Germany

Published in

Journal of the American Ceramics Society

DOI: 10.1111/jace.14313 (2016)

Abstract

Polycrystalline $BaTiO_3$-$Bi(Zn_{1/2}Ti_{1/2})O_3$ (BT-BZT) ceramics have superior dielectric properties for high temperature and high energy density applications as compared to the existing materials. While it has been shown that the addition of BZT to pure BT leads to an improvement in resistivity by two orders of magnitude, in this study impedance spectroscopy is used to demonstrate a novel change in conduction mechanism. While pure BT exhibits extrinsic p-type conduction, it is reported that BT-BZT ceramics exhibit intrinsic n-type conduction using atmosphere dependent conductivity measurements. Annealing studies and Seebeck measurements were performed and confirmed this result. For BT, resistivity values were higher for samples annealed in nitrogen as compared to oxygen, while the opposite responses were observed for BZT-containing solid solutions. This suggested a possibile unintentional donor doping upon addition of BZT to the solid solution, which may also be linked to the improvement in resistivity in BT-BZT ceramics as compared to pure BT.

Introduction

A significant amount of research has been devoted to the study of the dielectric properties of Bi-based perovskites over the last two decades to develop improved ceramics for lead-free piezoelectric and dielectric applications.[1-5] Environmental considerations and an ever-increasing demand to improve device performance are driving the current research on these Bi-based perovskites. While improvements have been made to the various electrical properties of these perovskites, research to understand the

underlying defect chemistry is still lagging. The defect chemistry affects the performance of devices based on perovskites and is generally considered the main factor behind phenomena like fatigue, aging, resistance degradation and others.[6-9] On the other hand, with the help of controlled dopants, defects can also be used to tailor ceramic properties and make them better suited for specific device requirements such as X7R $BaTiO_3$ or PZT-5H, for example, including those required for high temperature and high energy density applications.[10-13] One of the main reasons why something like $Pb(Zr,Ti)O_3$ (PZT) has been so successful in a plethora of applications is because of the relatively well-understood and controllable defect chemistry.[11, 14] The same approach is needed for Bi-based perovskites before they can be extensively employed in applications. This article focuses on one specific Bi-containing perovskite, $BaTiO_3$-$Bi(Zn_{1/2}Ti_{1/2})O_3$ (BT-BZT). It has been demonstrated that BT-BZT relaxor compositions have excellent dielectric properties that are well suited for high energy density or wide ranged temperature-stable dielectric applications.[15] Furthermore, it has been shown that the properties can be further modified by making additional substitutions through the creation of ternary systems with $BiScO_3$, $NaNbO_3$ and others.[15-18] Recently, inexpensive multilayer ceramic capacitors (MLCCs) were also fabricated based on these compositions which had superior performance compared to commercially available MLCCs based on barium titanate.[18, 19]

A significant improvement in the electrical resistivity was recently reported in these BT-BZT ceramics with addition of BZT in the solid solution.[20] The resistivity increased by approximately two orders of magnitude with the addition of small amounts

of BZT and the conduction mechanism gradually transitioned from an extrinsic p-type mechanism as is typical for nominally pure BT to an intrinsic-like mechanism with an activation energy that matched half of the band gap. In case of "undoped" BT, its p-type behavior is generally attributed to unintended low valence impurities such as Fe^{3+} or others that are commonly present with TiO_2 reagents.[21] These impurities are typically charge compensated by oxygen vacancies, which are then ultimately responsible for the observed p-type behavior as per the following defect reaction:

$$V_O^{\cdot\cdot} + \frac{1}{2} O_2 \rightarrow O_O^X + 2h^{\cdot} \qquad \text{Eq. 9.3.1}$$

where $V_O^{\cdot\cdot}$ represents doubly-ionized oxygen vacancies, O_O^X represents an oxygen ion located on an oxygen lattice site, and $h^{\cdot}$ represents a hole. In their previous report, the authors suspected that this increase in resistivity on adding BZT to the solid solution might be related to a decrease in concentration of holes.[20] To get a better insight into this, more extensive experiments were performed and are reported here. With the help of oxygen partial pressure dependent conductivity measurements, annealing in different atmospheres, and Seebeck measurements, it was established the addition of BZT has an effect equivalent to donor-doping the solid solution, leading to an increase in resistivity by orders of magnitude. This transition from p-type to n-type behavior with the addition of BZT to BT has not been reported before and may have important implications on the insulation properties of other solid solutions of BT with Bi-based perovskites.[22, 23]

Experimental Details

Polycrystalline ceramics were prepared using a conventional solid-state method. High purity powders of $BaTiO_3$ (Sakai Chemical Industry), $BaCO_3$ (>99.8%, Alfa Aesar), Bi_2O_3 (>99.9%, Aldrich), TiO_2 (>99.9%, Aldrich), and ZnO (>99.9%, Alfa Aesar) were mixed in the appropriate amounts to prepare stoichiometric compositions based on $(1-x)BaTiO_3$-$xBi(Zn_{1/2}Ti_{1/2})O_3$ (BT-BZT) ($0 \leq x \leq 0.075$). Henceforth, the $BaTiO_3$, $0.97BaTiO_3$-$0.03Bi(Zn_{1/2}Ti_{1/2})O_3$ and $0.925BaTiO_3$-$0.075Bi(Zn_{1/2}Ti_{1/2})O_3$ samples will be referred to as BT, 3BZT and 7.5BZT respectively. The $BaTiO_3$ ceramics were prepared from $BaTiO_3$ powders from Sakai Chemical Industry and required no calcination. For the rest of the compositions, the mixed powders were ground using a vibratory mill for 6 hours and then dried overnight in an oven (~80 °C). The BT-BZT powders were calcined in alumina crucibles at 950 °C-1000 °C for 4 hours and then milled with ~3 wt% binder (Rhoplex HA-8, Dow Chemical Company, USA) and dried again. Green pellets in the shape of thin discs were prepared by uniaxial cold-pressing at a pressure of 200 MPa and then sintered on a bed of calcined powder in a closed alumina crucible between 1250 °C-1350 °C for 4 hours. All the sintered pellets were polished to ~800 μm thickness. X-ray diffraction (Bruker AXS D8 Discover, Madison, WI, USA) were performed on ground pellets for checking phase purity. For electrical measurements, silver or platinum electrodes were used. In case of silver electrode, paste was applied on both sides of the pellets and then fired at 700 °C for 30 min. In case of platinum, it was either sputtered on both sides of the sample or Pt paste was applied on both sides and fired at 900 °C for 15 min before performing the measurements. The electrodes used for a given experiment are

specified below. The impedance measurements were performed using either a high temperature measurement cell (NorECs AS ProbostatTM, Oslo, Norway) and an impedance analyzer (Solartron SI1260A equipped with Solartron 1296A dielectric interface, Farnborough, UK) at Oregon State University, USA or using a home-built high-temperature sample holder and an impedance analyzer (Novocontrol Technologies, Montabaur, Germany) at Technische Universität Darmstadt, Germany. The SMaRT and WinDETA impedance measurement software programs were used respectively to collect the data in the frequency range of 5 MHz to 0.1 Hz. The data shown in Fig. 9.3.2 and Figs. 9.3.4-9.3.7 used sputtered Pt electrodes. Seebeck measurements were performed on selected samples using the Probostat set-up and a Keithley 6517A Electrometer, using fired Pt electrodes. For this measurement, bar samples with lengths of ~23 mm and cross-section of 4x4 mm^2 were used. They were cut to suitable size from a larger disc sample, prepared via conventional solid-state route. The temperature difference across the sample was measured using two different thermocouples.

Impedance measurements were performed on sintered ceramics at different temperatures (400 °C-800 °C) in vacuum, air and pure oxygen atmospheres. For each data point, in order to establish close to equilibrium values, the change in resistivity was monitored by conducting consecutive impedance measurements until no further noticeable change could be observed. Depending on the temperature, this typically involved hold times of approximately 30 min to more than an hour. For annealing studies, oxygen or nitrogen was flowed through the sample chamber at 1100 °C for ~8 hours and impedance measurements were subsequently performed in air over a temperature range of 200 °C to 500 °C.

Results and Discussion

All the samples prepared were single phase within the limits of the laboratory-scale x-ray diffraction instrument used and were suitably dense (>95% of theoretical density as determined by Archimedes method). Figure 9.3.1 shows the Arrhenius plots for the bulk resistivities of the BT-BZT samples in air. As previously reported, a significant increase in resistivity was observed upon adding BZT in solid solution with BT.[20] The activation energies for conduction also increased from around ~1 eV for pure BT to values close to ~1.5 eV for 7.5BZT, which is approximately half of the optical band gap previously determined from diffuse reflectance spectrometry.[20] This phenomenon is most likely controlled by changes to the defect equilibrium conditions in these ceramics, specifically those which determine the dominant charge carriers. The

precise mechanism for this effect is still not completely understood, so various experiments were performed to get a better insight into the nature of this phenomenon.

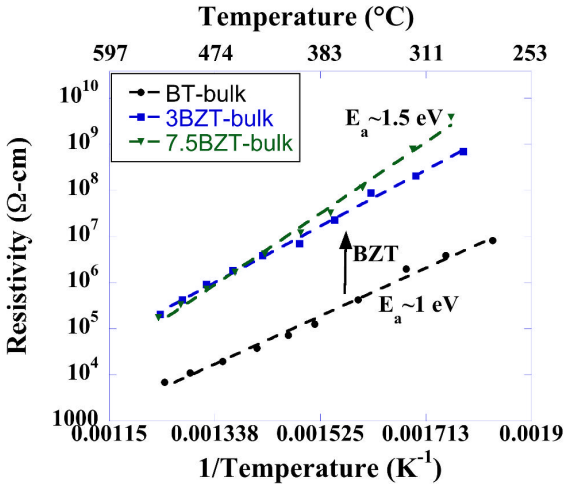

Fig. 9.3.1 The Arrhenius plots for the bulk resistivity of BT, 3BZT and 7.5BZT in air are shown. The resistivities were obtained from the Z* complex plane plots. The BZT containing ceramics had ~2 orders of magnitude higher resistivity as compared to the unmodified BT.

Figure 9.3.2 displays the results from impedance spectroscopy performed on the nominally pure BT samples under three different atmospheres–vacuum ($pO_2 \sim 10^{-5}$ atm), air ($pO_2 \sim 0.2$ atm) and oxygen ($pO_2 \sim 1$ atm) and at temperatures ranging from 400 °C to 800 °C. Figure 9.3.2(a) shows the complex plane plots for data taken in all three atmospheres at 400 °C. It can be observed that the samples were electrically heterogeneous, with distinct semicircles belonging to bulk (high frequency) and grain boundary (intermediate frequency), as is typical for BT ceramics.[24] A third semicircle could also be seen for all the three plots. To investigate its origin, the magnitude of the capacitance associated with each element was calculated using the relationship $\omega_{max}RC =$

1, where, ω_{max} is the angular frequency at the maxima and R and C are the resistance and capacitance associated with each RC element. The capacitance values for the third low frequency RC element were approximately ~6.5 μF, ~27 μF and ~67 μF for measurements performed in vacuum, air and oxygen, respectively. These values were too high to be associated with bulk or grain boundary for samples with geometry of ~0.8 mm thick and ~11 mm diameter. Instead these capacitance values were of the same order of magnitude as typical capacitances associated with the sample-electrode interface.[25] Therefore, the most likely origin of the third semicircle was due to sample-electrode interactions.

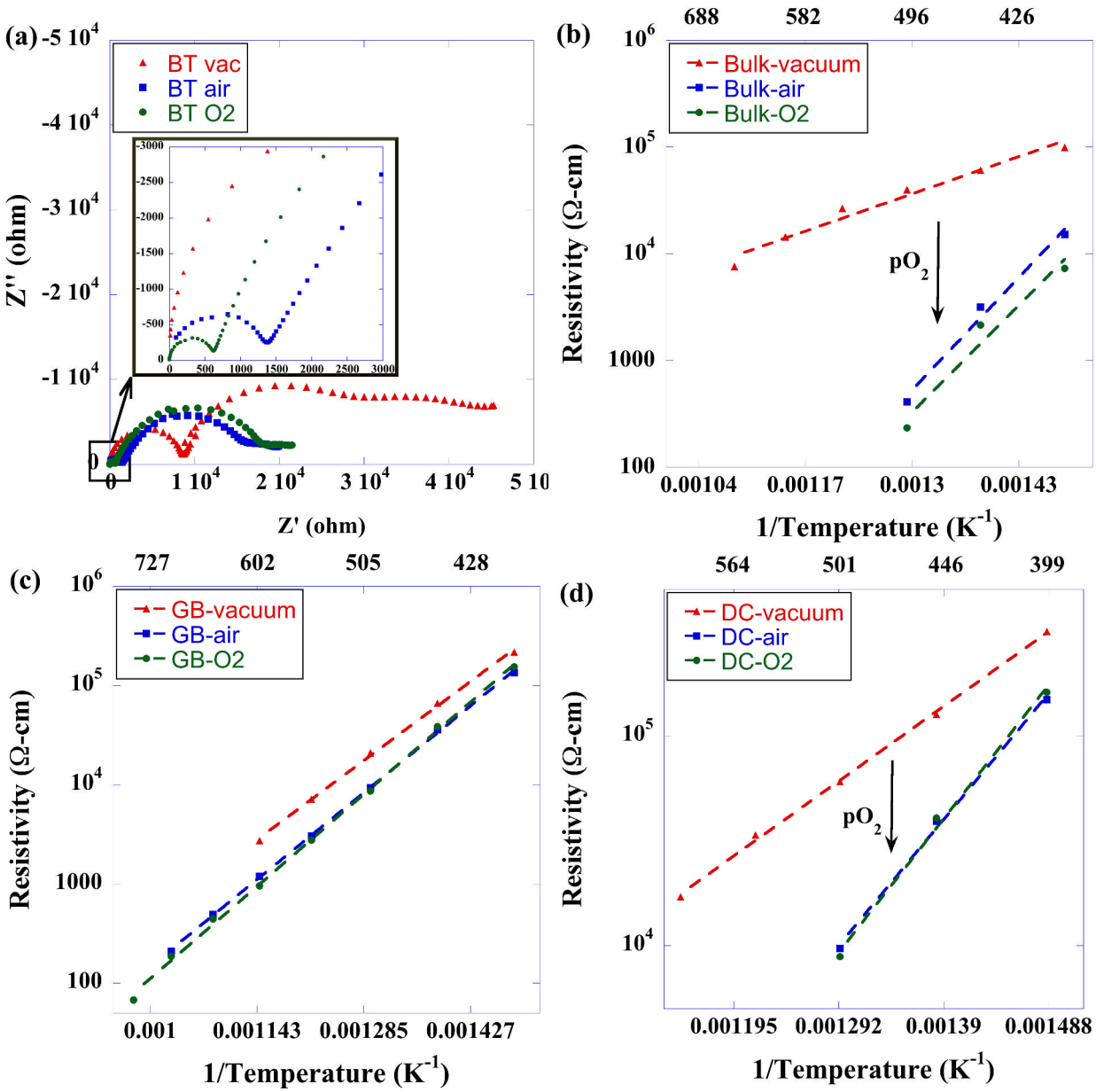

Fig. 9.3.2 (a) Complex plane plots for BT in vacuum, air and oxygen at 400 °C. The Arrhenius plots for data taken in vacuum, air and oxygen are also shown for (b) bulk, (c) grain boundary and (d) DC resistivities. The arrows in Arrhenius plots indicate the direction of increasing pO_2.

Figures 9.3.2(b) and 9.3.2(c) show the Arrhenius plots for bulk and grain boundary components, respectively, for BT in all three atmospheres; and Figure 9.3.2(d) shows the DC resistivity for BT in different atmospheres. The DC resistivities were not

calculated from direct DC measurements, but were estimated by extrapolating the low frequency AC impedance data to determine the intercept with the real axis in the complex plane impedance plots. Past experiments on this material system from this group and others have shown that DC resistivity values extrapolated from low frequency AC data typically closely correspond to resistivity values obtained though more conventional DC measurements.[20]

Typically, the DC resistance value of the ceramic is the sum of bulk and grain boundary components,

$$R_{DC} = R_B + R_{GB} \qquad \text{Eq. 9.3.2}$$

where, R_{DC}, R_B and R_{GB} are DC, bulk and grain boundary components of resistance. The corresponding resistivities were calculated by correcting the resistance values obtained from AC impedance for sample geometry. The bulk resistivity of BT was at least two orders of magnitude higher in vacuum and decreased sharply as the oxygen partial pressure increased. This pO_2 dependence is typical of p-type conduction and indicates that the conduction mechanism in BT was dominated by holes, as is expected.[26, 27] The grain boundary resistivity was not influenced significantly by the changes in atmosphere, which is also consistent with other reports in the literature.[28] The DC resistivity primarily reflected the trend in the bulk resistivities where it decreased as the oxygen partial pressure increased. The activation energy values for bulk and DC conduction also appeared to be higher in oxygen and air as compared to vacuum.

The change in bulk resistivity measured at different oxygen partial pressures suggests that electronic conduction was dominant as opposed to ionic conduction through oxygen vacancies. It is expected that the measurement durations and temperatures were too low to cause any significant oxygen vacancy migration in pure barium titanate.[29] However, an increase in resistivity was observed at temperatures as low as 400 °C upon changing the oxygen partial pressure. As can be seen from equation (9.3.1), oxygen vacancies can be compensated by holes via oxygen incorporation from the surroundings onto the ceramic surface. A simplified charge neutrality condition for $BaTiO_3$ would include the terms in equation (9.3.3) assuming that there are no other major charged defects:

$$n + [A'] = p + 2[V_O^{\cdot\cdot}] \qquad \text{Eq. 9.3.3}$$

where A', $V_O^{\cdot\cdot}$, p and n are acceptor, oxygen vacancy, hole concentration ($[h^{\cdot}]$), and electron concentration ($[e']$) respectively. As per equation (9.3.3), the concentration of electrons and holes are controlled by the oxygen vacancy concentration at low and high oxygen partial pressures since the concentration of acceptors should remain constant independent of the ambient atmosphere. Ambipolar diffusion in dense ceramic perovskites at the temperatures relevant to this study (400 °C -800 °C) is in general dominated by three mobile species: electrons, holes and oxygen vacancies. However, since the mobility of oxygen vacancies is significantly smaller in BT as compared to electronic charge carriers [29], the conductivity can be approximated by:

$$\sigma = \Sigma(\text{defect mobility})*(\text{defect charge})*(\text{electronic charge}) \approx q\mu_n n + q\mu_p p \qquad \text{Eq. 9.3.4}$$

where σ, q, μ_n, and μ_p are conductivity, electronic charge, electron mobility, and hole mobility respectively. Therefore when the ambient temperature and/or pressure of the BT sample changes, the change in conduction should be due to a change in the concentration of higher mobility electronic defects. The concentration of electronic defects, however, should be controlled by the change in concentration of the lower mobility oxygen vacancies.[29]

This can be further understood with the help of an idealized and widely accepted defect diagram presented in Figure 9.3.3.[26] It shows the variation in concentration of relevant defect species as a function of oxygen partial pressure. The diagram covers a wide range of oxygen partial pressures; however, due to practical limitations, measurements are confined to a comparatively narrow range close to the defect concentration minima in the case of barium titanate.[26] Over most of this region, the acceptor, electron and hole concentrations vary as per the following relationships[26]:

$$[A'] = 2[V_O^{\cdot\cdot}] \qquad \text{Eq. 9.3.5a}$$

$$p \alpha pO_2^{1/4} \qquad \text{Eq. 9.3.5b}$$

$$n \alpha pO_2^{-1/4} \qquad \text{Eq. 9.3.5c}$$

where pO_2 is the oxygen partial pressure. It can be noticed in Figure 9.3.3 that oxygen vacancies are the most abundant defect species over this range of oxygen partial pressure,

however their concentration remains independent of oxygen partial pressure. From equation (9.3.5), if the conductivity was dominated by oxygen vacancies (i.e. if the oxygen vacancies have significant mobility), the bulk resistivity should have remained constant with the change in oxygen partial pressure over the region where $[A'] = 2[V_O^{\cdot\cdot}]$. From the same argument, if the conductivity was dominated by electronic species, the slope of log(conductivity) vs log pO_2 should have a value of $-^1/_4$ just below and $+^1/_4$ just above the concentration/conductivity minima, in these acceptor doped ceramics. This finding is consistent with literature reports available on defect studies in perovskite ferroelectric ceramics.[26] For an example, it was shown that B-site acceptor (Ca) doped $BaTiO_3$ exhibited mixed conduction, and the conductivity minima became increasingly flat as the Ca concentration increased.[30, 31] This was attributed to an increase in the pO_2-independent ionic conductivity.[31] In a recent study on non-stoichiometric and doped $(Bi_{1/2}Na_{1/2})TiO_3$ (BNT), it was shown that by acceptor doping or creating Bi-deficient BNT, the ionic conductivity of the bulk increased significantly.[32, 33] In this case the bulk resistivity was not affected by the oxygen partial pressure used during the impedance measurements (oxygen, air or nitrogen atmospheres were used).[32, 33] The ionic transport number of acceptor (Mg)-doped BNT was ~0.95 and the conductivity did not change even when exposed to a highly reducing atmosphere ($5\%H_2/95\%N_2$). However, with donor doping of BNT, the ionic transport number became less than 0.1 and there was a significant dependence of resistivity on oxygen partial pressure. In this study, therefore, the dependence of the conductivity of BT on oxygen partial pressure indicated that electronic conduction was dominant. The fact that the conductivity decreased with decreasing oxygen partial pressure is indicative of p-type conduction.

According to equation (9.3.1), a decrease in oxygen partial pressure results in a corresponding decrease in the hole concentration.

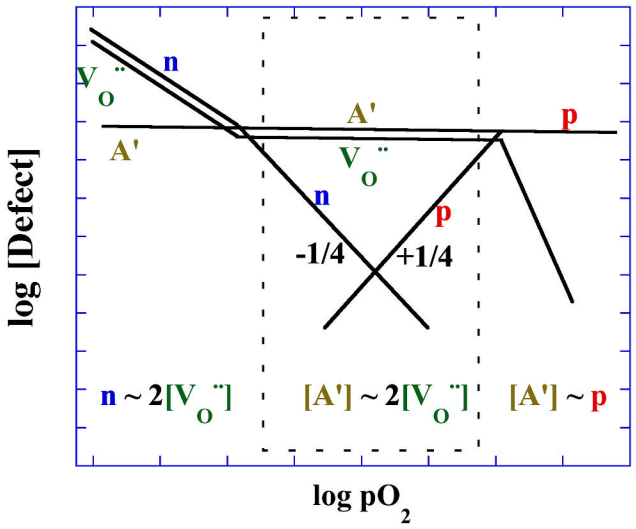

Fig. 9.3.3 The idealized defect diagram for undoped or acceptor doped barium titanate adapted from Smyth *et al*. [26]

Figure 9.3.4 depicts the impedance results for the 3BZT composition under the same atmospheres as BT in Figure 9.3.2. Figure 9.3.4(a) shows that the complex plane plots at 400 °C were not perfect semicircles as expected for a single RC (resistor-capacitor) element, but were suppressed. This is indicative of electrical inhomogeneity in the ceramics similar to that observed in BT. In contrast to the results for BT, no significant ceramic-electrode interaction was observed within the range of frequencies used for measurements. In Figures 9.3.4(b-d) the Arrhenius plots for the 3BZT composition obtained in different atmospheres are given. Based on arguments similar to that presented for BT, the dependence of conductivity on oxygen partial pressure indicated that the conduction mechanism was still predominantly electronic. However, the resistivity increased in response to an increase in the oxygen partial pressure. This

was directly opposite to the behavior exhibited by BT, which indicates that n-type conduction was dominant for this composition. This may be related to the improvement in resistivity observed on adding BZT to BT as seen in Figure 9.3.1. A possible oxygen incorporation reaction can be given by:

$$V_O^{\cdot\cdot} + 2e' + \frac{1}{2}O_2 \rightarrow O_O^X \qquad \text{Eq. 9.3.6}$$

It can be seen from equation (9.3.6) that higher oxygen partial pressure should increase the resistivity by reducing the electron concentration for n-type ceramics. Only a small change in resistivity was observed in comparing the measurements conducted in pure oxygen to air atmosphere because the oxygen partial pressures were only different by a factor of five. Measurements conducted in vacuum yielded comparably much lower oxygen partial pressures, and consequently the observed change in resistivity was much larger. In the case of BT, the grain boundary resistivity was nearly independent of the atmosphere used. However, for 3BZT, the grain boundary resistivity followed the same trend as the bulk and increased nearly two orders of magnitude with increasing oxygen partial pressure.

The mechanism behind the change in dominant carrier type with addition of BZT is not fully understood. However, from consideration of the overall defect equilibria conditions it seems likely that the addition of BZT compensates for the impurity acceptors associated with “pure” BT and hence there is no evidence for p-type conduction in this composition. This points towards the possibility of some donor doping mechanism, which becomes active when adding BZT to the solid solution. The donor doping could originate on both cationic and anionic sites of the perovskite.

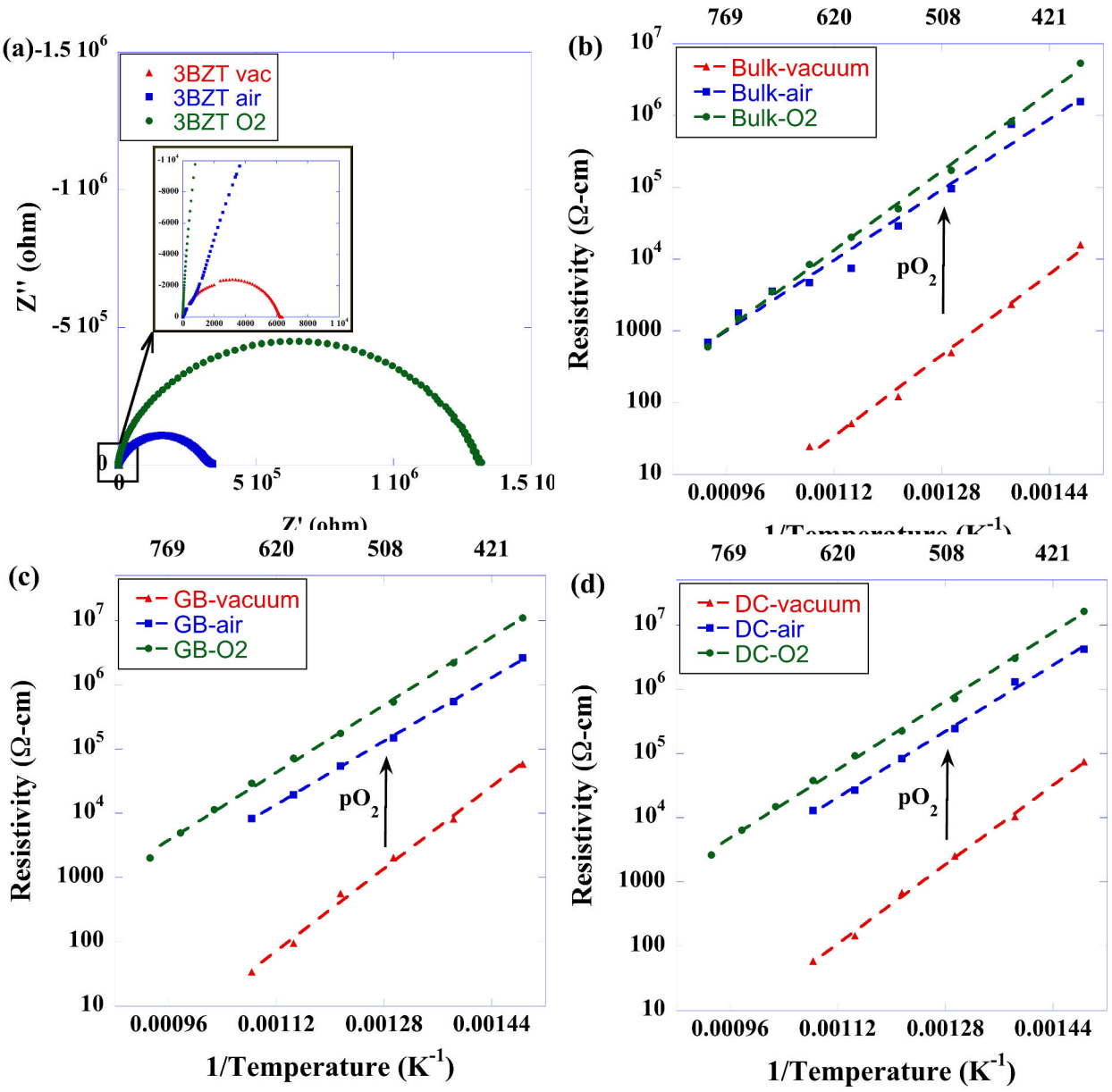

Fig. 9.3.4 (a) Complex plane plots for 3BZT ceramics in vacuum, air and oxygen at 400 °C. The Arrhenius plots in vacuum, air and oxygen have also been shown for (b) bulk, (c) grain boundary and (d) DC resistivities as a function of temperature. The arrows in Arrhenius plots indicate the direction of increasing pO_2.

In case of anionic sites, the possible "donors" can be doubly or singly ionized oxygen vacancies, which can be compensated by electrons. If the oxygen vacancy concentration is higher in the BZT-containing ceramics the result can be n-type behavior.

The presence of the volatile bismuth component on the A-site of the perovskite adds to the complexity of the situation since the presence of Bi-vacancies can also result in compensating oxygen vacancies in these ceramics.

Regarding doping on the cation-sites, for the composition with 3BZT added to the solid solution, essentially 3% of the A-sites are replaced with Bi^{3+} and 1.5% of the B-sites by Zn^{2+}. If the batch stoichiometry is retained after processing into the ceramic samples, there is no clear possibility of donor doping on the cationic sites since the substitutions of Bi^{3+} for Ba^{2+} and Zn^{2+} for Ti^{4+} are fully compensated. However, changes in the stoichiometry of the sintered ceramics due to the volatility of Bi and/or Zn could induce a change in the defect chemistry. Another unique feature of this solid solution is the formation of an interesting intermediate phase, $BaBiO_3$, which appears at moderate temperatures during ceramic processing and then ultimately becomes undetectable by x-ray diffraction at higher temperatures.[34] In the $BaBiO_3$ phase, the Bi ion resides on the B-site in the double perovskite structure with multiple possible valence states including 3+, 4+ or 5+.[35] If some of the Bi remains on the B-site, then depending upon the valence state it could directly influence the defect equilibria conditions.

Figure 9.3.5 shows the results from impedance measurements performed in different atmospheres for 7.5BZT. Like the BT and 3BZT compositions, the impedance plots also showed an electrically heterogeneous response with distinct bulk and grain boundary components. The heterogeneity was more apparent as compared to 3BZT in terms of peak suppression and separation of semicircles. Based on the dependence of the resistivity on oxygen partial pressure, these results showed n-type behavior similar to that obtained on 3BZT ceramics. This behavior can again be explained by equation (9.3.6)

above. Also similar to 3BZT samples, the grain boundary resistivities responded to the change in oxygen partial pressure.

The behavior of the 7.5BZT composition followed the same general trends as the other BZT-containing samples in terms of the trend in resistivity values and dominant charge carrier, however, there was a significant difference in the activation energy for conduction (Figure 9.3.1 and Kumar *et al.*[20]). For the 3BZT ceramics, the activation energy for conduction in air (pO_2 ~ 0.2 atm) was ~1 eV, but was increased to ~1.6 eV (or approximately half the band gap) for the 7.5BZT composition. This, combined with high resistivity values, suggested a change in conduction mechanism and that the concentration of uncompensated acceptors or donors present was lowered. Under reducing conditions the transition of Ti^{4+} to Ti^{3+} is likely to be the source of conduction since none of the other cations or anions are expected to be redox-active under the experimental conditions in this study. The loss of oxygen during sintering may act as the source of electrons for this transition. In other words, even though there might be just a small amount of uncompensated defects present in 7.5BZT ceramics, the unavoidable oxygen vacancies present due to limitations of processing may act as donor states to the conduction band, whose band edge predominantly consists of Ti *3d* states.[36]

While pure BT is p-type at the temperatures included in this study, the conductivity minimum occurs at oxygen partial pressures ~10^{-9} MPa (~10^{-8} atm) at 750 °C which is not far from experimental conditions using air (pO_2 ~ 0.2 atm).[26] At further elevated temperatures this conductivity minimum shifts to higher oxygen partial pressures and BT eventually becomes n-type above approximately 1100 °C in air. The

addition of BZT may also act to shift this conductivity minimum so as to induce n-type conduction at the temperatures and oxygen partial pressures included in this study.

Figure 9.3.6 shows a plot of conductivity against oxygen partial pressure. Even though the slopes may not be accurate in this figure due to problems in equilibration at these low temperatures and use of just three data points for each temperature, the schematic helps to show the trends in conductivity with oxygen partial pressure at a given temperature. It also shows that even though BZT-containing ceramics are more insulating in air and oxygen, BT can become more insulating in atmospheres where oxygen partial pressures are low. More importantly, it indicates that for the BZT-containing ceramics the conductivity minimum lies at a higher oxygen partial pressure than the range investigated in this study and for the non-modified BT the minimum is at lower oxygen partial pressure values. This suggests a shift in the conductivity minimum to higher oxygen partial pressures as the amount of BZT increased in the ceramics. As mentioned earlier, this shift may be due to a reduction in hole concentration with increasing amounts of BZT added to the solid solution.

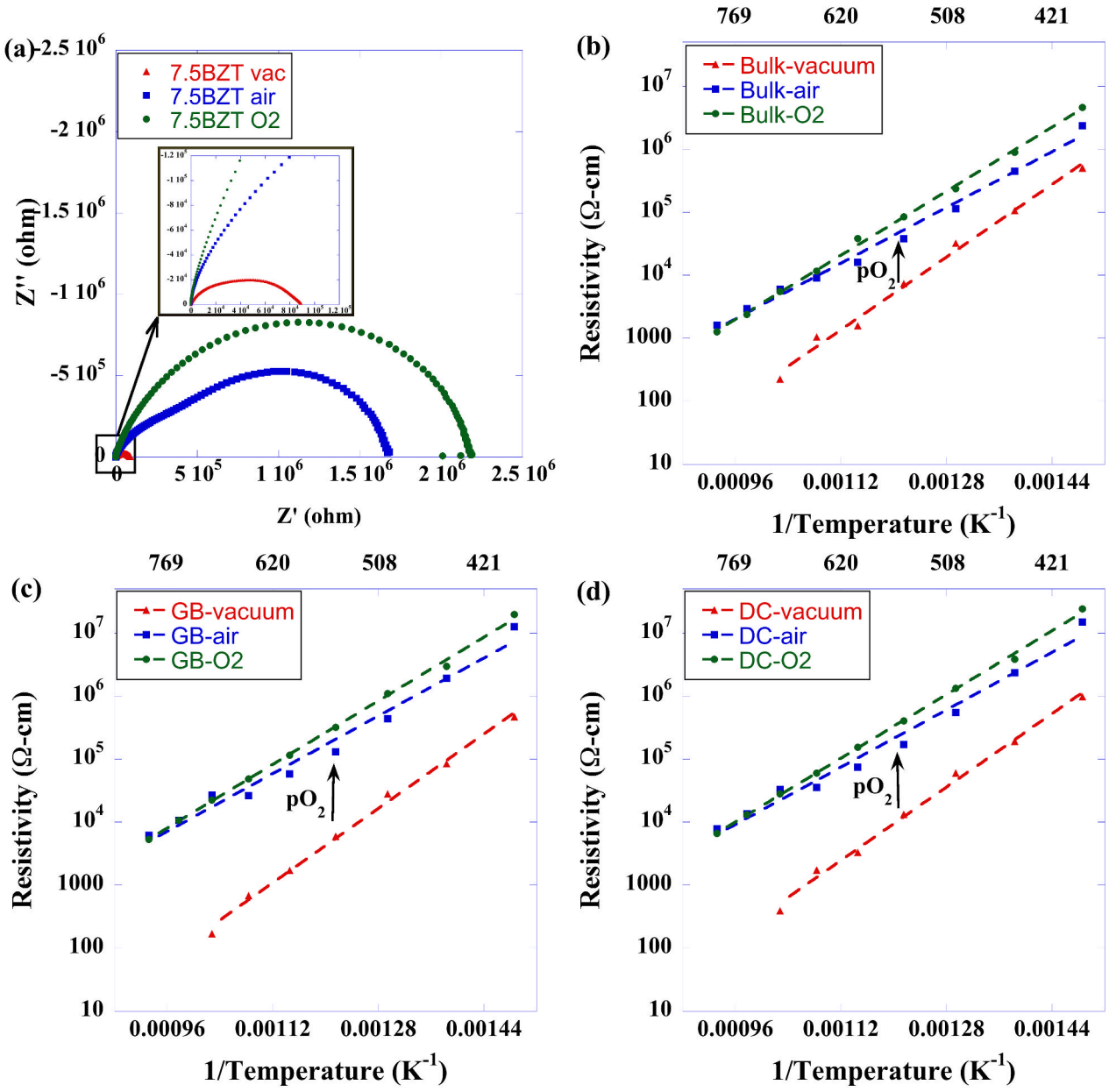

Fig. 9.3.5 (a) Complex plane plots for 7.5BZT ceramics in vacuum, air and oxygen at 400 °C. The Arrhenius plots in vacuum, air and oxygen have also been shown for (b) bulk, (c) grain boundary and (d) DC resistivities. The arrows in Arrhenius plots indicate the direction of increasing pO_2.

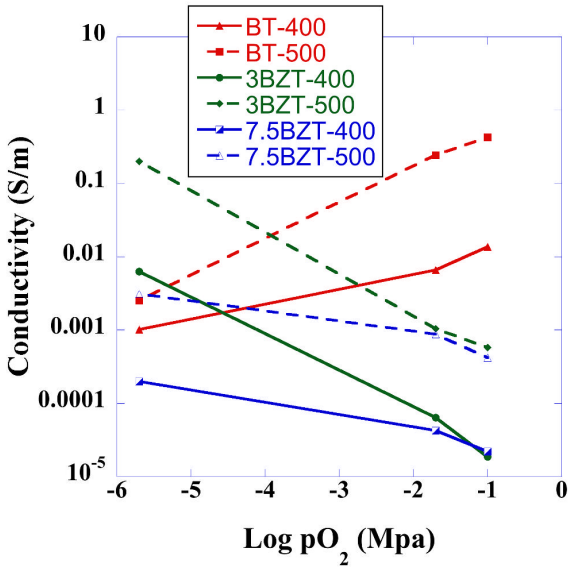

Fig. 9.3.6 Variation of conductivity with oxygen partial pressure for the three compositions at 400 °C and 500 °C.

The impedance spectroscopy data presented in Figures 9.3.2, 9.3.4 and 9.3.5 were obtained through measurements conducted in different atmospheres as a function of temperature. It was suggested that the change in conductivity behavior was due to the change in oxygen stoichiometry which resulted in a change in defect equilibrium affecting the conductivity values. To provide further proof of this phenomenon, annealing experiments were performed on all the three samples in pure oxygen and nitrogen, with subsequent impedance measurements conducted in air at increasing temperatures from 200 °C to 500 °C. The temperature and time for annealing were held constant at 1100 °C for ~8 hours, which was significantly higher than the temperatures and durations used during the previous impedance measurements in different atmospheres. Therefore, the concentration of defects introduced should be significantly greater and the difference

between the resistivities of samples annealed in different atmospheres should be exaggerated as compared to Figures 9.3.2, 9.3.4 and 9.3.5.

Figure 9.3.7(a-c) show the impedance spectroscopy results of BT samples annealed in nitrogen and oxygen. As expected for ceramics with hole-dominated conduction, the bulk resistivities of the samples annealed in nitrogen were higher than the samples annealed in oxygen. At low temperatures (close to 200 °C) where the ambient partial pressure is not expected to alter the resistivity of the annealed samples significantly, one could observe that the difference in bulk-resistivity of the samples was more than three orders of magnitude. Non-linearity started to appear in the oxygen annealed data as the temperature at which the impedance measurements were conducted increased with a sharp change near 350 °C. This could be attributed to the sample equilibrating with the oxygen partial pressure in the air atmosphere at higher temperatures during the impedance measurement which was reflected by a change in the bulk resistivity. To prove that the non-linearity was due to interactions between the ceramic with air atmosphere, impedance measurements were performed a second time (data marked as "Bulk-O2 2nd run") on the sample annealed in oxygen. The bulk resistivities were indeed higher during the second run even at low temperatures and the original data ("Bulk-O2 1st run") was not retraced. Interestingly, similar to the grain boundary behavior of BT in Figure 9.3.2(e), the grain boundary resistivities did not seem to be affected significantly with these higher temperatures and longer annealing times in the different atmospheres.

Figure 9.3.7(d) shows the effect of annealing on the bulk resistivities for 3BZT ceramics. Again, this confirmed the n-type behavior previously observed, and the resistivity of the sample annealed in oxygen was nearly four orders of magnitude higher at low temperatures as compared to nitrogen. The effect of annealing in nitrogen was dramatic on both the bulk and grain boundary resistivities [Figure 9.3.7(e)] such that the resistivity was nearly independent of temperature. This data resembles the defect-dominated, temperature-independent conductivity region of a typical semiconductor at intermediate temperatures. As with Figure 9.3.7(a), the observed non-linearity in Fig 9.3.7(d) can certainly be attributed to surface-air interactions. A similar behavior was observed for the 7.5BZT composition (Fig. 9.3.7(g-i)) as the 3BZT samples. However, the effect of the nitrogen-anneal was not as severe as in the 3BZT case. In general, the annealing experiments corroborated the results that were obtained by performing impedance measurements in different atmospheres.

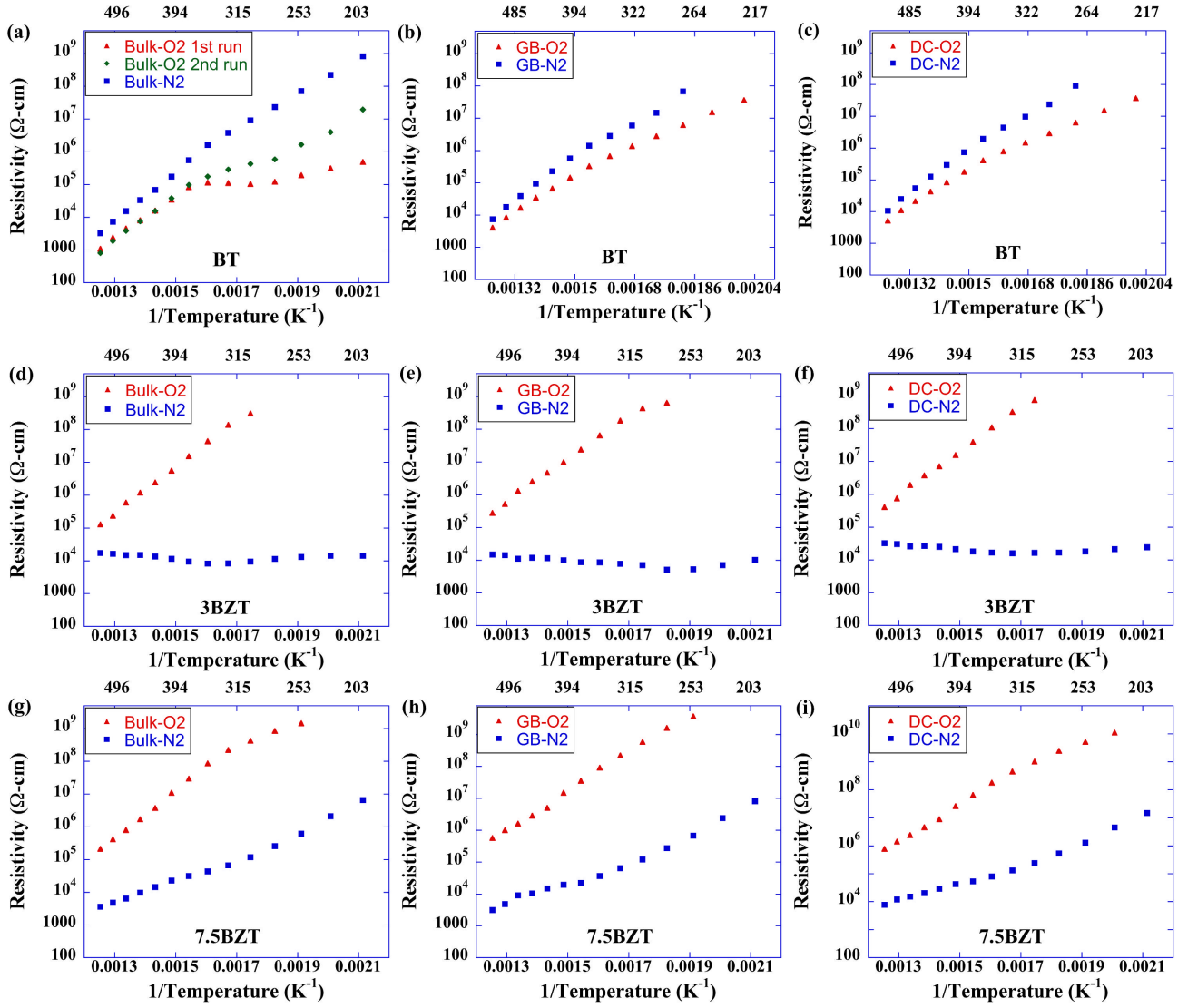

Fig. 9.3.7 The Arrhenius plots for various compositions after annealing in oxygen or nitrogen at 1100 °C for 8 hours. Plots (a-c) show the bulk, grain boundary and DC resistivity for BT. Figures (d-f) and (g-i) show the same for 3BZT and 7.5BZT ceramics, respectively.

Seebeck measurements were also performed on BT and 3BZT bar samples between 600 °C and 900 °C to further investigate the change from p-type to n-type

behavior with the addition of BZT to BT. In this technique, a temperature gradient is created across a sample and the corresponding voltage drop is measured.[37] The Seebeck coefficient (S) was estimated using the following relationship,

$$S = -\Delta V/\Delta T \qquad \text{Eq. 9.3.7}$$

where ΔV and ΔT were the voltage drop and corresponding temperature difference, respectively across the bar sample. The primary objective of these experiments was to directly confirm the dominant carrier type for these compositions. For the BT sample, a consistent positive sign was obtained for the Seebeck coefficient (+1.02 to +1.32 mV/K) in the entire temperature range of measurement. This is consistent with p-type behavior where the mobile defects are positively charged species (presumably holes in this case). Similarly, for the 3BZT sample, negative values of S (-0.81 to -1.21 mV/K) were reproducibly obtained over the entire temperature range, consistent with the predicted n-type behavior.

Conclusions

Ceramics of the composition $(Ba_{1-x}Bi_x)(Zn_{x/2}Ti_{1-x/2})O_3$ $(0 \leq x \leq 0.075)$ ceramics were prepared and impedance spectroscopy analysis was conducted at different temperatures and at different oxygen partial pressures. The addition of BZT to BT caused a >2 orders of magnitude improvement in resistivity that was accompanied by a transition from p-type to n-type behavior. This transition was determined from the change in resistivity as a

function of oxygen partial pressure, from annealing studies, as well as Seebeck measurements. This suggests an unintentional effective donor doping process occured by adding BZT to BT which can have implications for improvements in the resistivity behavior when adding other Bi-containing perovskites to $BaTiO_3$ as well. It also demonstrated that these ceramics interact appreciably with the ambient atmosphere even at low temperatures. These data suggest that the highly insulating properties of BT-BZT ceramics were intricately linked to changes in the defect equilibrium.

Acknowledgements

The authors would like to acknowledge Jürgen Rödel and Deutsche Forschungsgemeinschaft (DFG) through SFB595 for their help and support. This material is based upon work supported by the National Science Foundation under Grant No. DMR-1308032. Thanks to Jurij Koruza and Daniel Isaia for their help with experimentation.

References

[1] Panda P. Review: environmental friendly lead-free piezoelectric materials. Journal of materials science 2009;44:5049-62.
[2] Rödel J, Jo W, Seifert KT, Anton EM, Granzow T, Damjanovic D. Perspective on the Development of Lead‐free Piezoceramics. Journal of the American Ceramic Society 2009;92:1153-77.
[3] Shrout TR, Zhang SJ. Lead-free piezoelectric ceramics: Alternatives for PZT? Journal of Electroceramics 2007;19:113-26.
[4] Takenaka T, Maruyama K-i, Sakata K. (Bi1/2Na1/2) TiO3-BaTiO3 system for lead-free piezoelectric ceramics. Japanese Journal of Applied Physics 1991;30:2236.
[5] Kishi H, Mizuno Y, Chazono H. Base-metal electrode-multilayer ceramic capacitors: past, present and future perspectives. Japanese Journal of Applied Physics 2003;42:1.
[6] Warren WL, Dimos D, Waser RM. Degradation mechanisms in ferroelectric and high-permittivity perovskites. MRS bulletin 1996;21:40-5.
[7] Stokes SJ, Islam MS. Defect chemistry and proton-dopant association in BaZrO 3 and BaPrO 3. Journal of Materials Chemistry 2010;20:6258-64.
[8] Malavasi L. Role of defect chemistry in the properties of perovskite manganites. Journal of Materials Chemistry 2008;18:3295-308.
[9] Tsekouras G, Irvine JT. The role of defect chemistry in strontium titanates utilised for high temperature steam electrolysis. Journal of Materials Chemistry 2011;21:9367-76.
[10] Hooker MW. Properties of PZT-Based piezoelectric Ceramics between-150 and 250 C. 1998.
[11] Jaffe B, Cook W, Jaffe H. Piezoelectric Ceramics Academic. New York 1971:115.
[12] Daniles J, Wernicke R. Defect chemistry and electrical conductivity of doped barium titanate ceramics (Part V): New aspects of an improved PTC model [J]. Philips Res Rep 1976;36:544-59.
[13] Hennings D, Rosenstein G. Temperature‐Stable Dielectrics Based on Chemically Inhomogeneous BaTiO3. Journal of the American Ceramic Society 1984;67:249-54.
[14] Raymond M, Smyth D. Defect chemistry and transport properties of Pb (Zr1/2Ti1/2) O3. Integrated Ferroelectrics 1994;4:145-54.
[15] Raengthon N, Brown-Shaklee HJ, Brennecka GL, Cann DP. Dielectric properties of BaTiO3–Bi (Zn1/2Ti1/2) O3–NaNbO3 solid solutions. Journal of Materials Science 2013;48:2245-50.
[16] Huang C-C, Cann DP. Phase transitions and dielectric properties in Bi (Zn 1/2 Ti 1/2) O 3-BaTiO 3 perovskite solid solutions. journal of Applied Physics 2008;104:024117--4.
[17] Raengthon N, Cann DP. High temperature electronic properties of BaTiO3–Bi (Zn1/2Ti1/2) O3–BiInO3 for capacitor applications. journal of Electroceramics 2012;28:165-71.
[18] Raengthon N, Sebastian T, Cumming D, Reaney IM, Cann DP. BaTiO3‐Bi (Zn1/2Ti1/2) O3‐BiScO3 Ceramics for High‐Temperature Capacitor Applications. Journal of the American Ceramic Society 2012;95:3554-61.
[19] Kumar N, Ionin A, Ansell T, Kwon S, Hackenberger W, Cann DP. Multilayer ceramic capacitors based on relaxor BaTiO3-Bi (Zn1/2Ti1/2) O3 for temperature stable and high energy density capacitor applications. Applied Physics Letters

2015;106:252901.
[20] Kumar N, Cann DP. Resistivity Enhancement and Transport Mechanisms in (1 − x)BaTiO3–xBi(Zn1/2Ti1/2)O3 and (1 − x)SrTiO3–xBi(Zn1/2Ti1/2)O3. Journal of the American Ceramic Society 2015;98:2548-55.
[21] Chan NH, Smyth D. Defect chemistry of BaTiO3. Journal of The Electrochemical Society 1976;123:1584-5.
[22] Choi DH, Baker A, Lanagan M, Trolier-McKinstry S, Randall C. Structural and Dielectric Properties in (1−x)BaTiO3–xBi(Mg1/2Ti1/2)O3 Ceramics ($0.1 \leq x \leq 0.5$) and Potential for High-Voltage Multilayer Capacitors. Journal of the American Ceramic Society 2013;96:2197-202.
[23] Ogihara H, Randall CA, Trolier‐McKinstry S. High‐Energy Density Capacitors Utilizing 0.7 BaTiO3‐0.3 BiScO3 Ceramics. Journal of the American Ceramic Society 2009;92:1719-24.
[24] Irvine JT, Sinclair DC, West AR. Electroceramics: characterization by impedance spectroscopy. Advanced Materials 1990;2:132-8.
[25] Sinclair DC. Characterization of Electro-materials using ac Impedance Spectroscopy. Boletín de la Sociedad Española de Cerámica y Vidrio 1995;34:55-65.
[26] Smyth DM. The defect chemistry of metal oxides. The Defect Chemistry of Metal Oxides, by DM Smyth, pp 304 Foreword by DM Smyth Oxford University Press, Jun 2000 ISBN-10: 0195110145 ISBN-13: 9780195110142 2000;1.
[27] Yoo H-I, Song C-R, Lee D-K. BaTiO3− δ: defect structure, electrical conductivity, chemical diffusivity, thermoelectric power, and oxygen nonstoichiometry. Journal of electroceramics 2002;8:5-36.
[28] Clark I, Marques F, Sinclair D. The influence of grain boundary impedances on the p-type conductivity of undoped BaTiO< sub> 3</sub> ceramics. Journal of the European Ceramic Society 2002;22:579-83.
[29] Müller A, Härdtl K. Ambipolar diffusion phenomena in BaTiO3 and SrTiO3. Applied Physics A 1989;49:75-82.
[30] Ren P, Masó N, Liu Y, Ma L, Fan H, West AR. Mixed oxide ion and proton conduction and p-type semiconduction in BaTi 0.98 Ca 0.02 O 2.98 ceramics. Journal of Materials Chemistry C 2013;1:2426-32.
[31] Han YH, Appleby JB, Smyth DM. Calcium as an acceptor impurity in BaTiO3. Journal of the American Ceramic Society 1987;70:96-100.
[32] Gil Escrig L, Prades M, Beltrán H, Cordoncillo E, Masó N, West AR. Voltage‐Dependent Bulk Resistivity of SrTiO3: Mg Ceramics. Journal of the American Ceramic Society 2014.
[33] Sinclair DC. The dramatic influence of A-site non-stoichiometry on the electrical conductivity and conduction mechanisms in the perovskite oxide Na0. 5Bi0. 5TiO3. Chemistry of Materials 2014.
[34] TRIAMNAK N, BRENNECKA GL, BROWN-SHAKLEE HJ, RODRIGUEZ MA, CANN DP. Phase formation of BaTiO 3–Bi (Zn 1/2 Ti 1/2) O 3 perovskite ceramics. Journal of the Ceramic Society of Japan 2014;122:260-6.
[35] Sakuma H, Hashizume H, Yamanaka A. Bi ordering in high-temperature structures of BaBiO3-x. Acta Crystallographica Section B: Structural Science 1990;46:693-8.
[36] Shahtahmassebi N, Hosseini M. Band structure of tetragonal BaTiO3. European Physical Journal B 2003;92.

[37] Schrade M, Fjeld H, Norby T, Finstad TG. Versatile apparatus for thermoelectric characterization of oxides at high temperatures. Review of Scientific Instruments 2014;85:103906.

9.4 DC-bias dependent impedance spectroscopy of $BaTiO_3$-$Bi(Zn_{1/2}Ti_{1/2})O_3$ ceramics

Nitish Kumar[1], Eric A. Patterson[2], Till Frömling[2] and David P. Cann[1]

[1]Materials Science, School of Mechanical, Industrial, and Manufacturing Engineering, Oregon State University, Corvallis, Oregon, USA

[2]Institute of Materials Science, Technische Universität Darmstadt, Darmstadt, Germany

Published in

Journal of Materials Chemistry C

Vol. 4, 1782 (2016)

Abstract

This report discusses the voltage-stability of the dielectric and transport properties of $BaTiO_3$-$Bi(Zn_{1/2}Ti_{1/2})O_3$ (BT-BZT) ceramics which have shown excellent properties for emerging energy applications. For p-type $BaTiO_3$, the ceramics deviated from Ohm's law behavior at very low voltage levels along with a reversible drop in bulk resistivity by several orders of magnitude starting at bias fields as low as 0.1 kV/cm (~8 V). In contrast, n-type BT-BZT ceramics exhibited a small (i.e. less than one order of magnitude) increase in resistivity on application of small field levels. These data indicate a hole-generation mechanism which becomes active at a low voltage threshold. The bulk capacitance values calculated using AC impedance spectroscopy, however, were relatively unaffected (<15% change) by this application of a DC bias (up to ~0.25 kV/cm). These findings provide important insights into the electric transport mechanisms in BT-based ceramics.

Main Text

Barium titanate ($BaTiO_3$ or BT) has been the subject of intense research for more than six decades and it remains the cornerstone of the capacitor industry today.[1] Pure BT should be highly insulating due its large band gap, however, small amounts of impurity dopants can significantly affect its electrical properties. Intentional doping has been used to tailor its properties and make it better suited for devices which have special requirements like a temperature-stable permittivity, linear dielectric response with electric field, and enhanced breakdown strength.[2-4] Unintentional doping may also arise due to unavoidable acceptor impurities that are concomitant with titania precursors,

incomplete re-oxidation during processing and other mechanisms. Another common approach to modify the properties of BT is to formulate solid solutions with other perovskites. This includes bismuth-based perovskites which have been the subject of a number of recent studies.[5-8]

It has been demonstrated in recent years that the $BaTiO_3$-$Bi(Zn_{1/2}Ti_{1/2})O_3$ (BT-BZT) ceramics have excellent properties (relative dielectric constant > 1000 with negligible temperature dependence over a wide temperature range, high breakdown strength) that enable the material to be used for high energy density and high temperature applications.[5, 9-11] Furthermore, multilayer ceramic capacitors based on BT-BZT have energy density values that approach ~3 J/cm^3, which is superior to most commercially available devices (< 2 J/cm^3) at comparable fields.[9-12] In an attempt to study the underlying defect chemistry, it was also found that upon addition of small amounts of BZT, the p-type behavior of BT changed to intrinsic n-type, and this change was also accompanied by a more than two order of magnitude increase in resistivity values.[13, 14] The p-type behavior in BT and other similar perovskites is often attributed to low-valence contaminants which come with precursors and frozen-in cation vacancies.[15-17] The glow discharge mass spectroscopy (Evans Analytical Group, USA) performed on BT samples used in this study indicated low levels of acceptor contamination from Na (~0.1 atom%) and Fe (~0.02 atom%), which may be one of the reasons for its observed p-type behavior.

Even though there are numerous reports of AC impedance spectroscopy on BT-based ceramics, studies involving the effects of DC bias are quite rare.[18, 19] In this report, the effect of a small DC bias on the resistivity and capacitance has been studied

for stoichiometric solid solutions of BT-BZT ceramics, none of which were intentionally doped. It will be shown that while for BT there is a significant defect-related change in conduction on applying a bias, for BZT-containing ceramics the conductivity remained comparatively stable. This represents an important result from the point of view of the fundamental defect chemistry as such small fields are not expected to alter the carrier concentration in these insulating ceramics. It also helps establish a relationship between traditional DC measurements that are used to study transport properties and AC impedance spectroscopy techniques.

The details for the preparation of polycrystalline BT, $0.97BaTiO_3$-$0.03Bi(Zn_{1/2}Ti_{1/2})O_3$ (BT-3BZT) and $0.925BaTiO_3$-$0.075Bi(Zn_{1/2}Ti_{1/2})O_3$ (BT-7.5BZT) ceramics can be found elsewhere.[13] For electrical measurements, Pt was sputtered on both sides of the sintered pellets. Some measurements were repeated with Ag and Au-Pd electrodes. The temperature dependent DC measurements (25 °C – 500 °C) were performed at electric field levels up to ~1.5 kV/cm using a high voltage source (Keithley 237 High Voltage Source Measure Unit, USA) and a high temperature measurement cell (NorECs AS ProbostatTM, Norway). For each measurement, the currents were applied and increased logarithmically and the corresponding voltages were measured. The impedance measurements were performed using a home-built high-temperature sample holder and an impedance analyzer (Novocontrol Technologies, Montabaur, Germany) with which a DC bias could be applied additional to the AC voltage. The WinDETA impedance measurement program was used to collect the data over the frequency range of 5 MHz to 0.1 Hz, using an oscillating voltage of 0.1 V and ZView software (Scribner Associates) was used for data analysis. The AC impedance spectroscopy was performed on all the

three samples in the temperature range 200 °C – 500 °C under a DC bias ranging from 0 V to 20 V (~0.25 kV/cm) with 2 V increments.

All compositions exhibited a single perovskite phase within the resolution of the laboratory XRD instrument used and were suitably dense (>95% of theoretical density by Archimedes method).[13] Figure 9.4.1 shows the voltage-current behavior of undoped BT and BT-BZT ceramics at ~ 200 °C and similar behavior was observed at all other temperatures examined between 25 °C-500 °C. Highly insulating ceramics are expected to follow Ohm's law at low fields, and the BZT-containing ceramics did appear to have an appropriate linear voltage-current (V-I) response. For the undoped BT samples, however, the response was not linear even at fields as low as 0.1 kV/cm, as can be seen in the inset of Figure 9.4.1(a). At the same field, the current levels were also significantly higher than BZT-containing samples, which should be a consequence of the lower resistivity values of BT. However, DC measurements alone were not sufficient to determine if non-linearity was caused by extrinsic factors like grain boundaries, electrodes, *etc*., or if it was an effect intrinsic to the bulk of the ceramics.

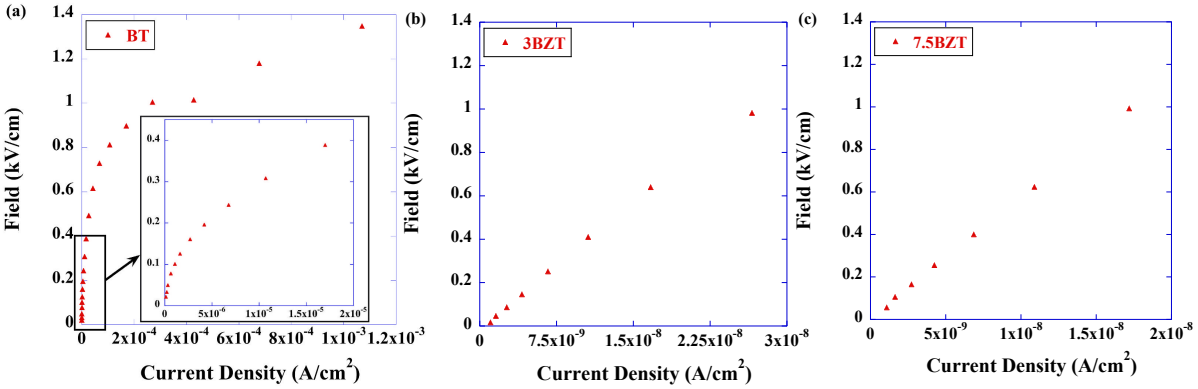

Figure 9.4.1. DC voltage-current characteristics of (a) BT, (b) BT-3BZT and (c) BT-7.5BZT ceramics at ~200 °C.

There are numerous reports on V-I characteristics of BT and other ferroelectric ceramics in the literature, and majority of them employ DC techniques like the one used for Fig. 9.4.1 in this study.[20-25] Especially for BT, in the absence of any major concentration gradient, it is a commonly accepted understanding that V-I characteristics should obey Ohm's law at lower fields before becoming a complex function of factors such as voltage level, energy level of traps, concentration and mobility of carriers, sample thickness, choice of electrodes and other factors at higher fields.[20-30] In general, the relationship $I \sim V^a$ is obeyed, where $a \sim 1$ for Ohm's law and $a > 1$ for higher field levels. There are several theories to explain the typical non-Ohmic behavior in BT, which include a space charge limited conduction with or without traps, quantum mechanical tunneling from the cathode to the conduction band, tunneling through Schottky barriers between grains, and other theories.[22, 27, 30-32] In a series of reports by Tredgold *et al.* on single crystal BT and $SrTiO_3$, the non-linearity in V-I characteristics was attributed to hole injection from the Au anode.[26-29] However, it should be noted that all of these proposed models explain non-Ohmic behavior only at higher field levels, meaning that the non-linear regime is always preceded by an Ohmic linear region.

For the BT sample in Figure 9.4.1(a), there was no indication of a linear regime at all. It is seemingly inconsistent with the theories proposed in the previous discussion, all of which expect a linear response before the onset of non-linearity. It is possible that linear regime may be observed at much lower current levels than what was measured in this study. Absence of linearity may be a consequence of orders of magnitude higher conductivity in BT as compared to BZT-ceramics (Figure 9.4.1, where currents were significantly higher for BT at same fields) at these temperatures and the limitations of the

instrument used.[13] However, this is also not the first time a non-linear behavior at low voltages in BT or similar ceramics has been reported. Hamann *et al.,* Baron *et al.* and Morrison *et al.* all observed non-linear behavior at very low voltages (~$6x10^{-5}$ kV/cm) and attributed it to presence of trap states.[20, 33, 34] In a study by Tennery *et al*., there was no linear V-I response above 1 V in a 1.5 mm thick (~0.007 kV/cm) rare-earth doped BT ceramic (0.15-0.3% doping level) and it was attributed to Joule heating caused by DC measurements.[23] For the BZT-containing ceramics in this study, on the other hand, the response appeared to be largely Ohmic with only minor deviations from linearity.

Based on the previous discussion, there are several potential explanations for the V-I behavior of BT-BZT ceramics. AC impedance spectroscopy was chosen to investigate the specific mechanism that is dominating conduction in these materials. Impedance spectroscopy is a powerful tool that can deconvolute long-range bulk conduction from grain boundary, electrode-interactions, inhomogeneity and other effects. The measurements were performed on samples of all three compositions over the temperature range 200 °C – 500 °C under a DC bias ranging from 0 V to 20 V (~0.25 kV/cm). A characteristic impedance data set taken at 300 °C is presented in Figure 9.4.2, the data at the other temperatures followed similar trends. Figure 9.4.2(a) shows the data for BT where clearly resolved semicircles could be observed. Along with a high frequency bulk component (inset), a low frequency grain boundary component was also present. The attribution of the lower frequency arc to the grain boundary was supported by the fact that it was observed independently of the electrodes used (Pt, Ag, Au-Pd) and therefore could not have been a result of electrode-interactions. Figure 9.4.2(a) and 2(d) show the effect of DC bias on transport properties and one can notice the orders of

magnitude decrease in resistivity on applying a bias. A voltage-dependent resistivity is often described by a double Schottky barrier (space charge layers) at the grain boundaries, where a positively charged grain boundary core is compensated by the negative charge of ionized impurities or dopants in the depleted space charge layers adjacent to the core.[35] Such grain boundaries have non-linear V-I characteristics and their resistivity values drop with applied bias. In the case of doped titanate perovskites, some authors have reported the barrier height for grain boundaries to be less than even 1 V.[35, 36] For 0.2 mol% Fe-doped $SrTiO_3$, the barrier height was reported to be ~0.63 V and Jonker estimated the barrier height to be ~0.65 V for a jump in resistivity of about four orders in magnitude.[35, 36] Therefore, the voltage levels applied for this report may be enough to alter grain boundary resistivity values. Moreover, a blocking contact can also give rise to a Schottky barrier at the electrode-ceramic interface.[37] However, as mentioned earlier, that is unlikely to be the case here since the bias-dependence was observed irrespective of the type of electrode used. In the data for BT (Figure 9.4.2(a) and 2(d)), the DC resistivity values rapidly decreased on application of a small bias, which is consistent with Figure 9.4.1(a), where the slope continuously decreased as the current levels increased nearly leading to a saturation of electric field. However, the Schottky barriers are unlikely to be the sole factors in the voltage dependence of the transport properties in this case. It is important to note that the grain boundary component of the resistivity did indeed decrease with increased bias field for BT, as one would predict if Schottky barriers were present. However, for the data here, high frequency bulk resistivity of the BT sample (shown in the inset of Figure 9.4.2(a) and in Figure 9.4.2(d)) also decreased over the same range of DC bias increase. This indicated that the inherent

long-range conduction of the bulk itself simultaneously increased on application of small DC-bias for BT, which was distinct from the extrinsic factors including the grain boundary and electrodes.

While the resistivity values of BT decreased on application of a small bias, for the BZT-containing ceramics there was a minor increase in resistivity values as can be seen in Figures 9.4.2(b,e) and 9.4.2(c,f). Both of these phenomena were reversible, i.e. the resistivity came back to their unbiased values soon after the DC-bias was removed. The increase in resistivity in the case of BZT-ceramics, however, was not as extensive as the decrease observed for BT. Again, Schottky barriers cannot explain an increase in resistivity, as a bias should always lead to a decrease in barrier height and an increase in conductivity.

As previously mentioned, the BZT-containing ceramics possess n-type majority charge carriers as opposed to the p-type, nominally pure BT.[13] The bias-dependence of the resistivity in these various samples then indicates possible hole-creation occurring during application of a small DC-bias. If the point defect 'A' is a presumed source of holes ($h^{\cdot}$), a DC bias can lead to an increase in conductivity in p-type ceramics by increasing carrier concentration (Equation 9.4.1a) or a decrease in the conductivity in n-type ceramics by reducing electron (e') concentration (Equation 9.4.1b) as given by:

$$A^X \rightarrow A' + h^{\cdot} \qquad \text{Eq. 9.4.1a}$$

$$A^X + e' \rightarrow A' \qquad \text{Eq. 9.4.1b}$$

The source of holes could be ejection from trap states as suggested by Hamann *et al.*[33], reducible Ti^{4+} cations, a decrease in oxygen vacancy concentration, among other possibilities. This change in resistivity under DC bias during AC impedance

measurements was very recently also observed by West *et al.* in n- and p-type doped perovskites.[18, 19, 38-41] In Mg-doped $SrTiO_3$ and Zn-doped $BaTiO_3$, both p-type ceramics, it was shown that the bulk resistivity decreased on application of DC bias, similar to the p-type BT in this study.[18, 38] In n-type Mn-doped $BaTiO_3$, the opposite phenomenon was observed, where the bulk resistivity increased on applying a DC bias (10 V).[42] It was proposed that on applying small DC bias, the under-bonded oxygen in the regions neighboring acceptor impurities could be ionized and the resulting electrons could become trapped at surface states, thus explaining the change in resistivity. The parameter 'A' in Equation 9.4.1b could thus be interpreted as originating from these under-bonded oxygen states in this case. These results also suggest that similar voltage conditions should be employed while making comparisons of transport properties of different ceramics, especially for doped systems.

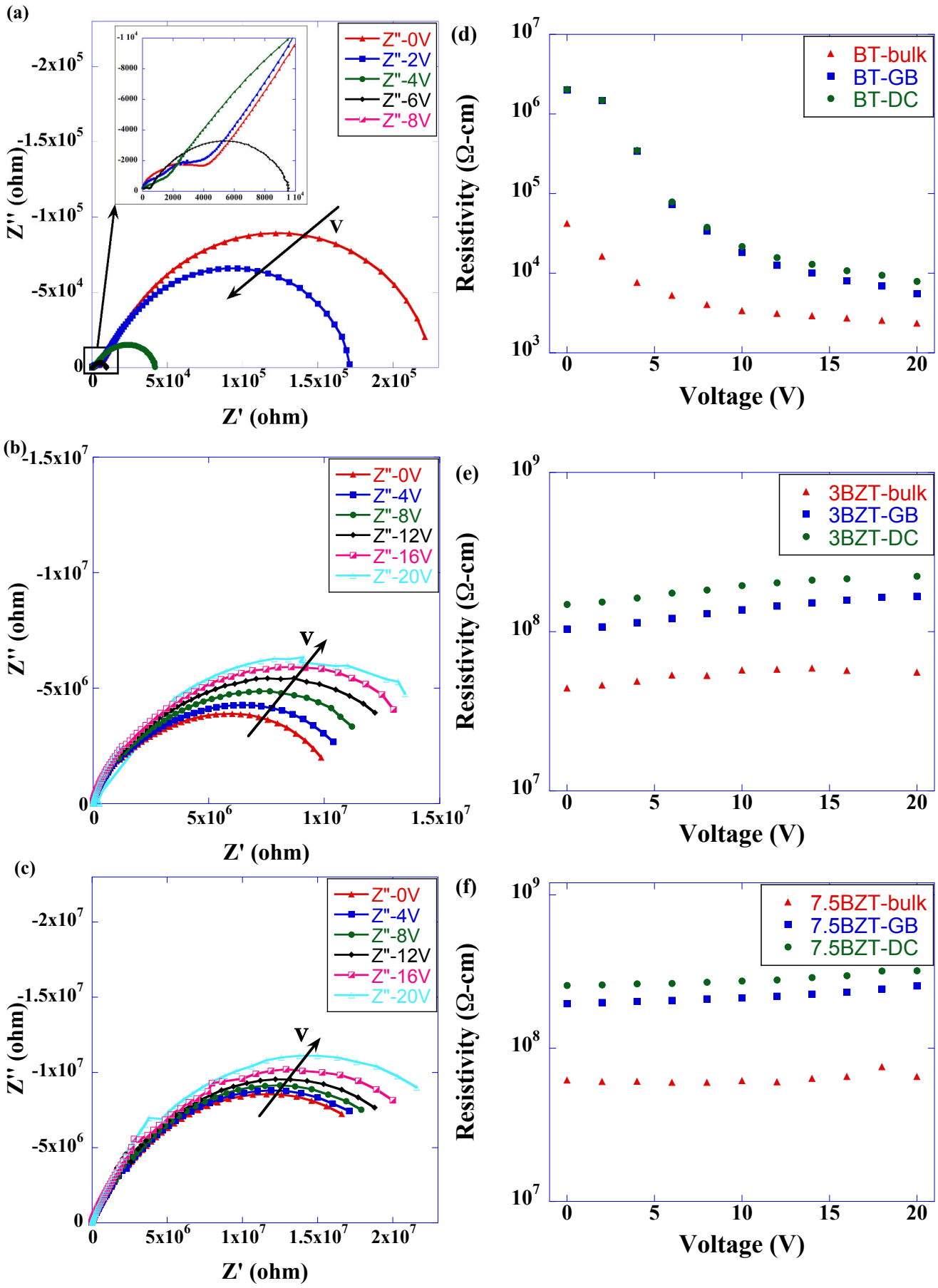
(a)
Z''-0V
Z''-2V
Z''-4V
Z''-6V
Z''-8V
V
Z'' (ohm)
Z' (ohm)
(b)
Z''-0V
Z''-4V
Z''-8V
Z''-12V
Z''-16V
Z''-20V
V
Z'' (ohm)
Z' (ohm)
(c)
Z''-0V
Z''-4V
Z''-8V
Z''-12V
Z''-16V
Z''-20V
V
Z'' (ohm)
Z' (ohm)
(d)
BT-bulk
BT-GB
BT-DC
Resistivity (Ω-cm)
Voltage (V)
(e)
3BZT-bulk
3BZT-GB
3BZT-DC
Resistivity (Ω-cm)
Voltage (V)
(f)
7.5BZT-bulk
7.5BZT-GB
7.5BZT-DC
Resistivity (Ω-cm)
Voltage (V)

Figure 9.4.2 (a) Complex plane plots for BT with DC bias between 0-8 V at 300 °C, (b) Complex plane plots for 3BZT with DC bias between 0-20 V at 300 °C, (c) Complex plane plots for 7.5BZT with DC bias between 0-20 V at 300 °C. Variation in bulk, grain boundary and DC resistivities with DC bias for (d) BT, (e) 3BZT and (f) 7.5BZT ceramics. The DC resistivity reported here was obtained from Z* complex plane plots by extrapolating the AC impedance data on the low-frequency side to the x-axis intercept.

Figure 9.4.3 demonstrates the change in the imaginary electrical modulus at a representative data set at 300 °C with a bias voltage as calculated from AC impedance spectroscopy data. Normally the peak value of $M''(f)$ spectra is inversely proportional to the capacitance of the corresponding process.[19] The change in the modulus spectra for BT was less obvious with respect to voltage, as compared to impedance. The peak value corresponding to the high frequency bulk component increased by ~15% and also shifted towards higher frequency as the bias was increased to 20 V (~0.25 kV/cm), suggesting a drop in bulk capacitance. For the BZT-containing ceramics, there was hardly any observable difference in bulk capacitance with application of DC-bias. Similar small variations in capacitance on application of a low bias have been previously reported as well.[19, 43] A similar shift of the modulus peak maximum to higher frequency was reported for acceptor doped $CaTiO_3$.[19] Consistent with these reports and based on our data for BT-BZT ceramics, it is suggested that the polarization mechanisms were largely unaffected by application of small DC bias (*i.e.* $< 0.1\ E_C$), unlike their conduction counterparts.

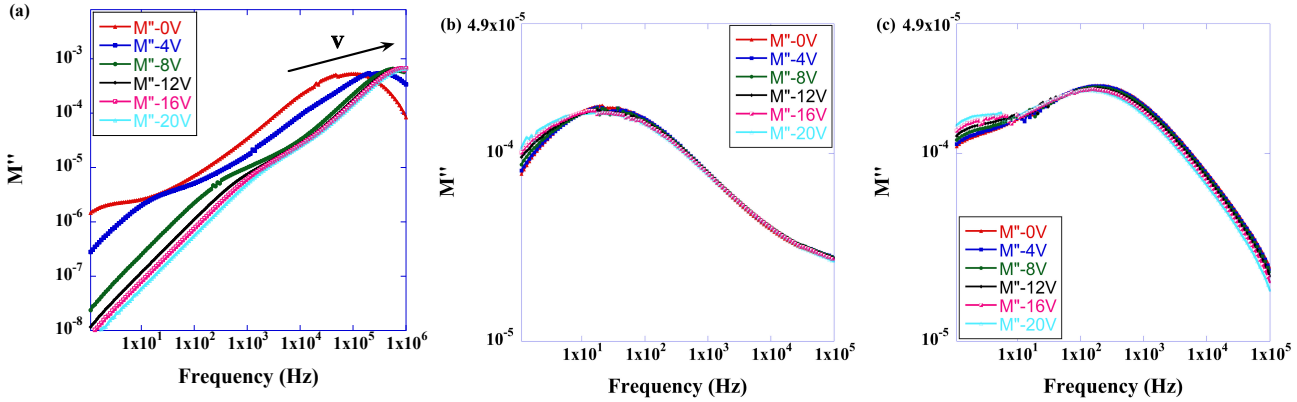

Figure 9.4.3. Imaginary modulus as a function of DC-bias (V) for (a) BT, (b) BT-3BZT and (c) BT-7.5BZT ceramics.

In summary, the results suggested fundamentally different underlying defect mechanisms in BT-BZT ceramics as compared to BT, and it was shown that small bias fields could induce a defect chemistry-related change in long-range bulk conduction in BT-BZT ceramics without affecting the polarization mechanisms significantly. It is proposed that the observed non-linearity in V-I characteristics at low fields, which is often ascribed to extrinsic factors like Schottky barriers in case of BT-based systems, may also be a direct consequence of change in bulk transport properties. These results are also important for underlining the importance of using similar bias conditions and oscillating voltages while making comparisons of AC impedance data among different materials. The relatively stable voltage characteristics and higher resistivities of BZT-containing ceramics may have important implications in the use of capacitors for energy applications.

This material is based upon work supported by the National Science Foundation under Grant No. DMR-1308032. The authors would like to acknowledge Jürgen Rödel

and Deutsche Forschungsgemeinschaft (DFG) through SFB595 for their help and support.

References

[1] Von Hippel A. Ferroelectricity, domain structure, and phase transitions of barium titanate. Reviews of Modern Physics 1950;22:221.
[2] Daniles J, Wernicke R. Defect chemistry and electrical conductivity of doped barium titanate ceramics (Part V): New aspects of an improved PTC model [J]. Philips Research Reports 1976;36:544-59.
[3] Hennings D, Rosenstein G. Temperature‐Stable Dielectrics Based on Chemically Inhomogeneous BaTiO3. Journal of the American Ceramic Society 1984;67:249-54.
[4] Jaffe B, Cook W, Jaffe H. Piezoelectric Ceramics1971.
[5] Huang C-C, Cann DP. Phase transitions and dielectric properties in Bi (Zn 1/2 Ti 1/2) O 3-BaTiO 3 perovskite solid solutions. Journal of Applied Physics 2008;104:024117--4.
[6] Zhang H, Chen C, Deng H, Ren B, Zhao X, Lin D, et al. Ultrahigh ferroelectric response in Fe modified 0.95 (Na 1/2 Bi 1/2) TiO 3-0.05 BaTiO 3 single crystals. Journal of Materials Chemistry C 2014;2:10124-8.
[7] Choi DH, Baker A, Lanagan M, Trolier‐McKinstry S, Randall C. Structural and Dielectric Properties in (1− x) BaTiO3–xBi (Mg1/2Ti1/2) O3 Ceramics (0.1≤ x≤ 0.5) and Potential for High‐Voltage Multilayer Capacitors. Journal of the American Ceramic Society 2013;96:2197-202.
[8] Ogihara H, Randall CA, Trolier‐McKinstry S. High‐Energy Density Capacitors Utilizing 0.7 BaTiO3–0.3 BiScO3 Ceramics. Journal of the American Ceramic Society 2009;92:1719-24.
[9] Raengthon N, Brown-Shaklee HJ, Brennecka GL, Cann DP. Dielectric properties of BaTiO3–Bi (Zn1/2Ti1/2) O3–NaNbO3 solid solutions. Journal of Materials Science 2013;48:2245-50.
[10] Raengthon N, Cann DP. High temperature electronic properties of BaTiO3–Bi (Zn1/2Ti1/2) O3–BiInO3 for capacitor applications. journal of Electroceramics 2012;28:165-71.
[11] Raengthon N, Sebastian T, Cumming D, Reaney IM, Cann DP. BaTiO3‐Bi (Zn1/2Ti1/2) O3‐BiScO3 Ceramics for High‐Temperature Capacitor Applications. Journal of the American Ceramic Society 2012;95:3554-61.
[12] Kumar N, Ionin A, Ansell T, Kwon S, Hackenberger W, Cann DP. Multilayer ceramic capacitors based on relaxor BaTiO3-Bi (Zn1/2Ti1/2) O3 for temperature stable and high energy density capacitor applications. Applied Physics Letters 2015;106:252901.
[13] Kumar N, Cann DP. Resistivity enhancement and transport mechanisms in (1-x)BaTiO3-xBi(Zn1/2Ti1/2)O3 and (1-x)SrTiO3-xBi(Zn1/2Ti1/2)O3. Journal of American Ceramics Society 2015
;98:2548-55.
[14] Kumar N, Patterson EA, Frömling T, Cann DP. Bipolar conduction mechanisms in BaTiO3-Bi(Zn1/2Ti1/2)O3 ceramics. Submitted to Journal of American Ceramics Society Manuscript in preparation.
[15] Chan NH, Smyth D. Defect chemistry of BaTiO3. Journal of The Electrochemical Society 1976;123:1584-5.
[16] Tsur Y, Randall CA. Point defect concentrations in barium titanate revisited. Journal of the American Ceramic Society 2001;84:2147-9.

[17] Moos R, Härdtl KH. Dependence of the intrinsic conductivity minimum of SrTiO3 ceramics on the sintering atmosphere. Journal of the American Ceramic Society 1995;78:2569-71.
[18] Gil Escrig L, Prades M, Beltrán H, Cordoncillo E, Masó N, West AR. Voltage‐Dependent Bulk Resistivity of SrTiO3: Mg Ceramics. Journal of the American Ceramic Society 2014.
[19] Zhang Q-L, Masó N, Liu Y, Yang H, West AR. Voltage-dependent low-field resistivity of CaTiO 3: Zn ceramics. Journal of Materials Chemistry 2011;21:12894-900.
[20] Morrison F, Zubko P, Jung D, Scott J, Baxter P, Saad M, et al. High-field conduction in barium titanate. Applied Physics Letters 2005;86:2903.
[21] Cann D, Randall C. Electrode effects in positive temperature coefficient and negative temperature coefficient devices measured by complex‐plane impedance analysis. Journal of Applied physics 1996;80:1628-32.
[22] Mallick Jr G, Emtage P. Current‐Voltage Characteristics of Semiconducting Barium Titanate Ceramic. Journal of Applied Physics 1968;39:3088-94.
[23] Tennery VJ, Cook RL. Investigation of Rare‐Earth Doped Barium Titanate. Journal of the American Ceramic Society 1961;44:187-93.
[24] Leret P, Fernandez JF, De Frutos J, Fernandez-Hevia D. Nonlinear I–V electrical behaviour of doped CaCu 3 Ti 4 O 12 ceramics. Journal of the European Ceramic Society 2007;27:3901-5.
[25] Osak W, Tkacz K. Investigation of IV characteristics in polycrystalline BaTiO3. Journal of Physics D: Applied Physics 1989;22:1746.
[26] Branwood A, Hughes O, Hurd J, Tredgold R. Evidence for space charge conduction in barium titanate single crystals. Proceedings of the Physical Society 1962;79:1161.
[27] Branwood A, Tredgold R. The electrical conductivity of barium titanate single crystals. Proceedings of the Physical Society 1960;76:93.
[28] Cox G, Tredgold R. Double space charge injection in solids. Physics Letters 1963;4:199-200.
[29] Cox G, Tredgold R. Time dependence of the electrical conductivity in strontium titanate single crystals. British Journal of Applied Physics 1965;16:427.
[30] MacChesney J, Potter J. Factors and mechanisms affecting the positive temperature coefficient of resistivity of barium titanate. Journal of the American Ceramic Society 1965;48:81-8.
[31] Yang G, Lian G, Dickey E, Randall C, Barber D, Pinceloup P, et al. Oxygen nonstoichiometry and dielectric evolution of BaTiO3. Part II—insulation resistance degradation under applied dc bias. Journal of applied physics 2004;96:7500-8.
[32] Hölbling T, Waser R. Simulation of the charge transport across grain boundaries in p-type SrTiO3 ceramics under dc load: Debye relaxation and dc bias dependence of long-term conductivity. Journal of applied physics 2002;91:3037-43.
[33] Hamann C, Burghardt H, Frauenheim T. Electrical Conduction Mechanisms in Solids: Vch Pub; 1988.
[34] Willardson K, Beer AC, Rose A. Semiconductors and Semimetals, Vol 6: Injection Phenomena. Physics Today 2008;24:51-2.
[35] Rodewald S, Fleig J, Maier J. Microcontact Impedance Spectroscopy at Single Grain Boundaries in Fe‐Doped SrTiO3 Polycrystals. Journal of the American Ceramic Society 2001;84:521-30.

[36] Jonker G. Some aspects of semiconducting barium titanate. Solid-State Electronics 1964;7:895-903.
[37] Heinen B, Waser R. Influence of the thickness and area of NiCr/Ag electrodes on the characteristics of BaTiO3-ceramic based positive-temperature-coefficient thermistors. Journal of Materials Science 1998;33:4603-8.
[38] Beltrán H, Prades M, Masó N, Cordoncillo E, West AR. Voltage‐Dependent Low‐Field Bulk Resistivity in BaTiO3: Zn Ceramics. Journal of the American Ceramic Society 2010;93:500-5.
[39] Ren P, Masó N, Liu Y, Ma L, Fan H, West AR. Mixed oxide ion and proton conduction and p-type semiconduction in BaTi 0.98 Ca 0.02 O 2.98 ceramics. Journal of Materials Chemistry C 2013;1:2426-32.
[40] Prades M, Masó N, Beltrán H, Cordoncillo E, West AR. Field enhanced bulk conductivity of BaTiO 3: Mg ceramics. Journal of Materials Chemistry 2010;20:5335-44.
[41] Beltrán H, Prades M, Masó N, Cordoncillo E, West AR. Enhanced conductivity and nonlinear voltage–current characteristics of nonstoichiometric BaTiO3 ceramics. Journal of the American Ceramic Society 2011;94:2951-62.
[42] Prades M, Beltrán H, Cordoncillo E, Alonso PJ, Masó N, West AR. Non‐ohmic phenomena in Mn‐doped BaTiO3. Physica Status Solidi (a) 2012;209:2267-72.
[43] Liou J-W, Chiou B-S. Effect of direct-current biasing on the dielectric properties of barium strontium titanate. Journal of the American Ceramic Society 1997;80:3093-9.

9.5. Synthesis and electrical properties of $BaBiO_3$ and $BaTiO_3$-$BaBiO_3$ ceramics

Nitish Kumar[1], Stephen L. Golledge[2] and David P. Cann[1]

1. Materials Science, School of Mechanical, Industrial, and Manufacturing Engineering, Oregon State University, Corvallis, Oregon 97331, USA
2. CAMCOR Surface Analytical Facility, University of Oregon, Eugene, Oregon 97403, USA

Abstract

Ceramics of the composition $BaBiO_3$ were sintered in oxygen to obtain a single phase with monoclinic *I*2/m symmetry as suggested by high-resolution x-ray diffraction. X-ray photoelectron spectroscopy confirmed the presence of bismuth in two valence states – 3+ and 5+. Optical spectroscopy showed presence of a direct band gap at ~2.2 eV and a possible indirect band gap at ~0.9 eV. This combined with determination of the activation energy for conduction of 0.25 eV, as obtained from *ac* impedance spectroscopy, suggested that a polaron-mediated conduction mechanism was prevalent in $BaBiO_3$. The $BaBiO_3$ ceramics were crushed, mixed with $BaTiO_3$, and sintered to obtain $BaTiO_3$-$BaBiO_3$ solid solutions. All the ceramics had tetragonal symmetry and exhibited a normal ferroelectric-like dielectric response. Using *ac* impedance and optical spectroscopy, it was shown that resistivity values of $BaTiO_3$-$BaBiO_3$ were orders of magnitude higher than $BaTiO_3$ or $BaBiO_3$ alone, indicating a change in the fundamental defect equilibrium conditions. A shift in the site occupancy of Bi to the A-site is proposed to be the mechanism for the increased electrical resistivity.

Introduction

The $BaBiO_3$ (BB) has a distorted crystal structure with an ordered alternating Bi^{3+} and Bi^{5+}.[1, 2] At room temperature, this charge disproportionation and ordering coupled with tilting of BiO_6 corner-shared octahedra, result in a cell with monoclinic symmetry (*I2/m*).[1, 3] It was reported that BB only has out-of-phase tilting, denoted by $a^0b^-b^-$ and $a^-a^-a^-$ in Glazer's notation.[4, 5] There have been a number of reports on the compound BB, especially polycrystalline BB ceramics doped with acceptors such as potassium,

lead, and other additives, for potential use in high-temperature superconductor applications.[6-13] The transition from semiconducting behavior to superconducting behavior occurs with doping and the critical temperature (T_c) also depends upon the doping concentration. For Pb-doped BB, a maximum T_c of ~13 K has been observed[6], while for K-doped BB the value lies around 30 K.[7] These systems have been of significant interest because they lack magnetic ions in the structure and Bardeen-Cooper-Schrieffer (BCS) theory does not appear to suitably explain the occurrence of superconductivity in oxygen-containing superconductors. It has been suggested that a phonon-mediated electron pairing mechanism for superconductivity may be significant. These are also perovskite-based structures with presumable three-dimensional charge-transport, unlike two-dimensional transport which is the case for copper oxide-based superconductors.[14]

While doped BB has been studied primarily for superconductor applications, $BaBiO_3$-doped $BaTiO_3$ (BT-BB) solid solutions have been studied by researchers for use as positive temperature coefficient of resistivity (PTCR) devices.[15, 16] In one study, it was shown that the addition of BB increased the Curie point so that the PTCR effect was initiated above ~150 °C.[17] However, as will be seen in the present work, BT-BB solid solution were not observed to exhibit any significant shift in the Curie point.

This report is focused on BT-BB solid solutions for the purpose of understanding the influence of BB additions on the electrical properties. At the same time, it also helps understand the defect chemistry of BT-BiMO$_3$ class of ceramics, where M is a metal

cation. Research over recent years have shown that the BT-$Bi(Zn_{1/2}Ti_{1/2})O_3$-based and other similar ceramics have excellent dielectric properties and are well-suited for high temperature and high energy density applications.[18, 19] Their dielectric permittivity values remain stable with temperature and under *dc*-bias unlike pure $BaTiO_3$, and the insulation properties are also relatively insensitive to bias fields.[19-21] The resistivity values also improved by more than two orders of magnitude with the addition of $Bi(Zn_{1/2}Ti_{1/2})O_3$ to BT and the transport mechanism gradually shifted to n-type behavior as compared to defect-dominated p-type behavior for undoped $BaTiO_3$.[22, 23] This should be a result of a defect mechanism, which is equivalent to effective donor doping, and becomes activated with the addition of $Bi(Zn_{1/2}Ti_{1/2})O_3$ to BT. A similar behavior was also observed in the $SrTiO_3$-$Bi(Zn_{1/2}Ti_{1/2})O_3$ and BT-$BiScO_3$ systems as well.[24] One mitigating factor could be the formation of $BaBiO_3$ as an intermediate phase.[23] In an extensive phase formation study on BT- $Bi(Zn_{1/2}Ti_{1/2})O_3$ ceramics, $BaBiO_3$ was detected at intermediate temperatures during processing, before becoming invisible to x-ray diffraction (XRD) techniques at higher calcination temperatures.[25] However, if an appreciable concentration of bismuth remains on B-site in the final BT-$Bi(Zn_{1/2}Ti_{1/2})O_3$ perovskite phase, it may have a significant influence on the defect equilibrium conditions. Direct approaches to verify the presence of bismuth on the B-site in BT- $Bi(Zn_{1/2}Ti_{1/2})O_3$ and other similar ceramics through techniques such as x-ray photoelectron spectroscopy and x-ray absorption spectroscopy were largely inconclusive. In this article, BT-BB solid solutions were prepared with a small mole fractions of BB to study the resultant dielectric and transport properties, with an additional aim to provide an indirect means of understanding the origin of the transport properties of BT- $Bi(Zn_{1/2}Ti_{1/2})O_3$ and similar

ceramics. This work also includes a full structural characterization of the BB and BB-BT ceramics prepared in this study.

Experimental

Solid-state methods was used to prepare $BaBiO_3$ ceramics using the precursors $BaCO_3$ (Alfa Aesar, >99.8%) and Bi_2O_3 (Aldrich, >99.9%). The powders were mixed together in the proper stoichiometric ratio, ground using a vibratory mill for 6 hours and dried overnight in an oven (~80 °C). The powders were then calcined in alumina crucibles at 725 °C for 24 hours and then milled with ~3 wt% Rhoplex binder and dried again. Green pellets in the shape of thin discs were prepared by cold-pressing uniaxially at a pressure of ~200 MPa and then sintered in oxygen at 825 °C for 12 hours. It was difficult to achieve single phase on sintering in air, as will be seen later. To make solid solutions of $BaTiO_3$ and $BaBiO_3$, the sintered $BaBiO_3$ pellets were ground into powder form and then mixed with appropriate amounts of $BaTiO_3$ (Sakai Chemical Industry). The mixture was then milled with ~3 wt% Rhoplex binder and dried. The green pellets were prepared using similar conditions as described above, and then sintered in air on a bed of calcined powder in closed alumina crucibles. The compositions investigated were (1-x)BT-xBB, where x = 0.001, 0.003, 0.005, 0.01 and 0.2, and will be henceforth abbreviated as 0.1BB, 0.3BB, 0.5BB, 1BB and 2BB respectively. These compositions were sintered at 1050 °C for 4 hours, 1000 °C for 4 hours, 950 °C for 4 hours, 990 °C for 8 hours and 990 °C for 8 hours, respectively. For purposes of comparison, some bismuth-doped ceramics were also prepared with 0.3 mol% Bi (or 0.15 mol% Bi_2O_3) and 0.5 mol% Bi (or 0.25 mol% Bi_2O_3) added to $BaTiO_3$. For this, excess Bi_2O_3 was added to

$BaTiO_3$ powders, so as to achieve the above-mentioned doping levels. The powders were milled with 3 wt% binder, dried, and then green pellets were sintered at 1000 °C for 4 hour and 950 °C for 4 hours, respectively, on a bed of calcined powders. All the sintered pellets were polished to sub-millimeter thicknesses.

X-ray diffraction (XRD) (Bruker AXS D8 Discover, Madison, WI, USA) was performed on ground pellets for phase and crystal structure determination. High-resolution synchrotron powder diffraction data were collected on $BaBiO_3$ powders using beamline 11-BM at the Advanced Photon Source (APS), Argonne National Laboratory. An appropriate amount of the sample was loaded into a Kapton tube, sealed and mounted on the base provided by the 11-BM beamline of the APS. The diffraction experiments were carried out at room temperature using monochromatic synchrotron radiation of wavelength 0.413639 Å and a step size of 0.001°. The crystal structure was refined using the Rietveld refinement program GSAS-II.[26] The Chebyschev profile was used to fit the background and the number of background parameters used was 10. Parameters refined included peak-shape parameters, scale, lattice parameters, atomic positions, isotropic displacement parameters, thermal occupancies and others.

Prior to any electrical measurements, Ag electrodes were applied on both sides of the pellets and then fired at 700 °C for 30 min. For undoped $BaBiO_3$ ceramics, instead of Ag, Pt electrodes were used and with a firing temperature of 700 °C for 2 hours in oxygen. The pellets were placed in a high temperature measurement cell (NorECs AS ProbostatTM, Oslo, Norway) or low temperature environmental chamber (Delta Design 9023, California, USA) and the dielectric properties were measured using an LCR meter (Agilent 4284A, Santa Clara, CA, USA). An impedance analyzer (Solartron SI1260A

equipped with Solartron 1296A dielectric interface, Farnborough, UK) was used to measure the impedance in the frequency range 0.1 Hz to 1 MHz. The SMaRT impedance measurement software program was used to collect the data. The optical measurements were carried out on crushed sintered pellets over the wavelength range of 200-1100 nm at room temperature using an Ocean Optics HR4000 UV-Vis Spectrometer (Ocean Optics, Dunedin, FL) with a balanced deuterium/tungsten halogen source. X-ray Photoelectron Spectroscopy (XPS) spectra from the $BaBiO_3$ ceramics were acquired on a ThermoScientific ESCALAB 250 spectrometer located at the Center for Advanced Materials Characterization in Oregon (CAMCOR). Photoemission was stimulated by a beam of monochromatized Al Kα x-rays with a nominal spot size at the sample surface of 500μm. A low energy electron source was used for charge neutralization. The spectra were acquired at a pass energy of 20 eV (high resolution spectra) or 150 eV (survey spectra). Data analysis, including peak fitting, was performed with Avantage software, provided by the manufacturer.

Results and Discussion

Part 1. $BaBiO_3$

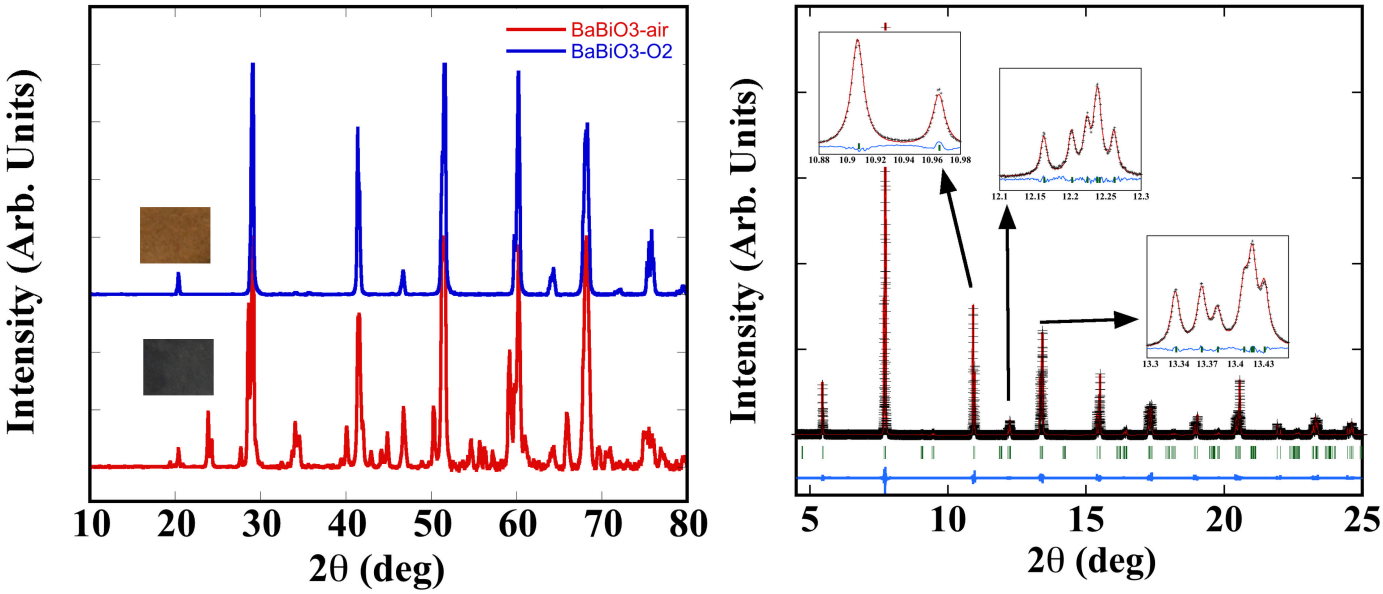

Fig. 9.5.1. (a) X-ray diffraction pattern of $BaBiO_3$ sintered in air (bottom) and oxygen (top). The square boxes show the color of the pellets after being sintered in air and oxygen. (b) Rietveld refinement of a high-resolution XRD pattern of $BaBiO_3$ sintered in oxygen. The data presented with (+) symbol is the observed data and the black curves are calculated intensities. The bottom-most curve (blue) is the difference between observed and calculated intensities.

Table 9.5.1. Parameters for *I*2/m space group from the Rietveld refinement.

	x	y	z	Occupancy	U_{iso} (Å^2)
Ba	0.4969(34)	0	0.2512(84)	0.999(3)	0.0039(6)
Bi(1)	0	0	0	1.021(6)	0.0001(1)
Bi(2)	0	0	0.5	1.023(4)	0.0001(8)
O(1)	-0.0637(33)	0	0.2420(46)	1	0.0119(5)
O(2)	0.2372(31)	0.2381(66)	0.0316(85)	1	0.0131(0)

Figure 9.5.1a shows the comparison between x-ray diffraction (XRD) patterns for the samples sintered in oxygen and air for the same temperature and time. The pellet which was sintered in air had much higher concentration of secondary phases and underscored the importance of oxygen partial pressure during processing of BB. The pellets were suitably dense after sintering and had density values greater than 94% of theoretical value, as measured via Archimedes' method. Figure 9.5.1b shows the room temperature high-resolution XRD pattern of $BaBiO_3$ sintered in oxygen, which was performed to confirm the phase purity and formation of $BaBiO_3$. Even within the detection limits of synchrotron radiation, no evidence of secondary phases was observed. Consistent with literature reports, a distorted perovskite structure with a monoclinic unit cell (*I*2/m) was used to fit the pattern.[3, 27, 28] The refinement resulted in a reasonably good fit as can be seen in the difference curve in Figure 9.5.1b (wR = 8.7%). The lattice parameters obtained were, a = 6.1865(7) Å, b = 6.1399(4) Å c = 8.6705(0) Å and β = 90.178°, and Table 9.5.1 shows the parameters obtained from the refinement – atomic coordinates, site occupancy and isotropic thermal parameters. All these parameters were within reasonable limits and corroborated the choice of unit cell and confirmed the phase purity of BB to be used later for fabricating the BT-BB solid solutions.

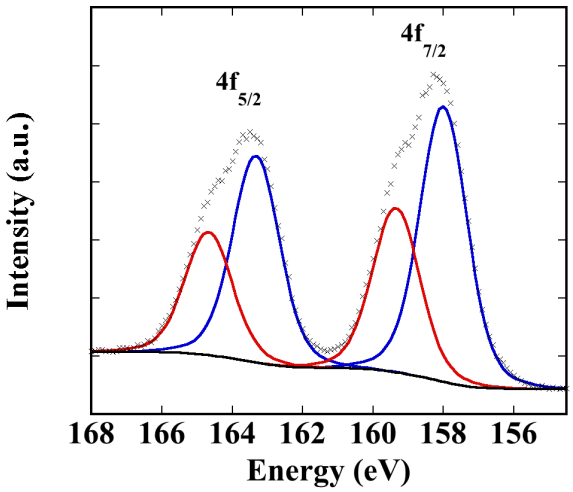

Fig. 9.5.2. X-ray photoelectron spectroscopy on powdered $BaBiO_3$ ceramics. The data shown with "x" symbols are actual data obtained from the experiment. The background and fitted peaks have also been indicated. The low intensity fitted peaks (red) are from Bi^{5+}.

Even though bismuth with two different valence states (Table 9.5.1) were used for the structural refinement above, x-ray diffraction may not be sensitive enough to properly differentiate between trivalent Bi^{3+} and pentavalent Bi^{5+}, which are the expected valence states of bismuth in BB.[27] To investigate the valence state of bismuth in BB, x-ray photoelectron spectroscopy (XPS) was performed and the results have been shown in Figure 9.5.2, where the Bi($4f_{5/2}$, $4f_{7/2}$) peaks have been presented. The XPS measurements were performed on powdered ground pellets. In considering past reports on $BaBiO_3$ in the literature, the photoemission studies performed by various groups are not in agreement. Jeon *et al.* and Kulkarni *et al.* reported the presence of multiple Bi 4f lines which they attributed to multiple valence states of bismuth.[29, 30] Several other groups have reported narrow bismuth core level spectra.[31-34] Some attributed it to the presence of just one bismuth state in the compound and some suggested that the level of disproportionation was too small to be detected by photoemission. As is evident in the Bi4f spectra presented in Figure 9.5.2, however, a shoulder is clearly evident on the high

binding energy side of the Bi4f peaks. As determined by peak fitting, the most intense component of the $Bi4f_{7/2}$ peak was at 157.7 eV; the higher binding shoulder was at 158.9 eV. These binding energies, and their separation, are close to those described in the work by Kulkarni *et al*. for Bi in the +3 state and +5 oxidation states, respectively.[29] In particular, the shoulder at 158.9 eV binding energy in Figure 2 corresponds to the binding energy reported by Kulkarni *et al.* for $NaBiO_3$. The peaks used in the fit were symmetric, and the relative intensities of each pair of $Bi4f_{7/2}$ and $Bi4f_{5/2}$ peaks were constrained to be 4:3. The widths of the peaks corresponding to the +5 state were slightly larger than those for the +3 state. In summary, the valence state of the target ion is directly proportional to the binding energy, and therefore, these shoulders can be attributed to the presence of Bi^{5+} in the sample, and therefore the data here clearly show evidence of the presence of multiple valence states for bismuth in the spectra for BB ceramics.

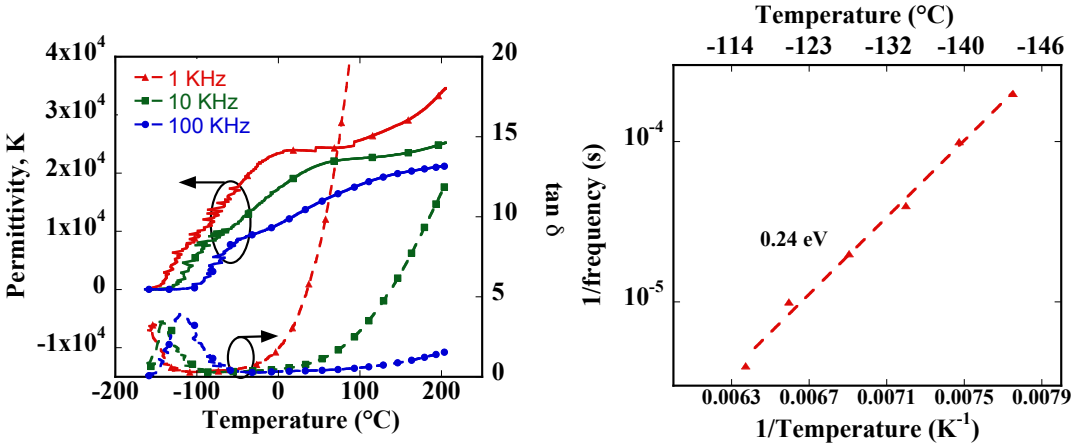

Fig. 9.5.3. (a) Permittivity and dielectric loss as a function of temperature at 1 KHz, 10 KHz and 100 KHz for $BaBiO_3$ ceramics, and (b) Arrhenius plot of applied frequency and $1/T_m$, where T_m are the temperatures at dielectric tangent maximum.

Figure 9.5.3 shows the dielectric permittivity and loss data for BB over the temperature range of approximately -150 °C to 200 °C. Past reports on $BaBiO_3$ suggest a phase transition from monoclinic $I2/m$ to rhombohedral $R\bar{3}$ at around 132 °C[35, 36], but this was not evident in the data in Figure 9.5.3 due to the effects of conduction losses. The dielectric permittivity values were high over the entire temperature range of measurement, however, which is a direct result of high losses. A frequency-dependent relaxation was observed in the dielectric loss at sub-zero temperatures and the temperature of the relaxation peak maxima increased with increasing frequency.

Lee *et al.* observed a similar thermally activated phenomenon in their study and attributed it to polaron hopping.[37] Debye theory can been used to analyze the dielectric relaxation involving polaron hopping. An Arrhenius plot of the frequency and the temperature of relaxation peak yielded the activation energy for relaxation as shown in Figure 9.5.3b.[37, 38] The activation energy calculated in Figure 3b was approximately

0.24 eV, which was consistent with literature reports.[30] It was also close to the activation energy for conduction calculated through *ac* impedance spectroscopy (~ 0.25 eV, Figure 9.5.4c), which may suggest that similar mechanisms control both the dielectric relaxation and conduction mechanism.

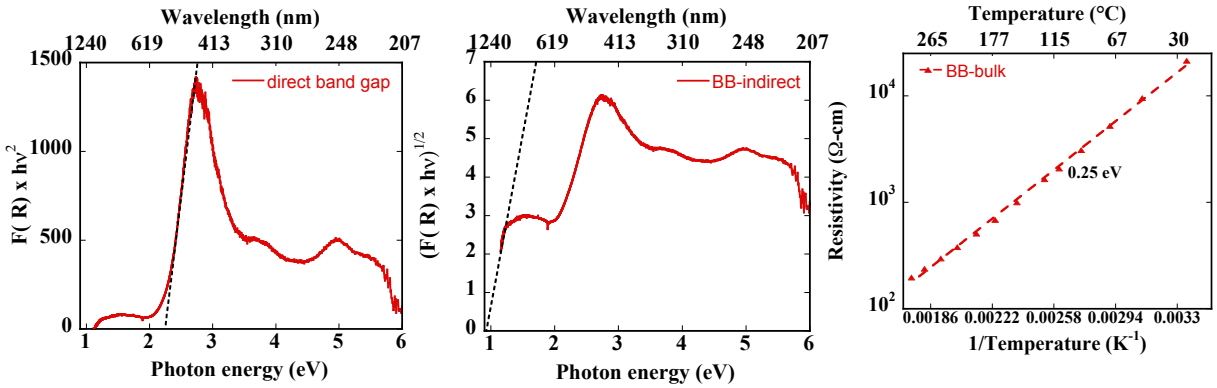

Fig. 9.5.4. Kubelka-Munk and Tauc plots for BB ceramics. The appropriate functions for direct and indirect band gaps were chosen for (a) and (b) respectively. Figures (a) and (b) also show representative fit lines used to estimate band gaps. Figure (c) shows Arrhenius plot with linear fit for bulk resistivity obtained from *ac* impedance spectroscopy.

The Kubelka-Munk function and Tauc plot were used to calculate the indirect and direct band gaps, which were estimated to be ~ 0.92 eV and ~2.2 eV respectively (Figure 9.5.4a and 4b).[39-41] These values were consistent with literature values.[42, 43] It is worth mentioning that previous literature reports have largely failed to directly assess the indirect band gap through techniques like optical reflectance, photoconductivity, photoacoustic spectroscopy and other techniques. The value of 0.92 eV reported here is based on the assumption that the rise in the intensity of the signal close to 1 eV in Figure 9.5.4b was due to the indirect band gap in BB. The presence of these band gaps makes

BB an indirect band gap semiconductor. Band-structure calculations have predicted that $BaBiO_3$ should be metallic if bismuth were present in the 4+ state as it would have a half filled Bi 6*s* conduction band.[44, 45] The origin of semiconduction in $BaBiO_3$ is believed to be a result of the disproportionation of bismuth into 3+ and 5+ valence states, followed by ordering and accompanied by alternate expansion and contraction of oxygen octahedra. In other words, the strong soft-phonon related electron-phonon interaction, which is considered to be responsible for superconductivity in BB-based ceramics, is completely softened leading to static displacement of the oxygen atoms in undoped BB. This, in turn, leads to a configuration called a charge density wave (CDW) or breathing mode distortion, and is believed to be responsible for the observed indirect band gap at the Fermi level, which then gives rise to semiconducting properties.[35, 37]

Figure 9.5.4b shows the activation energy for bulk conduction for BB, calculated using *ac* impedance spectroscopy. Impedance spectroscopy is a powerful tool and can effectively separate the bulk transport properties from other contributions such as interfaces, inhomogeneity and other mechanisms.[46] On plotting the bulk resistivity as a function of temperature using the Arrhenius equation, the conduction was shown to be a thermally activated process with an activation energy estimated to be ~0.25 eV. This is consistent with the activation energy values reported using Seebeck and Hall measurements.[42] This activation energy value is significantly lower than the measured band gap values reported above. However, it has been suggested that this is closely related to the indirect band gap and not related to impurities.[45] It was also supported by the fact that the number of states contributing to electrical conduction calculated by using

Hall measurements by Takagi *et al.* was comparable to the number of bismuth atoms in the crystal structure.[47] However, to explain the low activation energy (as compared to band gap measurements), it has been suggested that polaronic bands accommodating holes are formed above the top of occupied Bi 6*s* band (~0.25 eV below Fermi level) and a polaron band accommodating electrons are formed below the empty Bi 6*s* band (~0.25 eV above Fermi level).[45] Due to these polaron bands, the conductivity gap is reduced to ~0.5 eV, which can explain the measured activation energy of 0.25 eV obtained from impedance spectroscopy.

Part 2. $BaBiO_3$-$BaTiO_3$ ceramics

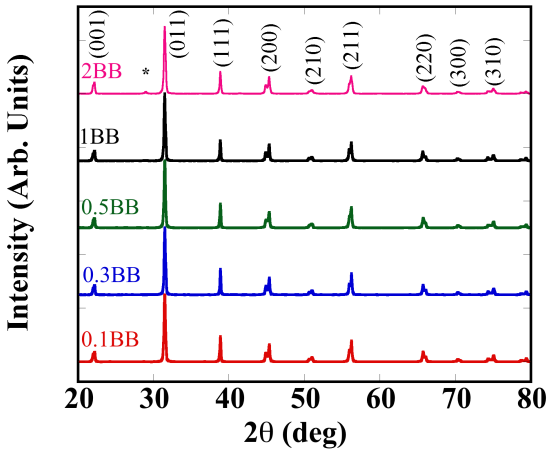

Fig. 9.5.5. X-ray diffraction pattern of (1-x)BT-xBB ceramics, where x lies between 0.1 mol% and 2 mol%. The "*" indicates secondary phase, if present.

Following the results of the synthesis and characterization of pure BB, this section aims to examine the change in transport properties on adding small amounts of BB to $BaTiO_3$. Figure 9.5.5 shows the XRD patterns of pulverized BT-BB solid solution ceramics. All the samples had split {200} peaks (~45°), indicating tetragonal symmetry. Within the resolution of laboratory XRD, it was difficult to note any change in lattice parameters with the addition of such small amounts of BB. Even though the sintering temperatures were reduced significantly (by 300 °C – 400 °C) on adding BB to BT, all sintered pellets had measured density values greater than 95% of the theoretical value, as measured via Archemedes' method. It can also be noted in Figure 9.5.5 that phase-pure perovskite could be achieved for BB-BT solid solutions with less than 2 mol% BB. The secondary phase shown for 98BT-2BB is believed to be $BaBiO_3$ itself as the peak

position matched well with the most intense peak of BB (Figure 1). The composition with 2 mol% BB was sintered at 990 °C and the presence of BB as an impurity peak presents an important result as some reports claim that $BaBiO_3$ is unstable in oxygen at temperatures over 850°C.[48] The $BaTiO_3$ matrix may have a stabilizing effect on BB, which might be preventing it from decomposing at relatively higher temperatures.

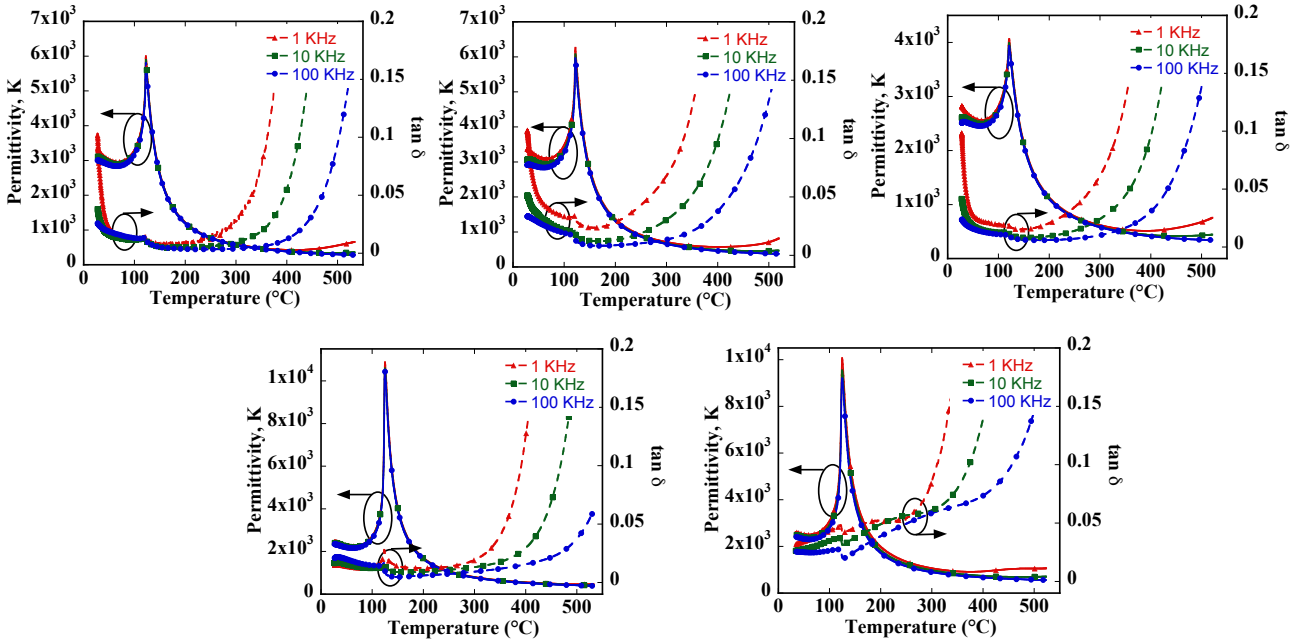

Fig. 9.5.6. Permittivity and dielectric loss as a function of temperature at 1 KHz, 10 KHz and 100 KHz for (a) BT-0.1BB, (b) BT-0.3BB, (c) BT-0.5BB, (d) BT-1BB, and (e) BT-2BB ceramics.

Figure 9.5.6 shows the dielectric constant as a function of temperature. All the compositions exhibited a sharp phase transition as expected for a normal ferroelectric material and the Curie point did not shift significantly with the addition of BB. It was

recorded to be between 122 °C and 125 °C for all compositions, and was in contrast with a previous report which claimed an increase in Curie point by ~30 °C on adding ~0.5% BB to BT.[17] The room temperature dielectric constant varied between ~2000 to ~3000. The dielectric loss values remain low (<5%) up to ~300°C at 1 KHz for all compositions and increased thereafter.

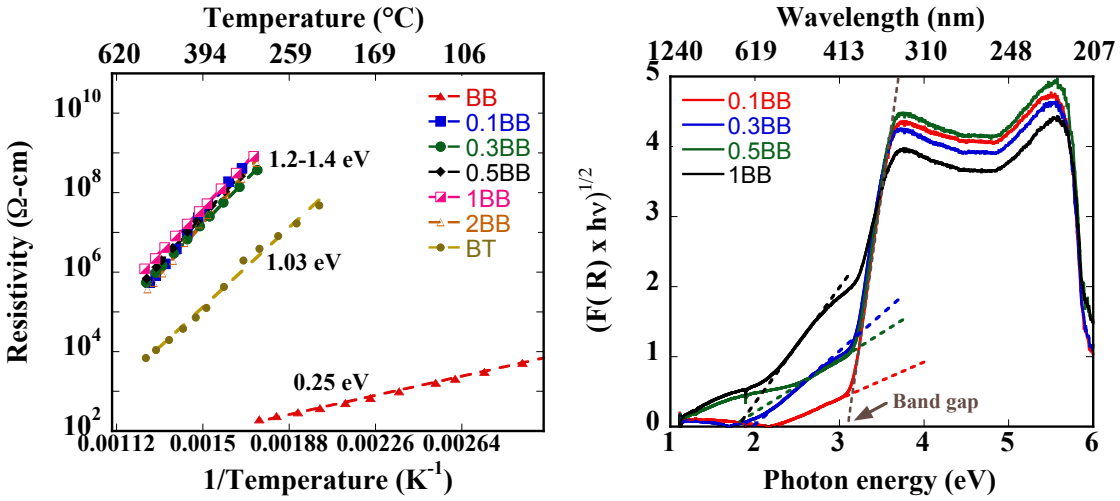

Fig. 9.5.7. (a) Arrhenius plots for bulk resistivity obtained from AC impedance spectroscopy for BT-BB ceramics. Plots for undoped BB and BT have been shown for reference. (b) Kubelka-Munk and Tauc plots for BT-BB ceramics. The appropriate function for indirect band gap was chosen. Representative fit lines have also been shown.

Figure 9.5.7a shows the Arrhenius plots of the bulk resistivity values for BT-BB ceramics, obtained through *ac* impedance spectroscopy. The data for undoped BT and BB have also been shown for reference. In the plots, the BT-BB ceramics appear to have multiple orders of magnitude higher resistivity than either BT or BB alone. The activation energy for conduction, estimated from the slopes of the plots, also increased significantly for the solid solution as compared to the end-member compounds. This suggests a dramatic change in the underlying defect chemistry in these solid solutions, which

warrants further examination. The undoped BT used in this study is characterized by a defect-dominated p-type conduction mechanism, as reported in a previous article.[23] In BT, the p-type behavior is commonly attributed to frozen-in cation vacancies formed during high temperature processing and low valence acceptor impurities associated with starting reagent oxides.[49-51] These vacancies and acceptors can be compensated by oxygen vacancies, which can in turn give rise to p-type behavior at high oxygen partial pressures as per following defect reaction:

$$V_O^{\cdot\cdot} + \frac{1}{2} O_2 \rightarrow O_O^X + 2h^{\cdot} \qquad \text{Eq. 9.5.1}$$

where $V_O^{\cdot\cdot}$ is a doubly-ionized oxygen vacancy, O_O^X represents an oxygen ion located on the anion sub-lattice, and $h^{\cdot}$ represents a hole. In considering the significant change in conductivity with the addition of BB, a number of factors could be responsible. First, the concentration of cation vacancies in BT-BB ceramics may be lower than BT alone owing to the significantly lower sintering temperatures (i.e. 1350 °C for BT and 950-1050 °C for BT-BB). Secondly, there may be an unintended donor dopant species present which is compensating for the holes and thus effectively increasing the resistivity values. One of the many possible candidates for donor doping could be the occupation of bismuth cations on the A-sublattice, where by replacing barium it will act as a donor. This possibility will be discussed in greater detail later in this article.

Figure 9.5.7b shows the Tauc plots using the Kubelka-Munk function, as was shown for undoped BB ceramics earlier. The indirect band gaps for all compositions were ~3.1 eV, which is close to the value expected for titanate-based perovskites and is

consistent with previous literature reports.[22] The peculiar characteristic present in all these plots were the Urbach tail-like features, which became more apparent with increasing BB concentrations. Generally, it is considered to originate from disorder in a crystal such as localized defects, lattice vibrations and other factors.[40] These features lead to electronic states just above the valence band or immediately below the conduction band, and the transition between these band tail states may give rise to Urbach tails. More details about these Urbach tails can be found elsewhere.[52, 53] Another observation which can be made is that the extrapolations of these tails intercept at the x-axis at ~1.8 eV – 2.2 eV, which is close to the value of direct band gap for BB. Therefore, these features may also be a direct result of a secondary BB phase which may be undetectable by laboratory scale x-ray diffraction techniques.

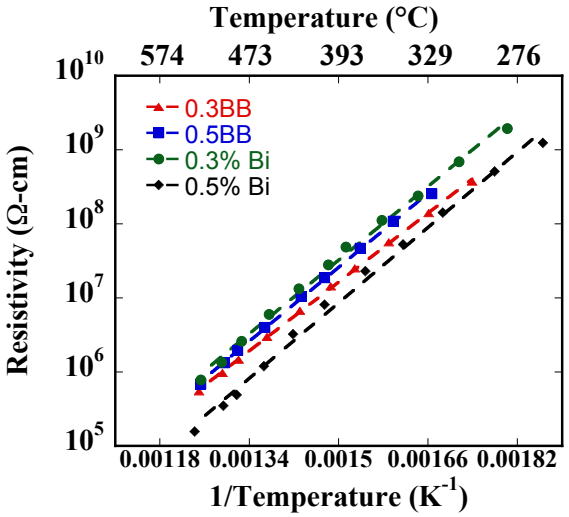

Fig. 9.5.8. Arrhenius plots for bulk resistivity obtained from AC impedance spectroscopy for Bi-doped BT ceramics. Data for BT-BB ceramics have been shown for reference.

In considering the mechanism for the increase in resistivity for BT-BB ceramics as compared to BT, unintentional donor doping due to changes in bismuth site occupancy is another possibility. Direct confirmation of bismuth on the A-site is extremely challenging due to the relatively low concentration of bismuth. Therefore, an indirect approach has been adopted here to characterize the site occupancy of bismuth. In this study, $BaTiO_3$ ceramics were prepared with excess additions of 0.3 mol% bismuth (BT+0.15%Bi_2O_3) and 0.5 mol% bismuth (BT+0.25%Bi_2O_3) so that the amount of bismuth added was same as in the solid solutions BT-0.3BB and BT-0.5BB, respectively. These compounds were intentionally sintered under the same conditions as the BT-BB ceramics so as to make a direct comparison. It is believed that under normal circumstances, excess bismuth would substitute onto the A-sublattice to replace barium due to thermodynamic considerations and this has also been confirmed through multiple reports in the literature with electrical property measurements.[53-55] The Bi-doped BT ceramics had similar density values as compared to BT-BB ceramics and the results from AC impedance spectroscopy performed on them have been presented in Figure 9.5.8. The Arrhenius plot for the bulk resistivity shows that the resistivity values of BT doped with bismuth was quite similar to BT-BB ceramics with similar bismuth content. The slopes were also almost identical, indicating similar activation energies for conduction. These results, therefore, suggest that it is the occupancy of bismuth on the A-site that leads to the observed improvement in resistivity.

Conclusions

Single-phase $BaBiO_3$ ceramics were fabricated and confirmed by high-resolution x-ray diffraction, and the coexistence of bismuth in 3+ and 5+ valence states was confirmed by x-ray photoelectron spectroscopy. Using AC impedance and optical spectroscopy, it was shown that polaron-hopping was the dominant conduction mechanism in $BaBiO_3$. Ceramics based on the solid solution of $BaTiO_3$-$BaBiO_3$ were fabricated to investigate the effect of adding small amounts of BB on the conduction mechanism of BT. It was observed that the BT-BB ceramics had significantly higher resistivity values as compared to undoped $BaTiO_3$ or $BaBiO_3$, suggesting a decrease in the concentration of mobile defect species. The resistivity values remained high even with a coexisting secondary $BaBiO_3$ phase. Data from *ac* impedance spectroscopy on Bi-doped $BaTiO_3$ suggested that a shift in the site occupancy of Bi onto the A-sublattice is the dominant mechanism resulting in donor doping which results in the observed high resistivities.

Acknowledgements

This material is based upon work supported by the National Science Foundation under Grant No. DMR-1308032. Use of the Advanced Photon Source at Argonne National Laboratory was supported by the U. S. Department of Energy, Office of Science, Office of Basic Energy Sciences, under Contract No. DE-AC02-06CH11357. Thanks to Fallon Fumasi for her help with XPS measurements.

References

[1] AW S. eight, JL Gillson and FE Bierstedt. Solid State Commun 1975;17:27.
[2] Flavell WR, Morris BC, Tweddell I, Purdie D, Thornton G, Wincott PL, et al. Materials chemistry communications. Pb and Bi Valencies in BaPb1–xBixO3. Journal of Materials Chemistry 1992;2:1209-10.
[3] Zhou Q, Kennedy BJ. High temperature structure of BaBiO 3—a synchrotron X-ray powder diffraction study. Solid state communications 2004;132:389-92.
[4] Glazer A. The classification of tilted octahedra in perovskites. Acta Crystallographica Section B: Structural Crystallography and Crystal Chemistry 1972;28:3384-92.
[5] Howard CJ, Kennedy BJ, Woodward PM. Ordered double perovskites–a group-theoretical analysis. Acta Crystallographica Section B: Structural Science 2003;59:463-71.
[6] Sleight AW, Gillson J, Bierstedt P. High-temperature superconductivity in the BaPb1-xBixO3 system. Solid State Communications 1975;17:27-8.
[7] Mattheiss L, Gyorgy E, Johnson Jr D. Superconductivity above 20 K in the Ba-K-Bi-O system. Physical Review B 1988;37:3745.
[8] Attfield JP. Chemistry and high temperature superconductivity. Journal of Materials Chemistry 2011;21:4756-64.
[9] Akhtar MJ, Catlow CRA. X-Ray absorption studies of bi-based superconductors. Journal of Materials Chemistry 1994;4:1081-91.
[10] Itoh M, Sawada T, Liang R, Kawaji H, Nakamura T. Oxygen-deficient and ordered perovskite-type solid-solution system Ba1+ xBi1− xOy (0≦ x≦ 0.5, 3.00≧ y≧ 2.75). Journal of Solid State Chemistry 1990;87:245-9.
[11] Hervieu M, Michel C, Caldes M, Pham A, Raveau B. The Cuprate Bi 6 Ba 4 Cu 2 O 15: A Double Collapsed 2201-Type Structure. Journal of Solid State Chemistry 1993;107:117-26.
[12] Darriet J, Dussarrat C, Weill F, Darriet B, Bontchev R. The system BaRuO 3-BaBiO 3. I. Crystal structures of Ba 3 Ru 2 BiO 9 and Ba 2 Ru x Bi 2-x O 6 (0. European Journal of Solid State and Inorganic Chemistry 1993;30:273-86.
[13] Sutto TE, Averill BA. Composition-and Annealing-Dependent Properties of Ba (Bi, Tl) O 3-δ. Journal of Solid State Chemistry 1993;105:263-70.
[14] Boyce J, Bridges F, Claeson T, Geballe T, Remeika J. X-ray absorption of BaBiO 3 and superconducting BaBi 0.25 Pb 0.75 O 3. Physical Review B 1990;41:6306.
[15] Luo Y, Liu X, Li X, Liu G. PTCR effect in BaBiO 3-doped BaTiO 3 ceramics. Solid State Ionics 2006;177:1543-6.
[16] Yuan Q, Pu Y, Cao B. Effects of different bismuth-based compounds additives on the positive temperature coefficient effect of BaTiO 3 ceramics. Materials Letters 2012;86:115-8.
[17] Chang-Lai Y, Xin-Yu L, Chang-Rong Z, Ji-Wen X, Yun Y. Characterization of the BaBiO3-doped BaTiO3 positive temperature coefficient of a resistivity ceramic using impedance spectroscopy with Tc= 155° C. Chinese Physics B 2011;20:048701.
[18] Huang C-C, Cann DP. Phase transitions and dielectric properties in Bi(Zn1/2Ti1/2)O3−BaTiO3 perovskite solid solutions. Journal of Applied Physics 2008;104:024117.

[19] Raengthon N, Sebastian T, Cumming D, Reaney IM, Cann DP. BaTiO3‐Bi (Zn1/2Ti1/2) O3‐BiScO3 Ceramics for High‐Temperature Capacitor Applications. Journal of the American Ceramic Society 2012;95:3554-61.
[20] Kumar N, Patterson EA, Frömling T, Cann DP. DC-bias dependent impedance spectroscopy of BaTiO 3–Bi (Zn 1/2 Ti 1/2) O 3 ceramics. Journal of Materials Chemistry C 2016;4:1782-6.
[21] Kumar N, Ionin A, Ansell T, Kwon S, Hackenberger W, Cann D. Multilayer ceramic capacitors based on relaxor BaTiO3-Bi (Zn1/2Ti1/2) O3 for temperature stable and high energy density capacitor applications. Applied Physics Letters 2015;106:252901.
[22] Kumar N, Cann DP. Resistivity Enhancement and Transport Mechanisms in (1− x) BaTiO3–xBi (Zn1/2Ti1/2) O3 and (1− x) SrTiO3–xBi (Zn1/2Ti1/2) O3. Journal of the American Ceramic Society 2015;98:2548-55.
[23] Kumar N, Patterson EA, Frömling T, Cann DP. Conduction mechanisms in BaTiO3-Bi(Zn1/2Ti1/2)O3 ceramics. Journal of the American Ceramic Society 2016.
[24] Kumar; N, Cann D. Tailoring transport properties through nonstoichiometry in BaTiO3–BiScO3 and SrTiO3–Bi(Zn1/2Ti1/2)O3 for capacitor applications. Journal of Materials Science 2016.
[25] Triamnak N, Brennecka GL, Brown-Shaklee HJ, Rodriguez MA, Cann DP. Phase formation of BaTiO 3–Bi (Zn 1/2 Ti 1/2) O 3 perovskite ceramics. Journal of the Ceramic Society of Japan 2014;122:260-6.
[26] Toby BH, Von Dreele RB. GSAS-II: the genesis of a modern open-source all purpose crystallography software package. Journal of Applied Crystallography 2013;46:544-9.
[27] Cox D, Sleight A. Crystal structure of Ba 2 Bi 3+ Bi 5+ O 6. Solid State Communications 1976;19:969-73.
[28] Reis KP, Jacobson AJ, Nicol JM. A Powder Neutron Diffraction Investigation of Structure and Cation Ordering in Ba 2+ x Bi 2-x O 6-y. Journal of Solid State Chemistry 1993;107:428-43.
[29] Kulkarni G, Vijayakrishnan V, Rao GR, Seshadri R, Rao C. State of bismuth in BaBiO3 and BaBi1− xPbxO3: Bi 4f photoemission and Bi L3 absorption spectroscopic studies. Applied Physics Letters 1990;57:1823-4.
[30] Jeon Y, Liang G, Chen J, Croft M, Ruckman M, Di Marzio D, et al. BaBiO 3 and the effect of potassium substitution using photoemission. Physical Review B 1990;41:4066.
[31] Wertheim G, Remeika J, Buchanan D. Electronic structure of Ba Pb 1− x Bi x O 3. Physical Review B 1982;26:2120.
[32] Ganguly P, Hegde M. Evidence for double valence fluctuation in metallic oxides of lead. Physical Review B 1988;37:5107.
[33] Hegde M, Barboux P, Chang C, Tarascon J, Venkatesan T, Wu X, et al. Electronic structure of high-T c Ba 0.6 K 0.4 BiO 3 by x-ray photoelectron spectroscopy. Physical Review B 1989;39:4752.
[34] Shen Z-X, Lindberg P, Wells B, Dessau D, Borg A, Lindau I, et al. Photoemission study of monoclinic BaBiO 3. Physical Review B 1989;40:6912.
[35] Cox D, Sleight A. Mixed-valent Ba2Bi3+ Bi5+ O6: structure and properties vs temperature. Acta Crystallographica Section B: Structural Crystallography and Crystal Chemistry 1979;35:1-10.

[36] Abbattista F, Vallino M, Delmastro A, Mazza D, Ronchetti S. Research on the BaBiO3-δ System (0≤ δ≤ 0.5). Journal of Solid State Chemistry 1995;117:55-63.
[37] Lee S-H, Jung W-H, Sohn J-H, Lee J-H, Cho S-H. Dielectric loss anomaly of BaBiO3. Journal of applied physics 1999;86:6351-4.
[38] Dominik L, MacCrone R. Dielectric Relaxations in Reduced Rutile (Ti O 2− x) at Low Temperatures. Physical Review 1967;163:756.
[39] Klaas J, Schulz-Ekloff G, Jaeger NI. UV-visible diffuse reflectance spectroscopy of zeolite-hosted mononuclear titanium oxide species. The Journal of Physical Chemistry B 1997;101:1305-11.
[40] Tauc J, Grigorovici R, Vancu A. Optical properties and electronic structure of amorphous germanium. physica status solidi (b) 1966;15:627-37.
[41] Umebayashi T, Yamaki T, Itoh H, Asai K. Band gap narrowing of titanium dioxide by sulfur doping. Applied Physics Letters 2002;81:454-6.
[42] Tajima S, Uchida S, Masaki A, Takagi H, Kitazawa K, Tanaka S, et al. Electronic states of BaPb 1− x Bi x O 3 in the semiconducting phase investigated by optical measurements. Physical Review B 1987;35:696.
[43] Kim KH, Jung C, Noh T, Kim S. Optical indirect transitions of semiconducting BaPb 1− x Bi x O 3. Physical Review B 1997;55:15393.
[44] Mattheiss L, Hamann D. Electronic structure of Ba Pb 1− x Bi x O 3. Physical Review B 1983;28:4227.
[45] Namatame H, Fujimori A, Takagi H, Uchida S, De Groot F, Fuggle J. Electronic structure and the metal-semiconductor transition in BaPb 1− x Bi x O 3 studied by photoemission and x-ray-absorption spectroscopy. Physical Review B 1993;48:16917.
[46] Elissalde b, Ravez J. Ferroelectric ceramics: defects and dielectric relaxations. Journal of Materials Chemistry 2001;11:1957-67.
[47] Takagi H, Uchida S, Tajima S, Kitazawa K, Tajima S. In: Engstrom O, editor. Proceedings of the International Conference on the Physics of Semiconductors. Stockholm: World Scientific, Singapore; 1986. p. 1815.
[48] Nakamura T, Kose S, Sata T. Paramagnetism and Semiconductivity in a Triclinic Perovskite BaBiO3. Journal of the Physical Society of Japan 1971;31:1284-.
[49] Chan NH, Smyth D. Defect chemistry of BaTiO3. Journal of The Electrochemical Society 1976;123:1584-5.
[50] Tsur Y, Randall CA. Point defect concentrations in barium titanate revisited. Journal of the American Ceramic Society 2001;84:2147-9.
[51] Moos R, Härdtl KH. Dependence of the intrinsic conductivity minimum of SrTiO3 ceramics on the sintering atmosphere. Journal of the American Ceramic Society 1995;78:2569-71.
[52] Chang Y, Badano G, Zhao J, Zhou Y, Ashokan R, Grein C, et al. Near-bandgap infrared absorption properties of HgCdTe. Journal of electronic materials 2004;33:709-13.
[53] Tran H, Du W, Ghetmiri SA, Mosleh A, Sun G, Soref RA, et al. Systematic study of Ge1− xSnx absorption coefficient and refractive index for the device applications of Si-based optoelectronics. Journal of Applied Physics 2016;119:103106.
[54] Zhang D, Wang T, Zhu Y, Wang C, Wu X. Some dielectric and photorefractive properties of Bi: BaTiO3 and Bi, K: BaTiO3 crystals. physica status solidi (a) 1998;168:297-304.

[55] Padmini P, Kutty T. Influence of Bi3+ ions in enhancing the magnitude of positive temperature coefficients of resistance in n-BaTiO3 ceramics. Journal of materials science: materials in electronics 1994;5:203-9.

9.6 Tailoring transport properties through non-stoichiometry in $BaTiO_3$-$BiScO_3$ and $SrTiO_3$-$Bi(Zn_{1/2}Ti_{1/2})O_3$ for capacitor applications

Nitish Kumar and David P. Cann

Materials Science, School of Mechanical, Industrial, and Manufacturing Engineering, Oregon State University, Corvallis, Oregon 97331, USA

Published in

Journal of Materials Science

Vol. 51, 9404 (2016)

ABSTRACT:

The ceramic perovskite solid solutions $BaTiO_3$-$BiScO_3$ (BT-BS) and $SrTiO_3$-$Bi(Zn_{1/2}Ti_{1/2})O_3$ (ST-BZT) are promising candidates for high temperature and high energy density dielectric applications. A-site cation non-stoichiometry was introduced in these two ceramic systems to investigate the effect on the dielectric and transport properties using temperature- and oxygen partial pressure-dependent AC impedance spectroscopy. For p-type BT-BS ceramics, the addition of excess Bi led to effective donor doping along with a significant improvement in insulation properties. A similar effect was observed on introducing Ba vacancies onto the A-sublattice. However, Bi deficiency had an opposite effect with effective acceptor doping and a deterioration in the bulk resistivity values. For n-type intrinsic ST-BZT ceramics, the addition of excess Sr onto the A-sublattice resulted in a decrease in resistivity values, as expected. Introduction of Sr vacancies or addition of excess Bi on A-site did not appear to affect the insulation properties in air. These results indicate that minor levels of non-stoichiometry can have an important impact on the material properties and furthermore it demonstrates the difficulties encountered in trying to establish a general model for the defect chemistry of Bi-containing perovskite systems.

Introduction

Titanate perovskites are technologically important and one of the most highly studied in the field of basic solid-state chemistry. Titanates based on Ba and Sr have long been studied for dielectric, piezoelectric and other applications.[1-4] Since the discovery

of barium titanate in 1940's[5], several modifications have been made to it to reduce the characteristic temperature dependence of its dielectric properties and to make it more suitable for devices.[6, 7] It remains the cornerstone of the ceramic capacitor industry even today. Several recently reported $BaTiO_3$ (BT)-based ceramics feature a permittivity greater than 1,000 with superior temperature-stability and improved insulation resistance, making them useful for emerging applications.[7, 8] On the other hand, $SrTiO_3$ (ST) has uses in metal oxide semiconductor field effect transistors where it is considered one of the preferred candidates to replace SiO_2 as a gate insulator, in tunable microwave electronics and other applications.[9] At the same time, $SrTiO_3$, owing to its similarity with BT and similar systems, has been widely studied as a model system to understand defects and transport behavior.[4, 10] Several of these titanates also exhibit a pronounced mixed conduction i.e. both mobile ions and electronic species contribute to the total conductivity. This allows oxygen to become incorporated into the ceramic and can modify the electronic properties, which is an essential function in oxygen-sensors.[11]

Bismuth-containing perovskites have gained attention in recent years, due to the similar electronic structure of Bi and Pb and their demonstrated promising properties. [7, 12, 13] It has been shown that solid solutions of BT with bismuth-perovskites exhibit relaxor behavior which makes them better suited for capacitor and actuator applications.[8, 14-20] Some of the examples of these bismuth end member compounds include $Bi(Zn_{1/2}Ti_{1/2})O_3$, $BiScO_3$, $Bi(Ni_{1/2}Ti_{1/2})O_3$, $Bi(Mg_{1/2}Ti_{1/2})O_3$ and others.[8, 17, 18, 21] Recently, multilayer ceramic capacitors (MLCCs) were also fabricated based on some of these compositions which had superior performance characteristics compared to

other commercially available MLCCs based on barium titanate.[17, 22] On the other hand, solid solutions of BT with bismuth end members such as $(Bi_{1/2}Na_{1/2})TiO_3$ (BNT), $(Bi_{1/2}K_{1/2})TiO_3$, $(Bi_{1/2}Li_{1/2})TiO_3$ and others show high piezoelectric coefficients.[23, 24] In addition, the addition of bismuth compounds have also been shown to modify the defect chemistry of titanate perovskites, which can be used to modify transport properties to suit application-specific requirements.[8, 25-27] Some of these phenomena will be emphasized in this report as well.

In the recent past, several thermodynamic and first principles studies have been performed to understand ferroelectricity and related properties in perovskites,[28, 29] however, research to understand the effects of non-stoichiometry and high temperature defects is often overlooked. This kind of a study becomes especially significant when volatile species such as bismuth are present in the ceramics. This report focuses on two such materials systems–BT-$BiScO_3$ (BT-BS) and ST-$Bi(Zn_{1/2}Ti_{1/2})O_3$ (ST-BZT). Ceramics based on BT-BS have shown promising properties for high temperature dielectric applications.[17, 30] Similar to recent findings on BT-BZT, ST-BZT ceramics exhibit significant improvement in the dielectric and insulation properties upon the addition of BZT to the solid solution.[8] In a separate report, it was shown that with BZT additions, acceptor doping was introduced from frozen-in cation vacancies formed during high temperature processing and as well as naturally occurring acceptor dopants associated with the precursor oxides. Both were compensated by an unintentional donor doping caused by the addition of BZT.[25] It will be shown here that small deviations in cation stoichiometry can have a significant impact on the dielectric and insulation

properties, the electrical homogeneity and the principal charge carrier type. Such a study will also potentially demonstrate a methodology to control defects and thus tailor transport and dielectric properties as per requirements. For example, high resistivity values are important to improve energy density of the ceramics and make them more suitable for extreme environment like high temperature and high electric field. Lower resistivity values, on the other hand, are favorable for applications requiring ionic conduction.

Impedance spectroscopy measurements as a function of oxygen partial pressure (pO_2) and temperature have been used to gain information about the electrical structure and transport properties. The electrical response of BT-based polycrystalline ceramics typically consists of bulk and grain boundary components, which can usually be modeled using an equivalent circuit consisting of two resistor-capacitor (RC) elements in series. In the case of other inhomogeneities (*e.g.* core-shell structure etc.), sample-electrode interactions and other effects, additional semicircles may also appear. The frequency at the maxima of the semicircles together with the position of maxima and real-axis intercepts of the plots can be used to calculate capacitance and resistance of each contributing process, the details of which can be found elsewhere.[31, 32] Impedance spectroscopy, if performed at different temperatures, can also be used to derive the activation energies for each conduction mechanism within each component. The Arrhenius equation for the same is given by:

$$\sigma = \sigma_0 \exp(-E_A/kT) \qquad \text{Eq. 9.6.1}$$

where, σ, σ_0, E_A, k and T represent the conductivity, pre-exponential factor, activation energy for conduction, Boltzmann constant and temperature, respectively. The pre-exponential factor can exhibit a temperature dependence as well. When performed at different pO_2 levels, impedance spectroscopy can provide other valuable information about the majority charge-carrier type and defect equilibrium conditions.[33]

Experimental Procedure

Conventional solid-state methods were used to prepare compositions based on $(Ba_{0.7}Bi_{0.3})(Ti_{0.7}Sc_{0.3})O_3$ (BT-BS). The stoichiometric BT-BS composition will henceforth be referred to as S. Intentional cation non-stoichiometry was introduced in BT-BS so as to introduce 0.02 charge excess or deficiency on the A-sub lattice. These compositions were $(Ba_{0.69}Bi_{0.3})(Ti_{0.7}Sc_{0.3})O_3$ (hereafter referred to as "Ba def"), $(Ba_{0.7}Bi_{0.2933})(Ti_{0.7}Sc_{0.3})O_3$ (hereafter referred to as "Bi def") and $(Ba_{0.68}Bi_{0.32})(Ti_{0.7}Sc_{0.3})O_3$ ("Bi Xs"). To prepare these compositions, $BaCO_3$ (Alfa Aesar, >99.8%), Bi_2O_3 (Aldrich, >99.9%), TiO_2 (Aldrich, >99.9%), and Sc_2O_3 (PIDC, >99.9%) were used as starting powders. The mixed powders were ground using a vibratory mill for 6 hours, dried overnight in an oven (~80 °C) and then calcined in alumina crucibles. The composition S was calcined at 1100 °C for 6 hours, the Ba def at 1000 °C for 6 hours, the Bi def at 1150 °C for 6 hours and Bi Xs at 1000 °C for 6 hours. The powders were then milled with ~3 wt% Rhoplex binder and dried again. Green pellets in the shape of thin discs were made by cold-pressing uniaxially at a pressure of ~200 MPa and then sintered on a bed of calcined powder in a closed alumina crucible. The composition S

was sintered at 1250 °C for 4 hours, the Ba def at 1200 °C for 4 hours, the Bi def at 1350 °C for 4 hours and Bi Xs at 1200 °C for 4 hours.

An identical route was used for $0.95SrTiO_3$- $0.05Bi(Zn_{1/2}Ti_{1/2})O_3$ (ST-BZT) ceramics as well. The titania and bismuth oxide precursors were the same as above. The other precursors used were $SrCO_3$ (Aldrich, >99.9%) and ZnO (Alfa Aesar, >99.9%). For these ceramics, the amount of charge excess/deficiency created through cation non-stoichiometry was 0.01. Henceforth, the stoichiometric composition will be referred to as S, the composition with 0.01 charge deficiency due to strontium vacancies will be referred to Sr def, the composition with 0.01 charge deficiency due to bismuth vacancies will be referred to as Bi def, and the composition with 0.01 charge excess due to extra bismuth will be referred to as Bi Xs. All of the compositions were calcined at 1000 °C for 6 hours and sintered at 1275 °C for 4 hours.

All the sintered pellets were polished to sub-millimeter thickness. X-ray diffraction (XRD) (Bruker AXS D8 Discover, Madison, WI, USA) was performed on ground pellets for phase and crystal structure determination. Prior to any electrical measurements, Ag or Pt electrodes were applied on both sides of the pellets. The Ag electrodes were fired at 700 °C for 30 min and Pt at 900 °C for 15 min. The pO_2-dependent measurements were performed using Pt electrodes. The pellets were placed in a high temperature measurement cell (NorECs AS ProbostatTM, Oslo, Norway) and dielectric properties were measured using an LCR meter (Agilent 4284A, Santa Clara, CA, USA). An impedance analyzer (Solartron SI1260A equipped with Solartron 1296A dielectric interface, Farnborough, UK) was used to measure the impedance over the

frequency range 0.1 Hz to 5 MHz as a function of temperature and pO_2. The SMaRT impedance measurement software program was used to collect the data.

Results and Discussions

Part I: $BaTiO_3$-$BiScO_3$

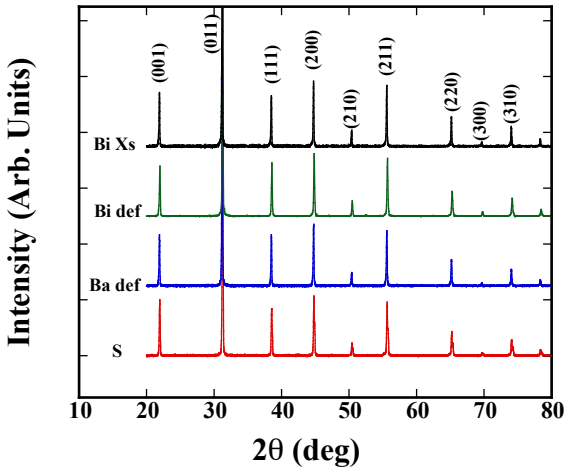

Fig. 9.6.1. X-ray diffraction patterns of as-sintered stoichiometric (S), barium deficient (Ba def), bismuth deficient (Bi def) and bismuth excess (Bi Xs) ceramics.

Stoichiometric and non-stoichiometric compositions based on $0.7BaTiO_3$-$0.3BiScO_3$ ceramics were prepared and figure 9.6.1 shows the x-ray diffraction (XRD) data on ground pellets. It was not possible to quantify the level of non-stoichiometry in the final ceramics due to limitations of analytical techniques available. Within the resolution of the laboratory instrument, all compositions exhibited a single perovskite phase with pseudo-cubic symmetry. Long-range pseudo-cubic structure is characteristic of relaxor ferroelectrics. Figure 9.6.2 provides more evidence of this relaxor behavior. All compositions were suitably dense (>92% of theoretical density). It can be noted that a

0.02 charge deficiency could also be created in these ceramics by adding extra barium to replace bismuth on A-sub lattice. However, the density values of these ceramics were extremely poor and the data for these specimens have not been reported here.

The dielectric properties of BT-BS ceramics as a function of temperature have been shown in figure 9.6.2. It could be noted that the peak permittivity values decreased slightly on introducing non-stoichiometry. The temperature stability of permittivity and dielectric losses seem to improve for the Ba def and Bi Xs ceramics. For the Bi def composition, however, the dielectric losses became high (>5%) at temperatures near 250 °C at 1 kHz frequency as opposed to ~400 °C for the stoichiometric sample. These data suggested a change in defect equilibrium conditions, which will be elucidated in the following sections of this article. All compositions exhibited a typical relaxor-like behavior with a characteristic broad and frequency-dependent dielectric anomaly. This is likely a result of disorder introduced with the addition of $BiScO_3$, which is an unstable perovskite under ambient conditions. The vast literature available on relaxors suggests that, above a threshold concentration, substitutions to $BaTiO_3$ of this kind destroy the macroscopic symmetry and lead to the formation of polar nano-regions (PNRs).[8, 34-37] Above the Burns temperature, relaxors lack any kind of dipole moment due to thermal fluctuations. However, as the temperature is lowered, the PNRs nucleate and grow, leading to a relaxor state in which the nano-domains are randomly oriented. At low enough temperatures, these PNRs start to mutually interact randomly and together with their statistical size and dipolar strength distribution, they give rise to broad and

frequency dependent dielectric permittivity.[35-37] A detailed analysis of relaxor behavior specific to the BT-BS system can be found elsewhere.[38-40]

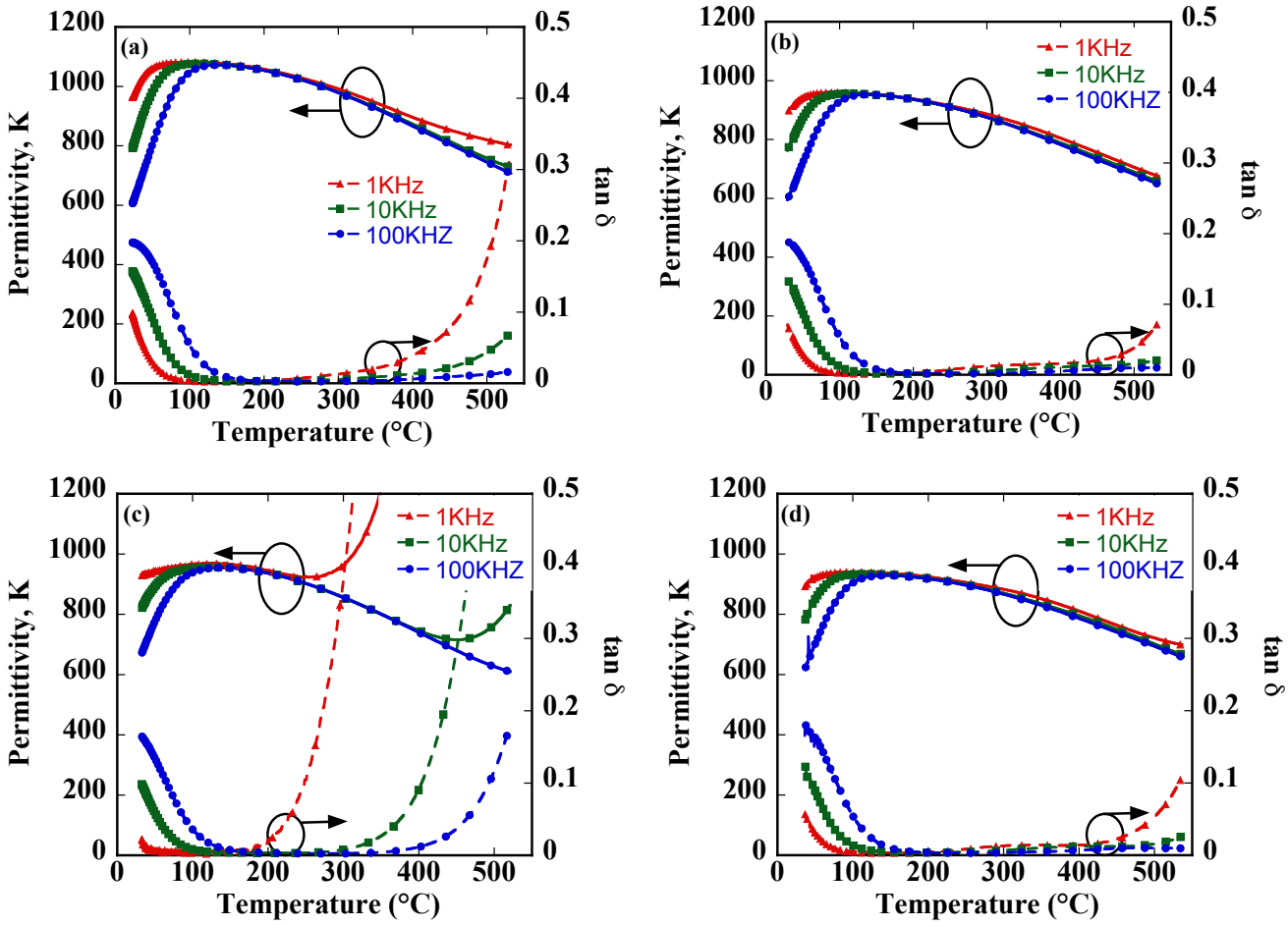

Fig. 9.6.2. Temperature dependent dielectric constant (solid lines) and dielectric loss (dashed lines) for **(a)** S, **(b)** Ba def, **(c)** Bi def, and **(d)** Bi Xs ceramics.

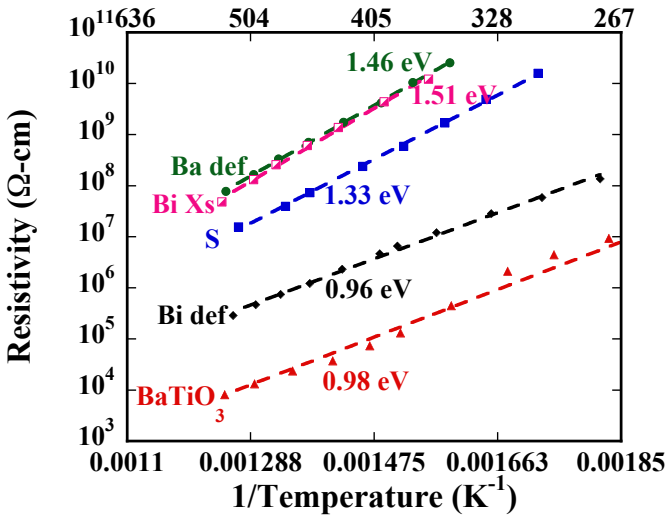

Fig. 9.6.3. The Arrhenius plots for bulk resistivity in air (pO_2 ~ 0.2 atm) for S, Ba def, Bi def and Bi Xs ceramics. The bulk resistivity values were extracted from AC impedance data. The top y-axis shows the corresponding temperatures in °C. The data for $BaTiO_3$ has also been shown for reference.

AC impedance spectroscopy was employed to investigate the transport properties. The Arrhenius plot for the bulk resistivity has been shown in figure 9.6.3. The activation energy values for conduction, calculated using equation 9.6.1, has also been indicated. Some important observations could be made from this figure. The p-type $BaTiO_3$ composition had lower resistivity values as compared to stoichiometric or non-stoichiometric BT-BS.[25, 26] The resistivity values of the S composition were ~3 orders of magnitude higher than for unmodified $BaTiO_3$. The activation energy for conduction also increased from 0.98 eV for unmodified $BaTiO_3$ to 1.33 eV for S. This suggests a shift towards a reduction in hole concentration with the addition of $BiScO_3$ to the BT solid solution. The resistivity and activation energy values further increased for the Ba def and Bi Xs composition, however they decreased significantly for the Bi def composition as compared to the S composition. The activation energy values of the Ba

def and Bi Xs ceramics were close to half of their measured optical band gap values.[8] High resistivity values in conjunction with high activation energy values for conduction suggested that the conduction mechanism was close to intrinsic-type for the Ba def and Bi Xs ceramics, as opposed to an extrinsic defect dominated conduction mechanism for rest of the compositions.

Figure 9.6.4 provides further insight into the change in conduction mechanism suggested by figure 9.6.3, using AC impedance measurements performed in atmospheres with different pO_2 (oxygen, air and nitrogen). The Ba def and Bi Xs ceramics appeared electrically homogeneous in all three atmospheres with only one observable semicircle over the frequency range employed (5 MHz – 0.1 Hz). The S sample was homogeneous in air and oxygen, but became electrically heterogeneous in nitrogen with small deviations from single-arc behavior occurring at lower frequencies. The Bi def sample was electrically heterogeneous in all three atmospheres. Focusing on the high frequency bulk components for all these ceramics, it can be noted that the bulk resistivity values were dependent on pO_2, which is indicative of a predominant electronic conduction mechanism in these ceramics rather than dominant oxide ion conduction.[25] The stoichiometric BT-BS (S) composition was p-type conducting, with resistivity values (related to the size of these arcs) highest in nitrogen and decreasing as the oxygen partial pressure increased.[25] This is expected since oxygen incorporation should lead to an increase in hole concentration and thus an increase in conductivity for a p-type ceramic as per the following defect reaction (equation 9.6.2):

$$V_O^{\cdot\cdot} + \frac{1}{2} O_2 \rightarrow O_O^X + 2h^{\cdot} \qquad \text{Eq. 9.6.2}$$

where, $V_O^{\cdot\cdot}$ is a doubly-ionized oxygen vacancy, O_O^X is an oxygen ion on an anion lattice site, and $h^{\cdot}$ represents a hole. The possible mechanisms responsible for this p-type behavior have been discussed elsewhere.[25] A similar p-type behavior can be seen for the Bi def ceramic as well (fig. 9.6.4c). The Bi Xs ceramic (fig. 9.6.4d), however, exhibited the opposite trend, with resistivity values highest in oxygen and lowest in nitrogen. This was indicative of n-type behavior since oxygen incorporation should lead to a decrease in electron concentration as per the following defect reaction:

$$V_O^{\cdot\cdot} + 2e' + \frac{1}{2} O_2 \rightarrow O_O^X \qquad \text{Eq. 9.6.3}$$

where, e' represents an electron. On the other hand, the Ba def sample exhibited an approximately similar trend as the Bi Xs sample, with resistivity values lowest in nitrogen atmosphere as compared to air and oxygen.

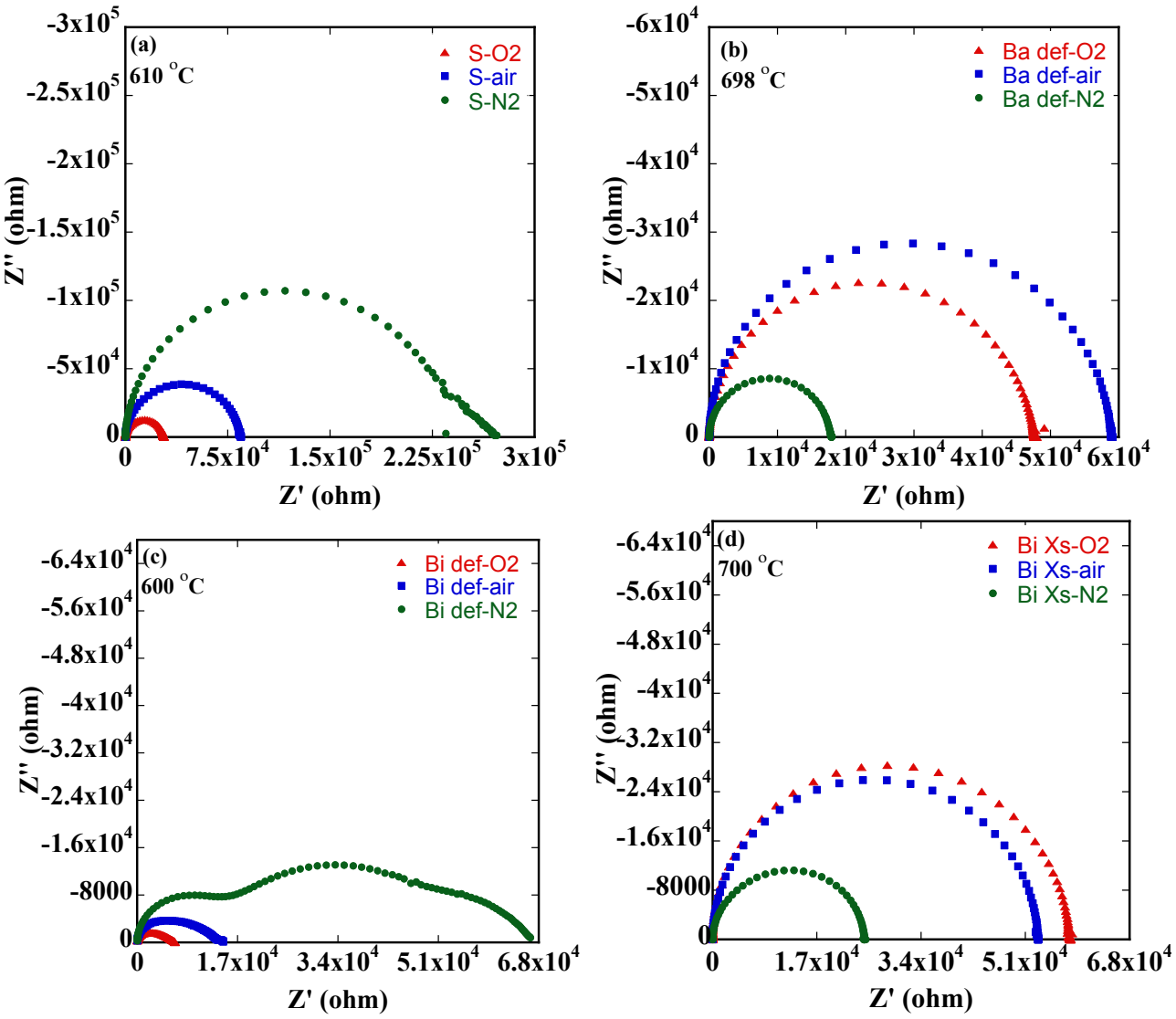

Fig. 9.6.4. The Z'' vs Z' Nyquist plots for S, Ba def, Bi def and Bi Xs ceramics for measurements performed in oxygen, air and nitrogen atmospheres. The measurements for Ba def and Bi Xs were performed at a higher temperature (~700 °C) for faster attainment of steady state. The frequencies decrease logarithmically on moving from left to right in these plots.

The data from figure 9.6.3 and 9.6.4 provide some important insights regarding the charge compensation mechanisms occurring on introducing cation non-stoichiometry. Replacing Ba^{2+} with Bi^{3+} in the Bi Xs sample should have the effect of donor doping. A positively charged donor dopant ($Bi_{Ba}^{\cdot}$), in general, can be compensated by negatively

charged cation vacancies ($V_{cation}^{n\prime}$) or electrons (e′) or both, depending upon the enthalpies associated with these compensation mechanisms. They can also reduce the concentration of pre-existing oxygen vacancies in the ceramics. If we consider only non-interacting point defects, which in reality may not be the case sometimes[41], cation vacancies should not lead to improvement in resistivity values, owing to their poor migration enthalpy in these perovskites systems.[42] Based on the improvement in resistivity observed in figure 9.6.3, therefore, the likely dominant mechanism for charge compensation for the Bi Xs sample should involve electrons and oxygen vacancies. Figure 9.6.4d, however, suggests towards a predominant electronic compensation mechanism as these ceramics were found to be n-type conducting. A possible charge neutrality equation can be expressed as:

Bi Xs: $[Bi_{Ba}^{\cdot}] + 2[V_O^{\cdot\cdot}] + [h^{\cdot}] \approx n[V_{cation}^{n\prime}] + [e\prime]$ Eq. 9.6.4

Following similar arguments, for the Bi def samples, the negatively charged bismuth vacancies ($V_{Bi}^{\prime\prime\prime}$) can theoretically be compensated by positively charged oxygen vacancies ($V_O^{\cdot\cdot}$) or holes ($h^{\cdot}$), thus acting as acceptor dopants. From the pO_2-dependent resistivity data (fig. 9.6.4c), it appears that holes dominate conduction in these ceramics, and therefore the likely compensation mechanism should be dominated by holes. It also agrees well with data presented in figure 9.6.3, where creating bismuth vacancies increases the conductivity of already p-type BT-BS. A possible charge neutrality in this case can be:

Bi def: $[V_{Bi}'''] + [e'] \approx 2[V_O^{\cdot\cdot}] + [h^{\cdot}]$ Eq. 9.6.5

The Ba def samples present an interesting case, because similar to Bi def case, the negatively charged barium vacancies (V_{Ba}'') could be compensated by relatively immobile oxygen vacancies or holes. Either of them would not be able to explain the increase in resistivity observed in figure 9.6.3 for Ba def samples. This may suggest towards a possible hole trapping mechanism becomes dominant in the Ba def sample leading to an increase in resistivity. There may be other mechanisms such as the precipitation of secondary phases that are rich in B-site cations, which would make the specimen effectively excess in bismuth on the A-site and thus it would be considered a donor-doped system. A behavior similar to the latter case was observed in $(Bi_{1/2}Na_{1/2})TiO_3$ (BNT) system where creating Na deficiency on A-sublattice resulted in a donor doping effect due to precipitation of TiO_2.[43] These findings present an important result and indicate that in the case of a sub-lattice site occupied by multiple cations with different valence states, the transport properties of cation-deficient ceramics are a strong function of the choice of cations used to create those vacancies.

Part II. $SrTiO_3$-$Bi(Zn_{1/2}Ti_{1/2})O_3$

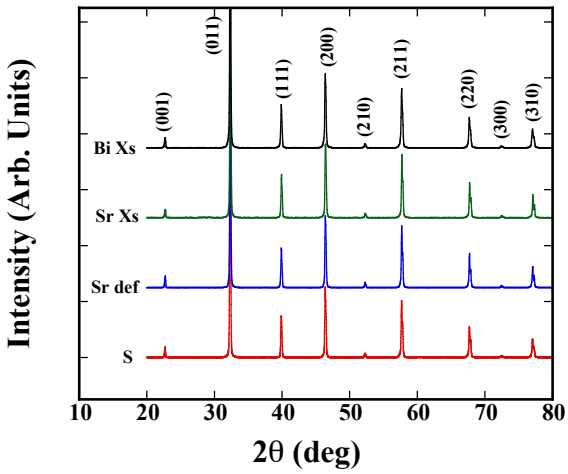

Fig. 9.6.5. X-ray diffraction patterns of as-sintered stoichiometric (S), strontium deficient (Sr def), strontium excess (Sr Xs) and bismuth excess (Bi Xs) ceramics.

Similar to the BT-BS system, stoichiometric and non-stoichiometric compositions based on $0.95SrTiO_3$-$0.05Bi(Zn_{1/2}Ti_{1/2})O_3$ ceramics were prepared and figure 9.6.5 shows their x-ray diffraction (XRD) data. As before, within the resolution limits of the laboratory instrument, all compositions exhibited a single perovskite phase and appeared cubic. All samples studied had measured density values greater than 95% of their theoretical value. The amount of charge excess or deficiency created in this case was limited to 0.01. Similar to the BT-BS experiments, a charge variance of 0.02 was attempted, however it was not possible to maintain single phase perovskite.

Figure 9.6.6 shows the dielectric permittivity and loss values for all the four stoichiometries as a function of temperature. Data were recorded over temperature range of 25 °C to ~550 °C which made it impossible to resolve the maxima in permittivity which occurred well below room temperature. However, in a different study, relaxor-like

characteristics were observed in stoichiometric ST-BZT ceramics close to -150 °C with a frequency-dependent permittivity maximum.[8] The dielectric loss values appear to be unaffected by introducing excess bismuth (Bi Xs) or creating strontium vacancies (Sr def) from the data in figure 9.6.6. However, for the Sr Xs composition, the losses increased significantly as compared to S.

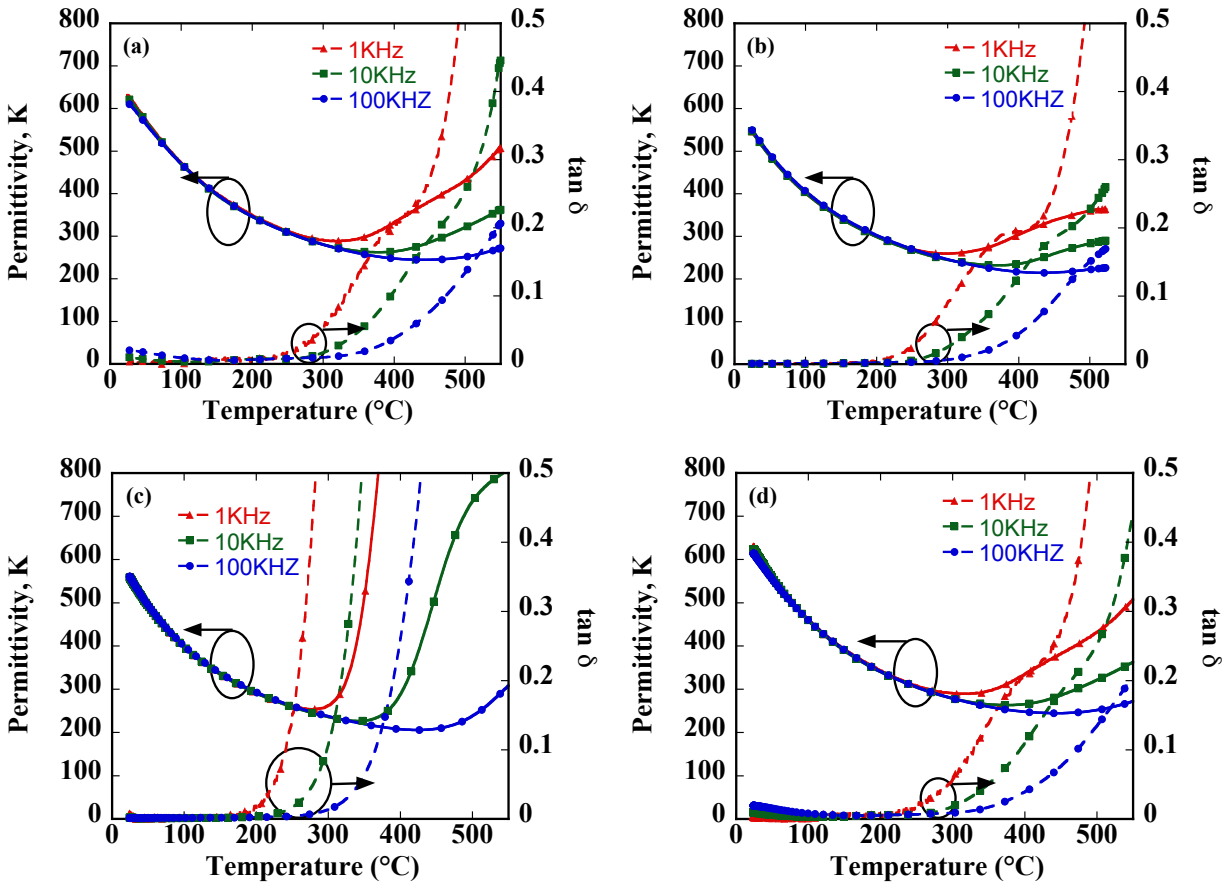

Fig. 9.6.6. Temperature dependent dielectric constant (solid lines) and dielectric loss (dashed lines) for **(a)** S, **(b)** Sr def, **(c)** Sr Xs, and **(d)** Bi Xs ceramics.

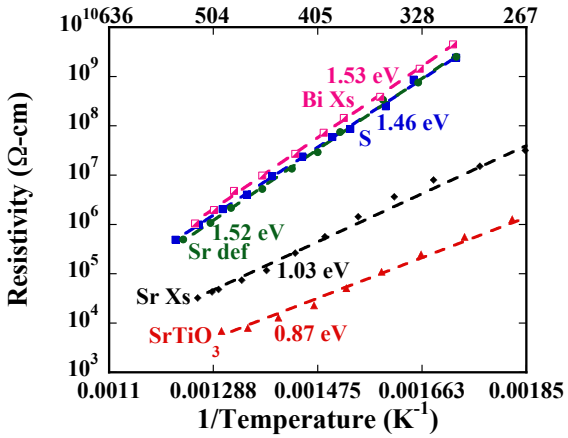

Fig. 9.6.7. The Arrhenius plots for bulk resistivity in air (pO_2 ~ 0.2 atm) for S, Sr def, Sr Xs and Bi Xs ceramics. The bulk resistivity values were extracted from AC impedance data. The top y-axis shows the corresponding temperatures in °C. The data for $SrTiO_3$ has also been shown for reference.

AC impedance spectroscopy was employed for these ceramics to provide insight into the transport properties. Figure 9.6.7 shows the Arrhenius plots for the bulk resistivity values obtained through extrapolation from AC measurements. Similar to the case of BT-BS, all the stoichiometric and non-stoichiometric samples had superior resistivity values as compared to p-type $SrTiO_3$. The stoichiometric ST-BZT (S) sample had resistivity values at least 2 orders of magnitude higher than $SrTiO_3$ and its activation energy for conduction was close to half the measured optical band gap[8], suggesting the conduction mechanism was close to intrinsic even in undoped ceramics. The stark differences in comparison to BT-BS however were that the Bi Xs and Ba def ceramics had almost same resistivity and activation energy values over the entire temperature range as S. This was interesting since this suggests that either these cation non-stoichiometries were not getting incorporated in the structure or they created compensating defects which were not capable of altering conductivity values. The Sr Xs sample, however, had significantly lower resistivity values as compared to rest of the ST-

BZT compositions, and their activation energy values were also lower suggesting an extrinsic conduction mechanism.

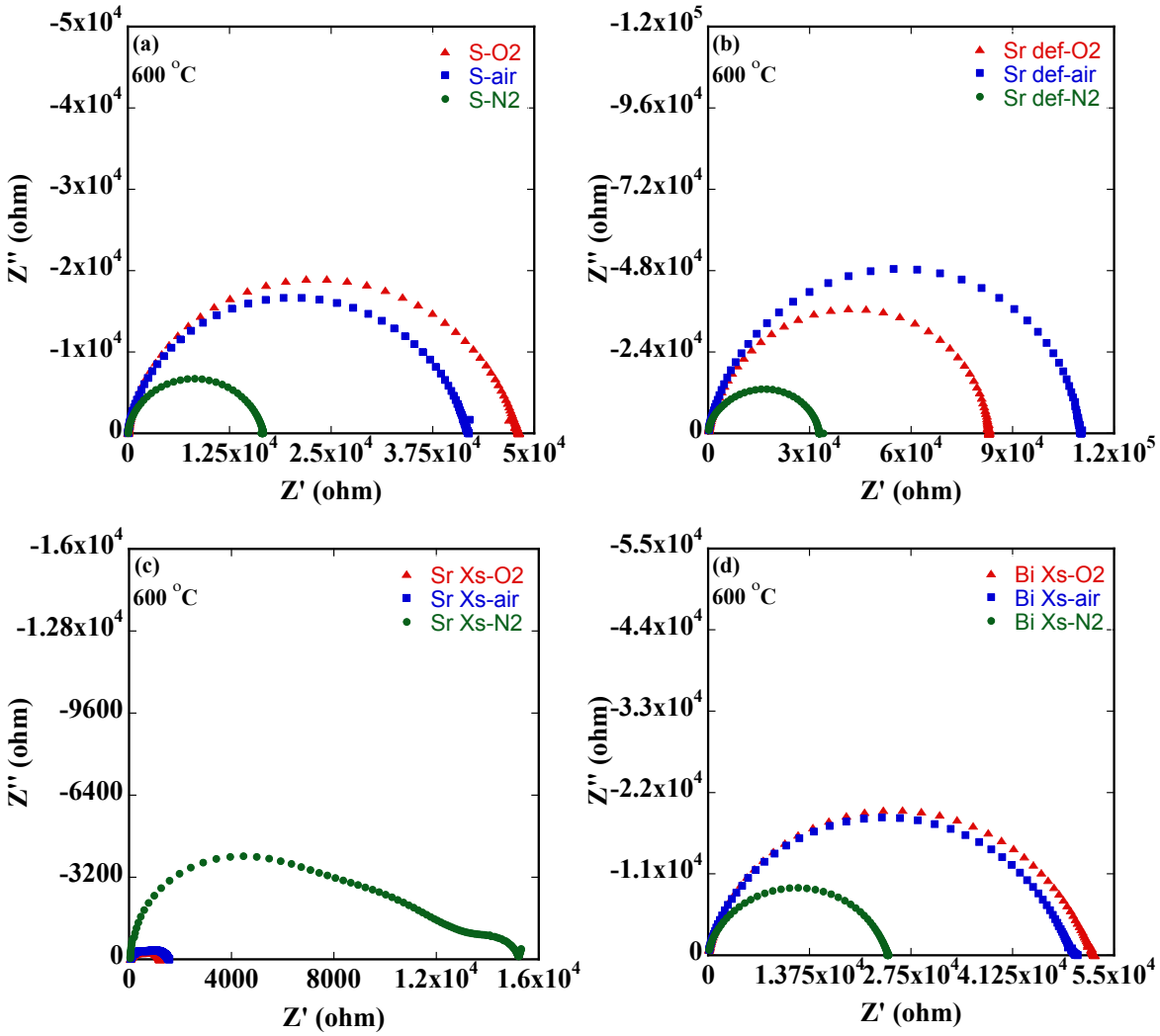

Fig. 9.6.8. The Z'' vs Z' Nyquist plots for S, Sr def, Sr Xs and Bi Xs ceramics for measurements performed in oxygen, air and nitrogen atmospheres. The frequencies decrease logarithmically on moving from left to right in these plots.

The pO_2-dependent Nyquist plots are shown in figure 9.6.8 for all four compositions. Based on arguments presented for BT-BS ceramics earlier, all these ceramics exhibited predominant electronic conduction as well. The S sample exhibited n-type conduction with bulk resistivity values highest in oxygen and lowest in nitrogen

atmosphere. This behavior was similar to the BT-BZT system studied in a separate report.[25] Similar to S, the Bi Xs sample (figure 9.6.8d) exhibited n-type conduction as well. The Sr Xs sample, on the other hand, showed p-type behavior since resistivity values were highest in nitrogen atmosphere and decreased with an increase in oxygen partial pressure. Similar to the case for the Ba def sample within the BT-BS system, the Sr def sample here approximately followed the behavior of the Bi Xs sample with resistivity values lower in nitrogen as compared to air or oxygen atmospheres.

Even though the ST-BZT (S) ceramic exhibited n-type conduction, given that the activation energy suggested nearly intrinsic conduction, acceptor doping may shift the defect equilibrium so as to increase the overall conductivity. This may explain the observed increase in conductivity on adding excess Sr to ST-BZT (Sr Xs sample). For the Bi Xs sample, it is expected that introducing Bi^{3+} to replace Sr^{2+} would result in an effective donor doping ($Bi_{Sr}^{\cdot}$). Donor doping can usually be compensated through negatively charged cation vacancies, electrons or the reduction of positively charged oxygen vacancy concentrations. However, since the resistivity values in this study did not significantly change, most likely the ionic compensation mechanism was predominant, assuming that the excess bismuth was incorporated in the crystal lattice.

Conclusions

The effect of minor non-stoichiometry in Bi-containing perovskites was highlighted in two material systems – p-type $BaTiO_3$-$BiScO_3$ and n-type $SrTiO_3$-$Bi(Zn_{1/2}Ti_{1/2})O_3$. Both these systems feature multiple cations with different valence states

on the same sublattice. For both these systems, acceptor doping (V_{Bi}''' for BT-BS or Sr_{Bi}' for ST-BZT) led to a deterioration in the insulation properties. Donor doping ($Bi_{Ba,Sr}^{\cdot}$) and creating cation vacancies by removing low-valence cations ($V_{Ba,Sr}''$) had no unfavorable effect on the resistivity behavior. While this led to a significant improvement in the resistivity for BT-BS ceramics, the resistivity values were relatively unchanged for ST-BZT ceramics. These results demonstrate the significant impact of cation non-stoichiometry in Bi-containing perovskites and suggest an important approach in tailoring the material properties in related materials. This study also highlights the difficulty in establishing a generic defect chemistry for all bismuth-containing perovskites.

Acknowledgements

This material is based upon work supported by the National Science Foundation under Grant No. DMR-1308032.

References

[1] Hennings D. Barium titanate based ceramic materials for dielectric use. International journal of high technology ceramics 1987;3:91-111.
[2] Aksel E, Jones JL. Advances in lead-free piezoelectric materials for sensors and actuators. Sensors 2010;10:1935-54.
[3] Maeder MD, Damjanovic D, Setter N. Lead free piezoelectric materials. Journal of Electroceramics 2004;13:385-92.
[4] Merkle R, Maier J. How Is Oxygen Incorporated into Oxides? A Comprehensive Kinetic Study of a Simple Solid‐State Reaction with SrTiO3 as a Model Material. Angewandte Chemie International Edition 2008;47:3874-94.
[5] Jaffe B, Cook WR, Jaffe H. Piezoelectric ceramics. 1971.
[6] Moulson AJ, Herbert JM. Electroceramics: materials, properties, applications: John Wiley & Sons; 2003.
[7] Zeb A, Milne S. High temperature dielectric ceramics: a review of temperature-stable high-permittivity perovskites. Journal of Materials Science: Materials in Electronics 2015;26:9243-55.
[8] Kumar N, Cann DP. Resistivity Enhancement and Transport Mechanisms in (1− x) BaTiO3–xBi (Zn1/2Ti1/2) O3 and (1− x) SrTiO3–xBi (Zn1/2Ti1/2) O3. Journal of the American Ceramic Society 2015;98:2548-55.
[9] Dai S, Lu H, Chen F, Chen Z, Ren Z, Ng D. In-doped SrTiO3 ceramic thin films. Applied physics letters 2002;80:3545.
[10] Denk I, Münch W, Maier J. Partial Conductivities in SrTiO3: Bulk Polarization Experiments, Oxygen Concentration Cell Measurements, and Defect‐Chemical Modeling. Journal of the American Ceramic Society 1995;78:3265-72.
[11] Gerblinger J, Meixner H. Fast oxygen sensors based on sputtered strontium titanate. Sensors and Actuators B: Chemical 1991;4:99-102.
[12] Choi SM, Stringer CJ, Shrout TR, Randall CA. Structure and property investigation of a Bi-based perovskite solid solution:(1-x) Bi (Ni 1/2 Ti 1/2) O 3–xPbTiO 3. Journal of applied physics 2005;98:034108--4.
[13] Smolenskii G, Isupov V, Agranovskaya A, Popov S. Ferroelectrics with diffuse phase transitions. Soviet Physics-Solid State 1961;2:2584-94.
[14] Raengthon N, Cann DP. High temperature electronic properties of BaTiO3–Bi (Zn1/2Ti1/2) O3–BiInO3 for capacitor applications. journal of Electroceramics 2012;28:165-71.
[15] Dittmer R, Jo W, Damjanovic D, Rödel J. Lead-free high-temperature dielectrics with wide operational range. 2011.
[16] Huang C-C, Cann DP, Tan X, Vittayakorn N. Phase transitions and ferroelectric properties in BiScO3-Bi (Zn1/2Ti1/2) O3-BaTiO3 solid solutions. Journal of Applied Physics 2007;102:044103.
[17] Ogihara H, Randall CA, Trolier‐McKinstry S. High‐Energy Density Capacitors Utilizing 0.7 BaTiO3–0.3 BiScO3 Ceramics. Journal of the American Ceramic Society 2009;92:1719-24.
[18] Fujii I, Nakashima K, Kumada N, Wada S. Structural, dielectric, and piezoelectric properties of BaTiO3-Bi (Ni1/2Ti1/2) O3 ceramics. Journal of the Ceramic Society of Japan 2012;120:30-4.

[19] Wang Y, Chen X, Zhou H, Fang L, Liu L, Zhang H. Evolution of phase transformation behavior and dielectric temperature stability of BaTiO 3–Bi (Zn 0.5 Zr 0.5) O 3 ceramics system. Journal of Alloys and Compounds 2013;551:365-9.
[20] Huang C-C. Structure and piezoelectric properties of lead-free bismuth-based perovskite solid solutions: ProQuest; 2008.
[21] Choi DH, Baker A, Lanagan M, Trolier‐McKinstry S, Randall C. Structural and Dielectric Properties in (1− x) BaTiO3–xBi (Mg1/2Ti1/2) O3 Ceramics (0.1≤ x≤ 0.5) and Potential for High‐Voltage Multilayer Capacitors. Journal of the American Ceramic Society 2013;96:2197-202.
[22] Kumar N, Ionin A, Ansell T, Kwon S, Hackenberger W, Cann D. Multilayer ceramic capacitors based on relaxor BaTiO3-Bi (Zn1/2Ti1/2) O3 for temperature stable and high energy density capacitor applications. Applied Physics Letters 2015;106:252901.
[23] Takenaka T, Maruyama K-i, Sakata K. (Bi1/2Na1/2) TiO3-BaTiO3 system for lead-free piezoelectric ceramics. Japanese Journal of Applied Physics 1991;30:2236.
[24] Shrout TR, Zhang SJ. Lead-free piezoelectric ceramics: Alternatives for PZT? Journal of Electroceramics 2007;19:113-26.
[25] Kumar N, Patterson EA, Frömling T, Cann DP. Conduction mechanisms in BaTiO3-Bi(Zn1/2Ti1/2)O3 ceramics. Journal of the American Ceramics Society 2016.
[26] Kumar N, Patterson EA, Frömling T, Cann DP. DC-bias dependent impedance spectroscopy of BaTiO 3–Bi (Zn 1/2 Ti 1/2) O 3 ceramics. Journal of Materials Chemistry C 2016;4:1782-6.
[27] Prasertpalichat S, Cann DP. Hardening in non-stoichiometric (1− x) Bi0. 5Na0. 5TiO3–xBaTiO3 lead-free piezoelectric ceramics. Journal of Materials Science 2016;51:476-86.
[28] Dawber M, Rabe K, Scott J. Physics of thin-film ferroelectric oxides. Reviews of modern physics 2005;77:1083.
[29] Vanderbilt D. First-principles based modelling of ferroelectrics. Current Opinion in Solid State and Materials Science 1997;2:701-5.
[30] Raengthon N, Sebastian T, Cumming D, Reaney IM, Cann DP. BaTiO3‐Bi (Zn1/2Ti1/2) O3‐BiScO3 Ceramics for High‐Temperature Capacitor Applications. Journal of the American Ceramic Society 2012;95:3554-61.
[31] Hirose N, West AR. Impedance spectroscopy of undoped BaTiO3 ceramics. Journal of the American Ceramic Society 1996;79:1633-41.
[32] Irvine JT, Sinclair DC, West AR. Electroceramics: characterization by impedance spectroscopy. Advanced Materials 1990;2:132-8.
[33] Smyth DM. The defect chemistry of metal oxides. The Defect Chemistry of Metal Oxides, by DM Smyth, pp 304 Foreword by DM Smyth Oxford University Press, Jun 2000 ISBN-10: 0195110145 ISBN-13: 9780195110142 2000;1.
[34] Cross LE. Relaxor ferroelectrics. Ferroelectrics 1987;76:241-67.
[35] Kleemann W. The relaxor enigma—charge disorder and random fields in ferroelectrics. Frontiers of Ferroelectricity: Springer; 2006. p. 129-36.
[36] Samara GA. The relaxational properties of compositionally disordered ABO3 perovskites. Journal of Physics: Condensed Matter 2003;15:R367.
[37] Shvartsman VV, Lupascu DC. Lead‐Free Relaxor Ferroelectrics. Journal of the American Ceramic Society 2012;95:1-26.

[38] Ogihara H, Randall CA, Trolier‐McKinstry S. Weakly coupled relaxor behavior of BaTiO3‐BiScO3 ceramics. Journal of the American Ceramic Society 2009;92:110-8.
[39] Bharadwaja S, Kim J, Ogihara H, Cross L, Trolier-McKinstry S, Randall C. Critical slowing down mechanism and reentrant dipole glass phenomena in (1− x) BaTiO 3 ‐ x BiScO 3 (0. 1⩽ x⩽ 0. 4): The high energy density dielectrics. Physical Review B 2011;83:024106.
[40] Bharadwaja S, Trolier-McKinstry S, Cross L, Randall C. Reentrant dipole glass properties in (1− x) BaTiO3− xBiScO3, 0.1≤ x≤ 0.4. Applied Physics Letters 2012;100:022906.
[41] Vance ER, Hanna JV, Hadley J. Cation vacancies in perovskites doped with La and Gd. Advances in Applied Ceramics 2012;111:94-8.
[42] Yoo H-I, Song C-R, Lee D-K. BaTiO3− δ: defect structure, electrical conductivity, chemical diffusivity, thermoelectric power, and oxygen nonstoichiometry. Journal of electroceramics 2002;8:5-36.
[43] Li M, Zhang H, Cook SN, Li L, Kilner JA, Reaney IM, et al. Dramatic influence of A-site nonstoichiometry on the electrical conductivity and conduction mechanisms in the perovskite oxide Na0. 5Bi0. 5TiO3. Chemistry of Materials 2015;27:629-34.

9.7. Defect Chemistry of $BaTiO_3$-Bi$M$$O_3$ Ceramics

Nitish Kumar[1], Edward Gorzkowski[2], Peter Eschbach[1], Ian Love[1], Steven R. Reese[4], Syed Khalid[3] and David P. Cann[1]

1. Materials Science, School of Mechanical, Industrial, and Manufacturing Engineering, Oregon State University, Corvallis, Oregon 97331, USA

2. Naval Research Laboratory, Washington, DC, 20375, USA

3. Brookhaven National Laboratory, Upton, NY 11973, USA

4. School of Nuclear Science and Engineering, Oregon State University, Corvallis, Oregon 97331, USA

Abstract

Several prospective candidates for n-type behavior in BT-BZT were studied—loss of volatile cations, oxygen vacancies, bismuth present in multiple valence states and precipitation of secondary phases. Combined x-ray and neutron diffraction, prompt gamma neutron activation analysis and electron energy loss spectroscopy suggested much higher oxygen vacancy concentration in BT-BZT ceramics as compared to BT alone. X-ray photoelectron spectroscopy and x-ray absorption spectroscopy did not suggest presence of bismuth in multiple valence states. At the same time, using transmission electron microscopy, some secondary phases were observed, whose compositions were such that they could result in effective donor doping in BT-BZT ceramics. Using experimentally determined thermodynamic parameters for BT and slopes of Kröger-Vink plots, it has been suggested that an ionic compensation mechanism is prevalent in these ceramics instead of electronic compensation. At the same time, these defects in BT-BZT ceramics have an effect of shifting the conductivity minimum in Kröger-Vink plots to higher oxygen partial pressure values, resulting in a significantly higher resistivity values in air atmosphere and n-type behavior. This provides an important tool to tailor transport properties and defects in BT-BiMO$_3$ ceramics, to make them better suited for dielectric or other applications.

Introduction

The Bi-based perovskites have been studied by researchers for many decades, due to their similarity with toxic Pb in terms of electronic structure and environmental as well as health considerations.[1] In last two decades, bismuth has found special attention in

following two fields of research– (1) the solid solutions of Bi-perovskite with $BaTiO_3$ (BT) helps improve their properties for energy storage applications across length scales[2-4], and (2) the Bi-perovskites, especially the ones based on $(Bi_{1/2}Na_{1/2})TiO_3$ (BNT)[5], have shown promising properties for replacement of harmful Pb in PZT[6] for actuator applications, and oxygen conduction applications[7, 8]. While significant progress has been made towards improving the material properties of these ceramics, an important aspect of materials' understanding—the defect chemistry, is often ignored, in most cases due to limitations of the techniques available, which can conveniently characterize local point defects. Defects, on the other hand, are critical for understanding of several phenomena such as electromechanical fatigue, aging, transport mechanisms, electric field/temperature-dependent phase transitions and others, the knowledge of which can be used to tailor material properties to suit specific requirements. In this article, the defect chemistry of $BaTiO_3$-$Bi(Zn_{1/2}Ti_{1/2})O_3$ (BT-BZT) ceramics has been studied and it is hoped that it may act as a template for studying defect chemistry of similar BT-BiMO$_3$ materials (M=metal). The BT- BiMO$_3$ ceramics have been extensively studied recently as they have exciting properties for many applications as compared to traditional BT-based ceramics in terms of temperature-stability of permittivity, energy density values, insulation properties and others, as can be found in several other publications.[3, 4, 9]

The BT-BiMO$_3$ ceramics typically crystallize with perovskite structures, which along with their properties are challenging to investigate. The study of structural changes that govern macroscopic properties in these ceramics is often complicated by differences in local and average displacements.[10] Undoped BT has a typical tetragonal (P4mm)

symmetry at room temperature and its origin of polarization is explained by a relative displacement of Ti ions along <111> pseudo-cubic directions, while average displacement visible to typical diffraction experiments lies along [110].[11] The case of solid solutions between BT and BiMO$_3$ ceramics is even more complex. It was shown that for BT-BiMO$_3$ ceramics, especially those which presumably exhibit relaxor characteristics, the macroscopic structure appears nearly cubic, while there are still significant distortions present at local level.[3, 12] Using the Pair Distribution Function approach, it was shown that local tetragonal distortion in BT-BZT is disrupted over a length scale of ~10 unit cells, leading to a pseudo-cubic behavior.[3] It was also recently reported that Bi and Ti exhibit strong correlated off-centering owing to bonding requirements, and oxygen atoms also displayed strong anisotropic probability density distributions with preferential displacements along <110> directions towards nearest Bi atoms.[12]

Apart from their complex crystal-chemistry, these BT-BiMO$_3$ ceramics exhibit several unique properties, some of which were mentioned above. Recently, using a time-resolved x-ray diffraction technique, a direct and simultaneous measurement of lattice strain and polarization reversal was studied, in an attempt to relate intrinsic and macroscopic properties.[13] In separate reports on macroscopic transport properties, it was shown that on adding small amounts of BiMO$_3$ to BT, their insulation properties improve by orders of magnitude, indicating a drastic change in underlying defect equilibrium conditions.[14, 15] At the same time, without any deliberate doping, it was accompanied by a reduction in hole concentration (which are dominant conducting

species in BT), sometimes leading to a complete transition to an n-type behavior.[16] A thorough study of their complex defect mechanisms has been performed in this article, which intends to explain the discernible modification in transport properties observed on adding Bi-perovskites to BT. The defect chemistry is expected to be strongly influenced by factors like solubility limits of different cations, volatile nature of Bi and other cations, oxygen stoichiometry, different bonding characteristics of cations sharing the same sublattice positions, enthalpies associated with specific defect species in a given condition, microstructure and others. Several techniques such as temperature and oxygen partial pressure (pO_2)- and temperature-dependent impedance spectroscopy, x-ray photoelectron spectroscopy (XPS), x-ray absorption spectroscopy (XAS), thermogravimetric analysis (TGA) with in-situ mass spectroscopy, synchrotron and neutron diffraction, prompt gamma neutron activation analysis (PGNAA), energy dispersive spectroscopy (EDS) and electron energy loss spectroscopy (EELS) have been used to study the same.

Brief review of defect chemistry of BT

Before discussing the defect chemistry of BT-BiMO$_3$, a concise summary of the defect chemistry of BT has been presented, which is crucial to understanding of the defect-chemistry of BT-based solid solutions. As site occupancy can have a signfiicant influence on defect chemistry BT-BiMO$_3$, a brief discussion of the past research on site occupancies in BT has also been made. There are several inconsistencies in the literature regarding the defect chemistry of BT, especially for the case of donor-doped ceramics.

Some of the factors responsible for this are—presence of multiple kinds of defects in comparable concentrations (intrinsic and extrinsic, electronic and ionic)[17], interaction between defects when they are present in high concentrations to form defect complexes and associates[18], presence of interfaces in polycrystalline ceramics[19], possibility of measurements being done in metastable equilibrium[20], unintentional impurities[21], inhomogeneity due to non-stoichiometry[22, 23] and others[17, 24].

The defect chemistry of undoped (or acceptor doped) BT is relatively well understood, under the assumption of non-interacting point defects, even though there may be some discrepancies on origin of acceptor defects. The acceptor dopants have been suggested to originate from low-valence impurities present in precursors[21] and/or negatively charged cation vacancies[25]. Owing to this reason, the defect chemistry of undoped and slightly acceptor doped BT are expected to be similar, and have been merged together here for brevity. For the sake of summarizing, the net acceptor content will be denoted by [A′], irrespective of their origin. Most authors agree that other important defect species in BT are oxygen vacancies ($V_O^{\cdot\cdot}$), electrons (e′) and holes ($h^{\cdot}$), and interstitials are often not considered to be energetically favorable to be present in these ceramics.[26, 27] The electrons, holes and oxygen vacancies govern the insulation properties, owing to their relatively higher mobility values. The various reactions along with their mass-action expressions can be written as the following.[21]

Reduction reaction:

$$O_O^X \leftrightarrow V_O^{\cdot\cdot} + 2e' + \tfrac{1}{2}O_2 \qquad \text{Eq. 9.7.1}$$

$$K_{red}=[V_O^{\cdot\cdot}]n^2pO_2^{1/2}$$

where, O_O^X is an oxygen atom at its own lattice position, as per the Kröger-Vink notation[28], and n is electron concentration (i.e. [e′]).

Oxidation reaction:

$$V_O^{\cdot\cdot} + \tfrac{1}{2}O_2 \leftrightarrow O_O^X + 2h^{\cdot} \qquad \text{Eq. 9.7.2}$$

$$K_{ox} = p^2 * pO_2^{-1/2}/[V_O^{\cdot\cdot}],$$

where, p is hole concentration.

The intrinsic electronic and Schottky disorder and their mass-action expressions can be written as:

$$nil \leftrightarrow e' + h^{\cdot} \qquad \text{Eq. 9.7.3}$$

$$K_i = np$$

$$nil \leftrightarrow V_{Ba}'' + V_{Ti}'''' + 3V_O^{\cdot\cdot} \qquad \text{Eq. 9.7.4}$$

$$K_s = [V_{Ba}''][V_{Ti}'''']{[V_O^{\cdot\cdot}]}^3$$

where, V_{Ba}'' and V_{Ti}'''' are barium and titanium vacancies, respectively. Later, oxidation by a hole trapping mechanism by acceptors and reduction by electron trapping by oxygen

vacancies was also considered by Smyth and Hardtl.[21, 29] Finally, the electroneutrality expression is given by:

$$n + [A'] = p + 2[V_O^{\cdot\cdot}] \qquad \text{Eq. 9.7.5}$$

These equations (9.7.1-9.7.5) can be used to construct a complete defect diagram, which can be found elsewhere[16, 21]. The defect diagram is usually divided into three regions, depending on dominant defect species dominating transport properties for acceptor-doped BT. The following can be readily seen using equations (9.7.1-9.7.5):

At extremely low pO_2, $n \approx 2[V_O^{\cdot\cdot}]$,

$$n \approx (2K_{red})^{1/3} pO_2^{-1/6} \qquad \text{Eq. 9.7.6}$$

At high pO_2, $[A'] \approx 2[V_O^{\cdot\cdot}]$,

$$n \approx (2K_{red}/[A'])^{1/2} pO_2^{-1/4} \text{ and } p \approx (K_{red}\,[A']/2)^{1/2} pO_2^{+1/4} \qquad \text{Eq. 9.7.7}$$

At high very pO_2, $[A'] \approx p$. In this region, the conductivity is expected to be independent of pO_2, however, this is often difficult to achieve experimentally. The concentration of other non-dominant defects in a region can easily be calculated using equations (9.7.1-9.7.5).

The defect chemistry of donor-doped BT is more controversial and different authors have suggested electrons, titanium vacancies, or a combination of barium and

titanium vacancies as compensating defects.[23, 30, 31] Furthermore, some authors believe the compensation mechanism to be dependent on donor concentration, [$D^{\cdot}$], while others disagree.[32] Based on the model presented by Smyth *et al.*[31], the defect diagram (or Kröger-Vink diagram) can be divided into four regions, depending on dominant defect species, assuming Schottky defects are favored ionic defects. It can be perceived using similar equations as the acceptor doped case, that for low pO_2, the n-type behavior can be described by equation 9.7.1 above with $n \propto pO_2^{-1/6}$. At intermediate pO_2, [$D^{\bullet}$] ≈ n and conductivity can be expected to be independent of pO_2. At higher pO_2, an ionic compensation (cation vacancies) mechanism is expected to dominate and $(n,p) \propto pO_2^{\pm 1/4}$, similar to equation 9.7.7 above. At very high pO_2, the behavior is dominated by $x[V_{cation}^{x\prime}] \approx p \propto pO_2^{-1/6}$. Some further details can be found later in the article, when donor doping in BT-BZT has been discussed.

Another important consideration for solid solutions such as BT-BiMO$_3$, which have multiple cations sharing the same sub-lattice, is the site occupancy. For BT, site occupancy has been studied in details especially for lanthanides, as they are considered "magic" dopants after they were found to increase the lifetime of devices based on BT under certain formulations and thermal history.[33, 34] Several of these rare earth cations were found to be amphoteric in nature (*e.g.* Dy, Gd, Er, Ho and others*.) i.e.* they could occupy either A- or B-sublattice and could exhibit multiple valence states.[33-35] Furthermore, their site occupancy was quite sensitive to Ba/Ti ratio in the ceramics, and by controlling this ratio and oxygen partial pressure of processing they could be forced to occupy the desired sub-lattice site. There are other examples, *e.g.* Ca, which can

substitute for either Ba or Ti in BT.[36] The bismuth cation can exist in two valence states +3 (radius = 1.38 Å in 12 coordination state by interpolation[37]), and +5 (radius= 0.76 Å in 6 coordination state[37]), which makes a site occupancy study relevant for BT-BiMO$_3$ ceramics as well.

Experimental Details

Polycrystalline ceramics were prepared using a conventional solid-state method. High purity powders of $BaCO_3$ (>99.8%, Alfa Aesar), Bi_2O_3 (>99.9%, Aldrich), TiO_2 (>99.9%, Aldrich), and ZnO (>99.9%, Alfa Aesar) were mixed in the appropriate amounts to prepare stoichiometric compositions based of $BaTiO_3$ (BT), 0.925BT-0.075$Bi(Zn_{1/2}Ti_{1/2})O_3$ (7.5BZT)and 0.75BT-0.25$Bi(Zn_{1/2}Ti_{1/2})O_3$ (25BZT). The mixed powders were ground using a vibratory mill for 6 hours and then dried overnight in an oven (~80 °C). The BT-BZT powders were calcined in alumina crucibles at 950 °C-1050 °C for 4 hours and then milled with ~3 wt% binder (Rhoplex HA-8, Dow Chemical Company, USA) and dried again. Green pellets in the shape of thin discs were prepared by uniaxial cold-pressing at a pressure of 200 MPa and then sintered on a bed of calcined powder in a closed alumina crucible between 1150 °C-1350 °C for 4 hours. Some $BaTiO_3$ ceramics were prepared from $BaTiO_3$ powders from Sakai Chemical Industry for comparison and exhibited similar electronic properties as the BT above. All the sintered pellets were polished to ~800 mm thickness. X-ray diffraction (Bruker AXS D8 Discover, Madison, WI, USA) were performed on ground pellets for preliminary phase analysis. For electrical measurements, silver or platinum electrodes were used. The Pt electrodes were used wherever pO_2-dependent measurements were performed. In case of silver electrode, paste was applied on both sides of the pellets and then fired at 700 °C for 30 min. In case of platinum, it was applied on both sides and fired at 900 °C for 15 min before performing the measurements. The impedance measurements were performed using a high temperature measurement cell (NorECs AS ProbostatTM, Oslo, Norway) and an impedance analyzer (Solartron SI1260A equipped with Solartron 1296A dielectric

interface, Farnborough, UK). The SMaRT impedance measurement software program was used to collect the data in the frequency range of 1 MHz to 0.1 Hz.

X-ray Photoelectron Spectroscopy (XPS) spectra from the 25BZT ceramics were acquired on a ThermoScientific ESCALAB 250 spectrometer located at the Center for Advanced Materials Characterization in Oregon (CAMCOR). Photoemission was stimulated by a beam of monochromatized Al Kα x-rays with a nominal spot size at the sample surface of 500μm. A low energy electron source was used for charge neutralization. The spectra were acquired at a pass energy of 20 eV (high resolution spectra) or 150 eV (survey spectra). Data analysis, including peak fitting, was performed with Avantage software, provided by the manufacturer.

High-resolution synchrotron powder diffraction data were collected on 25BZT powders using beamline 11-BM at the Advanced Photon Source (APS), Argonne National Laboratory. An appropriate amount of the sample was loaded into a Kapton tube, sealed and mounted on the base provided by the 11-BM beamline of the APS. The diffraction experiments were carried out at room temperature using monochromatic synchrotron radiation of wavelength 0.413639 Å and a step size of 0.001°. Time of flight (TOF) powder neutron diffraction data were collected on the POWGEN instrument at the Spallation Neutron Source (SNS) in the Oak Ridge National Lab (ORNL) for BT and 25BZT powders obtained by crushing sintered pellets. A vanadium container was filled with appropriate amount of powder and sent via the mail-in service to the SNS. Data were collected to cover a d-spacing range of 0.3−3.0 Å. The crystal structure was refined

using the Rietveld refinement program GSAS-II.[38] The Chebyschev profile was used to fit the background and the number of background parameters used was 10. Parameters refined included peak-shape parameters, scale, lattice parameters, atomic positions, isotropic displacement parameters, thermal occupancies and others.

High-resolution transmission electron microscopy (TEM), Energy-dispersive X-ray spectroscopy (EDS) and Electron Energy Loss spectroscopy (EELS) were used to investigate microstructural and microchemical features. The TEM samples were prepared using low-energy Focussed-ion beam (FIB), at cryogenic temperatures to minimize any structural damage and oxygen rearrangement due to local heating at Center for Advanced Materials Characterization in Oregon (CAMCOR). The measurements were also performed at cryogenic temperatures using FEI TITAN TEM operated at 200 kV, at Oregon State University. The spectra were recorded at an approximate collection angle of 7.7 mrad and convergence angle of 9.8 mrad. Gatan DigitalMicrograph and TIA software were used for image processing and acquirirng EDS and EELS spectra. The EELS spectra were taken from thin (<100 nm) regions of the sample to avoid plural scattering contribution. For background removal, a power law function was used. A constant signal integration window was used for all the spectra, which also covered near-edge fine structures. The quantification was performed through the following equation:

$$\frac{N_A}{N_B} = \frac{\sigma_B(\beta,\Delta)}{\sigma_A(\beta,\Delta)} \times \frac{I_A(\beta,\Delta)}{I_B(\beta,\Delta)} \qquad \text{Eq. 9.7.8}$$

where, N is relative number of atoms, I is integrated intensity, σ is partial cross-section for a given collection angle (β) and a given integration window (Δ). The theoretical cross section were not expected to be reliable for some atoms *e.g.* Ba $M_{4,5}$ edge, and there a *k*-factor approach was used for quantification, which basically provides quantification relative to a known standard.[39]

Extended X-ray absorption fine structure (EXAFS) was measured for L3 edges of bismuth in transmission and florescence modes, at Stanford Synchrotron Radiation Lightsource. The data was processed using Athena software.[40] Thermogravimetric analysis (TGA) with in-situ mass spectroscopy was performed on powdered sample at United States Naval Research Laboratory. X-ray absorption spectroscopy was performed on BT-BZT, NaBiO3 and Bi2O3 samples at Stanford Synchrotron Radiation Lightsource. Prompt gamma neutron activation analysis (PGNAA) was performed on BT and BT-BZT samples at Oregon State University (OSU) TRIGA reactor.

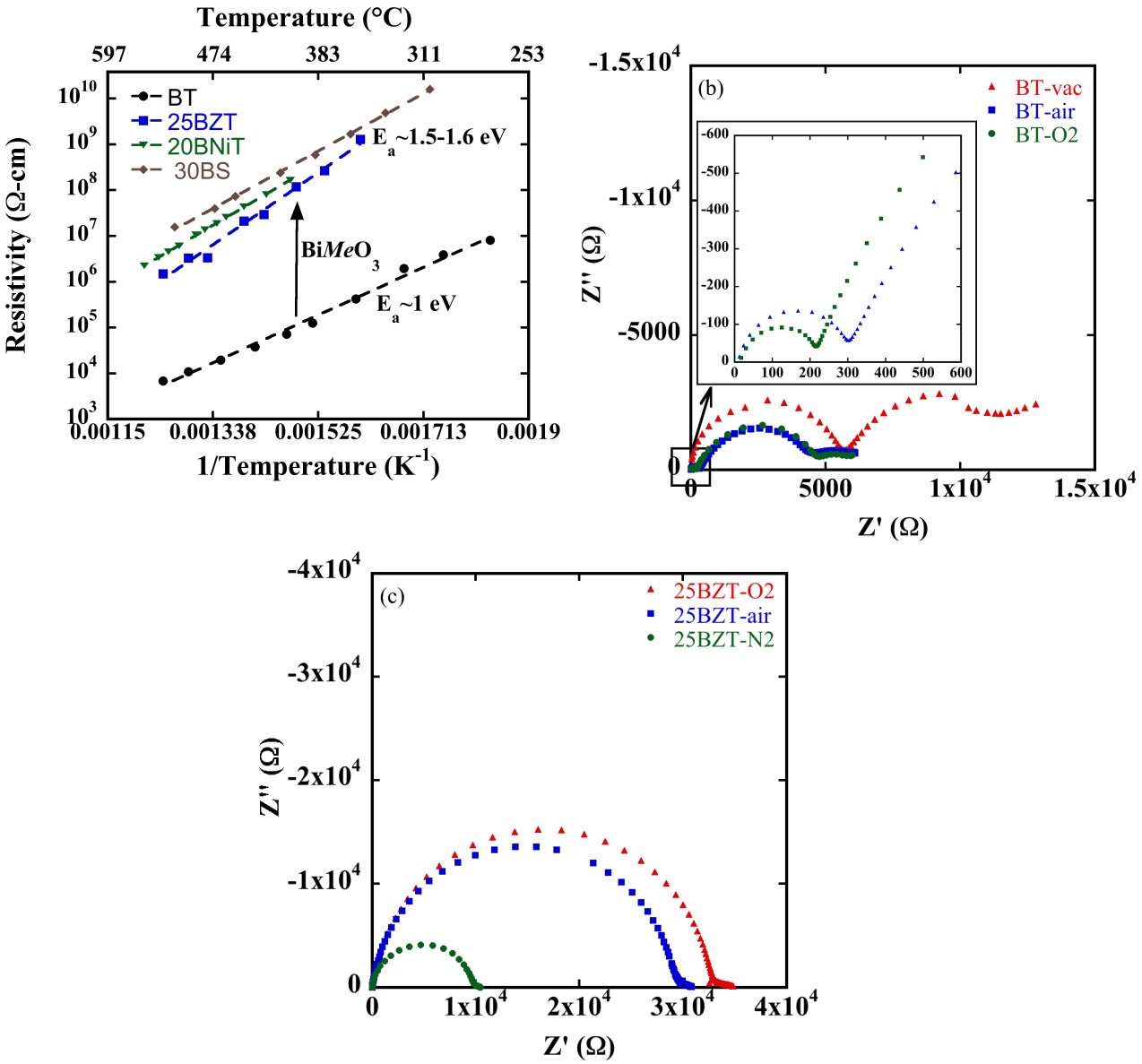

Fig. 9.7.1. (a) Arrhenius plots of bulk resistivity showing orders of magnitude improvement in resistivity on adding BiMO_3 to BT, for BT-0.25BZT, BT-0.3BiScO3 and BT-0.2Bi($Ni_{1/2}Ti_{1/2}$)O_3. (b) Nyquist plots for BT in vacuum (pO2~10^{-5} atm), air and O2 demonstration p-type behavior. (c) Nyquist plots for 25BZT in N2, air and O2 demonstration n-type behavior.

Figure 9.7.1a presents data from some solid solutions between BT and BiMO$_3$ compounds to show the resistivity enhancement that occurs with the addition of BiMO$_3$ to BT. Several BiMO$_3$ compounds *e.g.* Bi(Zn$_{1/2}$Ti$_{1/2}$)O$_3$, BiScO$_3$, Bi(Ni$_{1/2}$Ti$_{1/2}$)O$_3$, (Bi$_{1/2}$Li$_{1/2}$)TiO$_3$, Bi(Mg$_{2/3}$Nb$_{1/3}$)O$_3$, Bi(Mg$_{1/2}$Ti$_{1/2}$)O$_3$, Bi(Zn$_{2/3}$Nb$_{1/3}$)O$_3$, Bi(Zn,Sc,Ti)O$_3$ and others are known to exhibit this phenomenon of improvement in resistivity by orders of magnitude with respect to unmodified BT or ST as determined by measuring resistivity directly or through indirect methods like dielectric loss measurements.[3, 14, 41-46] The study to determine the type of charge carrier in these solid solutions is scarce, however, some of them have been shown to exhibit a p-type to n-type transition of charge carriers, including BT-BZT (Fig. 9.7.1b and 9.7.1c).[2, 15, 16] This article will mainly focus on BT-BZT ceramics with aim of understanding the transport mechanisms and to establish the defect chemistry of the BT-BiMO$_3$ class of materials in general. In Figure 9.7.1a, it can be seen that the 25BZT composition had bulk resistivity values >~2 orders of magnitude higher than BT. The activation energy values also improved from ~1 eV for BT to approximately half the band gap (~3.1 eV) for the BZT composition, suggesting a shift towards an intrinsic conduction mechanism.[14] Consistent with previous studies, it can also be seen (Fig. 9.7.1b and 9.7.1c) that holes were the dominant conducting species for BT, while it was electrons for 25BZT ceramics[16], as an increase in pO_2 should lead to an increase in conductivity for p-type ceramics and an increase in resistivity for n-type ceramics as per equations (9.7.1) and (9.7.2), respectively. An improvement in resistivity and activation energy values for conduction, together with a decrease in hole concentration or increase in electron concentration, suggests a mechanism of effective donor doping to be present in BZT-containing ceramics. Notably, there was no

intentional donor dopant present in these ceramics and, assuming the batch stoichiometry was preserved in the sintered ceramic embodiment, replacing 25% Ba^{2+} with Bi^{3+} and 12.5% Ti^{4+} with Zn^{2+} in BT to obtain the BT-25BZT solid solution should not lead to any donor doping behavior, as extra charge brought to A-site by Bi^{3+} should ideally be perfectly compensated by Zn^{2+} on B-sublattice. This suggests towards an unintentional donor doping mechanism leading to improvement in insulation properties. As mentioned earlier, the p-type behavior in nominally pure BT is believed to be a result of naturally occurring low-valence acceptor impurities, which are often concomitant with precursors, and cations vacancies which may be formed during high temperature processing.[16, 21, 29, 47] These defects can be compensated by oxygen vacancies (equation 9.7.4), which can then give rise to holes at relatively high oxygen partial pressures (equation 9.7.2). A net charge neutrality condition respecting all charged species in BT-BZT ceramics, can be given by:

$$x[V_{cation}^{x\prime}] + n + [A'] \approx [D^{\cdot}] + p + 2[V_O^{\cdot\cdot}] \qquad \text{Eq. 9.7.9}$$

where, $V_{cation}^{x\prime}$ is a generic cation vacancy. The improvement in resistivity on adding BZT to BT then can be due to reduction in cation vacancy concentration in BT-BZT ceramics leading to reduced hole concentration, which is a possibility since Bi-containing ceramics are usually sintered at a lower temperatures than BT. However, these ceramics also contain volatile cations like bismuth and zinc which actually increase the likelihood of cation vacancies and make qualitative prediction about cation vacancy concentration difficult. At the same time, a complete crossover to n-type behavior from p-type BT demands an additional donor doping mechanism to be present. This is because a

reduction in cation vacancies can reduce the hole concentration associated with them, however to obtain a complete transition to n-type behavior, the holes associated with low-valence acceptor impurities need to be compensated as well (equation 9.7.5). There can be several potential candidates for the unintentional donor doping, which are as follows. (1) A thorough phase-formation study of BT-BZT ceramics indicated the presence of an intermediate phase $BaBiO_3$, which is characterized by the presence of Bi^{5+} on the B-sublattice.[48] This intermediate phase develops at relatively lower temperatures and becomes undetectable by x-ray diffraction in the final sintered ceramics after sintering.[48] This is relevant because the presence of residual bismuth in +5 state in the final ceramics can act as a donor. (2) In addition, the loss of lower-valence cations (e.g. Ba^{2+} or Zn^{2+}) owing to processing and equilibrium conditions, can lead to effective donor-doping (discussed later in more detail) by certain mechanisms due to an excess of higher valence cations on the A- or B-sublattice. (3) Positively charged oxygen vacancies can be compensated by negatively charged electrons, for example, and result in donor doping. A higher oxygen vacancy concentration in 25BZT, therefore, may result in electron-dominated conduction. All these prospective candidates have been investigated in this study.

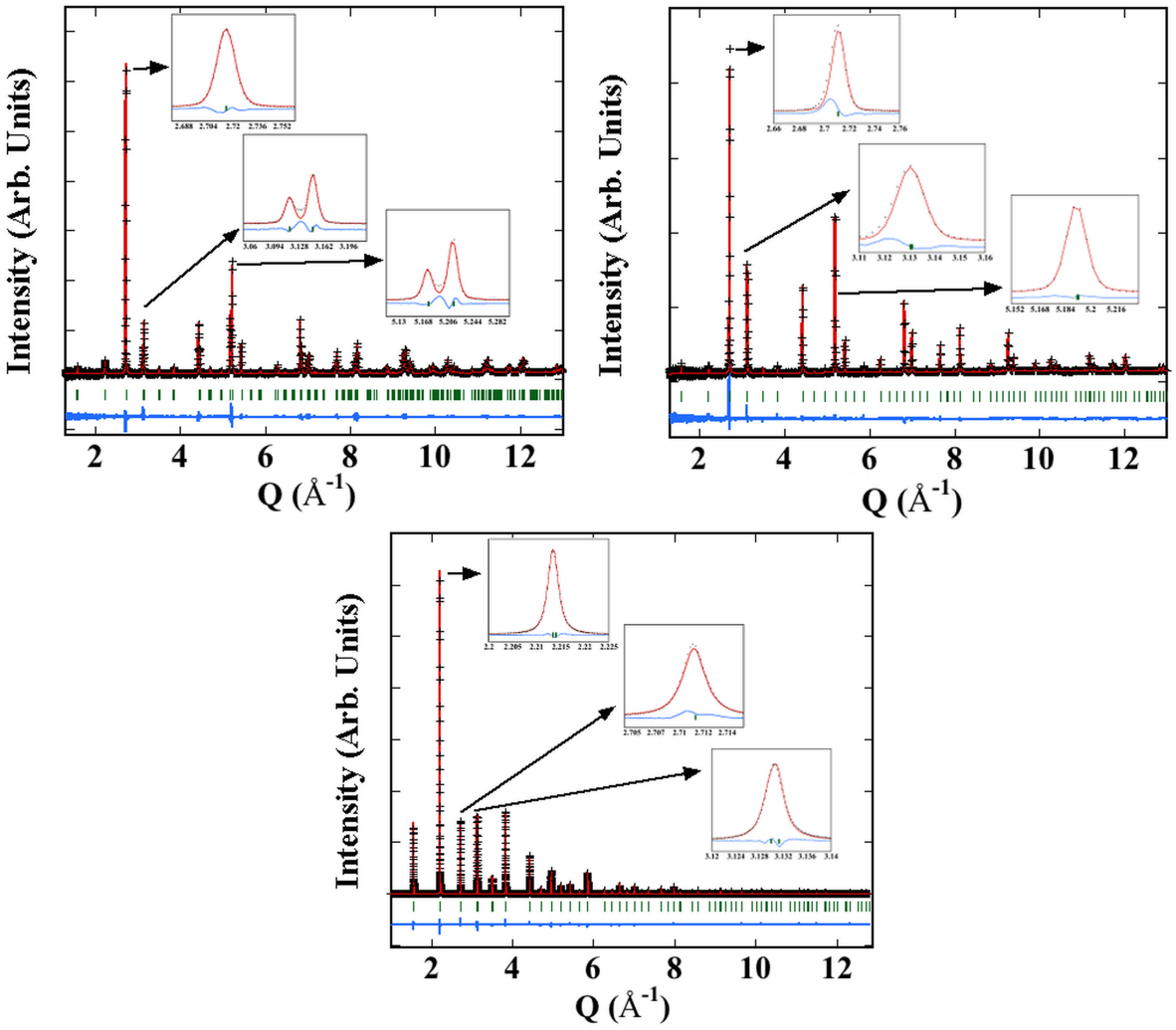

Fig. 9.7.2. (a) Rietveld refinement of a neutron diffraction pattern for BT. Combined neutron (b) and X-ray diffraction (c) was performed on BT-25BZT ceramics. The data presented with (+) symbol is the observed data and the black curves are calculated intensities. The bottom-most curve (blue) is the difference between observed and calculated intensities.

While small changes in defect concentration can have profound influence on transport properties, it is often difficult to probe them owing to limited sensitivity of many instruments. To get a rough idea of the relative concentration of cations and anions present in BT-25BZT, a combined Rietveld refinement was performed on room-temperature synchrotron X-ray and neutron diffraction data. A combined refinement was

used for couple of reasons—there were volatile cations present and therefore using constraints like sum of cation occupancies on A or B-site equals unity was not appropriate, and the use of both x-rays and neutrons ensured sufficient sensitivity for all ions present in BT-BZT, including oxygen. The data for the same has been presented in Figure 9.7.2 and Table 9.7.1 shows the parameters from the refinement – atomic coordinates, site occupancy and isotropic thermal parameters, goodness of fits and lattice parameters. The P4mm space group was used to fit the patterns and no secondary phases were observed within the resolution of the instrument. The refinement resulted in a reasonably good fit as can be seen in the difference curves (wR = 6.2%, GOF = 1.46). The lattice parameters obtained were, a = b = 4.0137(3) Å and c = 4.0150(5) Å. No significant loss of volatile bismuth or zinc was indicated by the refinement results and the other cations (barium and titanium) also appeared to be close to the expected compositions. The oxygen occupancy values however indicated ~5% vacancies to be present. To obtain a direct comparison with the oxygen occupancy in BT, neutron diffraction was performed on BT ceramics (Figure 9.7.2a). The fits were quite reasonable (wR=4.4%, GOF=3.5) and Table 9.7.1 shows the parameters extracted after refinement. All the cation and anion sites appear to be almost completely filled from this data for BT, and thus this suggests that BT-BZT may have higher oxygen vacancy concentration as compared to unmodified BT.

Table 9.7.1 Parameters for *P4mm* space group from the Rietveld refinement. Refinement was performed on neutron diffraction data for BT and combined x-ray and neutron data for BT-25BZT.

	x	y	z	Occupancy	U_{iso} (Å^2)
BaTiO3, wR=4.4%, GOF=3.5, P4mm, a = b = 3.9934(8) Å, c = 4.0349(5) Å					
Ba	0	0	0	1.0143	0.0038
Ti	0.5	0.5	0.51062	1.0216	0.00561
O1	0.5	0	0.48196	0.9985	0.00523
O2	0.5	0.5	-0.02571	0.9921	0.00545
BT-25BZT, wR=6.2% (3.3% for neutron data, 10.1% for xrd data), GOF=1.46, P4mm, a = b = 4.0137(3) Å, c = 4.0150(5) Å					
Ba	0	0	0	0.7493	0.01888
Bi	0	0	0	0.2472	0.01888
Ti	0.5	0.5	0.50075	0.8790	0.00208
Zn	0.5	0.5	0.50075	0.1778	0.00208
O1	0.5	0	0.49043	0.9525	0.00895
O2	0.5	0.5	-0.00973	0.9421	0.00901

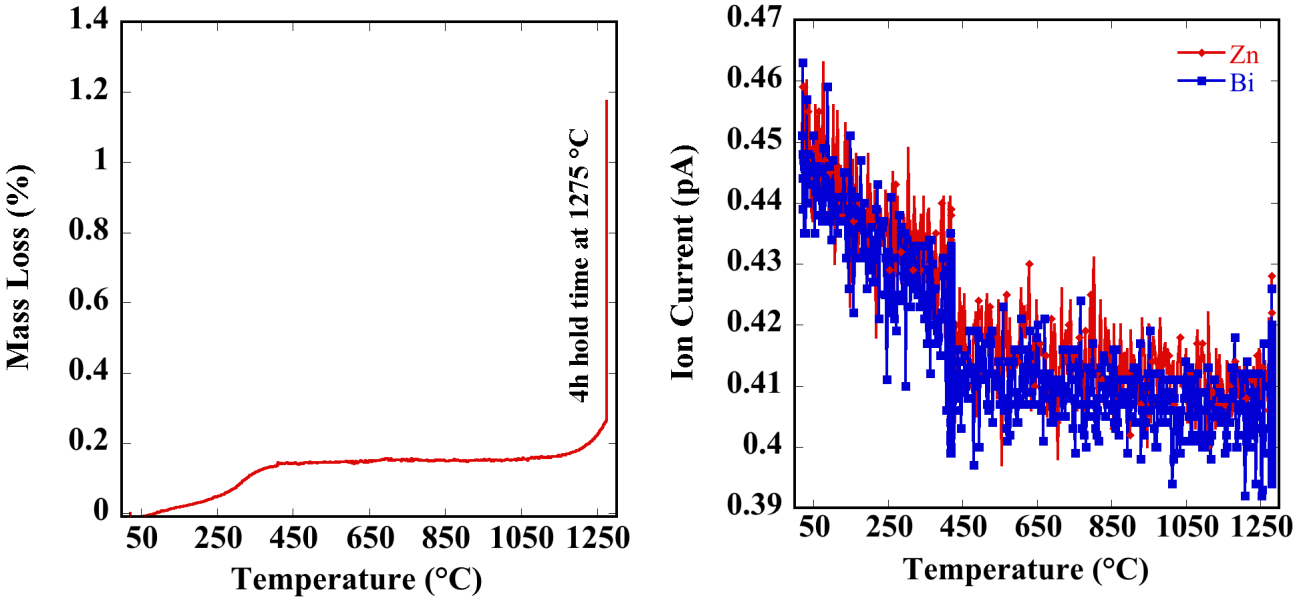

Fig. 9.7.3. Thermogravimetric analysis (TGA) with in-situ mass spectroscopy for BT-25BZT ceramics. The ion currents are shown for volatile Zn and Bi.

The bismuth and zinc cations in BT-BZT ceramics are relatively volatile and can affect the defect equilibrium if a change in stoichiometry results during high-temperature processing. Loss of zinc can potentially lead to either n-type behavior (as it shares the B-site with a higher valence Ti^{4+} and would thus create excess charge on the B-site. It could also lead to p-type behavior (through formation of cation vacancies) or could facilitate the formation of compensating oxygen vacancies, depending upon enthalpies associated with the different compensation mechanisms. A loss in bismuth, however, is almost always expected to promote conduction via holes or oxygen vacancies in BT-BZT ceramics. It is easy to visualize p-type behavior on losing Bi or Zn, as the resulting cation vacancies will be negatively charged (V''_{Zn}, V'''_{Bi}), and are expected to be compensated by

positively charged defect species. An n-type behavior can theoretically be expected on losing zinc when there is a mechanism present for losing proportional amounts of bismuth and barium as well, so that chemical formula becomes similar to $Bi_{0.25-x}Ba_{0.75-3x}Ti_{0.875}Zn_{0.125-0.5x}O_{3\pm\delta}$ for example, thus leading to excess Ti on B-site, which can lead to donor doping due to excess charge. A similar behavior was observed in BNT-based ceramics and donor-doped BT.[7, 8, 23] Even though the neutron and synchrotron data did not suggest a significant change in stoichiometry due to loss of these cations, for confirmation TGA experiments were performed with in-situ mass spectroscopy. The experiments were conducted on the composition BT-7.5BZT. This composition also exhibits orders of magnitude increase in resistivity as compared to BT and an n-type behavior similar to 25BZT, as was shown in a previous report.[14] The reason for choosing this composition was that the sintering temperatures of 7.5BZT was higher (by ~100 °C) than 25BZT, and therefore a loss of volatile cations, if occurring, was expected to be more pronounced. The powdered ceramics were heated up to 1275 °C and the dwell time at 1275 °C was 4h. Figure 9.7.3b shows the mass currents for Bi and Zn. There was negligible current observed for both bismuth and zinc and the signal just showed noise suggesting no measurable cation loss. The total mass (Fig 9.7.3a), however, showed a total mass loss of ~1.17%. Given that no bismuth or zinc were being lost, the dominant species for mass loss is presumed to be oxygen. A total mass loss of 1.17% corresponds to ~6.2% oxygen vacancies in the BT-7.5BZT composition. In summary, the in-situ TGA results indicated a negligible loss of volatile cations and called for further investigation of oxygen loss.

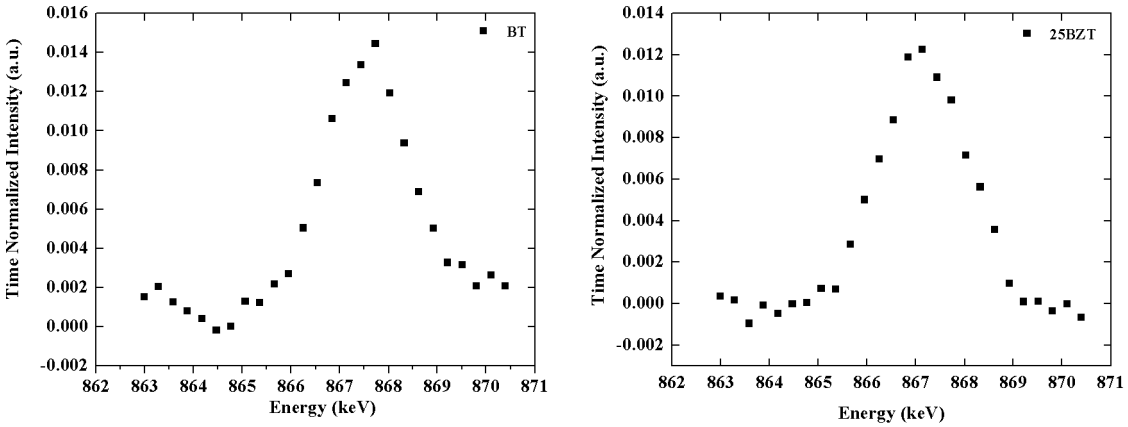

Fig. 9.7.4. Prompt gamma neutron activation analysis for (a) BT and (b) BT-BZT, indicating lower oxygen content in 25BZT ceramics as compared to BT.

To gain further confirmation of the oxygen concentration in these ceramics, PGNAA was performed on BT and 25BZT ceramics. In this technique an atomic nucleus is bombarded with neutrons, which results in a compound nucleus in an excited state after non-elastic collision.[49] The compound nucleus then immediately emits one or more characteristic prompt gamma rays to de-excite to a more stable state. For oxygen, the most intense energy peak occurs at ~870 keV[50] and the same has been shown for BT and 25BZT samples in Figure 9.7.4. Absolute quantification of these peaks is often difficult due to difficulties in obtaining accurate neutron cross-section functions and therefore, the oxygen concentration in 25BZT was computed relative to BT sample. Typically, the areas enclosed are directly proportional to concentration of that species. The results suggested a 93.7±3.4% oxygen occupancy in 25BZT, assuming that in BT all the oxygen sites were occupied. This indicated towards an oxygen vacancy concentration

of ~6.3±3.4%, which was again in good agreement with oxygen vacancy estimations determined by diffraction and TGA experiments.

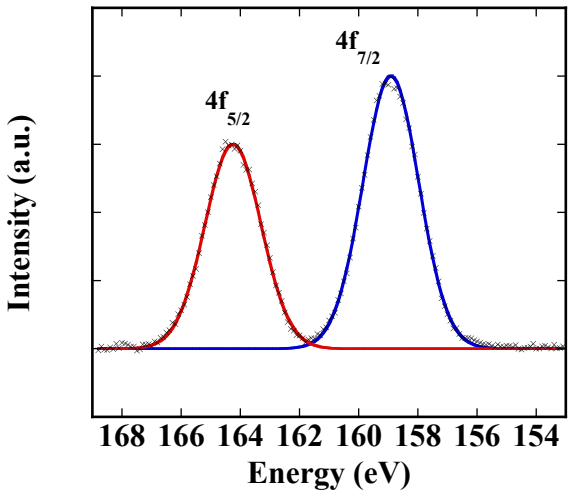

Fig. 9.7.5. X-ray photoelectron spectroscopy on powdered BT-25BZT ceramics. The data shown with "x" symbols are actual data obtained from the experiment. The background and fitted peaks have also been indicated.

One of the mechanisms for donor doping was suspected to be Bi^{5+}, which can act as a donor dopant as mentioned earlier. To establish whether or not Bi^{5+} was present in BT-BZT, XPS and extended x-ray absorption fine structure (EXAFS) measurements were performed. The XPS technique can theoretically distinguish between different valence states of an element as the binding energy values should be directly proportional valence states. However, a shoulder corresponding to a valence state which is lower in concentration may be difficult to resolve, if the chemical shift due to valence change is small. Figure 9.7.5 shows the XPS data for 25BZT, where the Bi($4f_{5/2}$, $4f_{7/2}$) peaks have been presented. The peak maxima of the singlet peaks were at energy values of 164.3 eV

and 158.9 eV, respectively, and there was no evidence of the presence of Bi^{5+}, which should usually appears as a shoulder to the dominant Bi^{3+} peak. To get a further confirmation, EXAFS measurements were performed as synchrotron sources often result in higher resolution and are better suited for detecting small concentrations of a particular species. The data for x-ray absorption near edge structure (XANES) has been shown in Fig. 9.7.6. In XANES, the edge energy (can be defined as energy corresponding to a normalized y-axis value of 0.5) values provide important information about valence state of a material. The line shapes are usually a function of oxidation state as well as local structure, and a higher valence state typically results in higher edge energy values.[51] The EXAFS was performed on three samples: Bi_2O_3—which should have only Bi in the +3 state, $NaBiO_3$—which should have majority of Bi in +5 state, and 25BZT ceramics—which is the sample of interest. The line shape of $NaBiO_3$ consists of three well-defined features (marked A, B and C), in contrast to just a single broad peak for Bi_2O_3. The single peak in Bi_2O_3 corresponds to a dipole-allowed transition of an electron to empty 6d states from a 2p state.[52] This broad peak splits into two (B and C) owing to a transition to 6d bonding (B) and antibonding states (C), if the energy gap is significant.[52] The peak A is vital to unambiguous identification of Bi^{5+} (which has empty 6s states), and corresponds to a transition from the 2p to 6s state. This bump is expected to be absent in Bi^{3+}, as it will have filled 6s states. From the plot it can be seen that the edge energy of 25BZT is very similar to Bi_2O_3, with no noticeable shift to higher energy values. One can also note that the signature pre-edge peak (feature A) was absent in 25BZT, and thus there was no evidence of the presence of Bi^{5+} in 25BZT ceramics, within the resolution limit of the instrument.

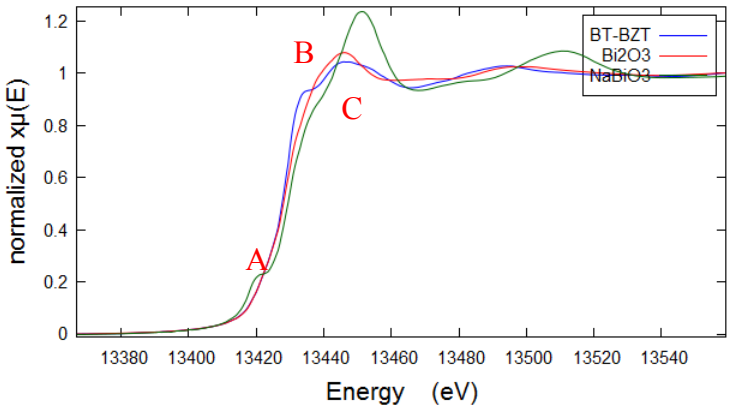

FIG. 9.7.6. X-ray absorption spectra focusing on XANES region for BT-25BZT sample. The data for Bi_2O_3 and $NaBiO_3$ have also been shown, which were used as a reference for 3+ and 5+ states.

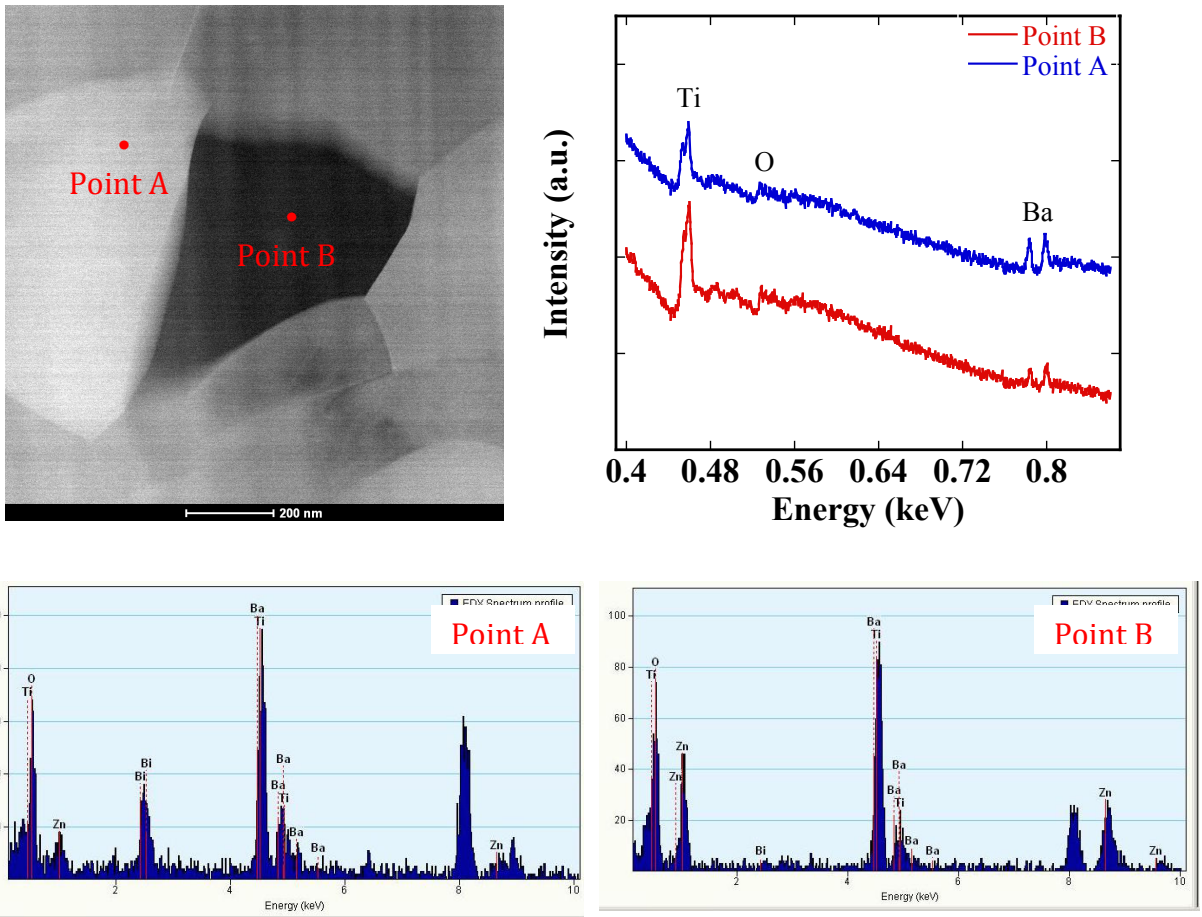

Fig. 9.7.7. Micrograph (Fig. a) EELS (Fig. b) and STEM EDS (Fig. c) and for BT-25BZT sample. It can be noted that relative amounts of cations were different in secondary phases (point B) as compared to bulk of 25BZT (point A) and that the secondary phases contain almost no Bi.

Transmission electron microscopy (TEM) was used for three purposes—to obtain micrographs to investigate if there were secondary phases present, to analyze the EDS spectra, and finally to analyze the EELS spectra to investigate compositional inhomogeneity. The EDS technique is based on x-rays and therefore is more sensitive to heavy elements like Ba and Bi. The EELS spectra was primarily performed to obtain an oxygen profile across the grain in both BT and 25BZT ceramics, in order to provide additional validation of the higher oxygen vacancy concentration in BT-BZT as suggested by neutron diffraction, in-situ TGA and PGNAA. The energy range selected for EELS was however sufficient to include Ti $L_{2,3}$ and Ba $M_{4,5}$ spectra as well in addition to O K, which was useful for Ba and Bi quantification as their peaks in EDS spectra overlap with other elements. The TEM results showed possibility of secondary phases being present in BT-BZT ceramics. In the STEM mode, several dark regions (*e.g.* point B in Fig. 9.7.7a and encircled region in Fig. 9.7.8a) were observed on which EELS and EDS were performed to obtain local chemical information. On looking at the EELS spectrum from the dark region and comparing it with the EELS spectrum from bulk phase of BT-BZT, one can easily notice that the relative intensities and thus atomic ratios of Ba, Ti and O were different in the dark regions, confirming the secondary nature of this phase, even though it was difficult to obtain its exact composition. On examining the EDS spectra, one can make couple of supplementary observations—the secondary phases contained almost no bismuth and the relative concentration of Zn appeared to be higher than the bulk phase of BT-BZT. From these results, one can conclude that these secondary phases were likely acting as sinks for Ba and Zn cations. This is expected to

leave the bulk of BT-BZT ceramics relatively rich in higher valence Bi on the A-site and deficient in lower valence Zn (and therefore, possibly rich in higher valence Ti, as discussed earlier) on B-site. Both of these scenarios are capable of giving rise to effective donor doping in BT-BZT ceramics. Thus the EELS+EDS results provided important insights in an unintentional donor doping mechanism in BT-BZT ceramics.

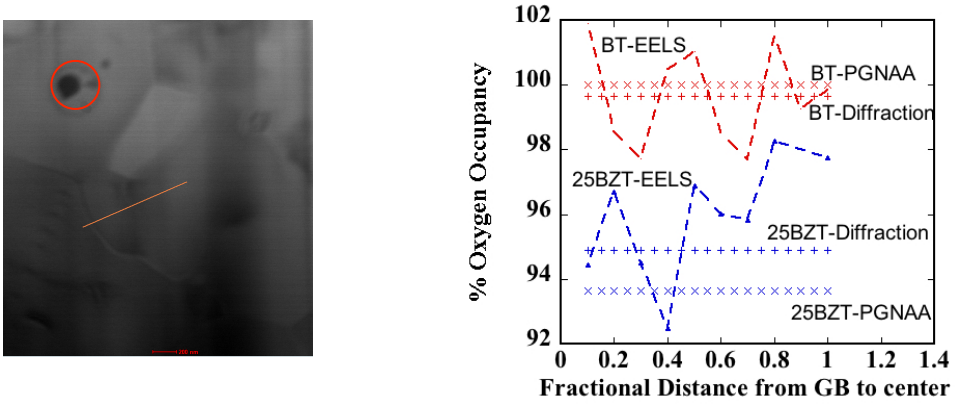

Fig. 9.7.8. (a) A typical grain of BT-25BZT with a representative line across the grain along which EELS was performed. The average oxygen occupancy was found to be 95.98+/-1.90 for BT-25BZT from the EELS data (b). A red circle in Figure a shows another dark-colored secondary phase.

As mentioned earlier, the EELS spectra were also used to obtain the oxygen concentration in BT and BT-BZT ceramics. Basically, the spectra were obtained across several points from grain boundary to middle of the grain, and the secondary phases were avoided to generate this profile. A representative picture has been shown in Fig 9.7.8a. The quantification was performed through a k-factor approach[39], and sensitivity factor $k_{Ti,O}$ were obtained across multiple grains. The results, similar to diffraction and PGNAA results, showed a higher oxygen vacancy concentration as compared to BT ceramics, as can be seen in Fig. 8b. An oxygen vacancy concentration of 4.02%±1.90% was estimated

for BT-25BZT ceramics. Similar to high valence cations, positively charged oxygen vacancies can theoretically be compensated by electrons or shift conductivity minimum in Kröger-Vink diagram to higher pO_2 to give rise to an n-type behavior.

All oxide ceramics are expected to have some concentration of oxygen vacancies due to thermodynamics considerations. There can be several reasons which may facilitate higher equilibrium oxygen vacancy concentration in BT-BiMO$_3$ ceramics in general—(1) loss of volatile cations and charge compensation by oxygen vacancies; however, as shown earlier, no loss of volatile Zn or Bi was detected by in-situ TGA measurements; (2) it was reported that in BT-BiMO$_3$ ceramics, several cations occupy off-center lattice sites from their usual positions[12], which may provide easy pathways for oxygen to diffuse out of the perovskite phase[53], (3) the bond strength of oxygen is expected to have a spatial variation depending on its near neighbors in a random matrix *e.g.* its bond strength with Zn may be different from Ti; therefore, it may be relatively easier for some oxygen to break their bonds and leave the system. On a side note, it is also a possibility that the secondary phases observed (Fig. 9.7.7.) might be a result of excessive oxygen vacancies, as it can destabilize the perovskite structure.[54] There were several dislocations and stacking faults observed in TEM as well, which may also be a direct result of oxygen vacancies.[55]

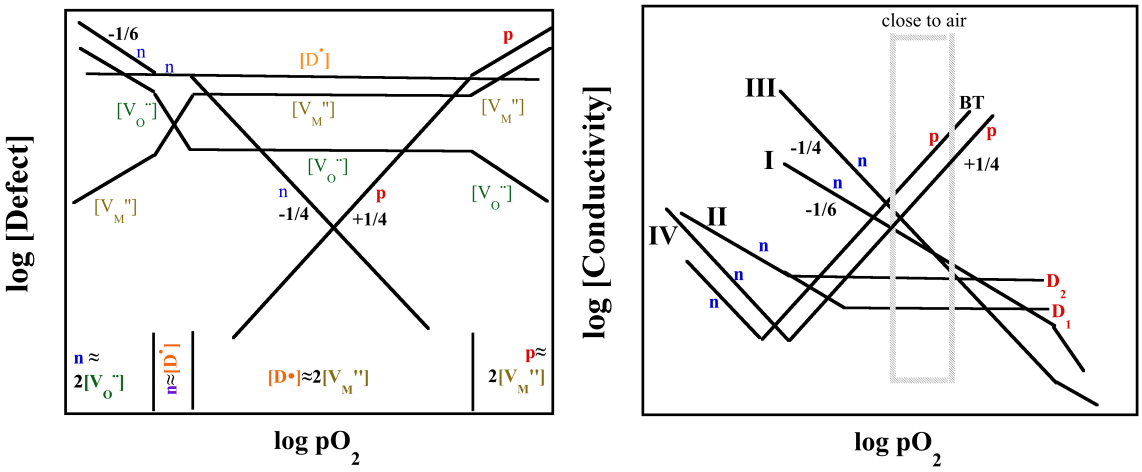

Fig. 9.7.9 (a) A generic defect diagram (or Kröger-Vink) of donor-doped BT, adapted from Smyth *et al.*[31] (b) Various possible mechanisms for donor doping in BT-BiMO$_3$ leading to improvement in resistivity. The D_1 and D_2 (>D_1) are donor levels for Mechanism II. Plot of BT has also been included for reference.

Figure 9.7.9 shows a typical defect diagram of BT to aid our understanding of defect chemistry of BT-BiMO$_3$. It is a challenging task since as mentioned earlier, defect chemistry for even donor-doped BaTiO$_3$ is still debated in the literature.[23, 56, 57] At the same time, the diagram in Fig. 9.7.9a may not apply to all BT-BiMO$_3$ ceramics in general for two reasons. First is the extent of donor doping. As mentioned earlier, for BT-BiMO$_3$ ceramics, the extent of donor doping may (e.g. BT-BZT or a similar ST-BZT) or may not (e.g. BT-BS) be sufficient to cause a complete crossover to n-type regime. If the crossover is not complete, the ceramics would be expected to continue exhibiting p-type behavior in air. The second factor is the dominant source of donor dopants at oxygen partial pressures close to air atmosphere. As one could see for the instance of BT-BZT, donor doping can be caused by cations or anions, and the concentration of oxygen vacancies can be greater than what is expected from the acceptor concentration. If the concentration of electrons is controlled by cation donors, the concentration of electrons

should remain constant with pO_2 and result in a pO_2-independent conduction. If the concentration of electrons is controlled by oxygen vacancies, then a log-plot of conductivity versus pO_2 should have a slope of -1/6, as will be seen in following paragraph. It should be noted that, in case of donor-doped BT, in general, it is expected that anion-controlled n-type behavior (at extremely low pO_2) results in very high conductivity values. The same may not be true for BT-BiMO$_3$ ceramics, since theoretically anion vacancies may be the only source of electrons present which compensate for the positively charged holes, without presence of any high valence cation donors. Finally, if ionic compensation is dominant, i.e. if cation donors or anion vacancies are being compensated by cation vacancies, then a log-plot of conductivity and pO_2 should have a slope of -1/4. The different mechanisms have been discussed further in the following section. For simplicity, it is assumed that only one dominant defect mechanism is present in a given situation.

Mechanism I. Electronic compensation dominated by oxygen vacancies

The reduction reaction, similar to BT in equation 9.7.1, is given by the following:

$$O_O^X \rightarrow V_O^{\cdot\cdot} + 2e' + 1/2O_2 \qquad \text{Eq. 9.7.10}$$

The mass action relationship, assuming dilute solute solution thermodynamics (so that concentrations and activities are equivalent) can be written as:

$$K_{red} = [V_O^{\cdot\cdot}]n^2 pO_2^{1/2} = K_0 \exp(-\Delta H_f/kT) \quad \text{Eq. 9.7.11}$$

where, K_0 is a constant, ΔH_f is formation enthalpy and k is Boltzmann's constant. In a case where there is a high oxygen vacancy concentration, i.e. more than what can be compensated by acceptor impurities, the excess oxygen vacancies can be compensated by electrons. This is similar to low pO_2 regime in Figure 9.7.9a (or the acceptor-doped BT at extremely low pO_2 as seen in introduction section), where the driving force for oxygen loss is low partial pressure. However, as mentioned earlier, there may be other mechanisms for oxygen loss in BT-BiMO$_3$ ceramics. In such a case, the following relation may hold using Brouwer approximation:

$$n \approx 2[V_O^{\cdot\cdot}] \quad \text{Eq. 9.7.12}$$

Combining 9.7.11 and 9.7.12, one can see that at a given temperature,

$$\sigma \propto n \propto \text{constant} * pO_2^{-1/6} \quad \text{Eq. 9.7.13}$$

where, σ is conductivity. Therefore, the slope of a log-plot between conductivity and pO_2 will be -1/6.

Mechanism II. Electronic compensation dominated by cation donors

When conduction is controlled by concentration of high valence cation impurities and electronic compensation is dominant, the following relationship should hold:

$$[D^{\bullet}] \approx n \qquad \text{Eq. 9.7.14}$$

where $[D^{\bullet}]$ is concentration of donor species. In this case, one can note that conductivity should be independent of pO_2,

$$\sigma \propto n \propto \text{constant} * pO_2^{\,0} \qquad \text{Eq. 9.7.15}$$

If this mechanism is dominant, the conductivity can also be expected to independent of temperature, if the temperature dependence of mobilities are ignored.[23]

Mechanism III. Ionic compensation regime

The case where ionic compensation may be the dominant mechanism, the following relationship may hold for cation donors,

$$[D^{\bullet}] = 2[V_M''] \qquad \text{Eq. 9.7.16}$$

Therefore, $[V_M'']$ will be fixed by donor level and be independent of pO_2. The $[V_O^{\cdot\cdot}]$ should also be then independent of pO_2, as enthalpy of intrinsic Schottky disorder (*e.g.* equation 9.7.4) should be a constant at a given temperature. In the same way, in case of anion donors, the following relationship may hold,

$$2[V_O^{\cdot\cdot}] = 2[V_M''] \qquad \text{Eq. 9.7.17}$$

Using equation 9.7.11 then, one can see that

$$\sigma \propto n \propto \text{constant} * pO_2^{-1/4} \qquad \text{Eq. 9.7.18}$$

Therefore, the log-plot between conductivity and pO_2 should have a slope of -1/4. It can also be noted that the point of intrinsic conduction minimum occurs within the region of dominant ionic compensation for both acceptor and donor-doped BT (Figure 9.7.9a and ref[21, 31]).

Mechanism IV. Incomplete crossover to n-type regime

In this case, the ceramics will still be p-type conducting close to air atmosphere, and equation 9.7.2 will still be valid, and the following mass action relationship can be written,

$$K_{ox} = p^2 pO_2^{-1/2} / [V_O^{\cdot\cdot}] \qquad \text{Eq. 9.7.19}$$

$$\sigma \propto p \propto \text{constant} * pO_2^{+1/4} \qquad \text{Eq. 9.7.20}$$

However, due to lower net acceptor concentration, the conductivity minimum should shift to the right towards higher pO_2. It is easy to imagine that if the conductivity minima shifts to a higher pO_2 (>0.21 atm), then one can expect a change to n-type behavior, which is in reality equivalent to Mechanism III above, and equation 9.7.18 should be valid.

After the discussion of different possible mechanisms for defect compensation, it is suggested that for the case of BT-BZT, the likely dominant compensation mechanism is ionic compensation (Mechanism III) close to air atmosphere, for the following two reasons. First, the slope of log-plot between pO_2 and conductivity was estimated to be -¼, which is indicative of Mechanism III dominating compensation mechanisms. The slopes for BT-BS and unmodified BT were found to be close to +¼, indicating dominant ionic compensation (Mechanism III, IV) for them as well and consistent with their p-type behavior. The slopes for BT-BS haven't been reported before, however, the slope for BT was consistent with literature values.[21] However, it is imperative to note that the slopes were calculated from only 3 oxygen partial pressure values. Therefore, these cannot be considered as proof of a specific mechanism, rather as merely supporting evidence.

The second reason is based on thermodynamic parameters, which have been reported after extensive studies on BT-based systems. Since any of the Mechanisms I, II or III can result in an n-type behavior for BT-BZT, all of them have been considered.

Mechanism II can be readily ignored, as the conductivity was not found to be independent of pO_2. The next candidate is Mechanism I, which can also be ruled out based on values of estimated formation enthalpy (ΔH_f) and conductivity. From equation 9.7.11 and 9.7.12, one can note that the following relationship holds at constant pO_2 for mechanism I:

$$\sigma \propto n \propto \text{constants}^* \exp(-\Delta H_f/3kT) \qquad \text{Eq. 9.7.21}$$

Therefore, ΔH_f can be calculated by performing conductivity measurements at a constant pO_2 at various temperatures. From data in Fig. 9.7.1a, this value was calculated to be ~4.6 eV, which is much lower than reported values of ΔH_f (5.89-7.3 eV[27]) for BT for reaction 9. Secondly, using equation 9.7.12, the electron concentration can be estimated for Mechanism I, since we have oxygen vacancy concentration from data on BT-BZT in this paper. Using reported values of mobilities for electrons (for example 0.26 $cm^2/V.s$ at 500 °C) [21, 58], the conductivity value was estimated and it was significantly higher than values measured using AC impedance spectroscopy (9.7.1a) by at least 8 orders of magnitude, even though the electron concentration was most likely underestimated since the room temperature oxygen vacancy concentration was used for this calculation. Ruling out Mechanisms I and II, leaves only Mechanism III, which is further supported by following arguments. In the ionic compensation regime, using equation 9.7.11, since $[V_O^{\cdot\cdot}]$ should practically remain constant, and one can note that the following relationship holds at constant pO_2:

$$\sigma \propto n \propto \text{constants}^* \exp(-\Delta H_f/2kT) \quad \text{Eq. 9.7.22}$$

Again, by performing conductivity measurements as a function of temperature, one can obtain ΔH_f, which is calculated be ~3.1 eV (Figure 9.7.1). This value is a very close match with the values reported in literature (2.9-3.15 eV[27]) for BT for the intrinsic electronic equilibrium constant (equation 9.7.3), also consistent with our claim that (1-x)BT-xBZT ($0.03 \leq x \leq 0.25$[14]) exhibits close to intrinsic conduction. Furthermore, it is possible to estimate the intrinsic conductivity (the value at the point of minimum where conductivities due to electrons and holes are equal in magnitude, $\sigma_{el,m}$) of BT at a given temperature using the following relationship, the details of which can be found elsewhere[59]:

$$\sigma_{el,m} = 2eK_i^{1/2}(\mu_h\mu_n)^{1/2} \quad \text{Eq. 9.7.23}$$

where, $\sigma_{el,m}$ is minimum conductivity for a given temperature, e is electronic charge, μ_h is mobility of holes and μ_n is mobility of electrons. Using reported values of K_i[27], μ_h[21, 27] and μ_n[27], at 600 °C for instance, $\sigma_{el,m}$ was calculated to be ~10^{-6} $ohm^{-1}cm^{-1}$. This value is very close to the values obtained for BT-BiMO$_3$ ceramics (measured to be ~0.8-2x10^6 $ohm^{-1}cm^{-1}$ in Fig 9.7.1a and ref[14, 60]), which is consistent with the claim that BT-BiMO$_3$ ceramics exhibited close to intrinsic conduction in air atmosphere. Hence, the estimated thermodynamic parameters also suggest a dominant ionic compensation mechanism in BT-BiMO$_3$ ceramics and a shift in the conductivity minima to higher pO_2 upon adding BiMO$_3$, leading to improved insulation properties.

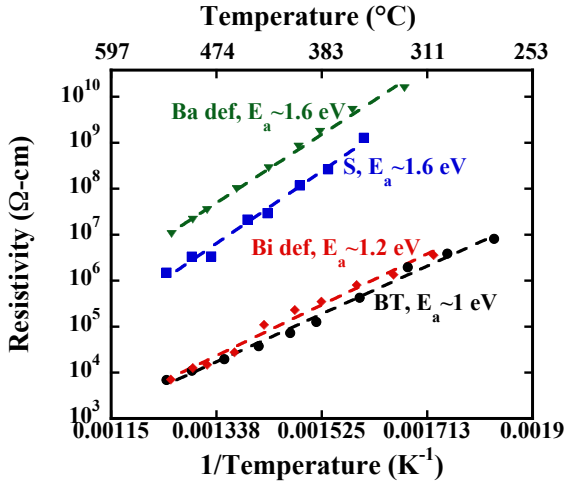

Fig. 9.7.10. Arrhenius plot of resistivity for stoichiometric (S), 2% Ba deficient (Ba def) and 2% Bi deficient (Bi def) ceramics. The data for unmodified BT has also been shown.

A robust defect chemistry model is extremely useful in tailoring electronic properties to suit application requirements. In the last section of this paper, it will be demonstrated using our understanding of defect chemistry for BT-BZT that intentional Ba or Bi deficiencies introduced by modifying the batch stoichiometry have very different effects on transport properties, even though both of them are ideally expected to create A-site cation vacancies. We noted earlier that donor doping shifts the conductivity minima towards higher pO_2 for BT, thereby decreasing the conductivity in air. Acceptor doping should have an opposite effect. In general, negatively charged cation vacancies are expected to act as acceptors. Non-stoichiometric compositions with Bi vacancies (designated as "Bi def") follow expectations, as can be seen in Figure 9.7.10, as the resistivity drops by ~2 orders of magnitude and the activation energy value for conduction also decreases as compared to stoichiometric 25BZT (S), indicating a defect-dominated conduction. As expected, this sample exhibited p-type conducting based on pO_2-dependent impedance measurements (data not shown). Non-stoichiometric

compositions with Ba-vacancies can theoretically follow the same behavior as Bi vacancies. However, there is also an alternative option. These compositions can actually exhibit effective donor doping through the formation of secondary phases rich in Zn and Ti, thus making the BT-BZT perovskite phase rich in Bi. This has been shown to be possible in BT-BZT ceramics, as was seen in Fig. 9.7.7. From the data in Fig. 9.7.10, it does appear that the introduction of Ba-vacancies results in a behavior which is close to an intrinsic conduction mechanism (i.e. high resistivity with an activation energy close to half the band gap value) with no deterioration in the insulation properties. In contrast to the Bi-def sample, the Ba-def sample was n-type conducting, supporting the claim of a donor-doping mechanism on introducing Ba vacancies. A similar behavior has been observed in a few other similar ceramics as well, *e.g.* Na-deficient BNT, Sr-deficient ST-BZT, and Ba-deficent BT-BS.[8, 15] Thus, it was shown via brief discussion that the knowledge of defect chemistry can be used to predict the consequence of introducing certain defect species in a BT-BiMO$_3$ ceramics and can be used to tailor properties e.g. increase conductivity for applications like solid oxide fuel cells or increase resistivity for high temperature dielectric applications.

Conclusions

The addition of BiMO$_3$ to p-type BT is accompanied by significant improvement in insulation properties, often even leading to an n-type behavior in BT-BiMO$_3$ ceramics. It was shown that donor doping can originate primarily due to two factors—the presence of secondary phases which modifies the stoichiometry of the perovskite phase to become

rich in high valence cations, and a higher oxygen vacancy concentration. It was proposed that donor doping had an effect of shifting the conductivity minima to higher pO_2 values in the Kröger-Vink diagram, as a means to explain both the higher resistivity values and shift to n-type behavior. A robust defect chemistry model for BT- BiMO$_3$ ceramics is expected to aid in engineering the material for high performance capacitor applications.

Acknowledgement

This material is based upon work supported by the National Science Foundation under Grant No. DMR-1308032. The neutron diffraction was conducted at Oak Ridge National Laboratory on POWGEN beamline by mail-in program. Use of the Advanced Photon Source at Argonne National Laboratory was supported by the U. S. Department of Energy, Office of Science, Office of Basic Energy Sciences, under Contract No. DE-AC02-06CH11357. The authors would also like to thank Melissa Santala for discussions on TEM and Steve Golledge for XPS measurements.

References

[1] Label PI, Label P, oHS Compliance Engineer R. Directive 2002/95/EC of the European Parliament and of the Council of 27 January 2003 on the restriction of the use of certain hazardous substances in electrical and electronic equipment. 2005.
[2] Kumar N, Patterson EA, Frömling T, Cann DP. DC-bias dependent impedance spectroscopy of BaTiO 3–Bi (Zn 1/2 Ti 1/2) O 3 ceramics. Journal of Materials Chemistry C 2016;4:1782-6.
[3] Michaela Beuerlein NK, Tedi-Marie Usher, Harlan Brown-Shaklee, Natthaphon Raengthon, David Cann, Jacob Jones, and Geoff Brennecka. Stability through Complexity: A Review of Structure-Processing-Property Relationships in BaTiO3-Bi(M)O3 Dielectrics. Journal of the American Ceramic Society Submitted.
[4] Zeb A, Milne S. High temperature dielectric ceramics: a review of temperature-stable high-permittivity perovskites. Journal of Materials Science: Materials in Electronics 2015;26:9243-55.
[5] Maurya D, Zhou Y, Wang Y, Yan Y, Li J, Viehland D, et al. Giant strain with ultra-low hysteresis and high temperature stability in grain oriented lead-free K0. 5Bi0. 5TiO3-BaTiO3-Na0. 5Bi0. 5TiO3 piezoelectric materials. Scientific reports 2015;5.
[6] Takenaka T, Nagata H, Hiruma Y. Current developments and prospective of lead-free piezoelectric ceramics. Japanese Journal of Applied Physics 2008;47:3787.
[7] Li M, Pietrowski MJ, De Souza RA, Zhang H, Reaney IM, Cook SN, et al. A family of oxide ion conductors based on the ferroelectric perovskite Na0. 5Bi0. 5TiO3. Nature materials 2014;13:31-5.
[8] Li M, Zhang H, Cook SN, Li L, Kilner JA, Reaney IM, et al. Dramatic influence of A-site nonstoichiometry on the electrical conductivity and conduction mechanisms in the perovskite oxide Na0. 5Bi0. 5TiO3. Chemistry of Materials 2015;27:629-34.
[9] Kumar N, Ionin A, Ansell T, Kwon S, Hackenberger W, Cann D. Multilayer ceramic capacitors based on relaxor BaTiO3-Bi (Zn1/2Ti1/2) O3 for temperature stable and high energy density capacitor applications. Applied Physics Letters 2015;106:252901.
[10] Usher T-M, Levin I, Daniels JE, Jones JL. Electric-field-induced local and mesoscale structural changes in polycrystalline dielectrics and ferroelectrics. Scientific reports 2015;5.
[11] Comes R, Lambert M, Guinier A. The chain structure of BaTiO 3 and KNbO 3. Solid State Communications 1968;6:715-9.
[12] Krayzman V, Levin I, Woicik JC, Bridges F. Correlated rattling-ion origins of dielectric properties in reentrant dipole glasses BaTiO3-BiScO3. Applied Physics Letters 2015;107:192903.
[13] Gorfman S, Simons H, Iamsasri T, Prasertpalichat S, Cann D, Choe H, et al. Simultaneous resonant x-ray diffraction measurement of polarization inversion and lattice strain in polycrystalline ferroelectrics. Scientific reports 2016;6.
[14] Kumar N, Cann DP. Resistivity Enhancement and Transport Mechanisms in (1− x) BaTiO3–xBi (Zn1/2Ti1/2) O3 and (1− x) SrTiO3–xBi (Zn1/2Ti1/2) O3. Journal of the American Ceramic Society 2015;98:2548-55.
[15] Kumar N, Cann DP. Tailoring transport properties through nonstoichiometry in BaTiO3–BiScO3 and SrTiO3–Bi(Zn1/2Ti1/2)O3 for capacitor applications. Journal of Materials Science 2016.

[16] Kumar N, Patterson EA, Fromling T, Cann DP. Conduction Mechanisms in BaTiO3–Bi(Zn1/2Ti1/2)O3 Ceramics. Journal of the American Ceramic Society 2016:DOI: 10.1111/jace.14313.
[17] Nowotny J, Rekas M. Defect structure, electrical properties and transport in barium titanate. II. Consistency requirements between defect models and crystal properties. Ceramics international 1994;20:217-24.
[18] Eichel R-A. Structural and dynamic properties of oxygen vacancies in perovskite oxides—analysis of defect chemistry by modern multi-frequency and pulsed EPR techniques. Physical Chemistry Chemical Physics 2011;13:368-84.
[19] Nowotny J. Science of ceramic interfaces II: Newnes; 1995.
[20] Tsur Y, Randall CA. Point defect concentrations in barium titanate revisited. Journal of the American Ceramic Society 2001;84:2147-9.
[21] Smyth DM. The defect chemistry of metal oxides. The Defect Chemistry of Metal Oxides, by DM Smyth, pp 304 Foreword by DM Smyth Oxford University Press, Jun 2000 ISBN-10: 0195110145 ISBN-13: 9780195110142 2000;1.
[22] Lee S, Randall CA, Liu ZK. Comprehensive Linkage of Defect and Phase Equilibria Through Ferroelectric Transition Behavior in BaTiO3‐Based Dielectrics: Part 2. Defect Modeling Under Low Oxygen Partial Pressure Conditions. Journal of the American Ceramic Society 2008;91:1753-61.
[23] Chan HM, HARMER MR, SMYTH DM. Compensating Defects in Highly Donor‐Doped BaTiO3. Journal of the American Ceramic Society 1986;69:507-10.
[24] Rothschild A, Menesklou W, Tuller HL, Ivers-Tiffee E. Electronic structure, defect chemistry, and transport properties of SrTi1-x Fe x O3-y solid solutions. Chemistry of materials 2006;18:3651-9.
[25] Daniels J, Härdtl K. Electrical conductivity at high temperatures of donor-doped barium titanate ceramics. Philips Res Rep 1976;31:489-504.
[26] Nowotny J, Rekas M. Defect chemistry of BaTiO 3. Solid State Ionics 1991;49:135-54.
[27] Yoo H-I, Song C-R, Lee D-K. BaTiO3− δ: defect structure, electrical conductivity, chemical diffusivity, thermoelectric power, and oxygen nonstoichiometry. Journal of electroceramics 2002;8:5-36.
[28] Kröger F, Vink H. Relations between the concentrations of imperfections in crystalline solids. Solid state physics 1956;3:307-435.
[29] Moos R, Hardtl KH. Defect Chemistry of Donor‐Doped and Undoped Strontium Titanate Ceramics between 1000° and 1400° C. Journal of the American Ceramic Society 1997;80:2549-62.
[30] Jonker G, Havinga E. The influence of foreign ions on the crystal lattice of barium titanate. Materials Research Bulletin 1982;17:345-50.
[31] Smyth DM. The defect chemistry of donor-doped BaTiO3: a rebuttal. Journal of electroceramics 2002;9:179-86.
[32] Morrison FD, Coats AM, Sinclair DC, West AR. Charge compensation mechanisms in La-doped BaTiO3. Journal of Electroceramics 2001;6:219-32.
[33] Dunbar TD, Warren WL, Tuttle BA, Randall CA, Tsur Y. Electron paramagnetic resonance investigations of lanthanide-doped barium titanate: dopant site occupancy. The Journal of Physical Chemistry B 2004;108:908-17.

[34] Hennings DF. Dielectric materials for sintering in reducing atmospheres. Journal of the european ceramic society 2001;21:1637-42.
[35] Tsur Y, Hitomi A, Scrymgeour I, Randall CA. Site occupancy of rare-earth cations in BaTiO3. Japanese Journal of Applied Physics 2001;40:255.
[36] Han YH, Appleby JB, Smyth DM. Calcium as an acceptor impurity in BaTiO3. Journal of the American Ceramic Society 1987;70:96-100.
[37] Shannon RT, Prewitt CT. Effective ionic radii in oxides and fluorides. Acta Crystallographica Section B: Structural Crystallography and Crystal Chemistry 1969;25:925-46.
[38] Toby BH, Von Dreele RB. GSAS-II: the genesis of a modern open-source all purpose crystallography software package. Journal of Applied Crystallography 2013;46:544-9.
[39] Hofer F. EELS quantification of M edges by using oxidic standards. Ultramicroscopy 1987;21:63-8.
[40] Ravel B, Newville M. ATHENA, ARTEMIS, HEPHAESTUS: data analysis for X-ray absorption spectroscopy using IFEFFIT. Journal of synchrotron radiation 2005;12:537-41.
[41] Wang T, Jin L, Li C, Hu Q, Wei X. Relaxor ferroelectric BaTiO3–Bi (Mg2/3Nb1/3) O3 ceramics for energy storage application. Journal of the American Ceramic Society 2015;98:559-66.
[42] Rawat M, Yadav K. Compositional effects on structural, dielectric, ferroelectric and transport properties of Ba 1− x (Bi 0.5 Li 0.5) x TiO 3 ceramics. Materials Chemistry and Physics 2014;148:655-63.
[43] Zeb A, Milne SJ. Stability of High‐Temperature Dielectric Properties for (1− x) Ba0. 8Ca0. 2TiO3–xBi (Mg0. 5Ti0. 5) O3 Ceramics. Journal of the American Ceramic Society 2013;96:2887-92.
[44] Chen X, Chen J, Huang G, Ma D, Fang L, Zhou H. Relaxor Behavior and Dielectric Properties of Bi (Zn2/3Nb1/3) O3-Modified BaTiO3 Ceramics. Journal of Electronic Materials 2015;44:4804-10.
[45] Ogihara H, Randall CA, Trolier‐McKinstry S. High‐Energy Density Capacitors Utilizing 0.7 BaTiO3‐0.3 BiScO3 Ceramics. Journal of the American Ceramic Society 2009;92:1719-24.
[46] Raengthon N, Sebastian T, Cumming D, Reaney IM, Cann DP. BaTiO3‐Bi (Zn1/2Ti1/2) O3‐BiScO3 Ceramics for High‐Temperature Capacitor Applications. Journal of the American Ceramic Society 2012;95:3554-61.
[47] Moos R, Härdtl KH. Dependence of the intrinsic conductivity minimum of SrTiO3 ceramics on the sintering atmosphere. Journal of the American Ceramic Society 1995;78:2569-71.
[48] Triamnak N, Brennecka GL, Brown-Shaklee HJ, Rodriguez MA, Cann DP. Phase formation of BaTiO 3–Bi (Zn 1/2 Ti 1/2) O 3 perovskite ceramics. Journal of the Ceramic Society of Japan 2014;122:260-6.
[49] Robinson JA, Hartman MR, Reese SR. Design, construction and characterization of a prompt gamma activation analysis facility at the Oregon State University TRIGA® reactor. Journal of radioanalytical and nuclear chemistry 2010;283:359-69.
[50] Molnar G. Handbook of prompt gamma activation analysis: with neutron beams: Springer Science & Business Media; 2004.

[51] Jiang N, Spence JC. Can near-edge structure of the Bi L3 edge determine the formal valence states of Bi? Journal of Physics: Condensed Matter 2006;18:8029.
[52] Blanchard PE, Chapman KW, Heald SM, Zbiri M, Johnson MR, Kennedy BJ, et al. Direct Observation of Pressure-Driven Valence Electron Transfer in Ba3BiRu2O9, Ba3BiIr2O9, and Ba4BiIr3O12. Inorganic chemistry 2016.
[53] Sinclair UcwD. 2016.
[54] Szot K, Speier W. Surfaces of reduced and oxidized SrTiO 3 from atomic force microscopy. Physical Review B 1999;60:5909.
[55] Metzmacher C, Albertsen K. Microstructural Investigations of Barium Titanate‐Based Material for Base Metal Electrode Ceramic Multilayer Capacitor. Journal of the American Ceramic Society 2001;84:821-6.
[56] Morrison FD, Sinclair DC, West AR. An Alternative Explanation for the Origin of the Resistivity Anomaly in La‐Doped BaTiO3. Journal of the American Ceramic Society 2001;84:474-76.
[57] Wu TB, Lin JN. Transition of Compensating Defect Mode in Niobium‐Doped Barium Titanate. Journal of the American Ceramic Society 1994;77:759-64.
[58] Seuter AMJH. Defect chemistry and electrical transport properties of barium titanate: Philips Research Laboratories; 1974.
[59] Song C-R, Yoo H-I. Chemical diffusivity of BaTiO 3− δ: Defect chemical analysis. Physical Review B 2000;61:3975.
[60] Kumar N, Cann DP. Tailoring transport properties through nonstoichiometry in BaTiO3. Journal of Materials Science:1-11.

Chapter 10: The $Bi(Mg_{1/2}Ti_{1/2})O_3$-$(Bi_{1/2}K_{1/2})TiO_3$-$(Bi_{1/2}Na_{1/2})TiO_3$ Ceramics

10.1 Electromechanical Strain and Bipolar Fatigue in $Bi(Mg_{1/2}Ti_{1/2})O_3$-$(Bi_{1/2}K_{1/2})TiO_3$-$(Bi_{1/2}Na_{1/2})TiO_3$ Ceramics

Nitish Kumar and David P. Cann

Materials Science, School of Mechanical, Industrial, and Manufacturing Engineering,

Oregon State University, Corvallis, Oregon 97331, USA

Published in

Journal of Applied Physics

Volume 114 (5), 054102 (2013)

Abstract

Lead-free ceramics of composition $Bi(Mg_{1/2}Ti_{1/2})O_3$-$(Bi_{1/2}K_{1/2})TiO_3$-$(Bi_{1/2}Na_{1/2})TiO_3$ were prepared using solid state synthesis techniques. The dielectric spectra showed a T_{max} of more than 320 °C for all compositions and the transitions became increasingly diffuse as the $Bi(Mg_{1/2}Ti_{1/2})O_3$ content increased. A lower temperature transition, indicating a transformation from an ergodic to a non-ergodic relaxor state, was also seen for all compositions and this transition temperature decreased as the mole fraction of $Bi(Mg_{1/2}Ti_{1/2})O_3$ increased. The composition with 1% $Bi(Mg_{1/2}Ti_{1/2})O_3$ showed characteristic ferroelectric-like polarization and strain hysteresis. However, compositions with increased $Bi(Mg_{1/2}Ti_{1/2})O_3$ content became increasingly ergodic at room temperature with pinched polarization loops and no negative strain. Among these compositions, the magnitude of d_{33}* increased with $Bi(Mg_{1/2}Ti_{1/2})O_3$ content and the composition with 10% $Bi(Mg_{1/2}Ti_{1/2})O_3$ exhibited a d_{33}* of 422 pm/V . Fatigue measurements were conducted on all compositions and while the 1% $Bi(Mg_{1/2}Ti_{1/2})O_3$ composition exhibited a measurable, but small loss in maximum strain after a million cycles; all the other compositions from 2.5% to 10% $Bi(Mg_{1/2}Ti_{1/2})O_3$ were essentially fatigue-free. Lastly, optical and AC impedance measurements were employed to identify intrinsic conduction as the dominant conduction mechanism. These compositions were also highly insulating with high resistivities (~10^7 Ω-cm) at high temperatures (440 °C).

Introduction

$Pb(Zr_xTi_{1-x})O_3$ (PZT)-based piezoceramics currently dominate the industry however the search for an appropriate lead-free replacement due to concern over

environmental concerns continues.[1] Developing a material that could serve as a drop-in replacement for PZT is a significant technical challenge. A different approach aims at developing Pb-free alternative materials targeted at specific applications. There have been a number of promising developments in the last decade. For example, textured $(K,Na)NbO_3$ (KNN) based compositions were shown to have excellent piezoelectric properties.[2] In addition, various binary and ternary systems based on $(Bi_{1/2}Na_{1/2})TiO_3$ (BNT), $(Bi_{1/2}K_{1/2})TiO_3$ (BKT), $BaTiO_3$ (BT), and KNN, have been widely investigated and have shown promising piezoelectric properties compared to Pb-based compositions.[3-17]

In particular, the BNT-based systems have been extensively studied since its discovery by Smolenskii *et al*.[18] Under an applied electric field, BNT-based compositions undergo a phase transformation to a polar ferroelectric phase where domains become stable. This is considered to play an important role in high strain exhibited in compositions based on BNT.[3-6, 9, 11-13, 19] Jo *et al.* recently proposed that all BNT-based compositions could be classified into two kinds of relaxors: non-ergodic and ergodic.[20] While the former transforms irreversibly to a ferroelectric state, the latter undergoes a reversible transformation on application of an electric field. The reversible phase transformation for these ergodic relaxors is indicated by the absence of a remnant strain in these compositions. As a result, all of the induced strain can be used for actuator applications and consequently these compositions feature large high-field piezoelectric coefficients. A second peculiar phenomenon observed with BNT-based systems is a transition from an ergodic to a non-ergodic state at approximately 100-200°C.[3-5, 10, 11, 13, 17, 21] Above this transition temperature, the polarization loops

are pinched and electromechanical strain data shows no negative values which is characteristic of a reversible field-induced phase transformation.

Fatigue properties are important for the long-term reliability of these systems. In PZT, a severe degradation in the maximum strain and polarization has been observed beyond 10^5 cycles at field levels close to twice the coercive field E_c.[22] In BNT-based compositions, it has been shown that the degradation in properties due to fatigue is not as severe and asymmetric as in PZT.[9, 23, 24] In fact, in many systems fatigue is absent especially in compositions which are ergodic at room temperature.[9, 24] It is expected that the reversible field-induced phase transformation might be responsible for absence of fatigue.[24] This study will demonstrate the basic piezoelectric properties and fatigue behavior of $Bi(Mg_{1/2}Ti_{1/2})O_3$-BKT-BNT piezoelectric ceramics with the aim of identifying the fatigue mechanism. While most piezoelectric actuator devices are activated in unipolar mode, all of the fatigue studies in this work were conducted under bipolar driving fields. The primary reason for this is that it has been shown that bipolar operating fields have a more severe impact on the electromechanical strain and thus the differences between the behaviors of different compositions will be more pronounced.

Experimental

Ceramics of the composition $xBi(Mg_{1/2}Ti_{1/2})O_3$-0.4BKT-(0.6-x)BNT ($0.01 \leq x \leq 0.1$) were prepared via conventional solid state processing. For convenience, henceforth, a composition designated as X-Y-Z would represent X% $Bi(Mg_{1/2}Ti_{1/2})O_3$ (BMT), Y% BKT and Z% BNT. The precursor powders used were Bi_2O_3 (>99.9%), $MgCO_3$ (>99%), TiO_2 (>99.9%), K_2CO_3(>99%) and Na_2CO_3(>99.5%). The mixed

powders were ground using a vibratory mill for 6 hours using ethanol as a medium and then dried overnight in an oven (~80°C). All the compositions were calcined between 950 °C and 1050 °C for 6 h and then milled and dried again. Green pellets in the shape of thin discs were made by cold-pressing uniaxially at a pressure of 150 MPa and then sintered on a bed of calcined powder in a closed alumina crucible at 1100 °C-1125 °C for 3-4 hours. All the sintered pellets were polished to around 0.8 mm thickness. X-ray diffraction (Bruker AXS D8 Discover, Madison, WI, USA) was used for phase and crystal structure determination. Prior to any electrical measurements, silver electrodes were applied on both sides of the pellets and then fired at 700°C for 30 min. The pellets were placed in a high temperature measurement cell (NorECs AS ProbostatTM, Oslo, Norway) and temperature dependent dielectric properties were measured using an LCR meter (Agilent 4284A, Santa Clara, CA, USA). An impedance analyzer (Solartron SI1260A equipped with Solartron 1296A dielectric interface, Farnborough, UK) was used to measure the impedance in the frequency range 1 Hz to 1 MHz. The SMaRT impedance measurement software program was used to collect the data. Polarization hysteresis was measured at room temperature and 1 Hz (using Radiant Technologies RT66A, Albuquerque, New Mexico). Strain measurements were conducted at 0.1 Hz in conjunction with a interferometric sensor (MTI Instruments 2100 Fotonic Sensor, Albany, New York). Fatigue tests were conducted on unpoled samples by applying a bipolar triangular waveform at 10 Hz with a peak field of 50 kV/cm. The optical measurements were carried out on the sintered pellets over the wavelength range of 200-1100 nm at room temperature using an Ocean Optics HR4000 UV-Vis Spectrometer (Ocean Optics, Dunedin, FL) with a balanced deuterium/tungsten halogen source.

Results and Discussion

All compositions in this study exhibited a single perovskite phase within the limits of the x-ray diffraction instrument used. The {200} reflections showed splitting that is characteristic of tetragonal symmetry and as is evident from the Fig.10.1.1, the splitting diminished as the BMT content increased. The radial shrinkages after sintering for all compositions were typically greater than 13% with high sintered densities.

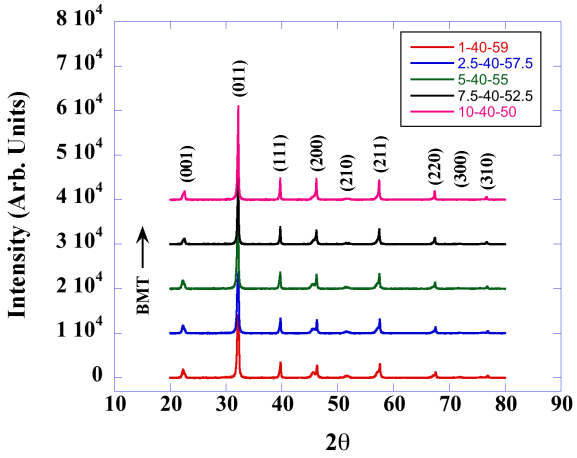

FIG. 10.1.1: XRD data for the indicated compositions where X-Y-Z corresponds to the BMT-BKT-BNT mole fractions, respectively.

Figure 10.2.2 shows the evolution of dielectric properties with composition. The dielectric loss (tanδ) for all compositions at 1 kHz remained below 5% up to 400 °C. As is typical of BNT-based systems, the temperature at which the relative permittivity was maximum (T_{max}) ranged between 320°C and 350°C for all compositions. As shown in the data, the transitions became increasingly diffuse as the BMT content increased. In a similar system, this dielectric maximum corresponded to the gradual disappearance of local tetragonal distortions.[11] Also typical of BNT-based systems, a low temperature transition can be seen which is linked to the transition from a high temperature ergodic state to a non-ergodic relaxor state.[20] This transition shifted to lower temperatures as

the BMT content increased, indicating that the ergodic nature of these compositions increased with the addition of BMT.

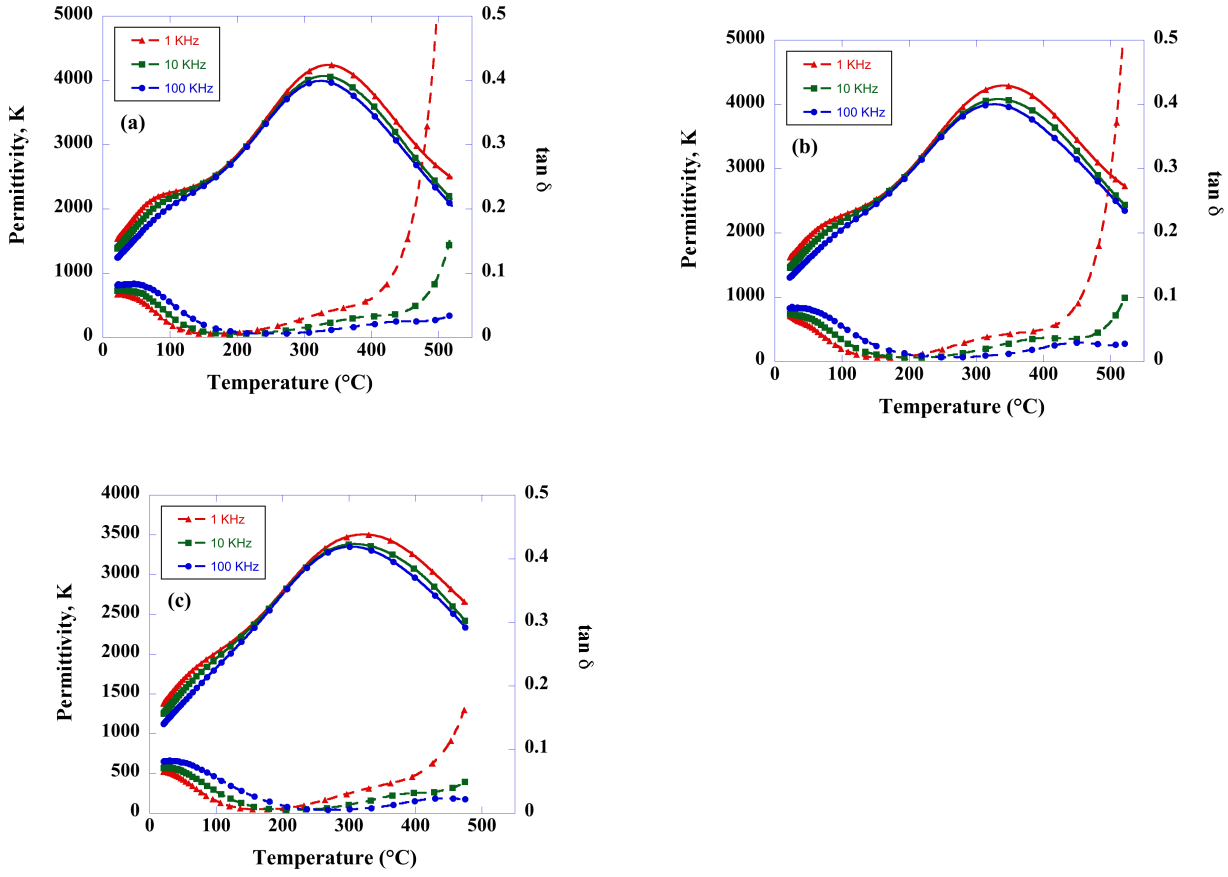

FIG. 10.1.2. Temperature dependence of dielectric constant (solid lines) and dielectric loss (dashed lines) for (a) 1-40-59, (b) 5-40-55 and (c) 10-40-50 compositions.

The polarization hysteresis data for the 1% BMT composition exhibited characteristics approaching normal ferroelectric behavior (Fig. 10.1.3(a)) including a remanent polarization and negative strain indicative of domain switching, typical of non-ergodic relaxors. However, as the BMT content increased the polarization loops became

increasingly pinched with a decreasing remanent polarization and the maximum polarization decreased with an increase in BMT content as well. The strain data for the 1-40-59 composition showed a typical butterfly shape which is again characteristic of ferroelectricity, induced irreversibly in non-ergodic relaxors on application of electric field. However, consistent with polarization data, the negative strains vanished as the BMT content increased indicating that there was no domain switching for these compositions. Among the compositions with exhibited no domain switching, the maximum strain increased as the BMT content increased, with the 10-40-50 composition showing a highest effective piezoelectric coefficient (d_{33}*) of 422 pm/V. The low remanent polarization and negligible remanent strain for higher BMT compositions is indicative of a non-polar phase at zero electric field, which is consistent with the dielectric data.

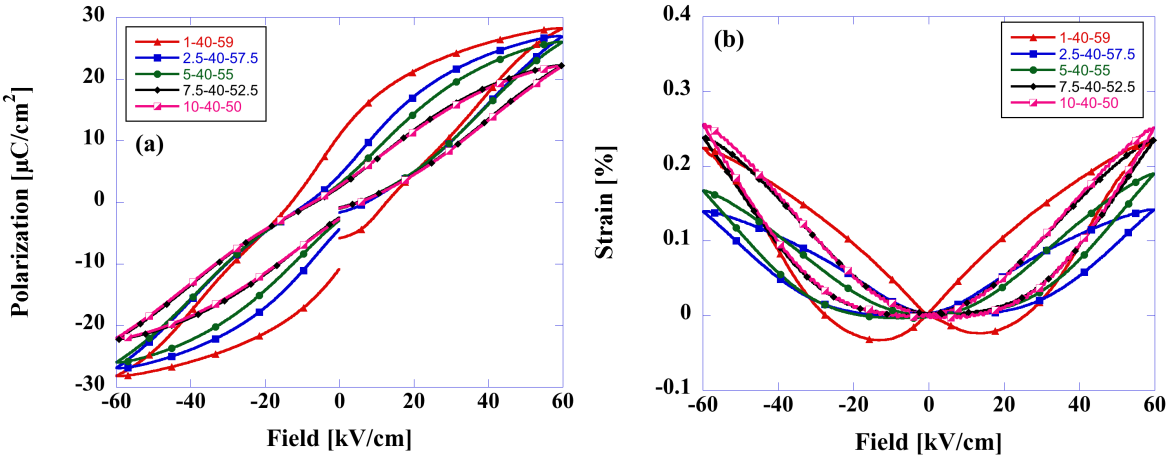

FIG. 10.1.3. (a) Polarization at 1 Hz and (b) electromechanical strain at 0.1 Hz for various compositions fatigued at 60 kV/cm and 10 Hz.

Figure 10.1.4 shows the effects of fatigue on the polarization for various compositions. The fatigue tests were conducted by applying a bipolar triangular waveform with a peak field of 50 kV/cm at 10 Hz. It is clear that there was no significant change in the polarization after 10^6 cycles as is seen in the case of PZT.[22] A closer examination revealed that the coercive field decreased by 2% to 15% over the various compositions. This is in contrast to the behavior shown by PZT where coercive field typically increases after many cycles; it is however, consistent with the behavior shown in the composition $Bi(Zn_{1/2}Ti_{1/2})O_3$-$(Bi_{1/2}K_{1/2})TiO_3$-$(Bi_{1/2}Na_{1/2})TiO_3$ (BZT-BKT-BNT).[9, 25] In addition, the maximum polarization increased by a small amount of 2%-6% after 10^6 cycles, similar to observations in BZT-BKT-BNT, but again different from PZT which shows a decrease of more than 50% after a similar number of cycles.[22]

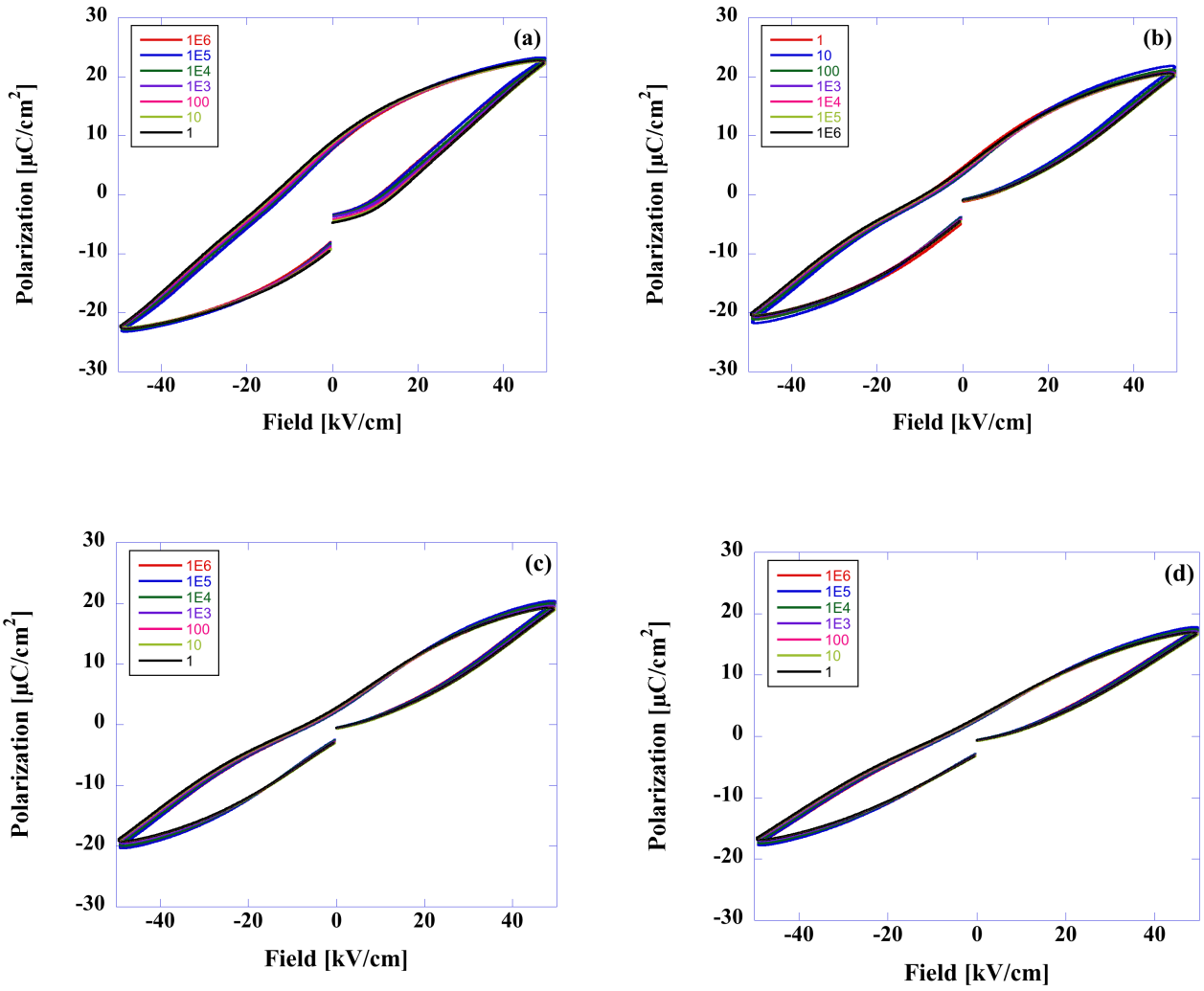

FIG. 10.1.4. Effect of fatigue on polarization (at 1 Hz) for (a) 1-40-59, (b) 2.5-40-57.5, (c) 5-40-55 and (d) 10-40-55 compositions tested at 50 kV/cm and 10 Hz up to a million cycles.

The magnitude of the degradation in the electromechanical strain data strongly depended on the BMT content (Fig. 10.1.5). In particular, composition that exhibited clear evidence of domain switching (*i.e.* 1-40-59) experienced a ~40% decrease in maximum strain. It is also important to note that the magnitude of the degradation was largely symmetric. This is in contrast to observations during bipolar fatigue studies of PZT where the degradation of the strain can be severely asymmetric. In one study, the

maximum strain decreased by ~90% along one field direction and ~58% for the opposite polarity.[22] For the other compositions, the degradation of strain was minimal. For the 10-40-50 composition, for an applied field of 50 kV/cm the degradation of strain was only 0.9%. The maximum strain for the 2.5-40-57.5 composition, in fact, increased by approximately 10% after 10^6 cycles. Overall, it can be summarized that the composition range from 2.5% to 10% BMT were essentially fatigue free.

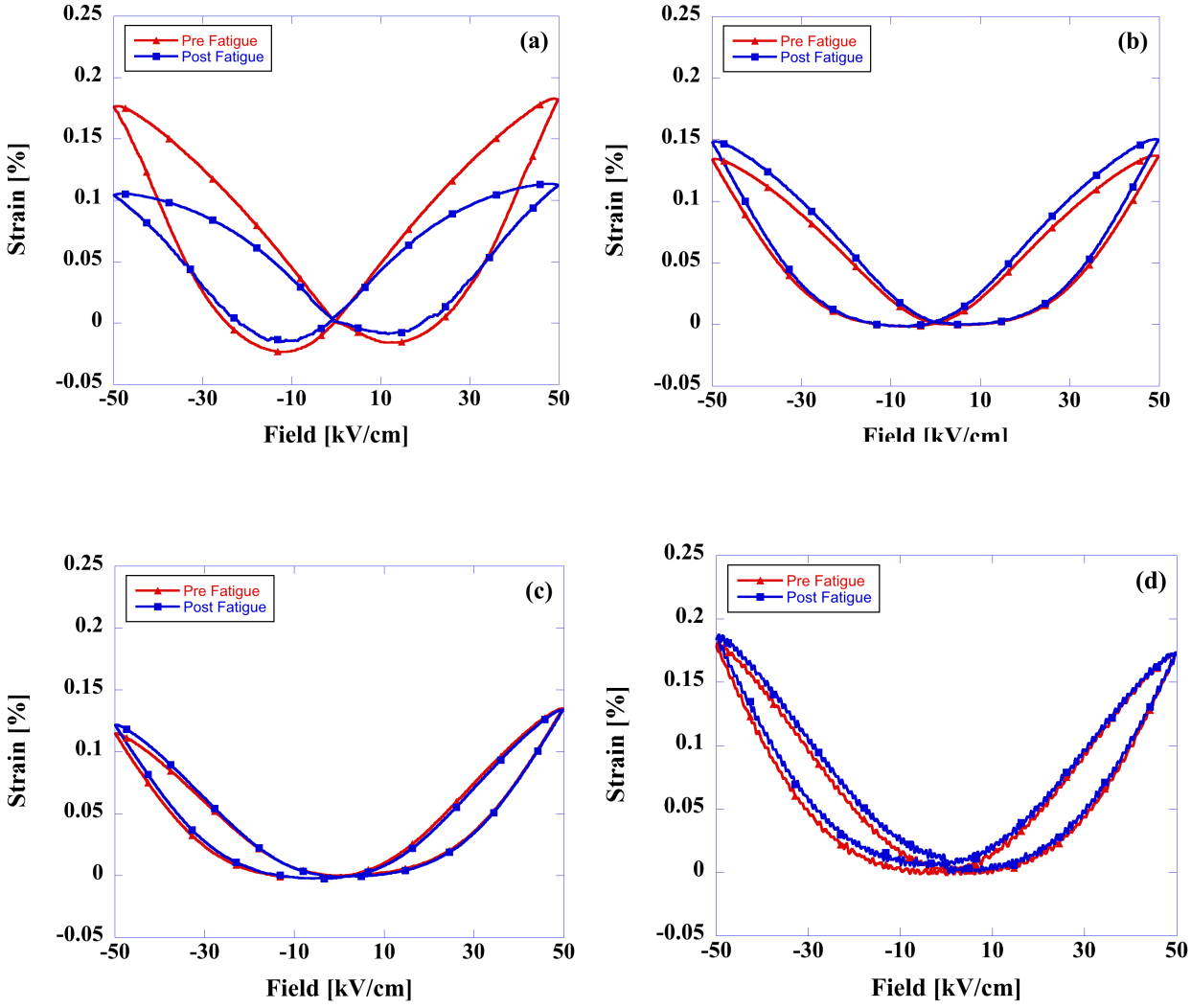

FIG. 10.1.5. Effect of fatigue on electromechanical strain (at 0.1 Hz) for (a) 1-40-59, (b) 2.5-40-57.5, (c) 5-40-55 and (d) 10-40-55 compositions tested at 50 kV/cm and 10 Hz up to a million cycles.

The results from AC impedance are shown in Fig. 10.1.6. The resistivities of these compositions were ~10^7 Ω-cm at 440 °C which is at least two orders of magnitude higher than PZT.[26] The activation energies for conduction, calculated from Arrhenius plot, were between 1.4 eV and 1.7 eV. Diffuse reflectance measurements were carried out following the method of related work using Kubelka-Munk[27] and Tauc equations[28, 29] to plot Fig. 10.1.7. The optical band gap can be calculated to values between 3 eV and 3.1 eV. The high resistivities measured in these compositions and that the activation energies for conduction that are nearly half of the optical band gap suggest that intrinsic conduction is the dominant transport mechanism in these compositions. Other titanate perovskites often exhibit activation energies close to 1 eV due to ionization of oxygen vacancies.[30] In PZT, the fatigue behavior is strongly influenced by the presence of these oxygen vacancies and the domain wall mobility is severely affected by defect agglomerates.[31] The predominance of oxygen vacancies in PZT is also supported by the activation energy of conduction close to 1 eV for PZT.[26]

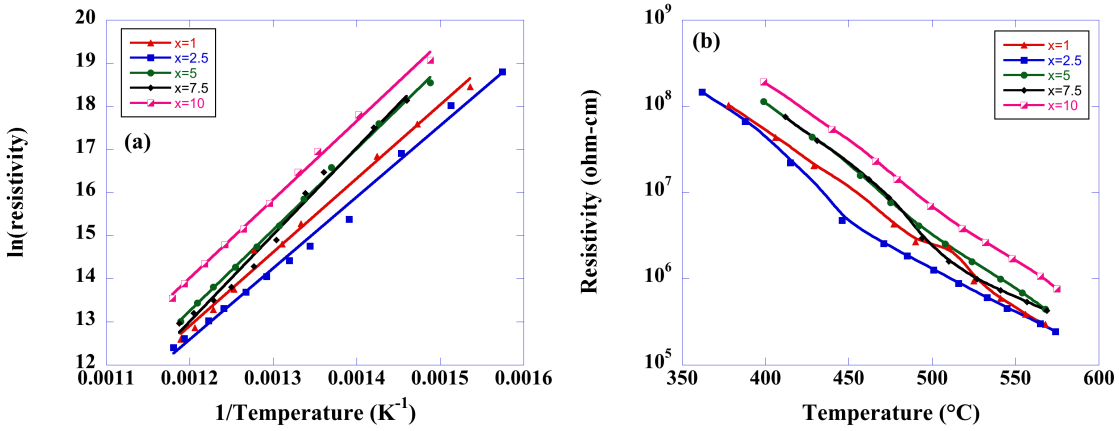

FIG. 10.1.6. (a) Arrhenius plot, ln(resistivity) with inverse temperature and (b) Variation of resistivity with temperature.

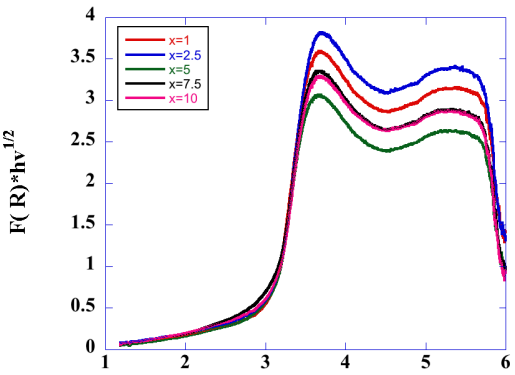

FIG. 10.1.7. Tauc plot, where F(R) is the ratio of effective absorption and scattering coefficients and hν is photon energy for various compositions.[27]

To this point, the amount of literature available on piezoelectric fatigue of bismuth-based perovskites is scarce and almost all the studies are on BNT-based systems.[9, 23, 24, 32, 33] Luo *et. al.* studied the fatigue behavior of BNT-$BaTiO_3$-$K_{1/2}Na_{1/2}NbO_3$ (BNT-BT-KNN) and found that KNN destabilized ferroelectric long range order in the system which had a obvious effect of fatigue, analogous to BMT in this study.[24] They attributed the observed fatigue in low KNN composition to domain wall pinning and formation of microcracks and to the repeated field induced phase transition in the high KNN composition. A major distinction from this study was that the ergodic composition (higher KNN) was not fatigue free. A bipolar fatigue study on binary BNT-BT compositions revealed significant degradation in material properties including a decrease in the maximum polarization by more than 33% and a decrease in the maximum strain by 60% after one million cycles.[23] Ehmke *et al.* showed that addition of 1% CuO improved the fatigue property of BNT-BT.[32] In a different study, fatigue in BNT-BT was proposed to be a two-stage mechanism, including a transformation to a ferroelectric

structure from a relaxor state followed by cyclic domain wall pinning and fragmentation.[33] In a system similar to this study, BZT-BKT-BNT, Patterson *et al.* demonstrated fatigue-free behavior for an ergodic composition with 5% $Bi(Zn_{1/2}Ti_{1/2})O_3$.[9] There was no degradation in maximum polarization or strain after a million cycles for this composition. All these materials, however, show a significant improvement in fatigue resistance compared to PZT. Table 10.1.1 summarizes the compositions studied and fatigue results.

Table 10.1.1: Table summarizing the bipolar fatigue results of bismuth-based compositions. The values represent the change in material properties due to fatigue with respect to their original values. '+' sign indicates increase and '–' sign a decrease in that property after fatigue. Data in asterisk (*) are approximate values extrapolated from plots wherever exact values were not available in the text.

Composition	Number of Fatigue cycles	Driving Field level (kV/cm)	Change in Remnant Polarization (P_r)	Change in Maximum Polarization (P_{max})	Change in Coercive Field (E_c)	Change in High field piezoelectric constant (d_{33}*)	References
BNT-BT-KNN (93-6-1)	10^6	60 ($3E_c$)	-37%*	-36%*	+100%	-50%*	22
BNT-BT-KNN (91-6-3)	10^6	60 ($4E_c$*)	+66%*	-14%*	+50%*	-7%	22
BNT-BT (94-6)	10^6	60 ($2E_c$)	-50%	-51%*	+22%	-60%	21
BNT-BT +1% Cu (94-6)	100	60 ($2E_c$)	+0%	+0%*	+0%*	+0%*	30
BZT-BKT-BNT (2.5-40-57.5)	10^6	50 ($2E_c$)	-5.1%	+1.4%	-20%	-13%	3
BZT-BKT-BNT (5-40-55)	10^6	50 ($5E_c$)	-7%	+6.8%	-20%	+4%	3
BMT-BKT-BNT (1-40-59)	10^6	50 (~$3.5E_c$)	-14.9%	+1.9%	-24.6%	-39%	The present work
BMT-BKT-BNT (2.5-40-57.5 to 10-40-50)	10^6	50 ($5E_c$ to $7E_c$)	-0.7% to -20%	+2% to +8%	-2% to -13%	+0% to +10%	The present work

Conclusions

Ternary solid solutions of BMT-BKT-BNT were prepared with BMT concentrations up to 10 mol%. For all compositions, T_{max} remained above 320 °C and a typical ergodic to non-ergodic relaxor transition was also evident near 200°C. The polarization and strain loops for the 1-40-59 composition exhibited characteristics consistent with ferroelectric behavior. However, with the addition of BMT the dielectric behavior became more diffuse and the polarization hysteresis became increasingly pinched without any measurable negative strain. All the compositions were evaluated under 50 kV/cm bipolar cycling and exhibited fatigue behavior significantly better than PZT. For all compositions, the maximum polarization was largely unaffected by fatigue cycling up to at least a million cycles. In addition, there was minimal effect of fatigue on the maximum electromechanical strain for compositions with 2.5% BMT to 10% BMT. Transport measurements in these compositions showed the presence of high resistivities (e.g. 10 MΩ-cm at 440 °C) and activation energies equal to half of the measured optical band gap. It is proposed that the lower defect concentrations and the nature of the relaxor-ferroelectric transition in these compositions are responsible for the fatigue resistance.

Acknowledgements

The authors would like to gratefully acknowledge the support from Hewlett-Packard company.

References

[1] Foster WJ, Meen JK, Fox DA. The effect of physiologic aqueous solutions on the perovskite material lead-lanthanum-zirconium titanate (PLZT): potential retinotoxicity. Cutaneous and ocular toxicology 2013;32:18-22.
[2] Saito Y, Takao H, Tani T, Nonoyama T, Takatori K, Homma T, et al. Lead-free piezoceramics. Nature 2004;432:84-7.
[3] Isupov V. Ferroelectric Na0. 5Bi0. 5TiO3 and K0. 5Bi0. 5TiO3 perovskites and their solid solutions. Ferroelectrics 2005;315:123-47.
[4] Jarupoom P, Patterson E, Gibbons B, Rujijanagul G, Yimnirun R, Cann D. Lead-free ternary perovskite compounds with large electromechanical strains. Applied Physics Letters 2011;99:152901.
[5] Jo W, Granzow T, Aulbach E, Rödel J, Damjanovic D. Origin of the large strain response in (K0. 5Na0. 5) NbO3-modified (Bi0. 5Na0. 5) TiO3–BaTiO3 lead-free piezoceramics. Journal of Applied Physics 2009;105:094102.
[6] Kounga AB, Zhang S-T, Jo W, Granzow T, Rödel J. Morphotropic phase boundary in (1-x) Bi0. 5Na0. 5TiO3-xK (0.5) Na (0.5) NbO (3) lead-free piezoceramics. 2008.
[7] Patterson EA, Cann DP. DIELECTRIC AND PIEZOELECTRIC PROPERTIES OF (K, Na) NbO3-BASED PIEZOELECTRIC CERAMICS. Journal of Advanced Dielectrics 2011;1:345-9.
[8] Patterson EA, Cann DP. Piezoelectric properties and unipolar fatigue behavior of KNN-based Pb-free piezoceramics. IEEE transactions on ultrasonics, ferroelectrics, and frequency control 2011;58:1835-41.
[9] Patterson EA, Cann DP. Bipolar piezoelectric fatigue of Bi (Zn0. 5Ti0. 5) O3-(Bi0. 5K0. 5) TiO3-(Bi0. 5Na0. 5) TiO3 Pb-free ceramics. Applied Physics Letters 2012;101:042905.
[10] Patterson EA, Cann DP. Relaxor to Ferroelectric Transitions in (Bi1/2Na1/2) TiO3–Bi (Zn1/2Ti1/2) O3Solid Solutions. Journal of the American Ceramic Society 2012;95:3509-13.
[11] Patterson EA, Cann DP, Pokorny J, Reaney IM. Electromechanical strain in Bi (Zn1/2Ti1/2) O3–(Bi1/2Na1/2) TiO3–(Bi1/2K1/2) TiO3 solid solutions. Journal of Applied Physics 2012;111:094105.
[12] Simons H, Daniels J, Jo W, Dittmer R, Studer A, Avdeev M, et al. Electric-field-induced strain mechanisms in lead-free 94%(Bi1/2Na1/2) TiO3-6% BaTiO3. 2011.
[13] Takenaka T, Nagata H, Hiruma Y. Phase transition temperatures and piezoelectric properties of (Bi 1/2 Na 1/2) TiO 3-and (Bi 1/2 K 1/2) TiO 3-based bismuth perovskite lead-free ferroelectric ceramics. IEEE transactions on ultrasonics, ferroelectrics, and frequency control 2009;56:1595-612.
[14] Zhang S, Shrout TR, Nagata H, Hiruma Y, Takenaka T. Piezoelectric properties in (K 0.5 Bi 0.5) TiO 3-(Na 0.5 Bi 0.5) TiO 3-BaTiO 3 lead-free ceramics. IEEE transactions on ultrasonics, ferroelectrics, and frequency control 2007;54:910-7.
[15] Zhang S-T, Kounga AB, Aulbach E, Ehrenberg H, Rödel J. Giant strain in lead-free piezoceramics Bi0. 5Na0. 5TiO3–BaTiO3–K0. 5Na0. 5NbO3 system. Applied Physics Letters 2007;91:112906.
[16] Zhao P, Zhang B-P, Li J-F. High piezoelectric d33 coefficient in Li-modified lead-free (Na, K) NbO3 ceramics sintered at optimal temperature. Applied physics letters 2007;90:2909.

[17] Zuo R, Fang X, Ye C, Li L. Phase Transitional Behavior and Piezoelectric Properties of Lead‐Free (Na0. 5K0. 5) NbO3‐(Bi0. 5K0. 5) TiO3 Ceramics. Journal of the American Ceramic Society 2007;90:2424-8.
[18] Smolenskii G, Agranovskaya A. Dielectric polarization of a number of complex compounds. Soviet Physics-Solid State 1960;1:1429-37.
[19] Zhang S-T, Kounga AB, Aulbach E, Granzow T, Jo W, Kleebe H-J, et al. Lead-free piezoceramics with giant strain in the system Bi0. 5Na0. 5TiO3–BaTiO3–K0. 5Na0. 5NbO3. I. Structure and room temperature properties. Journal of Applied Physics 2008;103:034107.
[20] Jo W, Dittmer R, Acosta M, Zang J, Groh C, Sapper E, et al. Giant electric-field-induced strains in lead-free ceramics for actuator applications–status and perspective. Journal of electroceramics 2012;29:71-93.
[21] Zhao W, Ya J, Xin Y, Zhao D, Zhou H. Fabrication of Na0. 5Bi0. 5TiO3‐BaTiO3‐Textured Ceramics Templated by Plate‐Like Na0. 5Bi0. 5TiO3 Particles. Journal of the American Ceramic Society 2009;92:1607-9.
[22] Balke N, Kungl H, Granzow T, Lupascu DC, Hoffmann MJ, Rödel J. Bipolar fatigue caused by field screening in Pb (Zr, Ti) O3 ceramics. Journal of the American Ceramic Society 2007;90:3869-74.
[23] Luo Z, Glaum J, Granzow T, Jo W, Dittmer R, Hoffman M, et al. Bipolar and Unipolar Fatigue of Ferroelectric BNT‐Based Lead‐Free Piezoceramics. Journal of the American Ceramic Society 2011;94:529-35.
[24] Luo Z, Granzow T, Glaum J, Jo W, Rödel J, Hoffman M. Effect of Ferroelectric Long‐Range Order on the Unipolar and Bipolar Electric Fatigue in Bi1/2Na1/2TiO3‐Based Lead‐Free Piezoceramics. Journal of the American Ceramic Society 2011;94:3927-33.
[25] Nuffer J, Lupascu D, Rödel J. Damage evolution in ferroelectric PZT induced by bipolar electric cycling. Acta Materialia 2000;48:3783-94.
[26] Dih J, Fulrath R. Electrical Conductivity in Lead Zirconate‐Titanate Ceramics. Journal of the American Ceramic Society 1978;61:448-51.
[27] Klaas J, Schulz-Ekloff G, Jaeger NI. UV-visible diffuse reflectance spectroscopy of zeolite-hosted mononuclear titanium oxide species. The Journal of Physical Chemistry B 1997;101:1305-11.
[28] Tauc J, Grigorovici R, Vancu A. Optical properties and electronic structure of amorphous germanium. physica status solidi (b) 1966;15:627-37.
[29] Umebayashi T, Yamaki T, Itoh H, Asai K. Band gap narrowing of titanium dioxide by sulfur doping. Applied Physics Letters 2002;81:454-6.
[30] Morrison FD, Sinclair DC, West AR. Electrical and structural characteristics of lanthanum-doped barium titanate ceramics. Journal of applied physics 1999;86:6355-66.
[31] Lupascu DC. Fatigue in ferroelectric ceramics and related issues: Springer Science & Business Media; 2013.
[32] Ehmke M, Glaum J, Jo W, Granzow T, Rödel J. Stabilization of the Fatigue‐Resistant Phase by CuO Addition in (Bi1/2Na1/2) TiO3–BaTiO3. Journal of the American Ceramic Society 2011;94:2473-8.

[33] Simons H, Glaum J, Daniels JE, Studer AJ, Liess A, Rödel J, et al. Domain fragmentation during cyclic fatigue in 94%(Bi1/2Na1/2) TiO3-6% BaTiO3. Journal of Applied Physics 2012;112:044101.

10.2. Role of Point Defects in Bipolar Fatigue Behavior of $Bi(Mg_{1/2}Ti_{1/2})O_3$ Modified $(Bi_{1/2}K_{1/2})TiO_3$-$(Bi_{1/2}Na_{1/2})TiO_3$ Relaxor Ceramics

Nitish Kumar, Troy Y. Ansell and David P. Cann

Materials Science, School of Mechanical, Industrial, and Manufacturing Engineering,

Oregon State University, Corvallis, Oregon 97331, USA

Published in

Journal of Applied Physics

Volume 115 (15), 154104 (2014)

Abstract

Lead-free $Bi(Mg_{1/2}Ti_{1/2})O_3$-$(Bi_{1/2}K_{1/2})TiO_3$-$(Bi_{1/2}Na_{1/2})TiO_3$ (BMT-BKT-BNT) ceramics have been shown to exhibit large electromechanical strains under high electric fields along with negligible fatigue under strong electric fields. To investigate the role of point defects on the fatigue characteristics, the composition 5BMT-40BKT-55BNT was doped to incorporate acceptor and donor defects on the A and B sites by adjusting the Bi/Na and Ti/Mg stoichiometries. All samples had pseudo-cubic symmetries based on x-ray diffraction, typical of relaxors. Dielectric measurements showed that the high and low temperature phase transitions were largely unaffected by doping. Acceptor doping resulted in the observation of a typical ferroelectric-like polarization with a remnant polarization and strain hysteresis loops with significant negative strain. Donor-doped compositions exhibited characteristics that were indicative of an ergodic relaxor phase. Fatigue measurements were carried out on all of the compositions. While the A-site acceptor-doped composition showed a small degradation in maximum strain after 10^6 cycles, the other compositions were essentially fatigue free. Impedance measurements were used to identify the important conduction mechanisms in these compositions. As expected, the presence of defects did not strongly influence the fatigue behavior in donor-doped compositions owing to the nature of their reversible field-induced phase transformation. Even for the acceptor-doped compositions, which had stable domains in the absence of an electric field at room temperature, there was negligible degradation in the maximum strain due to fatigue. This suggests that either the defects introduced through stoichiometric variations do not play a prominent role in fatigue in these systems

or it is compensated by factors like decrease in coercive field, an increase in ergodicity, symmetry change, or other factors.

Introduction

Lead zirconate titanate ($Pb(Zr_xTi_{1-x})O_3$ or PZT)-based piezoceramics are used in a wide range of applications owing to their excellent material properties as well as the opportunity to engineer their properties through chemical doping or optimization of the composition. However, the presence of lead oxides poses serious environmental and health concerns, especially during manufacturing and disposal after usage, and therefore the research community is actively engaged in developing Pb-free alternatives.[1] In particular, $(Bi_{1/2}Na_{1/2})TiO_3$ (BNT)-based relaxors have attracted a lot of attention during the last decade.[2-14] Upon application of an electric field, these systems exhibit large electromechanical strains as they undergo a field-induced phase transformation to a polar ferroelectric phase with metastable domains. This transformation is irreversible in non-ergodic compositions and reversible in ergodic compositions.[6-9, 11, 13, 14] A temperature-dependent transition from an ergodic to a non-ergodic state is also observed around 100-200 °C.[5, 6, 8, 9, 13, 14] Above this transition temperature, the polarization loops are pinched and electromechanical strain data shows no negative values, characteristic of a reversible field induced phase transformation in ergodic relaxors.

Another disadvantage of PZT is its poor electromechanical fatigue characteristics. These materials show significant and asymmetric degradation in their material properties under bipolar electrical cycles.[15] Even after extensive studies, the mechanisms for fatigue in PZT is not fully understood. Some of the proposed mechanisms for fatigue

include: domain wall pinning, microcracks along grain boundaries, and poor electrical contact between the electrode and sample.[15, 16] Recently, Balke *et al*. showed evidence of a damaged region close to the sample electrodes and attributed the degradation of properties to the presence of this damaged layer, thus attributing fatigue as a surface-related phenomena rather than bulk.[15] In BNT-based systems, the effect of fatigue has been shown to be not nearly as severe as in PZT and is often composition dependent.[4, 9-11, 17] Nonetheless, if these systems are to be used extensively in industry, the mechanism behind their fatigue must be understood. However, the amount of literature available focusing on this issue is scarce. The reversible field-induced phase transformation may be responsible for the improved fatigue properties of BNT-based solid solutions.[10] Another explanation for the excellent fatigue properties is the much lower defect concentrations in these systems owing to their lower processing temperatures.[9, 11] In addition, few reports have studied the contribution of surface phenomena to fatigue in these Pb-free materials, e.g. microcracks, damaged layers beneath electrode, etc.[4, 17]

Patterson *et al.* and Kumar *et al.* have reported that and $Bi(Zn_{1/2}Ti_{1/2})O_3$ (BZT) and $Bi(Mg_{1/2}Ti_{1/2})O_3$ (BMT) modified $(Bi_{1/2}K_{1/2})TiO_3$-$(Bi_{1/2}Na_{1/2})TiO_3$ (BNT-BKT) ergodic compositions exhibit negligible fatigue.[9, 11] The focus of the present work is to study the effect of point defects on fatigue phenomena in these systems with a focus on the composition 5BMT-40BKT-55BNT. Acceptor and donor doping was accommodated on the A and B-sites by altering the Na and Bi, and Mg and Ti stoichiometries, respectively.

Rayleigh analysis was also employed to gain further insight and separate intrinsic and extrinsic contributions to the non-linear dielectric properties. The intrinsic contribution is believed to emanate from the lattice or single domain structure, while the extrinsic contributions originate from the motion of domain walls.[18, 19]. The following basic equations can be used to determine the contributions to dielectric permittivity:

$$\varepsilon^* = \varepsilon' + \iota\varepsilon'' \quad \text{Eq. 10.2.1a}$$

$$\varepsilon' = \varepsilon'_{init} + \alpha' E_0 \quad \text{Eq. 10.2.1b}$$

$$\varepsilon'' = \alpha'' E_0 = \frac{4}{3\pi}\alpha' E_0 \quad \text{Eq. 10.2.1c}$$

$$P(E) = (\varepsilon'_{init} + \alpha' E_0)E \pm 0.5 \times \alpha'(E^2 - E_0^2) \quad \text{Eq. 10.2.1d}$$

where ε^*, ε' and ε'' are the complex, real and imaginary permittivities, respectively. The terms ε'_{init} and α' are the reversible and irreversible Rayleigh coefficients. The α'' is the imaginary irreversible Rayleigh coefficient and E_0 and P are amplitude of applied electric field and dielectric polarization, respectively. The peak-to-peak polarization is related to the magnitude of the complex permittivity and the area under the polarization loop gives the magnitude of the imaginary permittivity. These can be used to obtain the reversible and irreversible Rayleigh coefficients, the details of which can be found elsewhere.[19]

Experimental

Four non-stoichiometric ceramics were prepared around the composition $5Bi(Mg_{1/2}Ti_{1/2})O_3$-40BKT-55BNT via conventional solid state processing. The Bi and Na stoichiometries were modified on A-site and Mg and Ti on B-site in order to create either a 0.02 charge excess or deficiency as compared to the stoichiometric composition. For

convenience, the composition with deficiency on A-site will be referred to as A_A and the composition with deficiency on B-site as A_B. In the same way, compositions with 0.02 charge excess on A and B-sites will be denoted as D_A and D_B respectively.

The precursor powders used were Bi_2O_3 (>99.9%, Sigma-Aldrich), $MgCO_3$ (>99%, Sigma-Aldrich), TiO_2 (>99.9%, Sigma-Aldrich), K_2CO_3 (>99%, Sigma-Aldrich) and Na_2CO_3 (>99.5%, Alfa-Aesar). The powders were mixed and ground using a vibratory mill for 6 hours in ethanol medium and then dried in an oven at a temperature of ~80°C. All the compositions were calcined at 1050 °C for 6 h with or without intermediate milling. They were milled again post-calcination and dried. Green pellets in the shape of thin discs were made by cold-pressing uniaxially at a pressure of 150 MPa. They were sintered on a bed of calcined powder in a closed alumina crucible at 1125 °C for 4 hours. All the sintered pellets were polished to sub-millimeter thickness. X-ray diffraction (Bruker AXS D8 Discover, Madison, WI, USA) was used to check phase purity and determine crystal structure. Silver electrodes were applied on both sides of the pellets and fired at 700°C for 30 min before performing any electrical measurements. To measure the dielectric properties, the pellets were placed in a high temperature measurement cell (NorECs AS ProbostatTM, Oslo, Norway) and an LCR meter (Agilent 4284A, Santa Clara, CA, USA) was used. An impedance analyzer (Solartron SI1260A equipped with Solartron 1296A dielectric interface, Farnborough, UK) was used in the frequency range 1 Hz to 1 MHz, in conjunction with SMaRT impedance measurement software program to collect the data. Polarization hysteresis measurements were performed at room temperature and 1 Hz (using Radiant Technologies RT66A, Albuquerque, New Mexico) and strain measurements were conducted at 0.1 Hz with the

help of an interferometric sensor (MTI Instruments 2100 Fotonic Sensor, Albany, New York). Electromechanical fatigue tests were performed on unpoled samples by applying a bipolar triangular waveform with a peak field of 50 kV/cm at 10 Hz.

Results and Discussions

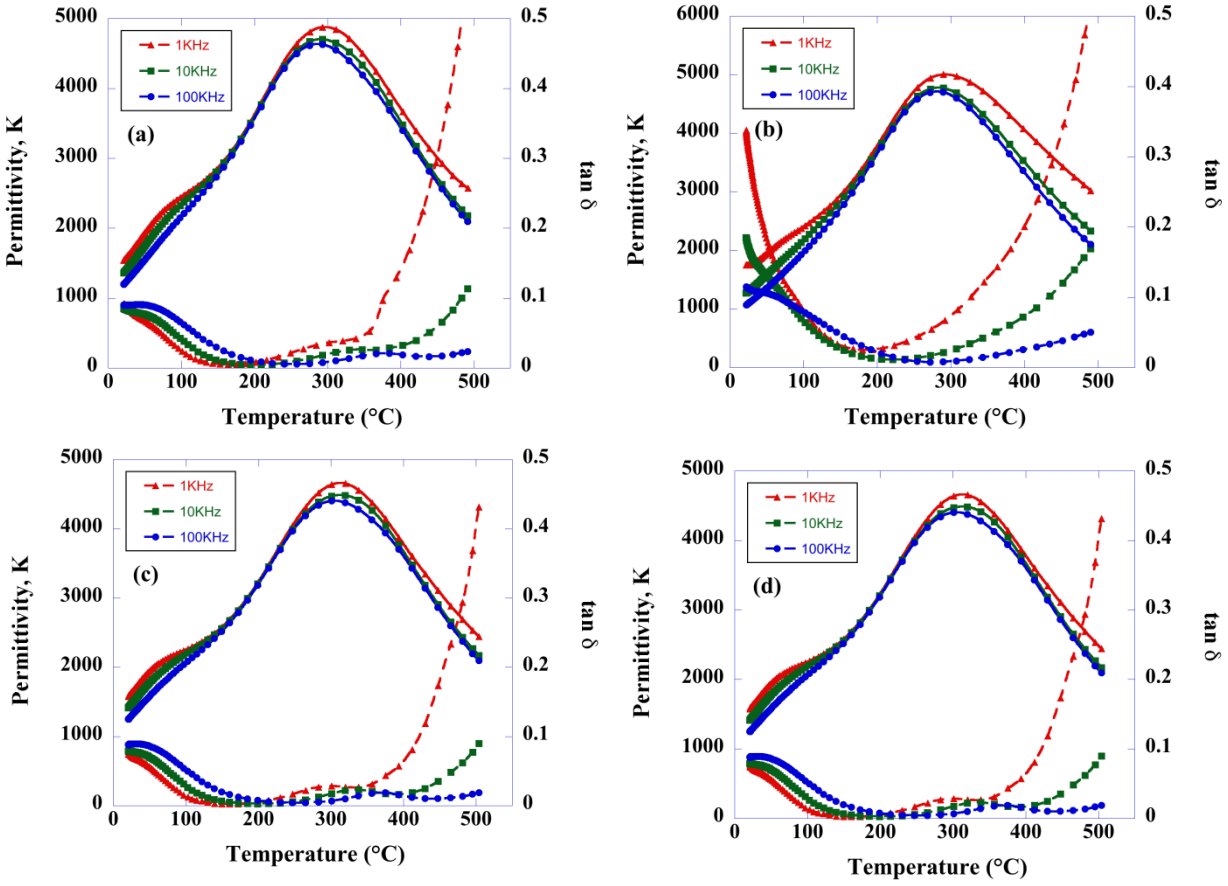

FIG. 10.2.1. Temperature dependence of dielectric constant (solid lines) and dielectric loss (dashed lines) for (a) A_A, (b) A_B, (c) D_A and (d) D_B compositions.

The dielectric permittivity and loss for the unpoled compositions are shown in Fig. 10.2.1. Typical of BNT-based systems, two temperature dependent transitions were clearly observed and the temperature at which the relative permittivity was maximum

(T_{max}) was close to 300°C. The dielectric maximum (T_{max}) has been previously shown to be correlated with the gradual disappearance of tetragonal distortions.[20] The low temperature shoulder (T'_{max}), which is related to the ergodic to non-ergodic transition, was observed at approximately 90°C. It has been reported by Levin *et al.* that T'_{max} in pure BNT marks the onset of a non-ferroelectric phase with an antiphase tilting scheme which persists nearly up to T_{max}.[21] The temperature T'_{max} also marks the threshold between two kinds dielectric relaxation processes, a linear decrease in permittivity with logarithm of frequency below T'_{max} and a complicated dependence above it.[12] It has also been reported that T'_{max} is simply a consequence of the correlation length distribution of polar nanoregions and no evidence of any structural transition has been observed.[14, 22] The peak in dielectric loss, in general, is observed at temperatures approximately 30-40 °C below T'_{max} and has been termed as the depolarization temperature by various authors.[12] It has been suggested that this temperature corresponds to the loss of long range ferroelectric order and might be a better indicator of onset of ergodicity. These arguments also suggest the possibility of the coexistence of ergodic and non-ergodic behavior over certain temperature ranges near the depolarization temperature and T'_{max}. This has been supported by the simultaneous observation of pinched polarization loops and negative strain in a number of compositions.[6, 9]

Rayleigh's analysis was performed on all the compositions to quantify the intrinsic and extrinsic contributions to dielectric properties. The Rayleigh's coefficients were calculated from the slope and intercept of the relative dielectric permittivity as a function of field (Fig. 10.2.2). Table 10.2.1 lists the Rayleigh's parameters obtained for

all the compositions. The data for the undoped composition has been included for reference. The ratio, $\alpha'/\varepsilon'_{r,init}$, which is indicative of amount of extrinsic contribution, has been reported to range between 0.07 $(kV/cm)^{-1}$ for hard PZT to 0.62 $(kV/cm)^{-1}$ for soft PZT.[19, 23-25] Although there were no significant changes in the dielectric data with temperature on doping (Fig. 10.2.1), Rayleigh's analysis showed clear differences. It could be seen that while acceptor doping enhanced the extrinsic contribution to the dielectric permittivity, donor doping suppressed it irrespective of the lattice site of doping. This might be indicative of the onset of non-ergodic behavior on acceptor doping as enhanced extrinsic contribution is indicative of increased domain stability. In the same way, comparatively smaller domain wall contributions to the total permittivity in donor-doped samples might be due to the fact that domain walls are relatively unstable in these compositions.

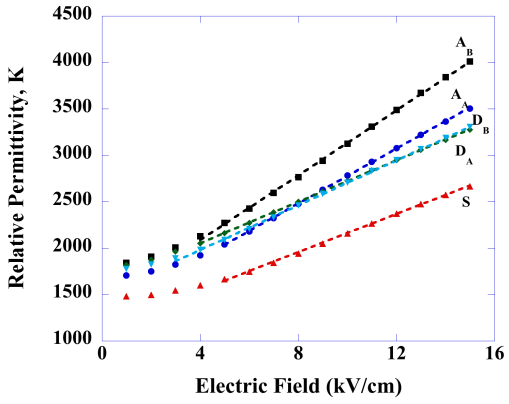

FIG. 10.2.2. The non-linear field dependent variation in dielectric response. The data for stoichiometric sample (S) has been included for reference.

Table 10.2.1: The reversible and irreversible Rayleigh parameters and ratio of irreversible to reversible contributions to dielectric nonlinearity for all compositions at room temperature.

	$\varepsilon'_{r,init}$	α' $(kV/cm)^{-1}$	$\alpha'/\varepsilon'_{r,init}$ $(kV/cm)^{-1}$
Stoichiometric	1130	103	0.09
Acceptor, A site	1300	148	0.11
Acceptor, B site	1390	170	0.12
Donor, A site	1600	110	0.07
Donor, B site	1500	120	0.08

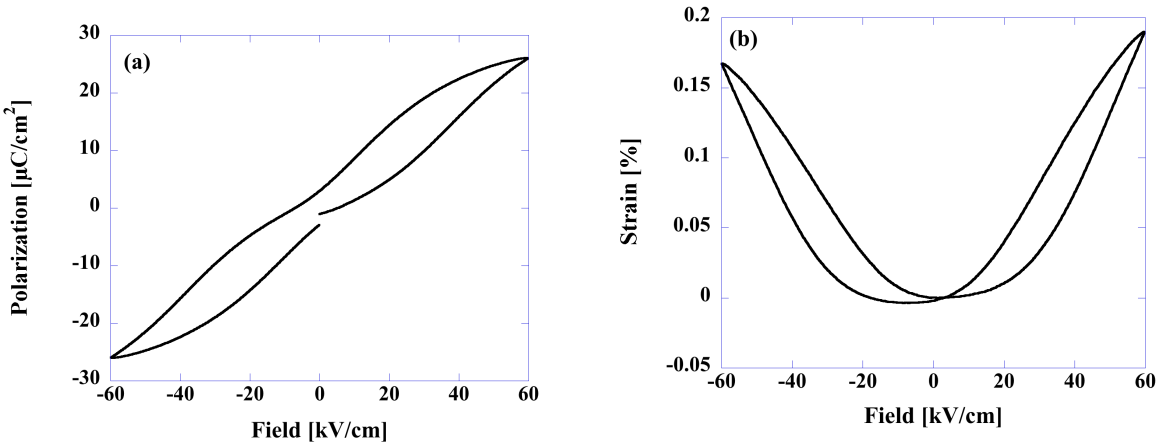

FIG. 10.2.3. Polarization and strain hysteresis loops for stoichiometric 5BMT-40BKT-55BNT measured at 1 Hz and 0.1 Hz respectively at room temperature.

Polarization and strain hysteresis loops for stoichiometric composition have been shown in Fig. 10.2.3 and the data for doped compositions are shown in Figs. 10.2.4 and 10.2.5. It can be seen (Figs. 10.2.4 and 10.2.5), the polarization loops become pinched and the negative strain disappears with donor doping while the converse is seen with acceptor doping. This indicates that these donor-doped compositions are mostly ergodic at room temperature, while the acceptor doped compositions are mostly non-ergodic.

These results are consistent with the Rayleigh analysis that suggested an increased extrinsic contribution in the acceptor-doped compositions. It is important to note that the Rayleigh analysis is conducted at relatively low fields (maximum electric field = 15 kV/cm) and thus the electric-field induced phase transformation is fully not realized.[26-28] Interestingly, no measureable shift in T'_{max} was observed for any of the compositions. Furthermore, the magnitude of the maximum permittivity and T_{max} were largely unaltered by the doping. The magnitude of the dielectric loss (tand), however, seems to have increased slightly compared to the stoichiometric composition. This was expected since the compensating defects created due to doping should lead to increased conduction losses.[9]

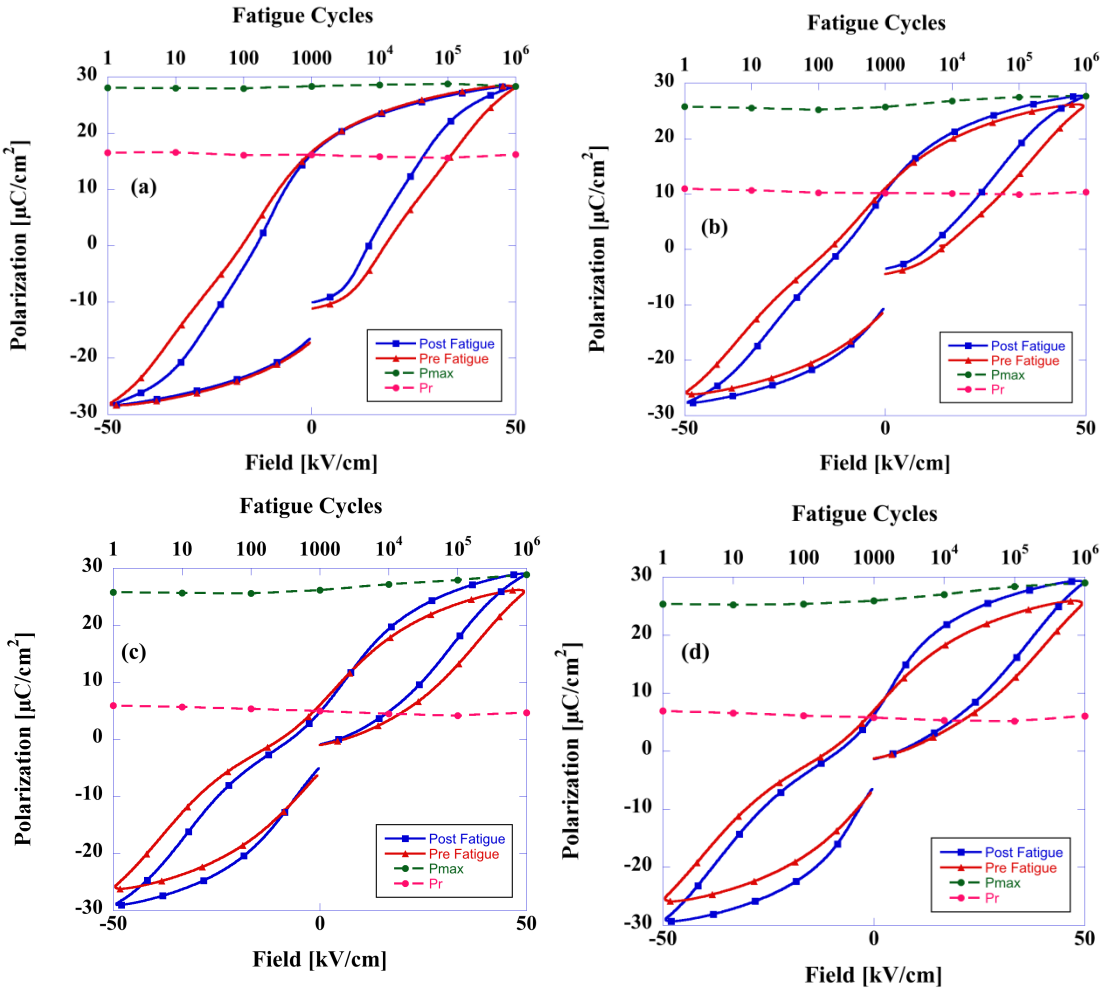

FIG. 10.2.4. Effect of fatigue on polarization hysteresis (at 10 Hz) for (a) A_A, (b) A_B, (c) D_A and (d) D_B compositions tested at 50 kV/cm and 10 Hz up to a million cycles. The plots also show the P_{max} and P_r with number of cycles (top x-axis).

The polarization hysteresis loops for all compositions before and after fatigue are shown in Fig. 10.2.4. The samples were subjected to a bipolar triangular waveform with a peak field of 50 kV/cm at 10 Hz for one million cycles. The variation in remnant polarization (P_r) and maximum polarization (P_{max}) at increasing cycles is also shown. Looking at the polarization data before the fatigue test for all four compositions, it is clear that acceptor doping resulted in an increased remnant polarization with ferroelectric-like hysteresis loops. In contrast, donor doping appeared to cause the loops to become constricted when compared to the stoichiometric composition, as expected.[9] Based on prior investigations on doped PZT and doping studies on other BNT-systems, acceptor doping is known to stabilize the ferroelectric domains (hardening) and donor doping to destabilize them (softening).[8, 25, 29, 30] Among many competing theories to explain the domain-stabilizing behavior by acceptor doping, the formation of defect associates between acceptor dopants and oxygen vacancies is more widely accepted.[31, 32] These defects presumably pin the domain walls and thus stabilize the domain-structure. Donor-doping has the opposite effect.

There was no degradation in maximum polarization after one million cycles for all four compositions, and the final maximum polarization was slightly greater than the initial value. In general, the remnant polarization decreased with an increasing number of cycles, which suggests an increase in the ergodicity under the cyclic application of the bipolar field. The coercive field (E_c) also decreased for all compositions after the fatigue

test, which meant that it became easier for the external electric field to align the domains as the number of cycles increased for these compositions. The data has been summarized in Table 10.2.2 below.

Table 10.2.2. Remnant and maximum polarizations, and coercive field before and after fatigue.

	P_r before fatigue ($\mu C/cm^2$)	**P_r after fatigue ($\mu C/cm^2$)**	**P_{max} before fatigue ($\mu C/cm^2$)**	**P_{max} after fatigue ($\mu C/cm^2$)**	**E_c before fatigue (kV/cm)**	**E_c after fatigue (kV/cm)**
Acceptor, A site	17	16	28	28	18	14
Acceptor, B site	11	10	26	28	14	10
Donor, A site	6.0	4.7	26	29	5.9	4.5
Donor, B site	6.9	6.1	25	29	6.8	6.1

Figure 10.2.5 shows the electromechanical strain data before and after fatigue. It is important to note that the stoichiometric composition showed typical ergodic behavior with no negative strain (Fig. 10.2.3).[9] In the doped compositions, consistent with the findings from the polarization data there were no significant negative strains observed for the donor-doped compositions indicating the absence of domains when the electric field was removed. A high field piezoelectric coefficient (d_{33}*) of 419 pm/V was observed for D_A composition before fatigue. The strain data for the acceptor-doped compositions exhibited a typical butterfly shape, characteristic of non-ergodic relaxors. It can be noted that the "total" strain (peak to peak strain) prior to fatigue was largely unchanged for all the four compositions, however the amount of "usable" strain (positive strain) was less in the acceptor-doped compositions due to the presence of negative or remnant strain.

The donor-doped compositions did not experience any fatigue in the strain data. For the acceptor-doped compositions, the A_B composition did not show any decay in maximum strain, while the A_A compositions exhibited a minimal loss in maximum strain (~9%) on the positive side of the electric field after one million cycles. This was in contrast to the behavior shown by PZT or non-ergodic BNT-based compositions which show appreciable degradation in maximum strain due to fatigue.[9-11, 15]

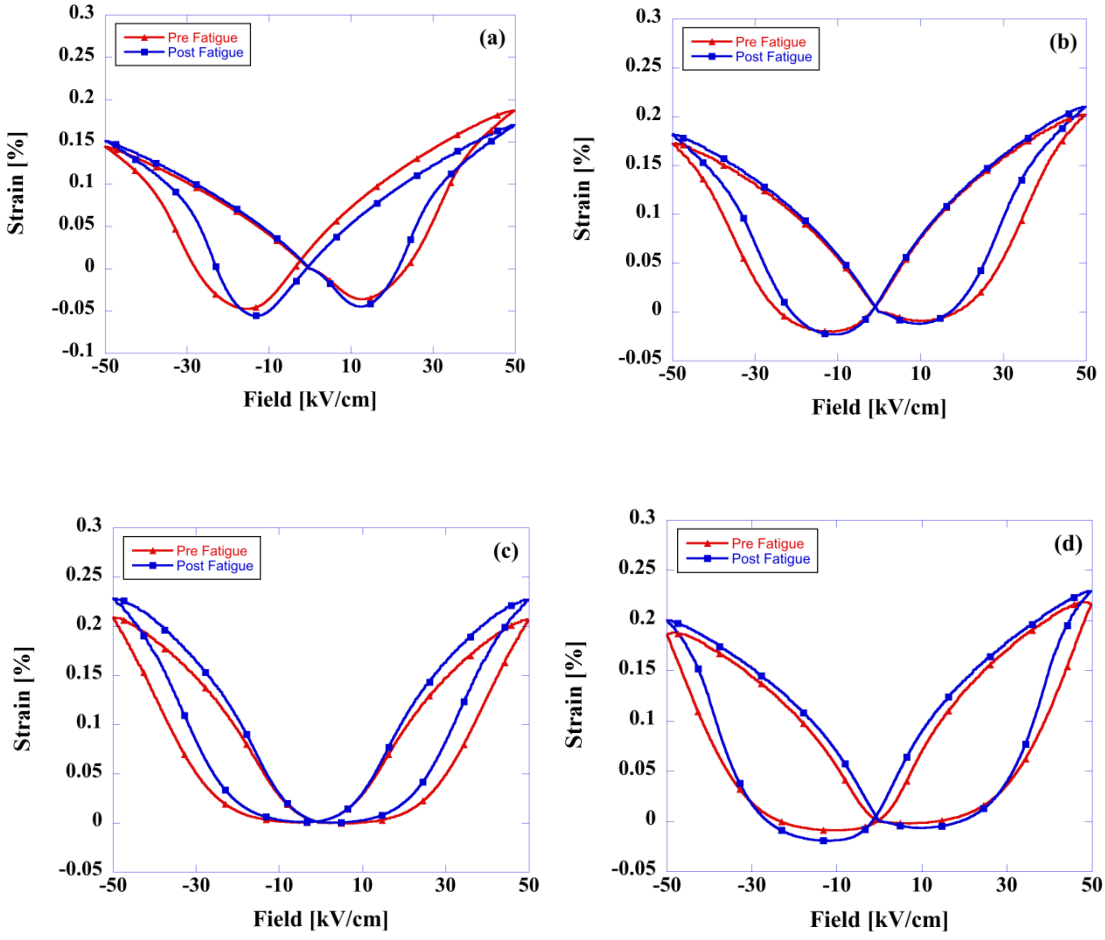

FIG. 10.2.5. Effect of fatigue on electromechanical strain (at 0.1 Hz) for (a) A_A, (b) A_B, (c) D_A and (d) D_B compositions tested at 50 kV/cm and 10 Hz up to a million cycles.

The acceptor- and donor-doping scheme aimed to control the dominant point defect in the material. Acceptor doping, in general, often results in a reduction in domain wall mobility which is described as hardening. In this study, acceptor doping was accomplished by manipulating the cation stoichiometry so as to replace Bi^{3+} with Na^{+} and Ti^{4+} with Mg^{2+} on the A and B sites, respectively. This approach leads to the formation of (Na_{Bi}'') and (Mg_{Ti}'') defects which must be compensated by positively charged defects to maintain charge neutrality. It is also known that cation vacancies are often present in ceramics containing volatile alkali cations, even in the intended stoichiometric compositions, as has been shown directly or indirectly by previous studies.[33, 34] Considering only non-interacting point defects, the charge balance equation can be written as:

$$A_A: \quad 2[Na_{Bi}''] + 3[V_{Bi}'''] + [V_{Na}'] + [V_K'] + e' \approx 2[V_O^{\cdot\cdot}] + h^{\cdot} \qquad \text{Eq. 10.2.2a}$$

$$A_B: \quad 2[Mg_{Ti}''] + 3[V_{Bi}'''] + [V_{Na}'] + [V_K'] + e' \approx 2[V_O^{\cdot\cdot}] + h^{\cdot} \qquad \text{Eq. 10.2.2b}$$

Very often, the negatively charged acceptor defects and positively charged oxygen vacancies form defect dipoles or even trimers resulting in partial charge compensation and have often been observed in doped PZT, (K,Na)NbO_3, and BNT-based systems.[35-38] In this case, the formation of $(Na_{Bi}'' - V_O^{\cdot\cdot})^x$ or $(Mg_{Ti}'' - V_O^{\cdot\cdot})^x$ is a possibility. They are thought to be responsible for reduced mobility of 180° domain walls or stabilized domain structure and may result in lower piezoelectric coefficients.[35-38] Domain wall pinning by doubly-ionized positively-charged defect sites like oxygen vacancies ($V_O^{\cdot\cdot}$) and defect dipoles involving oxygen vacancies are believed to play an important role in fatigue as well, especially in Pb-based ferroelectric perovskites.[16, 35]

Oxygen vacancy ordering into two-dimensional planar arrays have been shown to be capable of pinning domain walls.[39] Under high electric fields, point defects, especially highly mobile oxygen vacancies and defect complexes can migrate even at room temperature. Therefore, acceptor doping adversely affects material properties during electrical switching in ferroelectrics. Drawing on the extensive study of Pb-containing perovskites, it has been argued that presence of oxygen vacancies might be responsible for observed fatigue in BNT-based systems as well, especially in non-ergodic materials at room temperature with stable domains.[4, 10]

Donor-doping was accomplished in these materials by replacing Na^{+} with Bi^{3+} and Mg^{2+} with Ti^{4+} in this study. This should lead to the formation of ($Bi_{Na}^{\cdot\cdot}$) and ($Ti_{Mg}^{\cdot\cdot}$) defect centers which must be compensated with negatively charged defects such as cation vacancies. A possible charge neutrality equation can be:

$$D_A: \quad 2[Bi_{Na}^{\cdot\cdot}] + 2[V_O^{\cdot\cdot}] + h^{\cdot} \approx 3[V_{Bi}^{\prime\prime\prime}] + [V_{Na}^{\prime}] + [V_K^{\prime}] + e^{\prime} \qquad \text{Eq. 10.2.3a}$$

$$D_B: \quad 2[Ti_{Mg}^{\cdot\cdot}] + 2[V_O^{\cdot\cdot}] + h^{\cdot} \approx 3[V_{Bi}^{\prime\prime\prime}] + [V_{Na}^{\prime}] + [V_K^{\prime}] + e^{\prime} \qquad \text{Eq. 10.2.3b}$$

Donor doping destabilizes the domain structure, making switching of domain walls easier.[8, 40] In BNT-based systems, it is of special interest. As has been shown in this study as well, they can increase the amount of "usable" strain making them more suitable for actuator applications. In PZT and other normal ferroelectric like $BaTiO_3$, they have been shown to improve the fatigue characteristics which can be attributed to a reduction in the oxygen-vacancy concentration, a reduction in coercive field, and other factors.[41, 42] In BNT-based relaxors, donor-doping is expected to not only reduce oxygen vacancies but also impart greater ergodicity, both of which can have an impact on fatigue behavior.

Table 10.2.3. The DC resistivity values calculated by extrapolating AC impedance data.

	ρ (Ω-cm) before fatigue at 450 °C	**ρ (Ω-cm) before fatigue at 550 °C**
Stoichiometric[10]	1.6×10^7	9.9×10^5
Acceptor, A site	1.8×10^7	1.5×10^6
Acceptor, B site	7.8×10^6	1.1×10^6
Donor, A site	1.3×10^7	1.6×10^6
Donor, B site	4.6×10^7	2.8×10^6

Impedance spectroscopy measurements were carried out on all the compositions. The resistivities, as shown in Table 10.2.3, were still high (~10^7 Ω-cm) in comparison to the stoichiometric composition (and significantly higher than is typical for PZT with a published value of resistivity ~10^4-10^5 ohm-cm at ~450 °C[43]), showing that the overall resistivity was insensitive to stoichiometry. The Arrhenius plots were highly non-linear between 400 °C and 550 °C; the activation energies for conduction (E_a) were estimated to range between 1.2 eV to 1.6 eV. The optical band gap for the stoichiometric composition are approximately 3 eV.[9] These suggest that the point defects introduced by doping do not affect the resistivities appreciably and instead they are controlled by some other defect species (perhaps cation vacancies introduced during processing), the origin of which needs to be investigated further.

Upon integrating the results from the fatigue and impedance measurements, some noticeable inferences can be noted. Defects created as a consequence of donor doping did not result in any noticeable fatigue. This is likely due to the nature of the reversible field-

induced phase transformation. It has been suggested that a new domain structure is created during each electrical cycle, as a result defects cannot pin the domain walls effectively.[10] However, the acceptor-doped compositions showed evidence of stable domains at room temperature in the absence of an electric field, as indicated by the presence of an increased remnant polarization and strain. In spite of this fact, the acceptor-doped compositions exhibited a negligible effect on the maximum strain after fatigue. This behavior is certainly different from some other perovskite ferroelectrics where acceptor doping exaggerates the fatigue possibly due to enhanced domain wall pinning.[41, 44] This suggests that either defects do not play a prominent role in fatigue in these systems or it is compensated by other factors, which need to be investigated.

Drawing upon the past findings related to PZT, some of the other phenomena related to fatigue in PZT were investigated in this system as well. Extreme discoloration just beneath the electrodes was observed in all the samples, similar to the observations made by Balke *et al.* in PZT which they proposed to be the primary reason for fatigue.[15] Microcracks have been shown to have formed during fatigue in BNT-based compositions in other studies.[4, 17] Crack formation is a possibility in our ternary systems as well, however it was not investigated. While these mechanisms have been shown to lead to fatigue in PZT and arguably some other normal ferroelectrics, they do not seem to contribute to fatigue in the BNT-based ternaries discussed here.

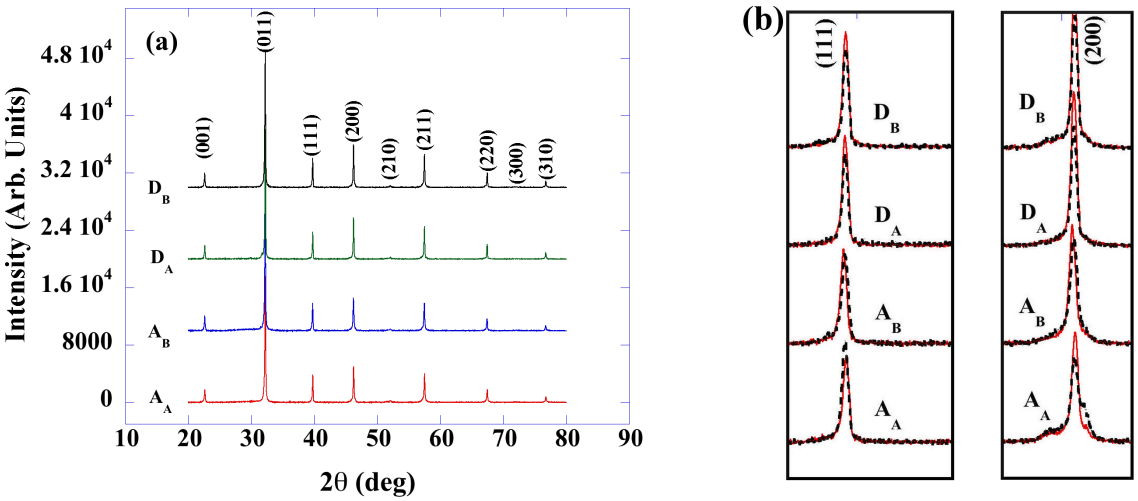

FIG. 10.2.6: (a) XRD data for the indicated compositions, (b) Slow-scan {111} and {200} peaks for all compositions before (red solid lines) and after fatigue (black dashed lines).

All the four compositions in this study exhibited a single perovskite phase within the limits of the x-ray diffraction instrument used (Fig. 10.2.6a). No peak splitting was seen and all the virgin compositions exhibited pseudo-cubic symmetry before fatigue, which is expected of relaxor materials. However, short-range non-cubic distortions might be present as is observed in other BNT-based piezoceramics.[4] Figure 10.2.6b shows slow-scan data on the {111} and {200} reflections for all the compositions before and after fatigue, it was not possible to fully resolve the peaks using a laboratory scale diffractometer. There was no evidence of peak splitting or asymmetry in the {111} peaks before or after fatigue for all compositions. However, a slight shoulder was observed in the {200} peaks before fatigue which is indicative of a tetragonal distortion. This finding is not unexpected as the BKT-to-BNT ratio in these ternary compositions are clearly in the tetragonal phase field based on the BKT-BNT binary phase diagram.[45] These

distortions are present before and after the fatigue test and there are no clear signs of an increase in tetragonality after fatigue. The lack of induced tetragonality might have implications on the fatigue properties for these systems as compared to some other BNT-based systems.[9] This behavior was different from some other BNT-based compositions where a clear symmetry change was observed on application of electrical cycles.[4-6] In BNT-$BaTiO_3$ (BNT-BT), it has been shown that the symmetry gradually changes from rhombohedral where both 180° and non-180° domain walls can switch, to tetragonal symmetry where 90° domains are constrained due to presence of grain boundaries and only 180° domain walls can switch.[4, 46] In experiments on CuO-doped BNT-BT, there was no evidence of induced tetragonal symmetry and the tetragonal symmetry of the virgin sample remained intact after electrical cycling. This composition was shown to be fatigue-free as compared to undoped BNT-BT.[4] Pronounced tetragonal distortions were observed in $LaFeO_3$ doped BNT on application of cyclic electric fields, however no detailed fatigue studies were reported.[6]

Despite the presence of factors which are known to cause fatigue in PZT and possibly other BNT-based systems e.g. defects, stable domains etc., these compositions exhibit little degradation in maximum polarization and minimal to no decay in maximum strain after one million bipolar cycles. However, the fatigue-free behavior was probably supported by some unusual observations in these compositions. These were: (i) the remnant polarization decreased after one million cycles, indicating an increase in the ergodic phase which is less prone to fatigue for these compositions, (ii) the coercive field decreased by ~20% for most compositions meaning that lower fields were needed to

align the domains, and (iii) among the fatigue-free compositions, there was no induced tetragonality which could degrade the material properties.

Conclusions

Acceptor and donor doping on A and B-sites were performed on ceramics of the composition 5BMT-40BKT-55BNT in order to investigate the role of point defects on fatigue behavior. All samples exhibited pseudo-cubic symmetry within the limits of laboratory x-ray diffractometer. Acceptor-doped compositions exhibited polarization and strain data which is characteristic of non-ergodic relaxor materials, while donor-doped compositions retained the ergodic behavior observed in the stoichiometric composition. Irrespective of polarity and lattice site of the dopant, all compositions maintained the high resistivities of the stoichiometric composition. This suggests the possibility that although domain stabilization is related to oxygen vacancies, the overall resistivity is controlled by some other defect species. Doping of either polarity did not show any effect during fatigue tests on the maximum polarization. Apart from a minor decrease observed in the maximum strain for the A-site acceptor-doped composition, none of the other samples showed any effects from fatigue on the maximum strain, despite the presence of domains and defects in non-ergodic compositions. These results suggest that the increase in ergodicity, the reduction in coercive field, and the lack of induced tetragonality during the fatigue cycles might be responsible for the excellent fatigue characteristics in these materials.

Acknowledgements

This material is based upon work supported by the National Science Foundation under Grant No. (DMR-1308032). The authors would also like to gratefully acknowledge the support from Hewlett-Packard Company.

References

[1] Foster WJ, Meen JK, Fox DA. The effect of physiologic aqueous solutions on the perovskite material lead-lanthanum-zirconium titanate (PLZT): potential retinotoxicity. Cutaneous and ocular toxicology 2013;32:18-22.
[2] Aksel E, Erdem E, Jakes P, Jones JL, Eichel R-A. Defect structure and mate-rial s "hardening" in Fe 2 O 3-doped (Bi 0.5 Na 0.5) T iO 3 ferroelectrics. Appl Phys Lett 2010;97:012903.
[3] Aksel E, Jakes P, Erdem E, Smyth DM, Ozarowski A, van Tol J, et al. Processing of Manganese‐Doped [Bi0. 5Na0. 5] TiO3 Ferroelectrics: Reduction and Oxidation Reactions During Calcination and Sintering. Journal of the American Ceramic Society 2011;94:1363-7.
[4] Ehmke M, Glaum J, Jo W, Granzow T, Rödel J. Stabilization of the Fatigue‐Resistant Phase by CuO Addition in (Bi1/2Na1/2) TiO3–BaTiO3. Journal of the American Ceramic Society 2011;94:2473-8.
[5] Glaum J, Simons H, Acosta M, Hoffman M. Tailoring the piezoelectric and relaxor properties of (Bi1/2Na1/2) TiO3–BaTiO3 via zirconium doping. Journal of the American Ceramic Society 2013;96:2881-6.
[6] Han H-S, Jo W, Rödel J, Hong I-K, Tai W-P, Lee J-S. Coexistence of ergodicity and nonergodicity in LaFeO3-modified Bi1/2 (Na0. 78K0. 22) 1/2TiO3 relaxors. Journal of Physics: Condensed Matter 2012;24:365901.
[7] Jo W, Dittmer R, Acosta M, Zang J, Groh C, Sapper E, et al. Giant electric-field-induced strains in lead-free ceramics for actuator applications–status and perspective. Journal of electroceramics 2012;29:71-93.
[8] Jo W, Erdem E, Eichel R-A, Glaum J, Granzow T, Damjanovic D, et al. Effect of Nb-donor and Fe-acceptor dopants in (Bi1/2Na1/2) TiO3–BaTiO3–(K0. 5Na0. 5) NbO3 lead-free piezoceramics. Journal of Applied Physics 2010;108:014110.
[9] Kumar N, Cann DP. Electromechanical strain and bipolar fatigue in Bi (Mg1/2Ti1/2) O3-(Bi1/2K1/2) TiO3-(Bi1/2Na1/2) TiO3 ceramics. Journal of Applied Physics 2013;114:054102.
[10] Luo Z, Granzow T, Glaum J, Jo W, Rödel J, Hoffman M. Effect of Ferroelectric Long‐Range Order on the Unipolar and Bipolar Electric Fatigue in Bi1/2Na1/2TiO3‐Based Lead‐Free Piezoceramics. Journal of the American Ceramic Society 2011;94:3927-33.
[11] Patterson EA, Cann DP. Bipolar piezoelectric fatigue of Bi (Zn0. 5Ti0. 5) O3-(Bi0. 5K0. 5) TiO3-(Bi0. 5Na0. 5) TiO3 Pb-free ceramics. Applied Physics Letters 2012;101:042905.
[12] Viola G, Ning H, Wei X, Deluca M, Adomkevicius A, Khaliq J, et al. Dielectric relaxation, lattice dynamics and polarization mechanisms in Bi0. 5Na0. 5TiO3-based lead-free ceramics. Journal of Applied Physics 2013;114:014107.
[13] Zhang S-T, Kounga AB, Aulbach E, Granzow T, Jo W, Kleebe H-J, et al. Lead-free piezoceramics with giant strain in the system Bi0. 5Na0. 5TiO3–BaTiO3–K0. 5Na0. 5NbO3. I. Structure and room temperature properties. Journal of Applied Physics 2008;103:034107.

[14] Jo W, Schaab S, Sapper E, Schmitt LA, Kleebe H-J, Bell AJ, et al. On the phase identity and its thermal evolution of lead free (Bi1/2Na1/2) TiO3-6 mol% BaTiO3. Journal of Applied Physics 2011;110:074106.
[15] Balke N, Kungl H, Granzow T, Lupascu DC, Hoffmann MJ, Rödel J. Bipolar fatigue caused by field screening in Pb (Zr, Ti) O3 ceramics. Journal of the American Ceramic Society 2007;90:3869-74.
[16] Lupascu DC. Fatigue in ferroelectric ceramics and related issues: Springer Science & Business Media; 2013.
[17] Luo Z, Glaum J, Granzow T, Jo W, Dittmer R, Hoffman M, et al. Bipolar and Unipolar Fatigue of Ferroelectric BNT‐Based Lead‐Free Piezoceramics. Journal of the American Ceramic Society 2011;94:529-35.
[18] Damjanovic D, Demartin M. Contribution of the irreversible displacement of domain walls to the piezoelectric effect in barium titanate and lead zirconate titanate ceramics. Journal of Physics: Condensed Matter 1997;9:4943.
[19] Eitel R, Shrout T, Randall C. Nonlinear contributions to the dielectric permittivity and converse piezoelectric coefficient in piezoelectric ceramics. Journal of applied physics 2006;99:124110.
[20] Patterson EA, Cann DP, Pokorny J, Reaney IM. Electromechanical strain in Bi (Zn1/2Ti1/2) O3–(Bi1/2Na1/2) TiO3–(Bi1/2K1/2) TiO3 solid solutions. Journal of Applied Physics 2012;111:094105.
[21] Levin I, Reaney I, Anton E, Jo W, Rödel J, Pokorny J, et al. Local structure, pseudosymmetry, and phase transitions in Na 1/2 Bi 1/2 TiO 3–K 1/2 Bi 1/2 TiO 3 ceramics. Physical Review B 2013;87:024113.
[22] Wanga H, Xu H, Luo H, Yin Z, Bokov A, Ye Z. Dielectric anomalies of the relaxor-based 0.9 Pb „Mg1/3Nb2/3… O3-0.1 PbTiO3 single crystals. system 2005;4:7.
[23] Krueger HH. Stress sensitivity of piezoelectric ceramics: Part 1. Sensitivity to compressive stress parallel to the polar axis. The Journal of the Acoustical Society of America 1967;42:636-45.
[24] Li S, Cao W, Cross L. The extrinsic nature of nonlinear behavior observed in lead zirconate titanate ferroelectric ceramic. Journal of applied physics 1991;69:7219-24.
[25] Morozov M, Damjanovic D, Setter N. The nonlinearity and subswitching hysteresis in hard and soft PZT. Journal of the European Ceramic Society 2005;25:2483-6.
[26] Jo W, Daniels JE, Jones JL, Tan X, Thomas PA, Damjanovic D, et al. Evolving morphotropic phase boundary in lead-free (Bi1/2Na1/2) TiO3–BaTiO3 piezoceramics. Journal of applied physics 2011;109:014110.
[27] Kling J, Tan X, Jo W, Kleebe HJ, Fuess H, Roedel J. In Situ Transmission Electron Microscopy of Electric Field‐Triggered Reversible Domain Formation in Bi‐Based Lead‐Free Piezoceramics. Journal of the American Ceramic Society 2010;93:2452-5.
[28] Patterson EA, Cann DP. Relaxor to Ferroelectric Transitions in (Bi1/2Na1/2) TiO3–Bi (Zn1/2Ti1/2) O3Solid Solutions. Journal of the American Ceramic Society 2012;95:3509-13.
[29] Jaffe B, Cook WR, Jaffe HL. Piezoelectric ceramics: Academic Press; 1971.
[30] Morozov MI, Damjanovic D. Hardening-softening transition in Fe-doped Pb (Zr, Ti) O3 ceramics and evolution of the third harmonic of the polarization response. arXiv preprint arXiv:08064055 2008.

[31] Eichel RA, Meštrić H, Dinse KP, Ozarowski A, van Tol J, Brunel LC, et al. High‐field/high‐frequency EPR of paramagnetic functional centers in Cu2+‐and Fe3+‐modified polycrystalline Pb [ZrxTi1− x] O3 ferroelectrics. Magnetic Resonance in Chemistry 2005;43:S166-S73.
[32] Warren WL, Tuttle BA, Rong EC, Gerardi GJ, Poindexter EH. Electron paramagnetic resonance investigation of acceptor centers in Pb (Zr, Ti) O3 ceramics. Journal of the American Ceramic Society 1997;80:680-4.
[33] Shen Z-Y, Wang K, Li J-F. Combined effects of Li content and sintering temperature on polymorphic phase boundary and electrical properties of Li/Ta co-doped (Na, K) NbO3 lead-free piezoceramics. Applied Physics A 2009;97:911-7.
[34] Zhao P, Zhang B-P, Li J-F. High piezoelectric d33 coefficient in Li-modified lead-free (Na, K) NbO3 ceramics sintered at optimal temperature. Applied physics letters 2007;90:2909.
[35] Eichel R-A. Defect structure of oxide ferroelectrics—valence state, site of incorporation, mechanisms of charge compensation and internal bias fields. Journal of Electroceramics 2007;19:11-23.
[36] Eichel R-A. Structural and dynamic properties of oxygen vacancies in perovskite oxides—analysis of defect chemistry by modern multi-frequency and pulsed EPR techniques. Physical Chemistry Chemical Physics 2011;13:368-84.
[37] Eichel R-A, Erünal E, Jakes P, Körbel S, Elsässer C, Kungl H, et al. Interactions of defect complexes and domain walls in CuO-doped ferroelectric (K, Na) NbO3. Applied Physics Letters 2013;102:242908.
[38] Eichel RA. Characterization of Defect Structure in Acceptor‐Modified Piezoelectric Ceramics by Multifrequency and Multipulse Electron Paramagnetic Resonance Spectroscopy. Journal of the American Ceramic Society 2008;91:691-701.
[39] Scott J, Dawber M. Oxygen-vacancy ordering as a fatigue mechanism in perovskite ferroelectrics. Applied Physics Letters 2000;76:3801-3.
[40] Jaffe B, Cook WR, Jaffe H. Piezoelectric ceramics: Academic Press London and New York; 1971.
[41] Chen J, Harmer MP, Smyth DM. Compositional control of ferroelectric fatigue in perovskite ferroelectric ceramics and thin films. Journal of applied physics 1994;76:5394-8.
[42] Smyth DM. Defect structure in perovskite titanates. Current Opinion in Solid State and Materials Science 1996;1:692-7.
[43] Dih J, Fulrath R. Electrical Conductivity in Lead Zirconate‐Titanate Ceramics. Journal of the American Ceramic Society 1978;61:448-51.
[44] Zhang Z, Wu P, Lu L, Shu C. Defect and electronic structures of acceptor substituted lead titanate. Applied Physics Letters 2008;92:112909.
[45] Zhang Y-R, Li J-F, Zhang B-P, Peng C-E. Piezoelectric and ferroelectric properties of Bi-compensated (Bi1/2Na1/2) TiO3–(Bi1/2K1/2) TiO3 lead-free piezoelectric ceramics. Journal of Applied Physics 2008;103:074109.
[46] Li J, Rogan R, Üstündag E, Bhattacharya K. Domain switching in polycrystalline ferroelectric ceramics. Nature materials 2005;4:776-81.

Chapter 11. Conclusions

The aim of this research is to develop a fundamental understanding of the dominant defect species and the relevant defect equilibrium conditions for bismuth-containing perovskites to help guide the development of these materials for emerging applications. While compositions based on Bi-perovskites (*e.g.* $(Bi,Ba)(B^{2+},Ti)O_3$) are promising for high performance capacitor applications, compounds such as $(Bi_{1/2}K_{1/2})TiO_3$ (BKT) and $(Bi_{1/2}Na_{1/2})TiO_3$ (BNT), and their solid solutions with $BaTiO_3$ and other end members exhibit useful piezoelectric properties and are considered to be promising candidates to replace Pb-based materials.

Chapter 9 focused on exploring defect chemistry and trans port properties in $BaTiO_3$-Bi$M$$O_3$ ceramics, with a special focus on relaxor $BaTiO_3$-$Bi(Zn_{1/2}Ti_{1/2})O_3$ (BT-BZT). The results obtained have been summarized below:

(1) The BT-BZT ceramics exhibit promising properties for use in high temperature and high temperature dielectric applications. In chapter 9.1 the feasibility of preparing them in the form of multilayer ceramic capacitors (MLCCs) has been demonstrated. The MLCCs had high capacitance values greater than 1 μF at room temperature and a temperature stable capacitance up to 350 °C. Energy density values greater than ~2.0 J/cm^3 were obtained at room temperature. The compatibility of Ag-Pd electrodes with BZT-BT-based MLCCs was also demonstrated, which is critical in reducing the cost. The electrical properties of the MLCC devices closely matched the properties of bulk ceramics which is indicative of the high quality of the MLCC devices.

(2) In chapter 9.2, with the help of dielectric measurements, AC-impedance measurements and DC measurements, it was demonstrated that there was a significant increase in resistivity with the addition BZT to BT and ST. The resistivity increased from ~10^5 Ω-cm for pure BT to ~10^7 Ω-cm for a solid solution containing only 3% BZT at 400 °C. The activation energy for conduction also increased gradually from ~1 eV for pure BT to ~1.5 eV (equivalent to ~$0.5E_g$) for the 7.5% BZT composition, signifying a change in conduction mechanism from one dominated by impurities or defects to an intrinsic mechanism. The effect persisted even after annealing for BT-BZT compositions. A similar improvement in insulation resistance was also demonstrated for ST-BZT system. This presents an important result as the increased resistivity can enable these materials to be used for demanding applications where high temperatures or high electric fields are needed.

(3) The >2 orders of magnitude improvement in resistivity was accompanied by a transition from a p-type to n-type behavior for BT-BZT ceramics. This transition was determined from the change in resistivity as a function of oxygen partial pressure, from annealing studies, as well as Seebeck measurements. This suggests an unintentional effective donor doping process occurred by adding BZT to BT which can have implications for improvements in the resistivity behavior when adding other Bi-containing perovskites to $BaTiO_3$ as well. It also demonstrated that these ceramics interact appreciably with the ambient atmosphere even at low temperatures. These data suggest that the highly insulating properties of BT-BZT ceramics were intricately linked to changes in the defect equilibrium.

(4) DC-bias dependent AC impedance spectroscopy provided another proof of p-type to n-type transition on adding BZT to BT. In summary, the results suggested fundamentally different underlying defect mechanisms in BT-BZT ceramics as compared to BT, and it was shown that small bias fields could induce a defect chemistry-related change in long-range bulk conduction in BT-BZT ceramics without affecting the polarization mechanisms significantly. It is also proposed that the observed non-linearity in V-I characteristics at low fields, which is often ascribed to extrinsic factors like Schottky barriers in case of BT-based systems, may also be a direct consequence of change in bulk transport properties. These results are also important for underlining the importance of using similar bias conditions and oscillating voltages while making comparisons of AC impedance data among different materials. The relatively stable voltage characteristics and higher resistivities of BZT-containing ceramics may have important implications in the use of capacitors for energy applications.

(5) With an aim to study presence of bismuth in 5+ states in BT-BZT ceramics, single-phase $BaBiO_3$ ceramics were fabricated and confirmed by high-resolution x-ray diffraction. The coexistence of bismuth in 3+ and 5+ valence states in $BaBiO_3$ was confirmed by x-ray photoelectron spectroscopy. Using AC impedance and optical spectroscopy, it was shown that polaron-hopping was the dominant conduction mechanism in $BaBiO_3$. Ceramics based on the solid solution of $BaTiO_3$-$BaBiO_3$ were fabricated to investigate the effect of adding small amounts of BB on the conduction mechanism of BT. It was observed that the BT-BB ceramics had significantly higher resistivity values as compared to undoped $BaTiO_3$ or $BaBiO_3$, suggesting a decrease in the concentration of mobile defect species. The resistivity values remained high even

with a coexisting secondary $BaBiO_3$ phase. Data from AC impedance spectroscopy on Bi-doped $BaTiO_3$ suggested that a shift in the site occupancy of Bi onto the A-sublattice is the dominant mechanism resulting in donor doping which results in the observed high resistivities.

(6) To demonstrate that the defect model for BT-BZT is followed by other similar materials, $BaTiO_3$-$BiScO_3$ and $SrTiO_3$-$Bi(Zn_{1/2}Ti_{1/2})O_3$ ceramics were fabricated. They also exhibited a transition away from p-type behavior on adding Bi-end member and a corresponding increase in resistivity, similar to BT-BZT ceramics. Additionally, the effect of minor nonstoichiometry in Bi-containing perovskites was also highlighted in these two material systems. Both these systems feature multiple cations with different valence states on the same sublattice. For both these systems, acceptor doping (V_{Bi}''' for BT-BS or Sr_{Bi}' for ST-BZT) led to a deterioration in the insulation properties. Donor doping ($Bi_{Ba,Sr}^{\cdot}$) and creating cation vacancies by removing low-valence cations ($V_{Ba,Sr}''$) had no unfavorable effect on the resistivity behavior. While this led to a significant improvement in the resistivity for BT-BS ceramics, the resistivity values were relatively unchanged for ST-BZT ceramics. These results demonstrate the significant impact of cation non-stoichiometry in Bi-containing perovskites and suggeste an important approach in tailoring the material properties in related materials. This study also highlights the difficulty in establishing a generic defect chemistry for all bismuth-containing perovskites.

(7) So far it has been shown that the addition of $Bi(Me)O_3$ to p-type BT is accompanied by significant improvement in insulation properties, often even leading to an n-type behavior in BT- $Bi(M)O_3$ ceramics. It is postulated that this is a result of unintentional

donor doping occurring on adding Bi-end member to BT or $SrTiO_3$. It was shown that donor doping could be originating primarily due to two factors—secondary phases which made the ceramics rich in high valence cations and higher oxygen vacancy concentration. Using the results obtained and experimentally determined thermodynamic parameters for BT, it was proposed that ionic compensation mechanism is prevalent in these ceramics instead of electronic compensation and donor doping had an effect of shifting the conductivity minima to higher pO_2 values in the Kröger-Vink diagram potentially explaining higher resistivity values and shift to n-type behavior. A well-understood defect chemistry of BT- Bi$M$$O_3$ ceramics is expected to help them be better suited for specialized and industrial capacitor applications.

The $Bi(Mg_{1/2}Ti_{1/2})O_3$-$(Bi_{1/2}Na_{1/2})TiO_3$-$(Bi_{1/2}K_{1/2})TiO_3$ (BMT-BKT-BNT) material system was investigated in chapter 10, as a candidate for replacement for lead zirconate titanate for sensors and actuator applications. This material features a field-induced relaxor-to-ferroelectric transition that is accompanied by a large piezoelectric strain values. The results have been summarized below:

(8) Ternary solid solutions of BMT-BKT-BNT were prepared with BMT concentrations up to 10 mol%. For all compositions, T_{max} remained above 320 °C and a typical ergodic to non-ergodic relaxor transition was also evident near 200°C. The polarization and strain loops for the 1-40-59 composition exhibited characteristics consistent with ferroelectric behavior. However, with the addition of BMT the dielectric behavior became more diffuse and the polarization hysteresis became increasingly pinched without

any measurable negative strain. All the compositions were evaluated under 50 kV/cm bipolar cycling and exhibited fatigue behavior significantly better than PZT. For all compositions, the maximum polarization was largely unaffected by fatigue cycling up to at least a million cycles. In addition, there was minimal effect of fatigue on the maximum electromechanical strain for compositions with 2.5% BMT to 10% BMT. Transport measurements in these compositions showed the presence of high resistivity values (e.g. 10 MΩ-cm at 440 °C) and activation energies equal to half of the measured optical band gap. It is proposed that the lower defect concentrations and the nature of the relaxor-ferroelectric transition in these compositions are responsible for the fatigue resistance.

(2) Acceptor and donor doping on A- and B-sites were performed on ceramics of the composition 5BMT-40BKT-55BNT in order to investigate the role of point defects on fatigue behavior. All samples exhibited pseudo-cubic symmetry within the limits of laboratory x-ray diffractometer. Acceptor-doped compositions exhibited polarization and strain data which is characteristic of non-ergodic relaxor materials, while donor-doped compositions retained the ergodic behavior observed in the stoichiometric composition. Irrespective of polarity and lattice site of the dopant, all compositions maintained the high resistivity values of the stoichiometric composition. This suggests the possibility that although domain stabilization is related to oxygen vacancies, the overall resistivity is controlled by some other defect species. Doping of either polarity did not show any effect during fatigue tests on the maximum polarization. Apart from a minor decrease observed in the maximum strain for the A-site acceptor-doped composition, none of the other samples showed any effects from fatigue on the maximum strain, despite the presence of

domains and defects in non-ergodic compositions. These results suggest that the increase in ergodicity, the reduction in coercive field, and the lack of induced tetragonality during the fatigue cycles might be responsible for the excellent fatigue characteristics in these materials.

12. Future work

There are several potential areas for both BT-BZT and BNT-based ceramics, where further research can be performed. Some of them have been mentioned below.

(1) Wider pO_2 range for defect chemistry

In this thesis, the defect chemistry has been mainly studied close to air (pO_2~0.2 atm), using three gases—nitrogen/vacuum, air and oxygen. For a full realization of defect chemistry, a greater range of oxygen partial pressure (pO_2) is required, *e.g.* Fig. 12.1. Furthermore, if possible, measurements should be performed on single crystals to estimate all the thermodynamic parameters from scratch, which will eliminate the need to extrapolate the research performed on $BaTiO_3$ ceramics. It will also minimize the artifacts originating from interfaces such as grain boundaries. Even though impedance spectroscopy, which is used extensively in this research, is a powerful tool and capable of separating bulk contributions to transport properties from interfacial contribution, single crystal measurements will validate that these conclusions drawn are correct. Similar approach is required to study defect chemistry in BNT-based binary or ternary ceramic systems as well.

(2) Lowering relaxation temperatures in BT-B*M*O_3 relaxor ceramics

In terms of properties of BT-based relaxors, the permittivity maxima should be pushed below room temperature, while maintaining the flatness and high

permittivity values, to make them technologically more attractive. Thus far, as per author's knowledge, high permittivity values (>1000), which are relatively temperature-independent, with maximum in dielectric permittivity significantly below room temperature has not been achieved for a particular ceramic composition.

(3) Compatibility of MLCCs with Ni electrodes

The compatibility of MLCCs with cheap Ni electrodes, which are widely used in capacitor industry, should be studied. The technology based on Ni electrodes requires co-firing at low oxygen partial pressures. This further necessitates studying transport properties over a wider range of oxygen partial pressure, especially lower oxygen partial pressures.

(4) Using defect chemistry for other applications *e.g.* oxygen conduction

It was demonstrated in this thesis that the knowledge of defect chemistry can be used to further increase the resistivity of these ceramics and make them better suited for high temperature and electric fields. However, the same knowledge can be used for other purposes e.g. improving oxygen conduction in these Bi-based ceramics and make them better suited for applications like solid oxide fuel cells (SOFCs). In case of BT-BZT, the results in this thesis indicate that BT-BZT already has higher oxygen vacancy concentration that unmodified BT. Preliminary studies using O-18 annealing experiments, followed by secondary ion mass spectroscopy to get depth profile (Fig. 12.1) also indicated higher

contribution of oxygen vacancies to total conduction in BT-BZT as compared to unmodified BT. The preliminary results for BT, BT-3BZT and BT-7.5BZT have been shown below in Fig. 12.1.

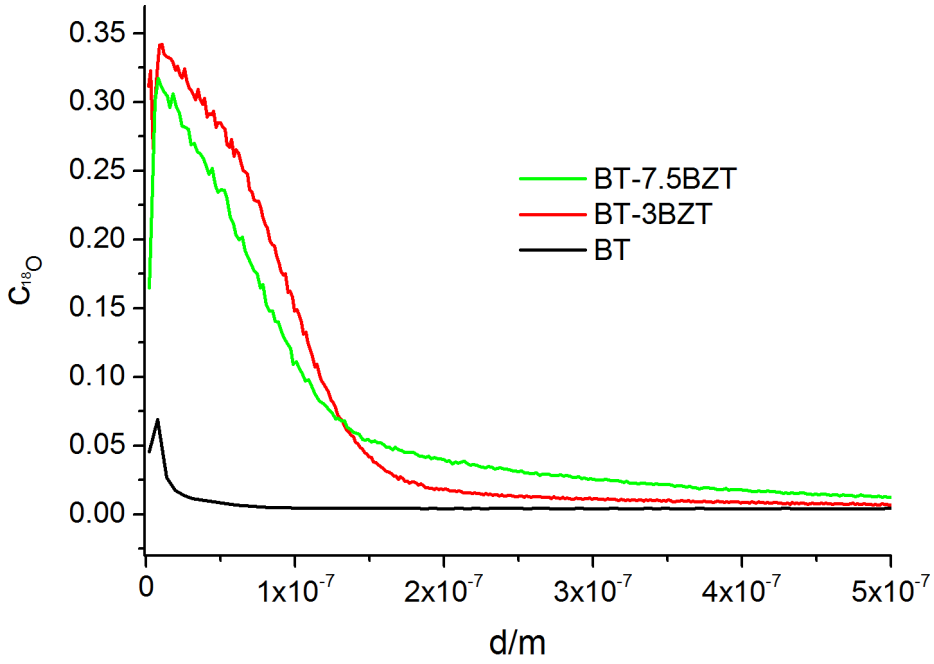

Fig. 12.1. O-18 diffusion profile in BT, BT-3BZT and BT-7.5BZT. The y-axis is O-18 concentration and x-axis is distance from grain boundary. It can be noted that just 3% BZT was sufficient to enhance oxygen conductivity by several times.

The oxygen ion conduction can be further improved by using several approaches *e.g.* band-gap engineering and defect engineering. Higher band gaps should favor ionic conduction as electronic conduction should become difficult on increasing band gaps owing to energy requirements. One way of improving band gaps is by increasing lattice volume (*e.g.* by replacing Ti with bigger cations like Zr), based on work by Randall *et al.* utilizing Vegard's law. [1] The second approach which can be used is defect engineering. A higher concentration of

acceptors may result in higher oxygen vacancy concentration, thus improving oxygen conduction. The same was attempted for BT-25BZT ceramics, where acceptor doping was accomplished by introducing 4% and 6% charge deficiency on A-site by intentionally creating bismuth vacancies during batching step of ceramic processing. The preliminary results show that oxygen transport number (t_i) does improve on doing this, where t_i increases from ~0.05 for BT to close to 0.5 at 500 °C for bismuth deficient BT-25BZT.

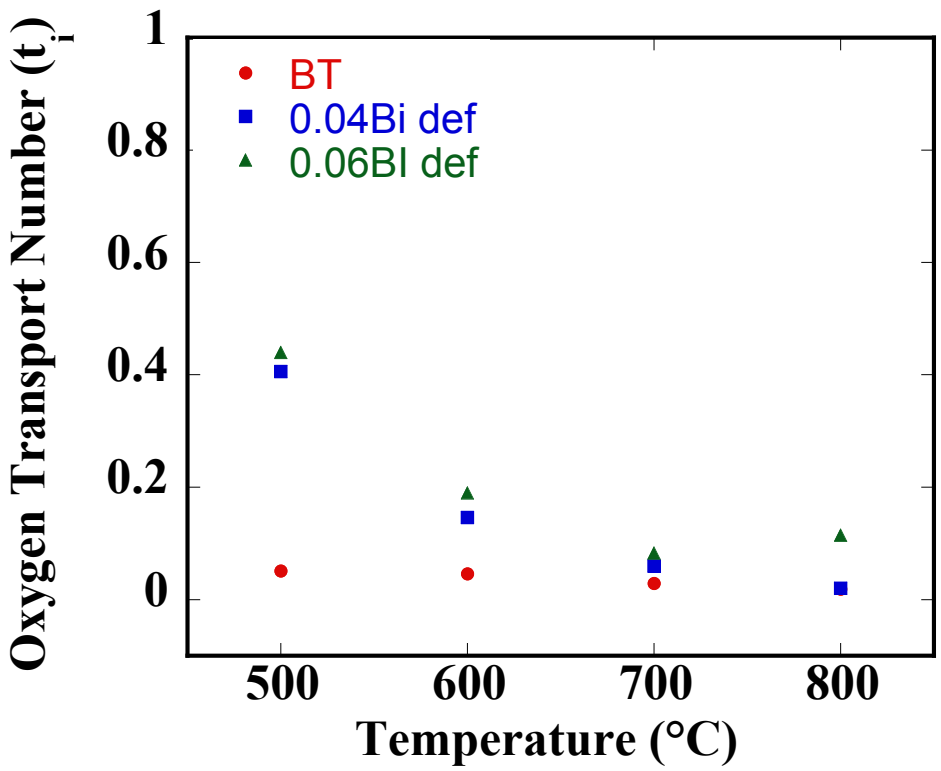

Fig. 12.2. Oxygen transport number for $BaTiO_3$ and 0.04 and 0.06 charge deficient BT-25BZT ceramics.

(5) First principle calculations

First principle calculations (*e.g.* Density Functional Theory) can be performed to model both static and dynamic processes in BT-BMO$_3$ ceramics. The results on electronic structure obtained can help understand the conduction and optical properties in a better way. Several thermodynamic parameters *e.g.* defect formation energy values can also be obtained, which can help minimize the reliance on defect chemistry of unmodified BT for defect calculations for BT-BMO$_3$ ceramics. Efforts should also be made to predict location of T_{max} in dielectric relaxors using first principle studies. As mentioned earlier, tailoring T_{max} without affecting permittivity gets challenging a lot of times. Making new compositions in laboratory via usual solid-state route is a time consuming process and first principle calculation can help researchers make better decisions about which compositions should be tried first. Researchers have tried to develop guidelines to predict degree of diffuseness, for example, based on tolerance factor (Fig. 12.3).[2] However, predicting degree of diffuseness, T_{max} and maximum permittivity at the same time, without first principle modeling tools, sounds difficult.

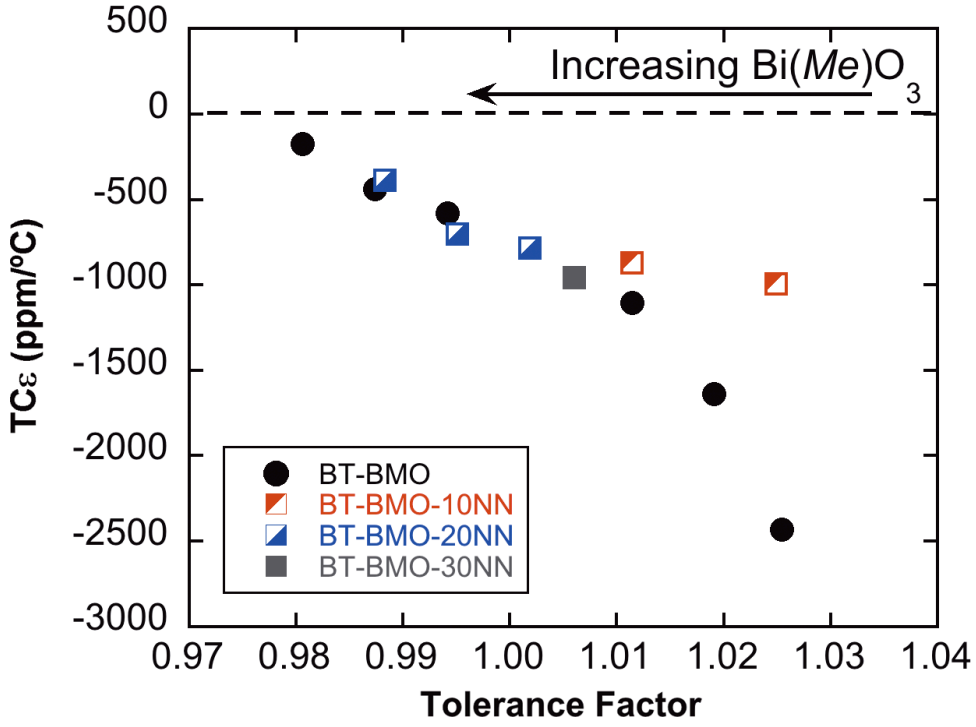

Fig. 12.3. Figure showing the relationship between tolerance factor and temperature coefficient of permittivity.[2] More such tools are required to enhance the predictive capabilities while designing new materials.

(6) Investigating the secondary phases

As was seen in Figs. 9.7.7 and 9.7.8, secondary phases were observed in transmission electron microscopy for BT-25BZT ceramics. Attempt should be made to extract the exact composition of these secondary phases and it should be tried to prepare ceramics of these compositions in the laboratory. Even though they were present in small quantities, this will help determine if they at all affect the dielectric or transport properties in Bi-containing perovskites.

(7) Enhancing depolarization temperature and low field piezoelectric coefficient

In case of Pb-free BNT-based ceramics, depolarization temperature represents an important parameter above which these ceramics cannot be used as sensors, as their remnant polarization and strain drop significantly. Even though significant progress has been made towards improving high field piezoelectric coefficients (d_{33}*), making them excellent candidates for actuator applications, the drop in low field d_{33} above depolarization temperature potentially limits their use as sensors at higher temperature. Even below depolarization temperature, the low field d_{33} haven't been able to match values exhibited by Pb-based systems like lead zirconate titanate. Increasing low field d_{33} and depolarization temperature (at the moment the limit seems to be ~200 °C), still remain a big hurdle for various applications.

(8) Need for simpler system to study fatigue mechanisms

As far as electromechanical fatigue in concerned in BNT-based systems, they are still not well understood. In fact, even fatigue in lead zirconate titanate is still debated upon, even though plethora of data is available for this system. To understand fatigue in BNT-based systems, simpler systems should be selected, unlike the complex ternary which was used in this thesis owing to requirement of anotherness. A simpler system will provide much better control over several variables including defects, agglomeration of cations, volatility, solubility limit, structural characterization and others. Fatigue studies in BNT-based systems get complicated by factors such as prominent temperature-dependent phase changes,

electric field-induced phase transformations and also composition-dependent phase changes.

(9) Other factors affecting fatigue in BNT-based ceramics

In this thesis, only the effect of defects has been investigated in an effort to understand fatigue mechanisms, However, there are several other factors which can have significant impact on fatigue. Some of them are mentioned below.

(9.1) Development and propagation of crack

(9.2) Interaction of electrodes with ceramics

(9.3) Formation of dead layers beneath electrode surface

(9.4) Domain fragmentation on electrical cycling

(9.5) Self-heating on repeated cycling

(9.6) Agglomeration of defects at interfaces such as grain boundaries

(9.7) Change in temperature and field required for phase transition with cycling

It should be noted that these are just some of the possible mechanisms, and a full-fledged study is required to elucidate more on fatigue mechanisms.

(10) Electrocaloric effect

Electrocaloric effect is defined as a material which shows reversible temperature change under electric field, and has use in potential applications *e.g.* computer cooling and others. The BNT-based relaxors, especially the ones which exhibit ergodic relaxor behavior can be attractive candidate for electrocaloric applications. They exhibit a reversible field induced phase transition, where at

high electric fields, one gets large polarization, which is lost on removing the field. Using the Maxwell relations, it can be shown that the following relationship holds true for change in polarization and temperature[3]:

$$\Delta T = -\frac{1}{\rho}\int_{E1}^{E2}\frac{T}{C}\left(\frac{\partial P}{\partial T}\right)_E dE \qquad \text{Eq. 12.1}$$

where, T is temperature, E is electric field, P is polarization, C is heat capacity and ρ is material density. Therefore, the reversible polarization change in ergodic relaxors can be associated with reversible temperature change and can be used for electrocaloric applications.

(11) Oxygen conduction

Recently, it was shown that BNT exhibits significant oxygen conduction [4]. The oxygen conduction in these systems can be improved using approaches mentioned above for BT-BZT system—band gap engineering and defect engineering. Oxygen conduction measurements were attempted on $(Bi_{1/2}Na_{1/2})ZrO_3$ which should have a higher lattice volume that BNT. The preliminary results have been shown in Figure 12.4 for 0.02 charge charge deficient $(Bi_{1/2}Na_{1/2})ZrO_3$. The charge deficiency was created by making the ceramics bismuth deficient intentionally.

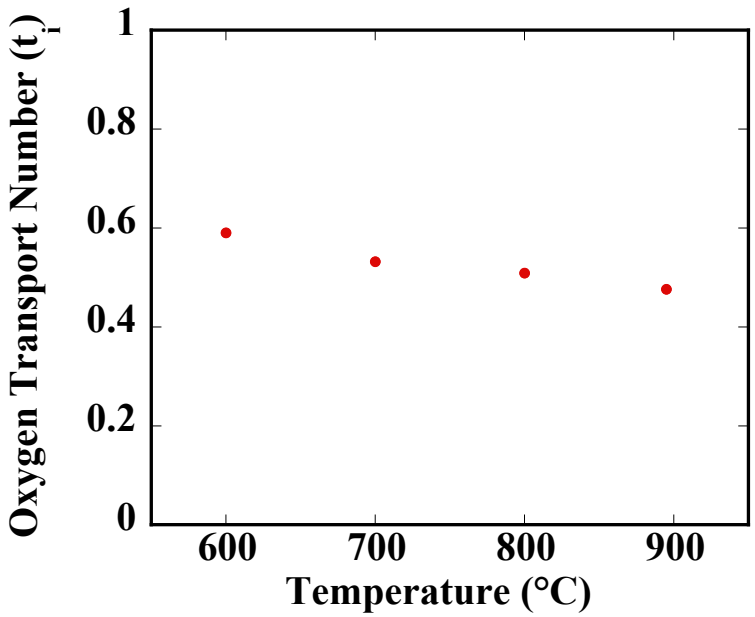

Fig. 12.4: Oxygen transport number for 0.02 charge deficient $(Bi_{1/2}Na_{1/2})ZrO_3$ ceramics.

However, these ceramics had extremely poor density values and it was hard to get single phase without introducing bismuth vacancies, which also indicates that there is significant scope of future research on these systems.

References

[1] Lee S, Levi RD, Qu W, Lee SC, Randall CA. Band-gap nonlinearity in perovskite structured solid solutions. Journal of Applied Physics 2010;107:023523.
[2] Raengthon N, McCue C, Cann DP. Relationship between tolerance factor and temperature coefficient of permittivity of temperature-stable high permittivity BaTiO3–Bi (Me) O3 compounds. Journal of Advanced Dielectrics 2016;6:1650002.
[3] Mischenko A, Zhang Q, Scott J, Whatmore R, Mathur N. Giant electrocaloric effect in thin-film PbZr0. 95Ti0. 05O3. Science 2006;311:1270-1.
[4] Li M, Pietrowski MJ, De Souza RA, Zhang H, Reaney IM, Cook SN, et al. A family of oxide ion conductors based on the ferroelectric perovskite Na0. 5Bi0. 5TiO3. Nature materials 2014;13:31-5.